HAL
open science

Sustainable Hydrogen Production on PGM-free Electrocatalytic Materials in Anion Exchange Membrane Water Electrolyzer (AEMWE)

Carlos Victor Mendonca Inocencio

To cite this version:

Carlos Victor Mendonca Inocencio. Sustainable Hydrogen Production on PGM-free Electrocatalytic Materials in Anion Exchange Membrane Water Electrolyzer (AEMWE). Analytical chemistry. Université de Poitiers, 2022. English. NNT : 2022POIT2299 . tel-04011299

HAL Id: tel-04011299

https://theses.hal.science/tel-04011299v1

Submitted on 2 Mar 2023

HAL is a multi-disciplinary open access archive for the deposit and dissemination of scientific research documents, whether they are published or not. The documents may come from teaching and research institutions in France or abroad, or from public or private research centers.

L'archive ouverte pluridisciplinaire **HAL**, est destinée au dépôt et à la diffusion de documents scientifiques de niveau recherche, publiés ou non, émanant des établissements d'enseignement et de recherche français ou étrangers, des laboratoires publics ou privés.

THÈSE

Pour l'obtention du Grade de

DOCTEUR DE L'UNIVERSITÉ DE POITIERS

(Faculté des Sciences Fondamentales et Appliquées)
(Diplôme National - Arrêté du 25 mai 2016)

École Doctorale : Chimie Écologie Géosciences Agrosciences « *Théodore Monod* »

Secteur de Recherche : Chimie théorique, physique, analytique

Présentée par :

Carlos Victor MENDONCA INOCENCIO

****

Réduction de l'eau en dihydrogène sur nanomatériaux d'électrode sans platinoïde

****

Directeur de Thèse : K. Boniface KOKOH
Co-directrice de Thèse : Cláudia GOMES DE MORAIS

****

Soutenue le 08 Décembre 2022 devant la Commission d'Examen

****

JURY

Elena SAVINOVA	Professeur ICPEES – Université de Strasbourg	Rapporteur
Frédéric FAVIER	Directeur de recherche au CNRS ICGM - Montpellier	Rapporteur
Sophie DIDIERJEAN	Professeur LEMTA – Université de Lorraine	Présidente
Frédéric FOUDA-ONANA	Docteur-ingénieur au CEA-LITEN Grenoble	Examinateur
Cláudia GOMES DE MORAIS	Maître de conférences IC2MP – Université de Poitiers	Examinateur
K. Boniface KOKOH	Professeur IC2MP – Université de Poitiers	Examinateur

Acknowledgements

This thesis was carried out in the SAMCat (Du Site Actif au Matériau Catalytique) team, belonging to the IC2MP (Institut de Chimie des Milieux et Matériaux de Poitiers), financed by Région Nouvelle-Aquitaine and Région Grand-Angoulême. Therefore, I would like to thank all these institutions for making it possible to carry out the study presented herein.

I also thank Mrs. Sophie Didierjean (Professor at Université de Lorraine) and Mr. Frédéric Fouda-Onana (Researcher at CEA-Liten) for having accepted the role of "Examinateurs" in my thesis defense. And this acknowledgement is extended to Mrs. Elena Savinova (Professor at Universié de Strasbourg) and Mr. Frédéric Favier (Research Director at CNRS) for assuming the double mission of "Examinateurs" and "Rapporteurs".

I would like to thank Cláudia Morais (Maître de Conférences at Université de Poitiers) and Mr. Boniface Kokoh (Professor at Université de Poitiers) very much for all the exchange of the last 3 years. It was an honor to be supervised by them during this period, which I could learn a lot about science, but also about the scientific career. Although they have always been close to support me in the project, I also received the space to express and pursue my ideas, an approach that resulted in my professional development.

During the last two years, I had the opportunity to co-supervise three interns (Clémence, Victor and Tokiniaina) who also deserve my thanks. By following the proposed methodology, they boosted quality data acquiring, which enabled me to evolve quicker the interpretation of my results.

I would like to thank all IC2MP members, in special Mr. Clément Comminges, Mr. Têko Napporn, Mr. Aurélien Habrioux, Mrs. Karine Servat, Mr. Jean-Christophe Guillon, Mrs. Isabelle Batonneau-Gener, Mrs. Julie Rousseau, Mrs. Nadia Guignard, Mrs. Sophie Morisset, Mrs. Sandrine Arrii, Mr. Lilian Eloy, Mrs. Laetitia Maziere, Mrs. Morgane Vilette, Mr. Nicolas Bion and Mrs. Céline Fontaine, for all availability, support and contribution since my arrival in Poitiers. I also would like to thank Mrs.

Christine Canaff for all the availability and patience during the XPS formation provided, besides all the contribution throughout this work.

I thank again Mr. Frédéric Fouda-Onana, at this case due to the collaboration in the development of a high-performance AEMWE system. Furthermore, I also would like to thank Mr. Anthony Thomas and Mr. Gaetano Squadrito for taking the time to teach me about membrane electrode assembly and operation of electrolyzer system.

I also would like to thank my peers from IC2MP. In the last years, a Brazilian community (Fabiano, Thamyres, André, Paula, Leonardo, Iane, Yuri, João, Lucas, Camila, etc.) has been established at IC2MP, and to all of them I want to say: *Muito obrigado pelos momentos, discussões e brincadeiras. São lembranças que levarei para sempre. Mas entendam, o certo é biscoito… não tem jeito.* Certainly, I also thank Paul, Karla, Perla, Lola, Franck, Roald, Damir, Charly, Nollwenn, Thibaud, Ilhem, Lucas, etc., for all experiences in this period.

Last, but far of being least, I would like to thank all my family who have been supporting me throughout my life; my mother, father, brother, nephews, (future) niece, mother-in-law, brothers-in-law and sisters-in-law. Finally, I would like to especially thank my wife, Camila, who was my biggest supporter in pursuing a doctorate in Europe. If it weren't for such an encouragement, I wouldn't be in Poitiers right now writing this text. Therefore, I dedicate this thesis to her.

Content Table

General Introduction……1

Chapter I: Bibliographic Study……..……...…5

I.1. Water splitting for sustainable hydrogen production: Challenges…....6

I.2. Hydrogen production from the electrochemical HER……9

I.2.1. Electrocatalysis of HER in aqueous medium: Fundamentals……...9

I.2.2. Experimental tools for testing, characterizing, and validating a HER electrocatalyst……..12

I.2.2.1. Electrode activity, onset potential and overpotential……...12

I.2.2.2. Tafel slope and exchange current density……14

I.2.2.3. Faradaic efficiency……15

I.2.2.4. Turnover frequency and turnover number……..15

I.2.2.5. Stability/Durability……..16

I.2.3. Synthesis and catalytic properties of noble metal-based electrocatalysts for HER……...17

I.2.4. Designing heterogeneous non-precious metal electrocatalysts for HER…….24

I.2.4.1. Metal sulfides as heterogeneous catalysts for HER…….25

I.3. New trends and challenges……62

I.3.1. From hydrogen to system: Storage challenges…….62

I.3.2. Instruction for designing new generation of robust and low cost electrocatalysts……..64

I.4. Conclusions and Outlooks……65

Chapter II: Experimental Part……66

II.1. Electrocatalysts preparation……..66

II.2. Physicochemical characterizations……..68

II.2.1. Inductively Coupled Plasma Optical Emission Spectrometry (ICP-OES)……68

II.2.2. X-ray Diffraction (XRD).....69

II.2.3. Raman Spectroscopy.....72

II.2.4. X-ray Photoelectron Spectroscopy (XPS)……...73
II.2.5. Electron Microscopy…….76
II.2.5.1. Scanning Electron Microscopy (SEM)……...77
II.2.5.2. Transmission Electron Microscopy (TEM) and Scanning Transmission Electron Microscopy (STEM)…….78
II.3. Electrochemical characterizations……80
II.3.1. Types of electrochemical measurements……..80
II.3.1.1. Linear Sweep Voltammetry (LSV) and Cyclic Voltammetry (CV)…….80
II.3.1.2. Chronoamperometry (CA)……..81
II.3.1.3. Electrochemical Impedance Spectroscopy (EIS)…….81
II.3.2. Adopted electrochemical methodology……...82
II.3.2.1. Three-electrode system……...82
II.3.2.2. Anion Exchange Membrane Water Electrolyzer (AEMWE) system……86
Chapter III: Taking Advantage of Teamwork: Unsupported Cobalt Molybdenum Sulfide as an Active HER Electrocatalyst in Alkaline Media...90
III.1. Introduction……..91
III.2. Results and Discussion……..92
III.2.1. Physicochemical characterizations……92
III.2.2. Electrochemical characterizations……101
III.3. Conclusion……107
Appendix A. Supporting Information Chapter III……109
Chapter IV: A Step Forward: Hydrogen Production on Cobalt Molybdenum Sulfide Electrocatalyst in Anion Exchange Membrane Water Electrolyzer..112
Appendix B. Supporting Information Chapter IV……124
Chapter V: HER Activity of Nickel Molybdenum Sulfide Electrocatalyst as Function of the Ionomer in the Ink Formulation……..128
V.1. Introduction……...129
V.2. Results and Discussion……...130
V.3. Conclusion……..148
Appendix C. Supporting Information Chapter V……..150

General Conclusion and Perspectives……..160
Scientific Production List…….164
REFERENCES…….165

General Introduction

The chemical composition of the atmosphere has a huge impact on Earth's surface temperature, and this is not a novelty. In 1896, Arrhenius calculated and published the influence of carbonic acid, which can be produced from carbon dioxide and water reaction, atmosphere concentration in world temperature[1]. Callendar correlated the artificial production of carbon dioxide, accrued from fuel combustion, with global warming in 1938[2]. Despite that, such subject was object of debate during decades, and little has been done to stop climate change. However, the impacts of climate change have been increasingly evident and, as result, world leaders have put efforts to promote climate actions.

Undoubtedly, the climate change and the energy sector are strongly correlated. The increase of industrialization levels and advances in technology resulted in more comfort to people; nonetheless, the raise of energy demand is the side effect. In addition, the continuous population growth is another factor that enlarges this demand. The obvious outcome has been the augmentation of energy consumption recorded during the last decades. The biggest environmental concern regarding the energy consumption is also related to where it comes from. Most of energy is still extracted from fossil feedstocks, e.g., petroleum and coal, due to their low price in comparison to other alternatives. However, it is a common sense that their use represents a big contribution for global warming. Hence, the remaining adoption of fossil feedstocks is very onerous for nature.

Energy transition is mandatory and the Sixth Assessment Report (AR6) of Intergovernmental Panel on Climate Change (IPCC) has made it clear that it is also urgent. Sunlight and wind emerge as interesting alternative green energy sources since they do not produce carbon footprint and possess renewable feature. Nonetheless, these sources have an intermittent character, i.e., they can alternate between periods of high and low, or even no, energy production without following any determined periodicity. This drawback can be overcome by applying convenient energy storage strategies.

Solar and wind energy can be used to produce green hydrogen, which plays a role as energy carrier, in a process called water electrolysis. Basically, in this process, water is split into hydrogen and oxygen, both containing high purity levels, with the use of electricity[3]. Oxygen is evolved in the anode compartment due to water oxidation, in a half-reaction called oxygen evolution reaction (OER), while water is reduced at the cathode compartment,

generating hydrogen as result of hydrogen evolution reaction (HER), in another half-reaction.

It is important to highlight that hydrogen already has a big importance in many chemical industry sectors, e.g., steel, fertilizers and biorefinery. Nonetheless, most industrial hydrogen production is based on hydrocarbon reforming and coal gasification processes. Therefore, as the reactants employed in these processes also compose the group of fossil feedstocks, the obtained hydrogen contributes for climate change. Thus, these sectors will need to replace their source of hydrogen to achieve the established decarbonization goals, and water electrolysis will also be important in this context.

The thermodynamic voltage of water splitting is 1.23 V at 25 ^{o}C. However, surplus potential, also known as overpotential, is required during operation to overcome activation barriers in the cathode and anode, besides resistances in the system[4]. The overpotentials related to the cathodic and anodic reaction can be reduced with the use of electrocatalysts. Nonetheless, the benchmarking catalysts are noble metal-based materials, which elevates the cost of the process, besides the concern related to their earth-abundance. For this reason, an important task pursued by researchers in electrochemistry field is the search for alternative low-cost and earth-abundant electrocatalysts, containing high activity, selectivity, and stability for HER and OER, i.e., candidate materials capable of replacing noble metal ones. This thesis focuses on proposing new materials for HER and, therefore, it will be the most studied reaction herein.

Profiting from a biomimetic approach, Nørskov group[5] showed theoretically and experimentally that MoS_2 can be a good HER electrocatalyst when nanostructured, due to high proton reduction activity. It shed light on the potential of molybdenum sulfides to catalyze this reaction, and it became one of the most promising class of materials to replace platinum in HER, resulting in the writing of several reviews focused only on the use of these materials for HER[6-8].

The HER process can be performed in different pH's, and this parameter will impact the ionic conductivity, besides the source of proton. Despite HER is favored at low pH's, it hinders the application of some materials due to corrosion issues. Furthermore, HER represents half-reaction, the other half concerns the sluggish OER, for which the most representative earth-abundant catalysts are transition metal oxides/hydroxides; these are

not stable in acidic environment. Thus, it exists an increasingly interest in performing the water electrolysis in alkaline media.

The technological device responsible to perform the reaction at large scale is called "electrolyzer", and it is classified according to the material used in the compartments' separation, which can be a diaphragm, membrane, solid oxide or ceramic[3]. Furthermore, these materials are also responsible for the ionic conduction during operation. This thesis focuses on the implementation of anion exchange membrane water electrolyzer (AEMWE) technology, which allows the permeation of hydroxyl species through the membrane from cathode to anode and operate at high pH. However, in alkaline media, an additional step of water dissociation is necessary to initiate the HER, and molybdenum sulfide is not a good catalyst for this step; for this reason, its HER activity is reduced in alkaline environment. Catalyst design strategies must be developed to maintain a good HER activity in molybdenum-based sulfides at high pH. Hence, the main goal of this thesis involves the development of molybdenum-based sulfides active for the HER in alkaline media, and their further implementation in an AEMWE device; this last step has never been reported.

In the first chapter, it is presented the bibliographical study of HER, concerning the fundamentals of reaction and relevant tools to evaluate the activity of the catalysts. Yet, it is reported the development of strategies for the synthesis of noble metal-based materials, besides transition metal sulfides, with special focus to the molybdenum-containing sulfides. Finally, a brief discussion about the hydrogen storage challenges and instructions concerning the development earth-abundant and cheap catalysts are provided. Therefore, this chapter fulfills its informative role concerning water splitting, being a good starting point for those who are making their debut in the field of water electrolysis and application of transition metal sulfides in the cathodic reaction, i.e., HER.

The second chapter presents the experimental information. Initially, it is presented, with details to enable further reproduction, the synthesis methodology employed in the production of transition metal sulfides reported herein. Subsequently, the characterizations performed are presented. The characterizations are an extremely important part of the work because they provide information about catalyst activity/stability and the phenomena taking place during reaction, besides to aid on the description of the catalyst before and after reaction. Therefore, the correct choice of characterization allows a quick "assembly of the puzzle", in other words, achieve the scientific conclusion, and avoids excessive experiments.

For this reason, a brief description of the applied characterizations, containing fundamentals and information that can be obtained from the techniques, was provided in the beginning of each sub-section; for deeper learning, the readers are encouraged to access the cited references. Finally, the parameters employed for obtaining the results of next chapters are presented in this second chapter.

The third chapter discusses the strategy of associate the nanostructured 2H-MoS_2 phase, a recognized HER catalyst, with cobalt to boost the water dissociation step required in alkaline media. A study on the synergy of both metals was performed in three-electrode cell, and different Co:Mo composition ratios were applied.

Due to the good performance of $Co_{0.5}Mo_{0.5}S_x$, as verified in third chapter, the fourth chapter was dedicated to the implementation of this material as cathode in an AEMWE device. It is important to highlight that, differently from proton exchange membrane water electrolyzer (PEMWE) applications, the maturity stage of AEMWE still requires the use of liquid support electrolyte in the system, normally potassium hydroxide solution. However, results in fourth chapter were obtained with a concentration ten-fold lower than commonly described in the literature, and $Co_{0.5}Mo_{0.5}S_x$ presented, to the best of our knowledge, the best performance among non-noble metals at such low concentration. Additionally, this is the first report on the application of molybdenum-based sulfide as cathode of AEMWE, representing then a milestone for the possible replacement of platinum by this class of electrocatalysts.

In the fifth chapter, the strategy of associating 2H-MoS_2 to another transition metal-based phase, as done in Chapter III, was expanded to the use of nickel as second metal once it is also recognized for its water dissociation ability. Furthermore, a study was performed by adding different ionomers (specifically, Nafion® and Sustainion® XB-7) to nickel molybdenum sulfide ink formulation. Although it is known that ionomer plays an important role on electrochemical behavior, this is a commonly ignored compound during studies. The fifth chapter makes it clear how huge can be its influence on HER activity and, consequently, how relevant is its interaction with the catalyst. Finally, as far as we know, this is the first report on the use of Sustainion® XB-7 ionomer, which was developed envisaging the application in alkaline environment, for the electrochemical study of transition metal sulfide catalysts.

Chapter I: Bibliographic Study

This chapter is based on the following publication: *"Electrochemical Hydrogen Generation Technology: Challenges in electrodes materials for a Sustainable Energy"*. C.V.M. Inocêncio, Y. Holade, C. Morais, K.B. Kokoh, T.W. Napporn, Electrochem. Sci. Adv. **2022**, e2100206.
https://doi.org/10.1002/elsa.202100206

Abstract

Foresee advanced and innovative strategies is a key approach and constitutes a cornerstone

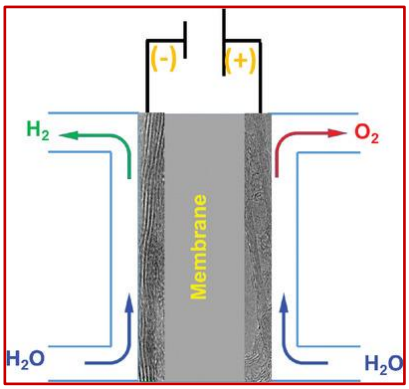

for accessing clean, affordable, and reliable energy to satisfy the world's increasing prosperity and economic growth. To this end, hydrogen energy technologies parade as promising sustainable solutions to the looming energy crisis at either the small or large industrial scale, which will enable to reduce significantly our dependence on conventional energy sources based on fossil fuels without increasing atmospheric CO_2 levels. Water electrolysis with renewable energy is one of the best solutions to produce hydrogen without CO_x (CO and CO_2) emissions. However, the practical realization of this elegant opportunity of paramount importance is facing several challenges, among which are: (i) the efficient design of cathode and anode catalytic materials exhibiting improved intrinsic and durable activity; (ii) the scale-up of the system for the large-scale hydrogen production through the electrochemical water splitting. This review puts these opportunities and challenges into a broad context, discusses the recent research and technological advances, and finally provides several pathways and guidelines that could inspire the development of groundbreaking electrochemical devices for hydrogen production. It also points out the materials design and preparation for the efficient electrochemical production of the molecular hydrogen in acidic and alkaline environments, from a simple electrolytic solution to the water splitting reaction, which is also considered in the process. Furthermore, the main technology keys for designing a reliable electrochemical system will be noticed.

I.1. Water splitting for sustainable hydrogen production: Challenges

The unavoidable increase of the global energy consumption because of the population and economic growth should be theoretical satisfied, in principle, by fossil energy resources, particularly coal. However, this global energy situation is undergoing mutation that is directly correlated to the pollution issues that require the reduction of greenhouse gases [9]. Hence, solving the cumulative nature of carbon dioxide (CO_2) emissions in the atmosphere requires invention and deployment of alternative strategies for carbon-neutral energy production [9]. There is an exciting and elegant alternative that relies on the possibility of converting chemical energy to electrical energy using a so-called electrochemical generator, namely fuel cell (FC), in which many fuels can be used. Particularly, molecular hydrogen (H_2, which has the highest gravimetric energy density among fuels, 122 kJ g^{-1}) enables harvesting a specific energy density of 33 kWh kg^{-1} *versus* 1-9 kWh kg^{-1} for organic/inorganic fuels [10] and produces only non-polluted water during its combustion; for this reason, it is proposed as the potential and ideal candidate for the future energy supply. Hence, a proton exchange membrane fuel cell (PEMFC) powered by hydrogen, from secure and renewable sources, as well as the unlimited oxygen (O_2) from air is the ideal solution to the direct production of electricity for non-polluting devices (vehicles, home). Taken solely, it is very important to notice that H_2 is not energy, but only an energy carrier for storing and transporting energy. In addition, H_2 is a critical chemical feedstock in the modern industry that is used in the synthesis of ammonia for fertilizer and petroleum refining, metallurgy as well as many other chemicals. Furthermore, H_2 does not exist in a free state in the earth's atmosphere, but combined in different molecules (water, biomass, and hydrocarbons, etc.). Thereby, it must be produced before it is used. The current processes for its production are largely based on fossil fuels, and lead to the emission of significant quantities of greenhouse gases [11]. Figure I.1 shows the current three main pathways for H_2 industrial production: steam methane reforming, coal gasification and water electrolysis. The examination of the outputs reveals that H_2 production techniques based on fossil fuels cannot really solve the pollution and CO_2 emission issues [11]. Indeed, in addition to the need of high temperature reaction between hydrocarbon/coal and water, the steam methane reforming and coal gasification lead to simultaneous generation of H_2, CO_2 and other carbon-based species.

Then, this carbon-source compounds as greenhouse gases are finally released into the atmosphere. As a matter, the approach apparently violates our original intention of reducing air pollution and global warming by the employment of hydrogen power. Hence, these two production routes not only aggravate the consumption of fossil fuels, but also contribute to the global CO_2 emission [12-13]. Therefore, seeking a clean, renewable, and efficient strategy for H_2 production is urgently needed.

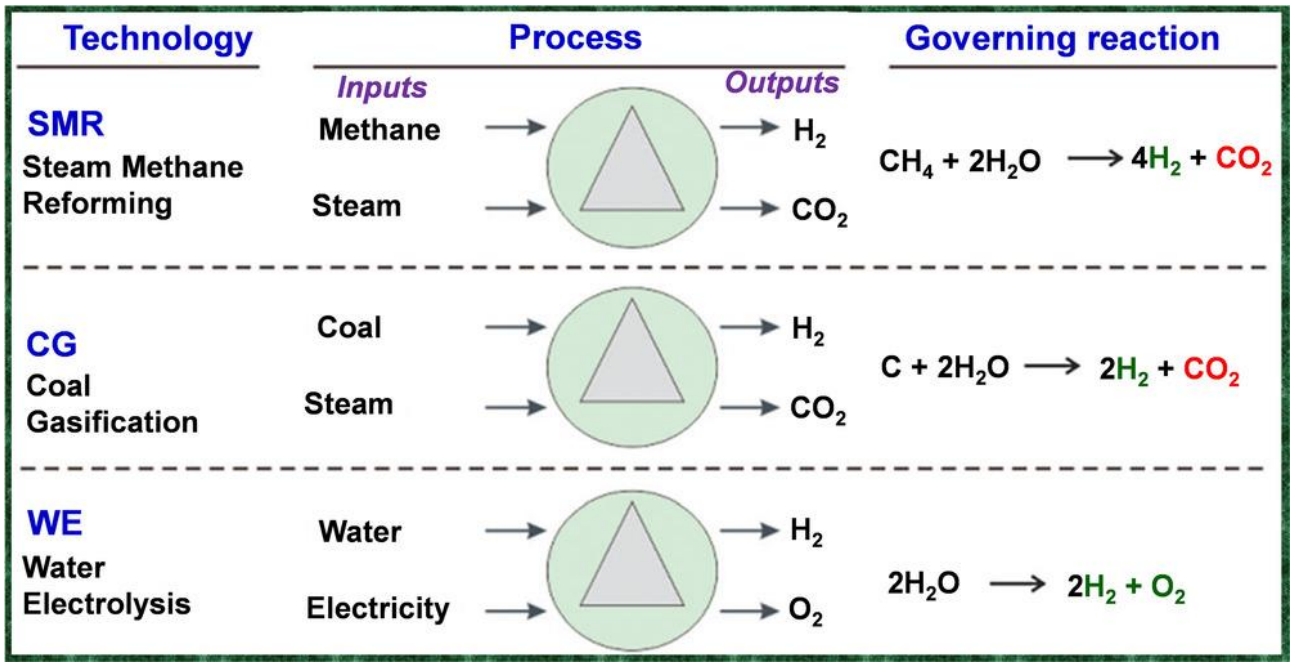

***Figure I.1**. The three main pathways for hydrogen industrial production. Reprinted and adapted with permission from Ref. [14]; Copyright 2015, The Royal Society of Chemistry.*

This problem has intensified interest in various sources such as solar, wind, hydro and other renewable electricity from electrolysis. Hence, H_2 can be cheaply produced by water splitting using solar-to-hydrogen conversion strategy and based on photochemical and photoelectrochemical methods [15-17].

The water splitting by electrolysis (with electricity provided by solar-, wind- or other renewable resources) is one of the promising approaches. A classic electrolyzer has three component parts: an electrolyte, a cathode, and an anode. When a driving force is applied to the electrodes through an external voltage, H_2O are decomposed into H_2 and O_2. It should be noticed that H_2 can be stored for fuel and O_2 released into the atmosphere (or recovered for medical applications). Thus, the water splitting reaction can be divided into two half-reactions: the water oxidation reaction also referred as OER, and the water reduction

reaction known as HER. Depending on the media in which water splitting takes place, the reaction can be expressed chemically in different ways (potentials are quoted against the Standard Hydrogen Electrode [SHE]).

In acidic medium, water is oxidized at the anode and protons are reduced at the cathode:

Anode: $2\ H_2O\ (l) \rightarrow O_2\ (g) + 4\ H^+(aq) + 4\ e^-$, E^0 = 1.23 V vs. SHE (25 °C) (Eq. I.1)

Cathode: $4\ H^+(aq) + 4\ e^- \rightarrow 2\ H_2\ (g)$, E^0 = 0 V vs. SHE (25 °C) (Eq. I.2)

Overall: $2\ H_2O(l) \rightarrow 2\ H_2\ (g) + O_2\ (g)$, ΔE^0 = 1.23 V at 25 °C (Eq. I.3)

with ΔG^0 = +237.2 kJ per mole of H_2.

In alkaline solutions, hydroxides are oxidized at the anode and water is reduced at the cathode:

Anode: $4\ OH^-\ (aq) \rightarrow O_2\ (g) + 2\ H_2O\ (l) + 4\ e^-$, E^0 = 0.40 V vs. SHE (25 °C) (Eq. I.4)

Cathode: $4\ H_2O\ (l) + 4\ e^- \rightarrow 2\ H_2\ (g) + 4\ OH^-\ (aq)$, E^0 = -0.83 V vs. SHE (25 °C) (Eq. I.5)

Overall: $2\ H_2O\ (l) \rightarrow 2\ H_2\ (g) + O_2\ (g)$, ΔE^0 = 1.23 V at 25 °C (Eq. I.6)

with ΔG^0 = +237 kJ per mole of H_2.

The overall reaction indicates that whatever the media in which water splitting takes place, the water electrolysis needs energy to proceed. In other words, energy (through cell voltage) must be applied to achieve the electrochemical water splitting. The minimal value corresponds to the thermodynamic voltage of water oxidation that is 1.23 V at 25 °C and 1 bar. This reaction is endothermic 286 kJ per mol and 163 J per mol K of enthalpy and entropy change for H_2, respectively. It is important to notice that this value is temperature-dependent and can thereafter be manipulated by increasing or decreasing the electrolytic temperature, and 1.48 V at 25 °C of thermoneutral voltage, which is the standard to evaluate energy efficiency. However, because of the resistance losses in the cell, applied voltages must be higher than the thermodynamic potential value to achieve electrochemical water splitting. The surplus of potential is known as overpotential (η) and it represents the voltage required to surmount especially the intrinsic activation barriers from the anode (η_a) and cathode (η_c), as well as some other polarizations (η_{other}) such as electrolyte and contact resistances. Thus, the practical operational voltage (E_{op}) can be described as

$E_{op} = \Delta E^0 + \eta_a + \eta_c + \eta_{other}$ [18]. Practically, η_{other} can be minimized by optimizing the design of the electrolytic cell, whereas η_a and η_c have to be minimized by highly active OER and HER catalysts, respectively [14]. Thus, it becomes obvious that the reduction of the overpotentials by using suitable robust and low-cost catalysts for both reactions is the central question to make the water splitting reaction energy-efficient and economic. Herein, the focus will be dedicated to the most important recent results on catalyst and electrode designs used for the electrochemical HER and OER. Prior to that, special attention will be drawn to key points for understanding the fundamentals of both reactions in acidic and alkaline environments from a simple electrolytic solution to the testing requirements.

I.2. Hydrogen production from the electrochemical HER

I.2.1. Electrocatalysis of HER in aqueous medium: Fundamentals

This introduction section to HER in aqueous medium provides key learning points about the basic principles of electrochemical HER and evaluation approaches of electrocatalysts. We focus on: (i) reactions (in acidic and neutral/alkaline medium), (ii) HER as a multistep reaction process involving different mechanisms and Tafel slopes, (iii) activity descriptors in both media. HER is described with Eq. I.7 in acidic environment (protons are reduced, $E^0(H^+/H_2)$= 0 V vs. SHE at 25 °C) and Eq. I.8 in alkaline media (water molecules are reduced, $E^0(H_2O/H_2)$ = -0.83 V vs. SHE at 25 °C). At the boundary of chemical reduction of H^+ or H_2O, $P_{H2}/P^0 = 1$. In literature, most of potentials are quoted against the Reversible Hydrogen Electrode (RHE), i.e., the apparent standard potential of the H^+/H_2 couple at the given pH. The potential of RHE is defined as E_{RHE} (V vs. SHE)= –0.059 pH. Thus, potentials measured *versus* any reference electrode (RE) can be converted *versus* the RHE value by using Eq. I.9. Hence, in aqueous medium, HER is expected to start at 0 V vs. RHE.

$$2\,H^+(aq) + 2\,e^- \rightarrow H_2(g),\ E(\text{V vs. SHE}) = -0.059\text{pH} \qquad \text{(Eq. I.7)}$$

$$2\,H_2O\,(l) + 2\,e^- \rightarrow H_2\,(g) + 2\,OH^-(aq),\ E(\text{V vs. SHE}) = -0.827 + 0.059(14 - \text{pH}) \qquad \text{(Eq. I.8)}$$

$$E(\text{vs. RHE}) = E(\text{vs. RE}) + E^0_{RE}(\text{vs. SHE}) + 0.059\text{pH} \qquad \text{(Eq. I.9)}$$

Basically, HER is a multistep reaction process. While the HER mechanism in alkaline media is still ambiguous and lead to debates, two different mechanisms involving three possible

reactions (also called steps) have been clearly identified and accepted by the electrochemists community in acidic medium. The dominant reaction mechanism in the HER process can be theoretically indicated by a Tafel slope, which can be obtained from experimental data and relates the rate of an electrochemical reaction to the overpotential (dependence of steady-state current densities on a variety of overpotentials) [13-14, 19]. In acidic media, the first step is the so-called Volmer step (also known as the discharge process) and concerns the reaction of an electron with a proton forming an intermediate state of an adsorbed hydrogen atom (H_{ads}) on the active site of the catalytic surface, as drawn by Eq. I.10. The corresponding Tafel slope is given by Eq. I.11.

$H^+(aq) + e^- \rightarrow H_{ads}$ (Step 1, Volmer reaction) (Eq. I.10)

$$b_V = 2.303\times10^3 \frac{RT}{\alpha F} \quad \text{(Eq. I.11)}$$

In this equation, b_V is the Tafel slope (mV dec^{-1}), α is the symmetry coefficient (typically, $\alpha \approx 0.5$), F is the Faraday constant (96 485 C mol^{-1}), R is the ideal gas constant (8.314 J K^{-1} mol^{-1}), and T is the absolute temperature (K). Hence, the Volmer reaction is characterized by a Tafel slope of b_V = 116.2, 118.2 and 120.2 mV dec^{-1} at 20, 25 and 30 °C, respectively. Thus, the temperature significantly affects the value of b_V.

After forming H_{ads}, HER can proceed by two other steps that are radically opposed (Faradaic and non-Faradaic reactions) to generate the final product that is H_2. The first scenario happens when the H_{ads} coverage is low, so that the adsorbed hydrogen atom prefers to couple with a new electron and another proton in the electrolyte to evolve H_2. This step (electrochemical desorption) constitutes the first mechanism and is named Heyrovsky reaction, Eq. I.12. The corresponding Tafel slope is given by Eq. I.13.

$H_{ads} + H^+(aq) + e^- \rightarrow H_2(g)$ (Step 2, Heyrovsky reaction) (Eq. I.12)

$$b_H = 2.303\times10^3 \frac{RT}{(1+\alpha)F} \quad \text{(Eq. I.13)}$$

Hence, the Heyrovsky reaction is characterized by a Tafel slope of b_H = 38.7, 39.4 and 40.1 mV dec^{-1} at 20, 25 and 30 °C, respectively.

However, at a relatively high H_{ads} coverage, the recombination between the adjacent adsorbed hydrogen atoms is dominant, which is called as Tafel reaction, also known as the chemical desorption step (Eq. I.14). The corresponding Tafel slope is given by Eq. I.15: the absence of the symmetry coefficient (α) is simply related to the fact that this step does not involve any adsorption process of an aqueous species.

$$H_{ads} + H_{(ads)} \rightarrow H_2\,(g) \text{ (Step 3, Tafel reaction)} \qquad \text{(Eq. I.14)}$$

$$b_T = 2.303\times10^3 \frac{RT}{2F} \qquad \text{(Eq. I.15)}$$

Hence, the Tafel reaction is characterized by a Tafel slope of b_T = 29.1, 29.5 and 30.0 mV dec^{-1} at 20, 25 and 30 °C, respectively. It can be concluded that the impact of the temperature on b_H and b_T values is less important. It is worth of nothing that the Tafel slope is the intrinsic property of an electrocatalyst. The Tafel equation that gives this value was first deduced experimentally before being later shown to have a theoretical justification. In practice, it is obtained from the slope of the linear part of Tafel plots (see ***Section I.2.2***). For the above calculations, if the experimental Tafel slope of an electrocatalyst is around 29 mV dec^{-1}, it is suggested that the Tafel reaction (chemical desorption step) is the rate determining step, and the HER catalyzed by this electrocatalyst proceeds via the Volmer-Heyrovsky mechanism (Eqs. I.10 and I.14). However, for an experimental value around 39 mV dec^{-1}, the Volmer reaction (electrochemical desorption step) is the rate determining step, and the HER catalyzed by this electrocatalyst proceeds through the Volmer-Heyrovsky mechanism (Eqs. I.10 and I.12). In practice, mix mechanisms are obtained. Regardless of the routes by which HER occurs, H_{ads} is always involved. Thus, the free energy of hydrogen adsorption (ΔG_H) is widely accepted to be a descriptor for a hydrogen-evolving material. Basically, using the acidic solution as model, the interaction of H^+ species with the catalyst surface should not be neither too weak (no adsorption via Volmer reaction, Step 1) nor too strong (no desorption via Heyrovsky (Step 2) or Tafel (Step 3) reaction, leading to the accumulation of the reaction intermediates: the active sites on the catalytic surface are always occupied by H_{ads}, hence poisoning the catalyst. The state-of-the-art HER catalyst is platinum (Pt) and its corresponding ΔG_H is roughly zero. For a large and negative ΔG_H, H_{ads} is bound strongly with the electrode surface, making the initial Volmer step easy, but the subsequent Tafel or Heyrovsky steps difficult (chemical or electrochemical desorption will not happen).

Contrariwise, a large and positive ΔG_H means that H_{ads} has a weak interaction with the electrode surface, resulting in a slow Volmer step that limits the overall turnover rate. Therefore, an optimal non-Pt HER catalyst should provide appropriate surface properties and have a nearly zero ΔG_H (not too negative nor too positive). The Volcano-plot construction is a quantitative relationship between a catalyst surface adsorbing property and its apparent catalytic activity (known as activity-adsorption Volcano plot), in which the abscissa is the calculated adsorption free energy (ΔG_H) as the activity descriptor and the ordinate is the experimentally measured catalytic activity (herein, it can be the exchange current density, the overpotential, or the turnover frequency) [12-14, 20-21]. The theoretical maximal activity of HER is given at the peak of the volcano, which is accompanied by the most-moderate intermediate ΔG_H.

I.2.2. Experimental tools for testing, characterizing, and validating a HER electrocatalyst

The key learning points developed within this section answer the simple question: "how to know whether the material I just come to make is suitable for HER?". Henceforth, the most relevant parameters that are required to be measured/calculated step-by-step and carefully are (i) electrode activity and overpotential, (ii) Tafel plot, (iii) Faradaic efficiency, (iv) turnover frequency, (iii) stability/durability.

I.2.2.1. Electrode activity, onset potential and overpotential

The electrochemical HER tests are currently performed in three-electrode cell having a working electrode (where any catalytic ink is coated), a reference electrode (which enables applying a potential to the working electrode) and a counter/auxiliary electrode (for the current flow). The most widely used technique is the linear sweep voltammetry (LSV) even if the electrode activity can also be generally estimated by performing cyclic voltammetry (CV). The working electrode potential (E) is scanned from the high value (slightly greater than 0 V vs. RHE) to the lower one (the fixed value depends on the nature of the catalyst and electrolyte). Scan rates of 1-50 mV s^{-1} are usually employed. In International Union of Pure and Applied Chemistry (IUPAC) convention, the recorded current is negative

(reduction). The obtained current is normalized by superficial geometric electrode area to get the current density (j). Occasionally, the measured currents can be normalized by the sample amount to achieve the activity per unit mass. These directly recorded j vs. E curves also contain significant contribution of non-Faradaic capacitive current, especially for supported catalysts. To precisely determine the catalytic activity of a material, the measurement of steady-state currents at various applied potentials with a dwell-time of at least 5 min (short-term chronoamperometry) is suggested [14]. Other strategies to substrate the contribution of the supporting material is to run the control test (experiment in the absence of the active component of the catalyst). As matter of fact, the best elegant way to minimize the non-Faradaic contribution, is the choice of a relatively slow scan rate, lesser than 5 mV s^{-1} (≤ 1 mV s^{-1} should be good, but is time consuming). The absolute value of the difference between E^0 and the electrode potential E is called overpotential: $\eta = |E\text{-}E^0|$. Note that for HER, E^0 is greater than E. To compare the activities between different electrocatalysts, two special overpotentials in HER (used as metrics) are often employed [14]. The first is the so-called ''onset overpotential, η_{onset}'', which is directly linked to the notion of onset potential (E_{onset}). For an electrocatalytic process, the onset potential is defined as the value of the electrode potential at which commences the Faradaic current characterizing the considered reaction. For HER, the notion of E_{onset} is a poorly defined term for the simple reason that there is no defined maximum threshold; the current continues increasing exponentially. Indeed, the electrochemical kinetics of a reaction having an electron transfer as *rds* is algebraically described by the classic Butler-Volmer (BV) relationship (Eq. I.16) [22-24]. For the case of HER, the anodic branch from hydrogen oxidation is negligible. Thereby, the BV model of HER is described by Eq. I.17, which can be written in semi-logarithmic form as Tafel equation.

$$j = \left\{ j_{0,a} \exp\left[\frac{\alpha_a n_a F}{RT} \left(E - E_{eq} \right) \right] \right\}_{anodic} - \left\{ j_{0,c} \exp\left[-\frac{\alpha_c n_c F}{RT} \left(E - E_{eq} \right) \right] \right\}_{cathodic} \quad \text{(Eq. I.16)}$$

$$j = -j_{0,c} \exp\left[-\frac{\alpha_c n_c F}{RT} \left(E - E_{eq} \right) \right] \Rightarrow E - E_{eq} = \frac{RT}{\alpha_c n_c F} \left[\ln|j_0| \right] - \frac{RT}{\alpha_c n_c F} \left[\ln|j| \right] = a - b \log|j| \quad \text{(Eq. I.17)}$$

By showing j vs. E polarization curves in $|j|$ range not exceeding 0.5-2 mA cm^{-2}, it is possible to estimate E_{onset}. The most used relevant overpotential is defined as the value

corresponding to current density of $|j| = 10$ mA cm^{-2} [14, 25-26]. Furthermore, during HER or water electrolysis, lots of bubbles are generated on the electrode surface and simultaneously some of them do not get away from the electrode immediately. This directly decreases the effective active area, and thus increases the η. Such bubbles can also cause a noise in the polarization curves and should not be ignored. The utilization of a rotating electrode is a relevant manner to promptly remove H_2 bubbles. There is another kind of overpotential known as resistance overpotential (or junction overpotential), which is due to the material morphology. Indeed, the resistance (R) across materials structure will cause extra potential drop, making the measured overpotential of the electrode larger than the true value. Experimentally, this kind of overpotential is eliminated by the so-called "iR compensation" that enables getting accurate overpotential. In a conventional three-electrode measurement, the resistance between the reference electrode and the surface of the working electrode is the main source. Many electrochemical workstations can measure R directly and proceed to the correcting of the polarization curves automatically. Alternatively, R can be determined separately using the electrochemical impedance spectroscopy (EIS) experiments (at the intersection between the Nyquist curve and X-axis at high frequencies).

I.2.2.2. Tafel slope and exchange current density

As shown with Eq. I.17, by re-plotting the classic polarization curves (j vs. E) into Tafel plots (η vs. $\log|j|$), the linear portion can be fitted by the Tafel equation: $\eta = a + b\log(|j|)$. From that, two important parameters can be easily assessed, Tafel slope (b) and exchange current density (j_0). It is assumed that b is related to the catalytic mechanism of the electrode reaction (see *Section 1*), whereas j_0, which is obtained when η is assumed to be zero, describes the intrinsic catalytic activity of the electrode material under equilibrium conditions [13-14]. Practically, a catalytic material having a high j_0 and a small b is desirable. Indeed, the smaller value of the Tafel slope means that increasing the same current density requires smaller overpotential, implying faster charge transfer kinetics [13-14]. Since j_0 (depending only on the catalyst material, electrolyte and temperature) reflects the ability of electron transfer and the difficulty of an electrode reaction [13], larger exchange current density implies less driving force, i.e., smaller electrode current density is needed to conduct the reaction (see Eq. I.11). In acidic medium, the state-of-the-art HER Pt electrocatalyst has the best j_0 of *ca.* 10^{-2} A cm^{-2},

which is highly larger than other HER electrocatalysts such as Pd or Rh (10^{-4} A cm^{-2}), Au or Fe (10^{-6} A cm^{-2}), Ni, Ag or Cu (10^{-7} A cm^{-2}), Sn or Al (10^{-10} A cm^{-2}), Zn (10^{-11} A cm^{-2}) and Hg (10^{-13} A cm^{-2}) [27].

It is important to highlight that obtaining the Tafel slope from polarization curves presents some limitations. Undoubtedly, this calculation presents some personal factor once the value can vary with overpotential range and ohmic drop compensation chosen by the experimentalist [28]. Additionally, when it comes to non-conductive catalysts it is not possible to isolate the catalyst resistance contribution [29]. In 2013, Hu's group [29] proposed a new methodology to obtain Tafel slopes in HER by applying EIS technique at different overpotentials. Thus, by plotting $\log(1/R_{ct})$ vs. η, the obtained Tafel slope is purely associated with the charge-transfer kinetics.

I.2.2.3. Faradaic efficiency

In general, the so-called Faradaic efficiency (also known as Faradaic yield, coulombic efficiency, or current efficiency) refers to the efficiency with which charge (electrons) is transferred in an electrochemical system, facilitating an oxidation or reduction reaction. It reflects the efficiency by which the electrons provided by external circuit are transferred to drive a Faradaic reaction in which Faradaic losses occur in the form of heat or byproducts of the electrode reaction. To evaluate the faradaic efficiency, both the theoretical and experimental H_2 produced amounts are needed. The theoretical H_2 production can be calculated from galvanostatic (constant current) or potentiostatic (constant potential) electrolysis by integration. Meanwhile, the experimental H_2 production can be measured by a gas chromatography or water-gas displacing method. Thereafter, the ratio between the practical and theoretical hydrogen production is the Faradaic efficiency. Of course, high efficiency close to 100% is highly desired.

I.2.2.4. Turnover frequency and turnover number

Taken solely or together, the concepts of turnover frequency (TOF, s^{-1}) and turnover number (TON, no unit), which are often used in catalysis research are still not well-defined and leads to confusion/debate [30-31]. TOF (=TON/reaction time) is defined as the number of

reactant that a catalyst can convert to a desired product per catalytic site per unit of time, which can exhibit the intrinsic activity of each catalytic site [14]. It is very difficult to get a precise TOF value for many solid-state catalytic materials, such as HER nanocatalysts that generally possess easily accessible surface atoms/catalytic groups as well as some inaccessible internal atoms/catalytic species [14]. For HER, TOF can be described as the number of protons being reduced per unit time and per active surface atom; the electrochemical version [25, 32-34] is expressed by Eq. I.18, which indicates that both TOF and TON are potential-dependent. Thus, their determination at the current density of j = -10 mA cm^{-2} should be a good metric in addition to the overpotential at this value. Since the number of the active sites cannot be precisely and rigorously determined, there is no consensus about the reported TOFs (then TONs) since they are based (i) solely on the surface atoms (or the easily accessible catalytic sites) or (ii) on the total catalytic species present in the materials (no matter whether they are all accessible, not equally accessible, or some even not accessible at all [14]). Hence, depending of the used approach, it is obvious that the results will be grossly under/over estimated compared with the real values of the active sites, because it is almost impossible to have every atom in a material like nanoparticles to be catalytically active or equally accessible [14].

$$\mathrm{TOF} = \frac{j \times N_A}{n \times F \times N_s} = \frac{j}{n \times e \times N_s} \quad \text{and} \quad \mathrm{TON} = \mathrm{TOF} \times \tau \qquad \text{(Eq. I.18)}$$

TOF is the turnover frequency (molecule $site^{-1}$ s^{-1}), j is the current density (mA cm^{-2}), n is the number of electrons involved (number of electrons produced by reduction of H^+ (acidic) or H_2O (alkaline medium) to produce 1 mol H_2, n = 2), N_A is the Avogadro constant (6.02 10^{23} mol^{-1}), F is the Faraday constant (96485 C mol^{-1}), Ns the number of active surface atoms (sites cm^{-2}), τ is the reaction time (s) and TON is the turnover number (molecule $site^{-1}$).

I.2.2.5. Stability/Durability

The stability is another indicator of performance (if not the most important) because of the economic impact. Currently, there are two ways to evaluate the stability: either by CV/LSV or galvanostatic/potentiostatic electrolysis. In CV or LSV approaches, potential cycles should be repeated in the region including E_{onset} for hundreds or thousands of times to get

accurate idea about the stability of the tested material. Practically, after several cycles, minor shift of the electrode potential (or overpotential) for the same current density means better stability of the electrocatalyst. In galvanostatic measurement, it is advised to use a current density of 10 mA cm^{-2}. The potentiostatic method that consists of setting the potential at a fixed value and recording the current is random and unregulated in literature for the simple fact that the electrode potential window where HER is run depends exclusively on the nature of the electrocatalyst. Nevertheless, the value should not be too far from E^0 because it means "waste of energy" or excessive driving force. The duration can last from several to dozens/hundreds/thousands of hours, and as universal law, longer duration means better stability and durability of the system.

I.2.3. Synthesis and catalytic properties of noble metal-based electrocatalysts for HER

The experimental high-throughput screening of electrocatalytic materials for HER relies almost exclusively on a thorough understanding of the reaction mechanisms. To minimize the experimental conditions, the computational calculations have been widely utilized to assist and elucidate the nature of the reaction intermediate, as well as the correlation between reaction kinetics and metal surface properties. Within the last fifteen years, the combination of density functional theory (DFT) calculations and experimental data demonstrates that the HER kinetics in terms of j_0 in both low- and high-pH regimes correlate to DFT-calculated hydrogen binding energies via a Volcano relationship, indicating that hydrogen binding energy can be used as the reaction descriptor [22, 24, 27]. This strategy has assisted to synthesize many types of efficient electrocatalysts including noble metal-based alloys, transition metal phosphides, chalcogenides, carbides, and even metal-free catalysts. Figure I.2a shows the so-called volcano plot translating the relationship between the experimental j_0 (in log-scale), for hydrogen evolution over different monometallic material surfaces and the calculated hydrogen chemisorption energy per atom, ΔE_H (top axis) or energy for hydrogen adsorption, $\Delta G_{H^*} = \Delta E_H + 0.24$ eV (bottom). The active metals are on the left ''leg'' of the volcano (low coverage of H_{ads}) and the non-active ones, Cu, Ag, and Au, are on the right (high coverage of strongly adsorbed hydrogen). As explained above, if the intermediates bind too weakly, it is difficult for the surface to activate them; but if they bind

too strongly, they will occupy all available surface sites and poison the reaction. Hence, intermediate binding energies permit a compromise between these extremes, which correspond to high exchange current densities. Since the best performing HER electrode material requires an optimum interaction, many strategies have been developed to tune the oxophilicity (the tendency of certain to form oxides by hydrolysis or abstraction of oxygen). Figure I.2b displays the trend shown as a function of the 3*d* transition elements M (M = Ni, Co, Fe, Mn) in overpotential for HER for the threshold fixed current density of 5 mA cm^{-2}. The histograms indicate that the overpotential can be much lowered by introducing hydr(oxy)oxide species. The inset plots showing a comparison of polarization curves for Pt(111) and Au(111) with 40% $Co(OH)_2$ for the HER demonstrate that the Au(111)/oxide surface is significantly less active than the Pt(111) counterpart. This essentially establishes the role played by the Pt–H_{upd} descriptor. On fixing this interaction and by using Pt(111) as the main substrate, Markovic et *al.* [35] focused on the 'pseudo' mono-functional reaction with the OH_{ad}^{*}–$M^{2+\delta}$ (OH_{ad} means "adsorbed" OH) interaction as the main descriptor. According to the scheme (Figure I.2b, bottom panel), water from the bulk of the electrolyte dissociatively adsorbs on the oxide cluster, forming OH_{ad} intermediate along with forming H_{ad} intermediate formed on the Pt substrate. H_{ad} groups re-combine to form H_2. Depending on the OH_{ad}^{*}–$M^{2+\delta}$ strength, the OH_{ad} is either stabilized (for Mn^{2+}, $Fe^{2+\delta}$) or destabilized (Ni^{2+}, Co^{2+}) on the oxide clusters, which is found to dictate the TOFs for these catalysts [35]. Hence, under alkaline environments, the overall catalytic activity for HER using Pt-based 3*d*-M hydr(oxy)oxides is a function of OH–$M^{2+\delta}$ bond strength ($0 \leq \delta \leq 1.5$), used as a descriptor. This relationship exhibits trends in reactivity Mn < Fe < Co < Ni, which is governed by the strength of the OH-$M^{2+\delta}$ energetic (Ni < Co < Fe < Mn).

Summarily, as the main HER descriptors have been identified to be either M-H or HO-M^{n+}, the synthesis procedures should be guided in order to provide these suitable species at low electrode potential. The common electrocatalysts preparation methods can be used to synthesize HER catalysts. Nørskov et *al.* [24] reported computational high-throughput screening of surface alloys to identify new electrocatalysts for HER by examining the theoretical activity of over 700 binary surface alloys (that can be formed from 16 metals Fe, Co, Ni, Cu, As, Ru, Rh, Pd, Ag, Cd, Sb, Re, Ir, Pt, Au and Bi), as well as the estimation of the stability of each alloy in electrochemical environments. These alloys, composed of a pure metal substrate with a solute element alloyed into the surface layer (Figures I.3a-d), can

exhibit surface properties that are vastly different from the properties of the bulk alloy. The calculated free energies of hydrogen adsorption on a subset of these surface alloys (1/3 monolayer (ML)) of solute in the surface layer clearly demonstrates that a number of binary surface alloys have high predicted activity for HER [24]. From these predictions, it turns out that BiPt surface alloy has a predicted activity comparable to, or even better than, pure Pt, the archetypical HER catalyst. Accordingly, they developed a method to synthesize a typical BiPt surface alloy (electrodeposition of an initial Pt film onto an inert support, spontaneous deposition of a sub-monolayer of irreversibly adsorbed Bi (Bi_{ir}) by Bi underpotential deposition and annealing of the Pt–Bi_{ir} precursor to form a BiPt surface alloy) and showed experimentally that its activity is superior to that of Pt, the state-of-the-art HER catalyst [24]. Figure I.3e depicts the plot of experimentally measured HER exchange current densities against ΔG_H values calculated using DFT, suggesting that an optimum in the measured HER exchange current densities is found for DFT-derived ΔG_H values very close to zero and the bimetallic alloys exhibit better HER performance than the polycrystalline or single-crystals pure metals.

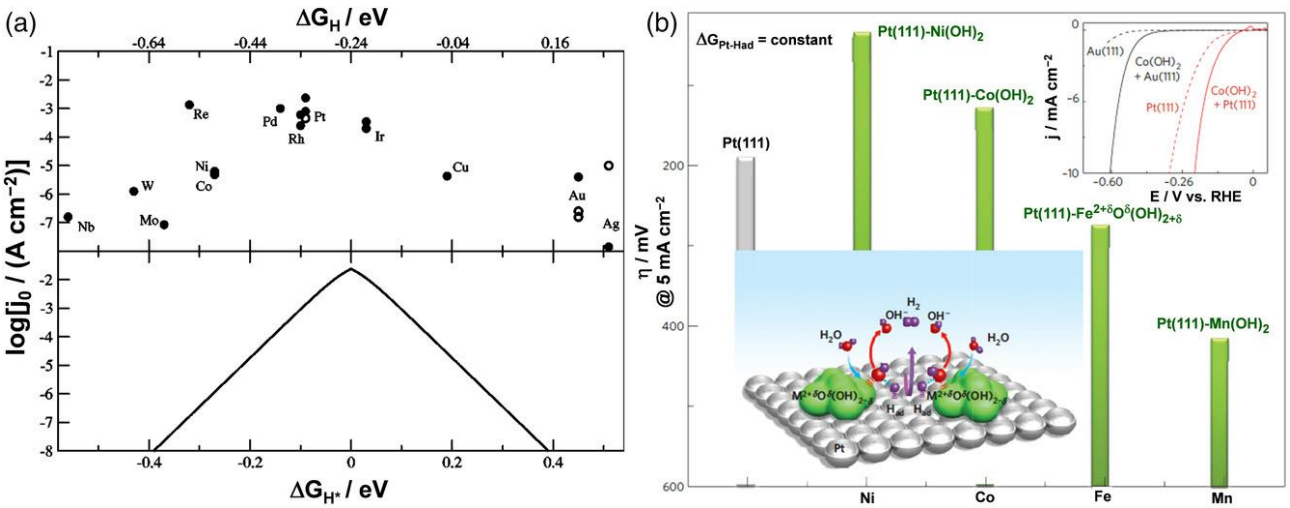

*Figure I.2. (a) Top: Experimentally measured exchange current, log(j_0), for hydrogen evolution over different metal surfaces plotted as a function of the calculated hydrogen chemisorption energy per atom, ΔE_H (top axis). Single crystal data are indicated by open symbols. Bottom: The result of the simple kinetic model now plotted as a function of the free energy for hydrogen adsorption, $\Delta G_{H^*} = \Delta E_H + 0.24$ eV. (b) Trend in overpotential for HER shown as a function of the 3d transition elements. Top inset: a comparison of polarization curves for Pt(111) and Au(111) with 40% $Co(OH)_2$ for the HER. Bottom inset: a schematic showing the HER. Note: the * denotes a site on the surface; thus, an*

** by itself denotes a free site and H* denotes a hydrogen atom adsorbed on the surface. (a) Reprinted and adapted from Ref.[27]; Copyright 2005, The Electrochemical Society. (b) Reprinted and adapted from Ref. [35]; Copyright 2012, Macmillan Publishers Ltd.*

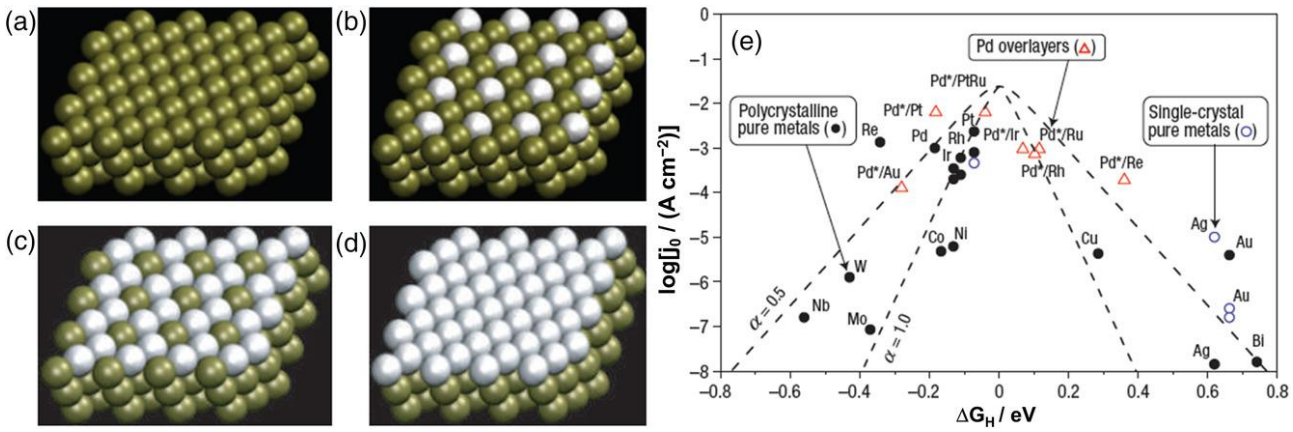

Figure I.3. (a-d) Schematic diagrams of surface alloys at the solute coverage for which calculations are carried out. The solute atoms are shown in white, and the host (substrate) atoms are indicated in dark green; all solute atoms are embedded in the surface layer of the corresponding host metal: a pure metal (a), a surface alloy with solute coverage = 1/3 ML (b), a surface alloy with solute coverage = 2/3 ML (c), one ML of solute atoms, forming an overlayer (d). (e) Volcano plot for the HER for various pure metals and metal over-layers: ΔG_H values calculated at 1 bar of H_2 (298 K) and at a surface hydrogen coverage of either 1/4 or 1/3 ML, and experimental data are compiled in refs. [27, 36-37]. The two curved lines correspond to the activity predictions of simple mean-field, microkinetic models, assuming transfer coefficients (α) of 0.5 and 1.0, respectively. Reprinted and adapted from Ref. [24]; Copyright 2006, Macmillan Publishers Ltd.

Since noble metals seem unavoidable elements in HER catalysts, the promising strategy for preparing such electrode materials consists of introducing an earth-abundant element that could reduce the cost without impacting the performance. Within such goals, Yoon and co-workers introduced the synthesis of hollow rhodium sulfide nanoparticles with well-defined crystalline facets, which show very high activity and excellent durability toward HER [38]. Figure I.4a illustrates the experimental procedure of such hollow nanoparticles via one-step formation of core-shell nanoparticles followed by selective etching of the core. Basically, the co-decomposition of Cu and Rh precursors yields to size and facet-controlled, core-shell structured $Cu_{1.94}S@Rh_2S_3$ nanoparticles, which are generated by the fast formation

of $Cu_{1.94}S$ nanoprisms, followed by the growth of the Rh_2S_3 phase. In a typical synthesis of hollow Rh_2S_3 nanoprisms, CuSCN and $Rh(acac)_3$ in oleylamine is prepared in a 100 mL Schlenk tube and placed under vacuum at 100 °C for 10 min (1 atm Ar gas). Then, after heating the Schlenk tube in a hot oil bath at 240 °C for 30 min, the reaction mixture is cooled down to room temperature, washed several times with toluene and methanol, followed by centrifugal separation to give $Cu_{1.94}S@Rh_2S_3$ nanoprisms. This is followed by the nanoprisms etching in a solution containing 1 mL of HCl, 3 mL of ethanol, and 3 mL of toluene for 3 hours with a magnetic stirring to give the final targeted products of hollow Rh_2S_3 nanoprisms. Representative transmission electron microscopy (TEM) and high-resolution TEM (HRTEM) images with fast Fourier transformation (FFT) patterns of Rh_2S_3 nanoprisms are shown in Figures I.4b-c. The average sizes measured from diagonal point to point of hexagonal $Cu_{1.94}S@Rh_2S_3$ nanoprisms and hollow Rh_2S_3 nanoprisms are 88.0 ± 4.1 nm and 84.1 ± 4.0 nm, respectively, which indicates that after the etching process, the size of the final product (hollow Rh_2S_3 nanoprisms) is slightly reduced from that of pristine material. The hexagonal faces of orthorhombic Rh_2S_3 nanoprisms are enclosed by $(1\bar{1}0)$ facets. The six sides of hexagonal nanoprisms are found to be (211) and $(2\bar{1}1)$ planes as verified by the HRTEM image and the FFT pattern. To better evaluate the electrochemical performances towards HER in acidic medium (0.5 M H_2SO_4), three Rh_2S_3 hollow nanoprisms, namely, ThinHNP, MedHNP, ThickHNP, were prepared by using 8:1, 8:2, 8:4 ratios of CuSCN:$Rh(acac)_3$, respectively with different cavity thickness of 0.79 nm, 2.2 nm, and 3.7 nm for the same sequence. This tight control of the size and thickness of the nanocrystals enable to investigate the relationship between the morphology and catalytic activity. For this purpose, the three Rh_2S_3 nanoprisms were supported on carbon black (Vulcan) with a nominal loading of 13 wt.% (namely HNP/C). The electrocatalytic activities of $C_{1.94}S@Rh_2S_3$_ThickNP/C, 20 wt.% Pt/C, and carbon black were used for better comparison, as gathered in Figure I.4d, which shows the polarization curves after the correction for iR and normalization of the current with the geometric surface area of the electrode (0.1257 cm^2). At the benchmark current density (cathodic) of -10 mA cm^{-2}, the driving force in terms of overpotential for ThickHNP/C is η = 122 mV, whereas the $C_{1.94}S@Rh_2S_3$_ThickNP/C, MedHNP/C and ThinHNP/C required larger overpotentials (higher driving force) of 175 mV, 175 mV, and 300 mV, respectively. Firstly, the comparison between ThickHNP/C and $Cu_{1.94}S@Rh_2S_3$_ThickNP/C highlights the importance of hollow

morphology that leads to superior HER performance. Secondly, since the non-etched sample ($Cu_{1.94}S@Rh_2S_3$_ThickNP/C) showed considerably high HER activity, which is similar to that of MedHNP/C, and even higher than that of ThinHNP/C samples, the active surface sites in the hollow Rh_2S_3 nanostructures originate from not only inside but also outside the hollow structure. According to the authors, the unusual shape of the polarization curve of ThinHNP/C electrode material could be attributed to the limited mass transport due to the relatively smaller void volume of ThinHNP compared to other hollow structure [38]. The results emphasize the importance of a relatively wide cavity for facilitating mass transport along with the enhanced catalytic active sites. The determined Tafel slope from the linear portion of Tafel plot was 30 mV dec^{-1} for 20 wt.% Pt/C indicating a Volmer-Tafel mechanism. The Tafel slopes of ThickHNP/C, MedHNP/C, and ThinHNP/C were approximately 44, 49, and 65 mV dec^{-1}, respectively. The relatively small Tafel slope of ThickHNP/C indicates faster kinetics for HER at this electrode material and substantiates the previous results derived from the overpotentials. All the Tafel slopes of 44-65 mV dec^{-1} for Rh_2S_3/C may suggest the Volmer-Heyrovsky HER mechanism where the limiting step is the Heyrovsky reaction (electrochemical desorption step) characterized by low H_{ads} coverage, so that H_{ads} prefers to couple with a new electron and H^+ in the electrolyte to evolve H_2. This determined Tafel slope of 44 mV dec^{-1} for ThickHNP is smaller than those of most metal sulfide-based HER catalysts, i.e., requires less driving force to perform HER. The long-term stability of the best performing ThickHNP/C electrocatalyst investigated by conducting consecutive potential cycles between 0.1 and -0.3 V vs. RHE at a sweep rate of 50 mV s^{-1} showed that after 10 000 cycles, the overpotential needed to reach a current density of -10 mA cm^{-2} was considerably reduced from 137 mV to 117 mV (without iR compensation). Such drastic and unexpected improvement of the electrocatalytic activity was explained by the removal of the inactive Cu impurities (dissolution) from the hollow Rh_2S_3 nanoprisms during the electrode potential cycling, which would increase the number of active Rh-based catalytic sites [38]. The authors observed experimentally the Cu leaching by measuring the content of Cu in the electrolyte before and after 10 000 potential cycles using inductively coupled plasma optical emission spectrometry (ICP-OES). Before cycling test, 0.000 mg L^{-1} was recorded and after cycling test, the Cu amount rises to 0.003 mg L^{-1} confirming the leakage. The above assumption is strengthened by the fact that the TEM images after potential cyclings revealed that the pristine structure of Rh_2S_3 nanoparticles is

well preserved and the nanoprisms are still uniformly distributed on the carbon support without agglomeration.

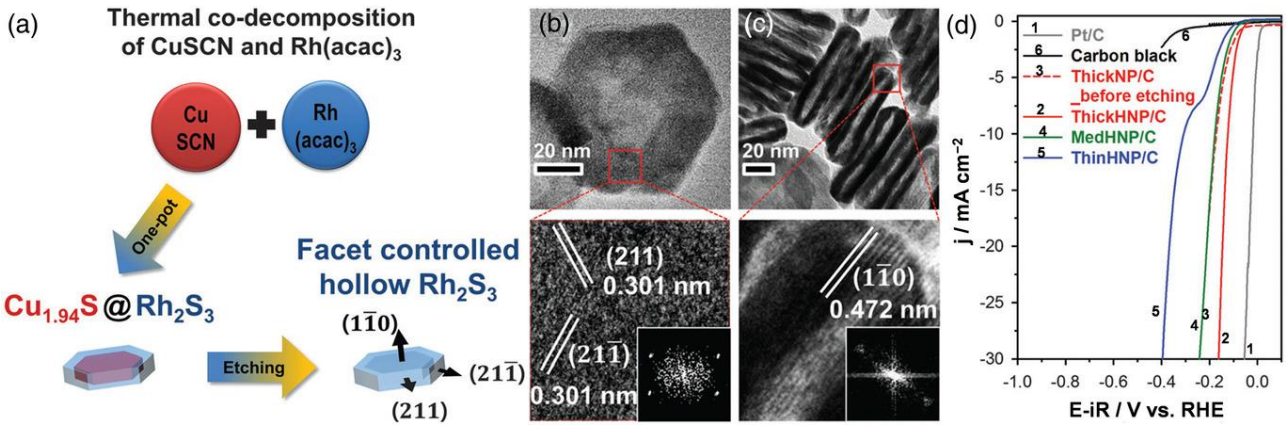

Figure I.4. (a) Schematic illustration of the formation process of facet-controlled hollow rhodium sulfide nanoprisms. HRTEM images of hexagonal facet of a nanoprism (b) and side of vertically standing nanoprisms (c), respectively; the enlarged views of image in the red square and the corresponding FFT patterns are shown below each figure. (d) iR-corrected HER polarization curves for Rh_2S_3_HNP/C, $Cu_{1.94}S@Rh_2S_3$_NP/C, 20 wt.% Pt/C, and carbon black in 0.5 M H_2SO_4 with a scan rate of 2 mV s^{-1}. Reprinted and adapted with permission from Ref. [38]; Copyright 2016, Royal Society of Chemistry.

In recent study, Dessources *et al.* [39] adopted similar strategy to reduce the costly precious Pt amount in the electrode materials by designing Pt_xNi_{1-x}/C materials, employing the so-called bromide anion exchange (BAE) method [40], a convenient and surfactant-free approach. Figure I.5a shows the typical TEM image of Pt/C nanocatalyst, composed of spherical-like particles of 2-10 nm (Figure I.5b). Figure I.5c highlights that the replacement of noble Pt metal by a cheaper and earth-abundant Ni element is not accompanied by a significant decrease of performance. The drawing of 100 amps per gram of Pt requires overpotentials of η = 155, 102, 115, 121 mV for Pt/C, $Pt_{0.7}Ni_{0.3}/C$, $Pt_{0.5}Ni_{0.5}/C$ and $Pt_{0.3}Ni_{0.7}/C$, respectively, which means less energy for $Pt_{0.7}Ni_{0.3}/C$. The exchange current density is j_0 = 3.6×10^{-5}, 2.2×10^{-5}, 1.9×10^{-5} and 1.3×10^{-5} A cm^{-2} for the same sequence. Importantly, the evaluated kinetic parameters indicate that the bimetallic material $Pt_{0.7}Ni_{0.3}/C$ (b = 160 mV dec^{-1}) and Pt/C (b = 157 mV dec^{-1}) have quite the same Tafel slopes. This indicates the excellent performance of $Pt_{0.7}Ni_{0.3}/C$ despite the reduced Pt amount within its composition. These results demonstrated that Pt amount can be reduced up to 30 at. % without any significant

loss of performance in alkaline medium. The main driving force that is responsible for the enhanced ability of the $Pt_{0.7}Ni_{0.3}/C$ catalyst is attributed to the heterogeneous character of the material itself (composed of Pt-enriched surface) that may prove optimal environment for the H_2O molecules splitting into H_{ads} and free hydroxyl ions (with particular affinity with nickel surface) [39].

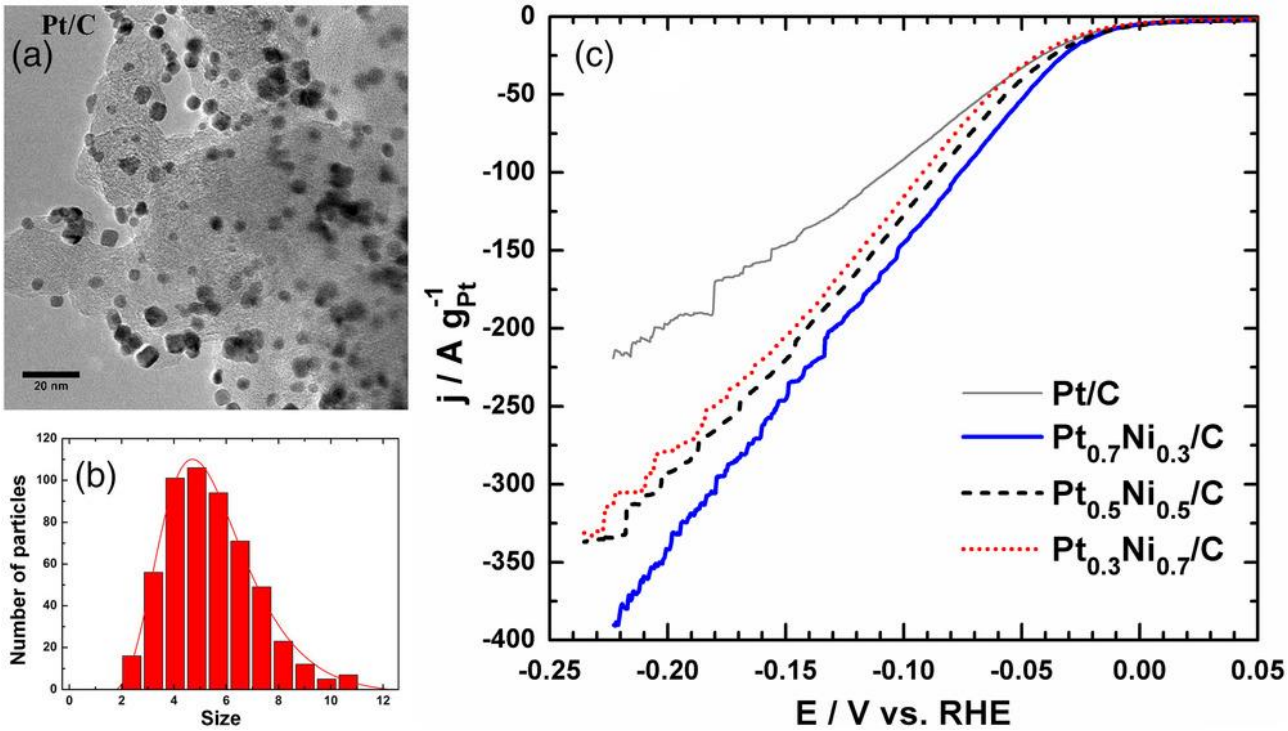

Figure I.5. (a) TEM micrograph of Pt/C (20 wt.% metal loading) nanomaterial synthesized by the BAE method. (b) The corresponding histogram for the particle size distribution. (c) Polarization curves (no iR-correction) for HER on Pt_xNi_{1-x}/C catalysts, recorded in a N_2-saturated 0.1 mol L^{-1} NaOH solution at 2 mV s^{-1} and 21 °C. Reprinted and adapted with permission from Ref. [39]; 2016 Wiley-VCH Verlag GmbH & Co. KGaA, Weinheim.

I.2.4. Designing heterogeneous non-precious metal electrocatalysts for HER

The primary argument in favor of transitioning from noble metal-based catalysts to earth-abundant electrocatalysts is indeed quite self-compelling: the scarcity of platinum group metals (PGMs) associated with their high price makes them impractical for global-scale hydrogen production applications. Therefore, the development of low-cost and high-performance alternative electrode materials that are suitable for HER is of paramount importance. One of the logical solutions to decrease the overpotential during HER is to

employ biological catalysts such as enzymes that have the unique specificity to perform most of the catalytic reactions without supplement of energy. For instance, hydrogenases (enzymes inter-converting hydrogen and water) and nitrogenases (enzymes performing the reduction of N_2 in the presence of H^+ into NH_3 and H_2) are effective biocatalysts for HER even though the catalytic active site of these enzymes contains non-noble metals such as iron (Fe), nickel (Ni), molybdenum (Mo) and vanadium (V). The dark side of these biocatalysts is their inherent property to operate only under specific conditions of pH and temperature. In other words, they cannot work under extreme conditions of pH (acidic or alkaline) and temperature. Furthermore, the immobilization of the enzymes at the electrode adds a layer of complexity and most enzymes within the resulting bio-electrodes are catalytically inactive. In addition, their production in the active form can hardly be scaled up to meet large-scale technological demand. Hence, it is quite impossible that enzyme-based devices will make a significant contribution to high-level hydrogen generation to satisfy the demand [41-43]. Thus, the elegant solution to overcome the aforementioned issues is to develop functional bio-inspired catalysts, which will constitute an important advance to bridge the gap towards good performance and large-scale sustainable hydrogen production. Hence, inspired by the structure/composition of nitrogenase and hydrogenase, researchers have exploited a series of heterogeneous metallic catalysts. This constitutes a profound achievement in the field of noble metal-free HER electrocatalysts. To date, various classes of heterogeneous metallic materials are investigated for HER: sulfides, selenides, carbides, nitrides, phosphides, borides, tellurides…, and heteroatom-doped nanocarbons. Indeed, monometallic catalysts based on molybdenum (Mo), tungsten (W), nickel (Ni), cobalt (Co), phosphorus (P), nitrogen (N), sulfur (S), etc. show poor HER activity as displayed in Figures I.2a and I.3e. However, it was successfully demonstrated that by designing heterogeneous materials including two or three non-PGM elements, their ability towards HER can be much improved. A few successful examples are MoS_2 [44-45], $MoSe_2$ [45-46], WS_2 [47], WSe_2 [46], Mo_2C [23], MoWP [48], $NiMoN_x$, Ni_2P [49], $Co_{0.6}Mo_{1.4}N_2$ [50], CoS_2 [51], BCN [52]. For instance, Figure I.6a shows that the addition of S to Mo to form MoS_2 leads to a significant decrease of the free energy barrier, thus promoting HER.

I.2.4.1. Metal sulfides as heterogeneous catalysts for HER

Molybdenum disulfide, MoS_2, which is one of the widely investigated alternative of PGMs for HER during the last fifteen years had been suggested as an inactive HER catalyst since early works on the electrochemistry of bulk natural MoS_2 crystals of Tributsch and Bennett, in the 1970s [53]. However, in 2005, Nørskov and co-workers found that sulfur species in the $(10\bar{1}0)$ Mo-edge structure of MoS_2 (Figures I.6b, I.6c) had a close resemblance to the sulfur active sites of nitrogenase, enzyme that is an effective hydrogen producing catalyst [54]. Their calculations, using DFT showed that the sulfided Mo$(10\bar{1}0)$ edge of MoS_2 possesses a hydrogen binding energy of approximately 0.1 eV at a hydrogen coverage above 25%, very close to the optimum value of 0 eV and which is similar to that observed on active precious metal catalysts, including Pt. Therefore, MoS_2 may be an active electrocatalyst for HER, but such activity comes from the edges, while the basal plane is inert. This assumption was confirmed by Jaramillo *et al.* [55] through a study with MoS_2/Au materials synthesized in ultra-high vacuum (UHV), with different proportions of basal and edge sites. It was shown that exchange current density values increased linearly with the quantity of edge sites, but the same linearity was not detected when related to total number of sites. It is worth mentioning that all synthesized MoS_2/Au composites exposed preferentially the sulfided Mo$(10\bar{1}0)$ edge on the edge structure.

After these works promoted by Chorkendorff and Nørskov's group [54-55], a trend has emerged. Many researchers devoted efforts on the development of syntheses to obtain MoS_2 structures with preferential exposition of edge sites. Their studies have shown that nanostructuring MoS_2 materials could significantly enhance HER activity [44, 54-58]. Given the unique layered crystal structure of MoS_2 (Figure I.6b), the nanosheets morphology dominates the whole synthesized MoS_2 [25, 44, 57, 59-63]. Many experimental approaches such as ball-milling [64], sonication [56], hydro(solvo)thermal [65-67] and chemical vapor deposition (CVD) [68-69] have been proven to be effective tools to prepare highly active MoS_2 nanosheets. Additionally, given the semi-conductive nature of MoS_2 that impacts its HER performance, the electronic conductivity engineering (doping suitable heteroatoms into the lattice of MoS_2 and coupling MoS_2 with conductive species, such as carbon nanotubes and graphene)[14] is another strategy widely explored for improving its catalytic activity.

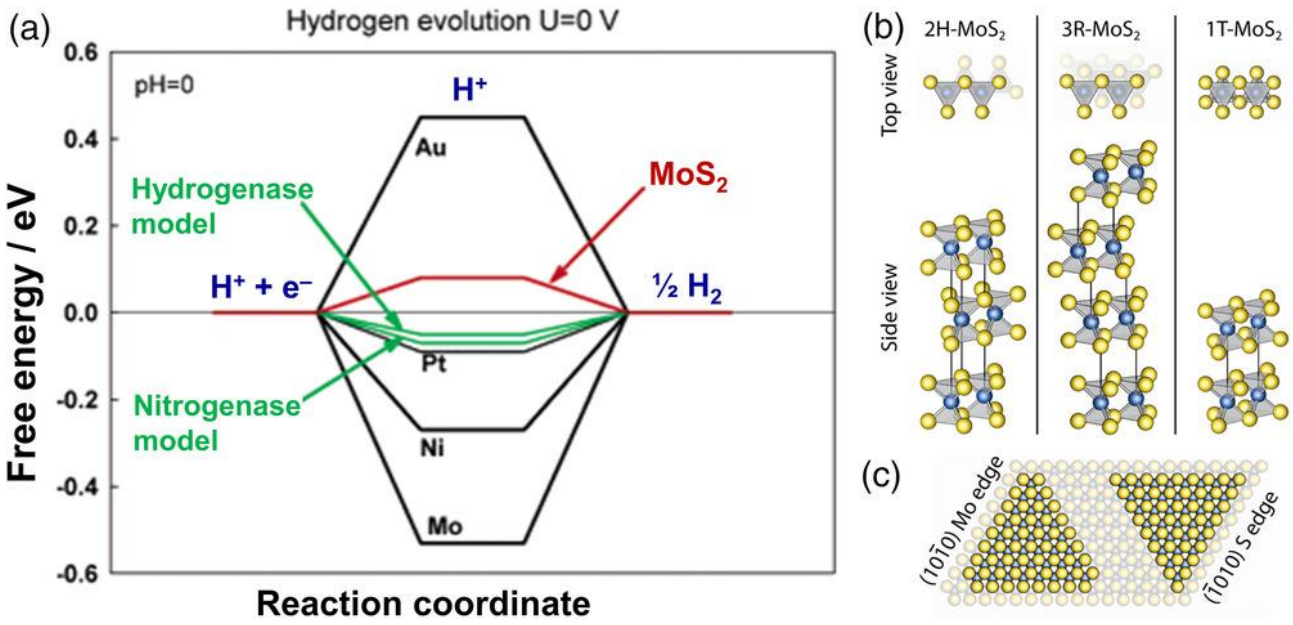

Figure I.6. (a) Calculated free energy diagram for HER relative to the SHE at pH = 0. (b) Structure of the 2H, 3R, and 1T poly-types of MoS_2. (c) Top view of the Mo edge and S edge of a bulk MoS_2 crystal. (a) Reprinted and adapted with permission from Ref. [54]; Copyright 2005, American Chemical Society. (b,c) Reprinted and adapted with permission from Ref. [25]; Copyright 2014, American Chemical Society.

Due to the many similarities between WS_2 and MoS_2, as morphology, possibility of phases, activity towards different reactions, electronic environment, etc., many researchers also drived their efforts to investigate the activity and behavior of tungsten sulfide-based materials in HER [46, 70-73].

Undoubtedly, Mo- and W-based sulfides are the most explored transition metal sulfides (TMS) for HER. They have been developed with different morphologies and using various strategies, as preferential edge exposition, exfoliation, doping, supporting, etc., to improve their electrocatalytic activity.

Most MoS_2 and WS_2 materials are composed of flat S-Mo(W)-S atomic sheets which may stack and form a structure similar to graphite, resulting in materials containing several layers of MoS_2 or WS_2. Furthermore, while in the same layer strong covalent bonds exist, different layers are connected by weak Van der Waals interactions, which results in a strong anisotropy of physical and chemical properties of the material. Resistivity is 2200 times larger between layers than along a same layer, for example [44-45, 62, 74-77]. The integration of sulfide materials on conductive substrates, generally carbon-based materials, is another

strategy which has been extensively explored to optimize charge-transfer resistance. Furthermore, the substrate may provide nucleation sites for the sulfide nanomaterials and avoid their agglomeration. This leads to materials containing higher surface areas and, consequently, higher accessibility to active sites [78-80].

Chorkendorff's group synthesized multi-walled MoS_2 nanotubes coated on multi-walled carbon nanotubes (MWCNT@MWMoS_2) [62]. This material showed η_{onset} = 150-200 mV for HER in 0.1 M $HClO_4$ at 20 mV s^{-1} and Tafel slope of ~109 mV dec^{-1} was calculated, which may be result of low electrical conductivity from outer to inner MoS_2 layers. The pristine material was annealed at 800 ^oC in Ar during 2 and 8 h which led to more parallel aligned MoS_2 sheets, in relation to MWCNT axial axis, and thicker walls, according to HRTEM. Consequently, reduced activities were verified due to lower exposition of edge sites for these annealed materials. It means that the MoS_2 sheets alignment has a great impact on material performance, therefore, a methodology which promotes a perpendicular alignment of MoS_2 sheets in relation to axial axis of MWCNT may result in the enhancement of activity. Interestingly, after cycling the annealed material for 8 h in oxidizing potentials region (around 1.0 V vs RHE), HER activity improved after the 2nd and 3rd cycles. This behavior was associated with possible etching in pyramidal structures or pits on the basal planes, besides etching that may be started from edges.

In another core@shell morphology proposal, Jaramillo's group nanoengineered a MoO_3@MoS_2 material through sulfidation of vertically aligned MoO_3 nanowires synthesized according to hot-wire chemical vapor deposition (HWCVD) method [74]. The sulfidation step proceeded with the reaction between MoO_3 and H_2S, which resulted in a substoichiometric MoO_3 core nanowire structure covered by MoS_2 layers. Different sulfidation temperatures, using a 10 % H_2S/H_2 stream, were tested and showed to play a key role in material activity towards HER in 0.5 M H_2SO_4 at 5 mV s^{-1}. The material obtained at lowest temperature, 150 ^oC, showed the best onset potential, but it was also the least stable material as a consequence of incomplete sulfidation of surface MoO_3 nanowires, which promotes both a higher density of exposed MoS_2 edge sites and higher exposition of MoO_3 to acidic environment, leading to its corrosion. Sulfidation at 300 ^oC or higher leads to low HER activity materials due to conductivity loss of FTO, the substrate used for MoO_3 synthesis; promoted by the chemical changes in sulfidation environment at high temperatures.

According to XPS analyses, when submitted to 200 °C sulfidation, besides the formation of MoS_2 layer, Mo^{6+} species of MoO_3 phase reduced partially to +5 or +4 charges, enhancing the electrical conductivity of the oxide. That was shown to be the optimum temperature of sulfidation. No occurrence of MoO_3 corrosion, η_{onset} = 150-200 mV, similarly to that reported by Chorkendorff's group [62], and Tafel slope equal 50-60 mV dec^{-1} were verified. The catalyst also showed to be stable after 10000 cycles at 50 mV s^{-1}. In line with Chorkendorff and coworkers' paper [62], a slightly increase of activity was noted in the beginning of stability test, assigned to the removal of contaminants at surface or slight removal of basal plane sites by oxidation [74]. This possible etching reported by both [62, 74] results in the improvement of edge sites exposition and may be further utilized as a methodology to improve HER activity of MoS_2-based materials.

Finally, despite the promotion in material surface area obtained from the core-shell nanotube array, TEM analyses showed that most of MoS_2 basal planes were parallel aligned to axial axis of MoO_3 nanotubes, as also verified for MWCNT@MWMoS_2 [62], which diminished the exposition of active edge sites.

It is also known that (nano)porous materials provide high surface area that leads to a greater contact area with reactants and sufficient transport of reactants and products. As a consequence, in order to synthesize a molybdenum sulfide which preferentially exposes active sites, Jaramillo's group reported the successful synthesis of a highly-ordered MoS_2 bicontinuous network containing a double-gyroid (DG) morphology and nanopores size of about 3 nm [44]. Molybdenum was electrodeposited in a previously synthesized silica double-gyroid template which covered an FTO electrode. Sulfidation, silica etching and another sulfidation step was sequentially applied, resulting in the MoS_2-DG, as resumed in the work of Kibsgaard *et al* [44]. Due to the curvature of the MoS_2 structure resulting from the constraint of the DG morphology, the as-prepared mesoporous MoS_2 material has a larger layer-to-layer spacing of 6.60 Å compared to the bulk MoS_2 (6.15 Å).

Different electrodeposition times were tested (10 s, 20 s and 60 s) and evaluated towards HER reaction in 0.5 M H_2SO_4 at 50 mV s^{-1}. As expected, the higher was deposition time, the thicker was the MoS_2 film. As consequence, the film deposited in 1 min was the most active, whereas the one deposited in 10 s was the least. However, when current densities were normalized by the capacitance of materials this order inverted. It may be a result of the resistance contribution of MoS_2-DG, as pointed out by EIS analysis. Despite that, onset

overpotential and Tafel slope of 150-200 mV and ~50 mV dec^{-1}, respectively, were obtained for all MoS_2-DG.

After iR compensation, MoS_2-DG (1 min of electrodeposition) presented higher activity than MoO_3-MoS_2 [74]. The density of active sites per surface area of MoS_2-DG film was estimated as 3.9 times higher than that of MoO_3-MoS_2; which may be the reason of the higher activity. On the other hand, the release of bubbles occurred easier in nanowire morphology than on double-gyroid one. Hence, the double-gyroid may be more impacted by mass transport limitation at high current densities.

Molybdenum sulfide with preferential orientation was also reported by Cui's group, which synthesized MoS_2 film with vertically aligned layers[45]. For that, a substrate material containing deposited Mo film was placed in the center of horizontal tube furnace, whereas a recipient filled with S powder was placed at the upstream side of the furnace. The tube furnace was pumped down to 100 mTorr and then flushed with Ar prior to the reaction. Finally, with Ar being fed into the reactor at 100 mL min^{-1}, substrate was heated until 550 ^{o}C in 20 min, and S powder was maintained at, approximately, 220 ^{o}C. The reactor was set at these temperatures for 10 min and then cooled down naturally. Transmission electron microscopy tomography was undertaken and showed that most of MoS_2 layers were perpendicularly aligned to the substrate. Authors reported that at high temperatures the conversion occurs faster than the diffusion of sulfur, so the latter is the rate-limiting process. Additionally, it is expected that diffusion occurs more quickly along the layers than across them, therefore, the layers tend to orient perpendicularly to the film.

This material deposited on glassy carbon electrode (GCE) was evaluated for the HER in 0.5 M H_2SO_4 at 2 mV s^{-1}. An excellent j_0 = 2.2 x 10^{-6} A cm^{-2} was calculated, probably as consequence of the high exposition of active edge sites. Despite that, Tafel slopes in the range 105-120 mV dec^{-1} were obtained, although EIS revealed negligible ohmic resistance, lower than 4 Ω, even at 0 V vs RHE. Yet, activity of material was evaluated before and after being cycled 1000 times until – 0.4 V vs RHE at 50 mV s^{-1}; no relevant activity loss was verified.

Hu et al. also investigated the effect of MoS_2 layers preferential orientation on HER activity in acidic media (0.5 M H_2SO_4) [81]. Syntheses were performed via hydrothermal route at 200 ^{o}C employing $NaMoO_4$ and thioacetamide as Mo and S sources, respectively, besides to soak carbon fiber paper (CFP) into reactant mixture so that it is the substrate of the resultant MoS_2

material. Three materials were produced only adjusting some synthesis parameters; hydrothermal process during 2 h in a regular oven (r-MoS_2), hydrothermal process in a microwave system for the same time (se-MoS_2) and also employing the microwave technique but maintaining only 50 min in final temperature (fe-MoS_2). The resultant mixtures were cooled down to room temperature at 20 ^{o}C min^{-1}. Flower-like, circle-like nanotube and flat-floor morphologies were verified by TEM for r-MoS_2. On the other hand, materials obtained by microwave technique showed perpendicular orientation of layers in relation to CFP, as expected. The microwave radiation interacts directly with chemical species which promotes faster and more homogeneous heating. As result, microwave-aided heating favors continuous and uniform seed layers covering CFP structure, which is important for the growth of perpendicular layers. Additionally, the faster heating promoted by the microwave system induces a rapid sulfurization, then sulfur diffusion becomes the rate-determining step. Once sulfur diffusion is faster along the layers than across them, the perpendicular growth is promoted in fe-MoS_2 and se-MoS_2 materials. The authors also verified that reaction time affects the morphology of the resultant material. After 40 min of reaction, MoS_2 nanosheets already exist, but molybdenum suboxide seeds are also still present. At 50 min of reaction (fe-MoS_2), only vertically aligned MoS_2 nanosheets exhibiting a flat edge surface are seen. A slight etching effect in the edges was verified by increasing reaction time to 90 min. Further etching occurred at 120 min of reaction (se-MoS_2), which resulted in well-defined stepped-edge surfaces. XRD, XPS, Raman and TEM confirmed the existence of 2H-MoS_2 in all samples.

The catalysts were tested towards HER at 5 mV s^{-1} and the activity order verified was se-MoS_2 > fe-MoS_2 > r-MoS_2. Although fe-MoS_2 presented an excellent η_{10} = 142 mV, it was further improved as result of the stepped configuration (η_{10} = 104 mV). According to theoretical calculations performed by the authors, the stepped morphology resulted in more thermoneutral adsorption than the flat one. Additionally, se-MoS_2 presented a Tafel slope of about 59 mV dec^{-1}, j_0 = 0.20 mA cm^{-2}, R_{ct} = 2.7 Ω at η = 200 mV and ~100 % of faradaic efficiency. Finally, no loss of activity was verified in chronopotentiometric analysis at – 20 mA cm^{-2}.

WS_2 nanosheets (WS_2 NSs) synthesis from a non-conventional method was reported [82]. Initially, WO_3 and S were mixed and ball-milled at 400 rpm in argon atmosphere for 24 h. Then, one boat containing this mixture and another containing additional S were placed in

a hot zone of an oven at 600 °C fed by argon. After 2 h, the oven was cooled down to room temperature and WS_2 powder was collected. Ball-milling step is important because, besides breaking WO_3 in smaller pieces and promoting higher surface exposition, it aids S to cover WO_3 homogeneously. During annealing, slow sulfurization of WO_3 surface occurs resulting in WS_2 layer that is peeled off and generates nanosheets. Then, additional S evaporates and covers again WO_3 particles repeating the previous mechanism until all WO_3 is consumed. A representative scheme of this synthesis is presented in Figure I.7a. TEM analysis showed that WS_2 individual NSs are, approximately, 5 nm thick. Besides that, SAED revealed a hexagonal 2H-WS_2 structure.

This catalyst was evaluated in the HER in 0.5 M H_2SO_4 at 2 mV s^{-1} and showed a current density of 9.66 mA cm^{-2} at 150 mV overpotential, besides a Tafel slope of 72 mV s^{-1}, as seen in Figure I.7b,c. A negligible cathode current loss was noticed even after 1 000 cycles. Therefore, this WS_2 nanosheets electrocatalyst presented higher activity than many aforementioned MoS_2-based electrode materials [44-45, 62, 74].

By varying annealing temperature, it was possible to verify that at 500 °C, the reaction rate was very slow, and most of WO_3 was not consumed. Above 800 °C, reaction rate was fast enough to generate a WS_2 stable shell, limiting WO_3 consumption (Figure I.7a). At 700 °C, the sulfurization step works as well as at 600 °C. It was also found that, at least 30 min was necessary at 600 °C to have all WO_3 reacted.

Dai's group reported WS_2 nanoflakes synthesis by solvothermal method, which employed WCl_6 and elemental S as metal and sulfur sources, respectively, besides a mixture of oleylamine (OM) and 1-octadecene as solvent [72]. EDS and XPS suggested the formation of WS_2 species, while XRD confirmed the existence of a 2H-WS_2 phase. Additionally, TEM analysis showed that lateral size of nanoflakes measured 5-20 nm.

Before deposition on a GCE and evaluation towards HER in 0.5 M H_2SO_4 at 10 mV s^{-1}, WS_2 nanoflakes were physically mixed with Ketjen carbon black, a conductivity additive. A Tafel slope of about 48 mV dec^{-1} and η_{onset} = 100 mV were measured. Authors also pointed-out the importance of an annealing step at 500 °C for the WS_2 nanoflakes after the synthesis. Without this step, the material showed a much lower performance assigned to the passivation of sulfide surface by organic molecules, which is likely the responsible of the inhibition of restacking too. WS_2 nanoflakes were submitted to 10 000 continuous cycles and presented loss of activity during the first 6 000 cycles. Despite that, an increase of only 10

mV in overpotential value was observed for the catalyst in its HER activity curve after stability test.

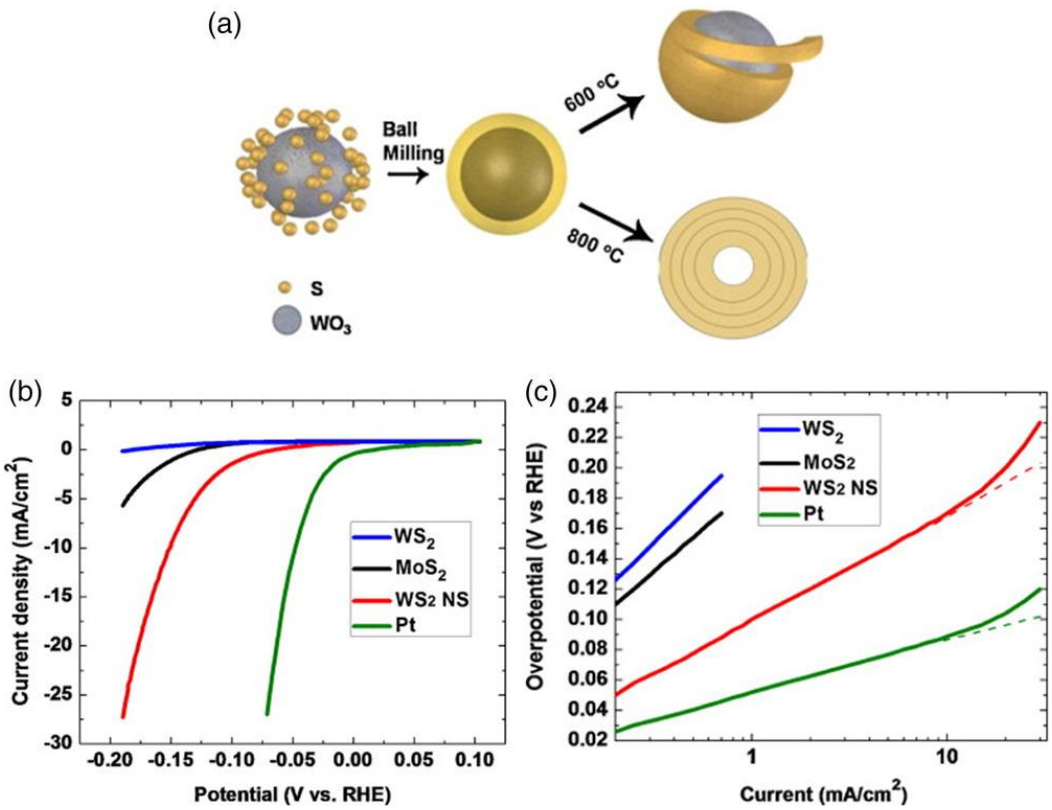

Figure I.7. (a) Schematic illustration of the formation processes of WS_2 NSs and fullerene nanostructures. (b) Polarization performance curves obtained in 0.5 M H_2SO_4 for various electrocatalysts. (c) Tafel plots derived for various electrocatalysts. Reprinted and adapted with permission from Ref. [82]; Copyright 2012, Elsevier.

A MoS_2/rGO catalyst was solvothermally synthesized by reacting $(NH_4)_2MoS_4$, hydrazine and graphene oxide (GO) in DMF at 200 °C for 10 h [83]. Nanosized MoS_2 flat particles of 3-10 layers deposited on rGO, with residual oxygen atomic percentage below 4 %, were obtained. When synthesized in the absence of GO, MoS_2 coalesced and presented a wide range of size. DMF was also important to guarantee a good coupling between MoS_2 and rGO, since its replacement by water resulted in two separate phases, MoS_2 particles and rGO sheets.

Liu's group produced composites of MoS_2 with mesoporous carbon nanospheres (MoS_2/MCNs) [84] and mesoporous graphene foams (MoS_2/MGF) [79] using the methodology proposed by Dai *et al.* [83], but replacing the GO by each carbon substrate and applying a heating time of 12 h. Both mesoporous substrates presented high specific surface areas, 719

and 819 m^2 g^{-1} for MCNs and MGF, respectively; that guarantee an enormous surface for high MoS_2 dispersion. On the other hand, mesoporous size of MGF (~25 nm) was much bigger than that of MCNs (~3 nm). TEM analysis identified MoS_2 particles with, approximately, 2 nm in MoS_2/MGF composite.

The effect of Mo/C molar ratio employed in the synthesis of MoS_2/MCNs was investigated. The HER activity order according to this ratio was 0.05 > 0.075 >> 0.1 > 0.025. TEM images revealed that lower molar ratios resulted in homogeneous growth of molybdenum sulfide, but when increasing them, aggregation initiates, therefore, tuning the sulfide/carbon ratio is extremely important [84].

HER activity of MoS_2/rGO, MoS_2/MCNs and MoS_2/MGF was evaluated in 0.5 M H_2SO_4 at 2 mV s^{-1}. All of them presented an onset overpotential of about 100 mV and a Tafel slope around 41 mV dec^{-1}, which suggests that reactions proceeded by the Volmer-Heyrovsky mechanism. Despite that, when compared at an overpotential of 200 mV, MoS_2/MGF performed much better than other materials; achieving a current density of about 100 mA cm^{-2}, while MoS_2/rGO and MoS_2/MCNs showed values in the range of 30-40 mA cm^{-2}. It must be taken into consideration that these values were obtained by an electrode geometric area normalization; the area available for reaction may be higher though. Additionally, both MoS_2/rGO and MoS_2/MGF presented negligible loss of cathodic current after 1 000 polarization cycles, operated at 100 mV s^{-1} for the first one and 10 mV s^{-1} for the second one. MoS_2/MCNs also showed good stability, although it operated only 100 successive scans.

The excellent catalytic activity of these materials was attributed to chemical and electronic coupling of the phases. The first is responsible for the high dispersion of MoS_2 in the substrates and the second results in rapid electron transport [79, 83-84].

GO also performs well as a support for WS_2 species. One-pot hydrothermal synthesis of WS_2/rGO was done by heating, at 265 ^oC for 24 h, a mixture containing WCl_6, thioacetamide (TAA) and graphene oxide in water [85]. H_2S, which was produced by the reaction between TAA and H_2O, reacts with WCl_6 to originate WS_2. GO worked as nucleation substrate for the sulfide and it was also reduced during the heating. At the end, the sample was freeze-dried and annealed at 300 ^oC. A sample synthesized without annealing step performed much worse on HER than the annealed one; it suggests the importance of crystallinity on WS_2 catalytic activity. Selected-area electron diffraction (SAED), TEM images, XRD, Raman spectroscopy and XPS suggested a 2H configuration for WS_2 nanosheets, with a number of

layers varying between 4 and 12. Additionally, even when using water as solvent, the integration of WS_2 and rGO was verified by microscopy. The same did not occur between MoS_2 and RGO in the synthesis methodology reported by Dai's group [83]. The material was deposited onto GCE and tested for HER in 0.5 M H_2SO_4 at 5 mV s^{-1}. A Tafel slope of 58 mV dec^{-1} and η_{onset} = 150-200 mV were obtained for the hybrid material. These are good results, although they are still inferior to results reported by Dai's group [83] for MoS_2/RGO. When WS_2 was synthesized in the absence of rGO, material's activity decreased to 350 mV of η_{onset} and a Tafel slope equal 140 mV dec^{-1} was calculated. Actually, the interconnection between WS_2 and rGO promoted a better electron transport.

Benchakar and coworkers reported the topotactic synthesis of MoS_2 onto Mo_2CT_x MXene substrate by one-pot approach [86]. Elemental sulfur powder (S_8) was mixed to Mo_2CT_x in 1:1 weight ratio followed by the addition of acetone; the mixture was grounded until the evaporation of organic solvent. The final mixture was placed into a tube furnace which was heated at 500 °C (5 °C min^{-1}) for 1 h under argon atmosphere. XRD and Raman spectroscopy confirmed the existence of 2H-MoS_2, besides residual sulfur (S_8). Such residual sulfur may be result of the weight ratio between sulfur and MXene applied in the synthesis. By combining XPS and ICP analyses, it was possible to observe that the molar ratio of Mo_2CT_x/MoS_2/S is equal 1/2.46/1.32. Additionally, MoS_2/Mo_2CT_x showed a capacitance four-fold higher than Mo_2CT_x. HER activity of the material was tested by LSV measurements in a N_2-saturated 1 M KOH solution at 5 mV s^{-1} and 1600 rpm. The MoS_2/Mo_2CT_x material exhibited a η_{10} = 150 mV and Tafel slope of about 70 mV dec^{-1}. By applying a current density of 10 mA cm^{-2} during 30 h, the catalyst also showed to be stable in the alkaline environment. Finally, the authors reported that MoS_2/Mo_2CT_x preserves its catalytic performance even after being stored one month inside a vacuum chamber.

On Nørskov's group work promoting the discovery of new active sites for HER [54], nitrogenase and hydrogenase enzymes were used as examples of active compounds without noble metals in their composition. The similarity between these enzymes and the edge active site of MoS_2 materials consists of the existence of unsaturated sulfur species [87]. Based on this assumption, a molecular Mo-based electrocatalyst approach, also containing these unsaturated sites, was investigated by Jaramillo et al. [87]. The authors synthesized incomplete cubane-type $[Mo_3S_4]^{4+}$ molecules by the reduction of $(NH_4)_2MoS_4$ or $[Mo_2O_2S_2 \cdot 6\ H_2O]^{2+}$ in the presence of $NaBH_4$; this material was deposited in carbon Vulcan XC-72 by

wet-impregnation. The creation of gas diffusion electrode (GDE) containing $[Mo_3S_4]^{4+}$ occurred by deposition of $[Mo_3S_4]^{4+}$/C in a graphite paper disk. Finally, the membrane electrode assembly (MEA) was obtained by pressing GDE containing $[Mo_3S_4]^{4+}$ with a 117 Nafion membrane and commercial Pt GDE at 130 °C and 32 bar for 5 min. The MEA was coupled to a fuel cell test setup, which operated with a flow rate of 20 mL min^{-1} of prehumidified H_2 in both electrode and scan rate of 5 mV s^{-1} [87]. CV analysis showed the presence of a reversible peak around 0.73 V vs NHE, which was correlated to desorption or readsorption of $[Mo_3S_4]^{4+}$. The reversible characteristics is result of low diffusion of $[Mo_3S_4]^{4+}$ on the Nafion membrane. Onset overpotential registered in LSV was, approximately, 150 mV, besides that, current density curve also showed similar results to previously reported MoS_2 materials [54-55]. Furthermore, current densities at high overpotentials decreased after every sweep, may be due to dissolution or agglomeration of clusters, though onset potential was maintained. The authors also prepared a $[Mo_3S_4]^{4+}$/HOPG electrode by dropcast method, which had its activity investigated in a three-electrode cell filled with a deaerated 0.5 M H_2SO_4 solution [87]. According to STM, sub-monolayer of independent molecules was obtained. CV measurements at 5 mV s^{-1} were performed and showed η_{onset} = 200 mV, besides a high Tafel slope of 120 mV dec^{-1}. Calculation of turnover frequency per $[Mo_3S_4]^{4+}$ compound exhibited a value of 0.07 s^{-1}. A cathodic peak, which has its intensity decreased after every sweep, was also detected; its occurrence was suggested to be related to desorption of $[Mo_3S_4]^{4+}$. XPS analysis after CV's showed a great decrease in Mo3d and S2p peaks, which is in-line with the aforementioned suggestion.

Amorphous Mo-based sulfides have also been receiving increasing attention due to their great activity towards HER. Hu's group presented great contributions for the investigation of these materials [88-90]. In an exploratory study, amorphous MoS_x films were synthesized by the electrochemical deposit of them in fluorine-doped tin oxide (FTO), indium tin oxide (ITO) and glassy carbon (GC)[88]. For materials preparation, electrode substrates were immersed in 2 mM $(NH_4)_2MoS_4$ aqueous solution containing $NaClO_4$ (0.1 M) and submitted to different electrochemical treatments, which impacted in final material. Two films were prepared by electrolysis, at anodic (0.5 V vs SHE) and cathodic (- 1.1 V vs SHE) potentials during 70 and 160 s, respectively. The authors stated that amorphous MoS_3 formation is favored at anodic potentials, whereas amorphous MoS_2 is preferentially grown on cathodic

potentials. Thus, they were labeled as MoS_3-AE and MoS_2-CE. Other two films were prepared applying cyclic voltammetry (CV) between – 0.8 and 0.3 V vs SHE at 50 mV s^{-1}. One of them started and finished at 0.3 V (MoS_3-CV), while the other at – 0.8 V (MoS_2-CV). As expected, XPS analyses of MoS_3-AE and MoS_2-CE proved the formation of MoS_3 and MoS_2, respectively. For materials synthesized by CV, MoS_2-CV resulted in MoS_2, and MoS_3-CV resulted in MoS_3, which highlights the influence of starting/ending potential. All materials presented activity towards HER, however, on first polarization curves of MoS_3-AE, MoS_3-CV and MoS_2-CV, a reduction peak was detected before HER occurs, albeit this peak presented lower intensity on MoS_2-CV. This characteristic peak was assigned to the reduction of MoS_3 to MoS_2 species. All these three materials presented similar behavior for HER in the subsequent polarizations, which supports the idea of an activation mechanism. XPS analysis was performed on MoS_3-CV after several polarization measurements, and confirmed the transformation of MoS_3 into MoS_2, at least on surface. In addition, MoS_2-CV and MoS_3-CV pre-catalysts presented highest activity and stability, with no evident difference. On the other hand, despite similar activity to aforementioned materials, MoS_3-AE presented a loss of activity due to re-dissolving of some MoS_3 species at cathodic potentials to generate $[MoS_4]^{2-}$ soluble species. MoS_2-CE presented the lowest activity, much lower than the others.

The MoS_3-CV pre-catalyst was further investigated. It was shown that its thickness could be controlled by the number of cycles employed and $[MoS_4]^{2-}$ concentration. Thickness of film is increased with more cycles until saturate at the 35th cycle. Similarly, the higher the $[MoS_4]^{2-}$ concentration, the higher the thickness of film. Films with thickness varying between 40 and 150 nm were synthesized. HER activity of MoS_3-CV synthesized by different number of cycles and, consequently, different thickness values, were tested. Thicker films showed higher activities, thus, this is a key parameter, although it is related to the number of active sites. Finally, MoS_3-CV synthesized on GCE by 25 cycles showed 14 mA cm^{-2} at 200 mV overpotential and a Tafel slope of 40 mV dec^{-1} for HER in 1 M H_2SO_4 at 2 mV s^{-1} and rotation rate of 4 500 rpm. These results are superior to those reported by Jaramillo's group for MoS2-DG (~4 mA cm^{-2} at a same overpotential and ~50 mV s^{-1}) [44]. It highlights the great potential of amorphous MoS_x as HER catalysts.

Hu's group also proposed a chemical route to synthesize amorphous MoS_3 and evaluated its deposition onto different substrates (FTO, GCE and carbon paste) by several methods [90].

Initially, MoO_3 was added to an aqueous solution containing Na_2S ([Na_2S]/[MoO_3] = 5), which has then been acidified with a 6 M HCl solution until pH = 4 was achieved. After the solution being boiled for 30 min and cooled down to room temperature, a dark paste was obtained and transferred to a recipient which was filled with 1 L of acetone. This solution was used for drop-casting and spray-casting application since it had been previously stirred and sonicated. To obtain a powder, the dark paste was dried at 80 ^{o}C for 12 h. Subsequently, the solid was grounded to originate the MoS_3 powder. The material presented no crystallinity and S to Mo ratio equal 3, according to TEM and XPS analyses.

Electrodes were produced by drop-casting and spray-casting of MoS_3 onto FTO and glassy carbon substrates. Besides that, carbon-paste electrodes were also produced by pressing MoS_3 onto home-made carbon-paste electrode surface. All catalysts were tested towards HER in a 1 M H_2SO_4 solution at 5 mV s^{-1}. The modified carbon-paste electrode showed a good catalytic activity. Due to its production technique, it was not possible to calculate the quantity of MoS_3 on a mass basis for this electrode. For the other deposition methods, different loadings of MoS_3 were tested and an optimum value was always obtained. Noteworthy, glassy carbon performed better than FTO for drop-casting and spray-casting methods, probably due to its lower resistance. Additionally, MoS_3 films produced by spray-casting were more uniform than those produced by drop-casting. Consequently, the optimum loadings for the former ones are higher than for latter. Hence, spray-casted electrodes showed higher geometrical normalized current density (mA cm^{-2}). Nevertheless, unexpectedly, drop-casted electrode presented better mass normalized current densities (mA $\mu g^{-1}_{sulfide}$). Yet, Tafel slope for all films obtained by spray-casting technique were about 40 mV dec^{-1}, while for drop-casting technique the higher was the MoS_3 loading, the higher was Tafel slope in a range of 41-63 mV dec^{-1}. It was suggested that loading increase had a negative effect on electron and proton transfer, resulting in a higher Tafel slope. To prove this assumption, MWCNT was added to the drop-casting solution to act as a conducting additive. As result, higher current densities were achieved and Tafel slope maintained the value of 40 mV dec^{-1} even in higher loadings of MoS_3. No gain of performance was verified when MWCNT was added to the spray-casting solution.

The comparison made by Hu's group, shows the current densities obtained at 150 and 200 mV overpotential for best electrodes produced in any category. Current densities recorded

for the best catalysts are similar to that reported for MoS_2-DG [44], albeit they are still lower than observed for electrochemical deposited MoS_3 catalyst [88].

The activity of MoS_3-modified electrodes has raised during the first six polarization curves and, especially in the first polarization, a cathodic peak appeared in more positive potential than those required for HER, as also reported by Hu *et al.*[88]. XPS analyses were performed after 8 polarization scans until – 0.3 V vs RHE and also after electrolysis performed during 5 and 10 min. XPS spectra were similar, albeit different from the spectra of MoS_3 synthesized by electropolymerization [88], in which MoS_3 was reduced to MoS_2 species. It corroborates the idea that MoS_3 is, in fact, a "pre-catalyst" and the active phase is produced by its reduction[90]. For chemically synthesized MoS_3 [90], no reduction of Mo was detected and S_2^{2-} species were not completely vanished; it was suggested that MoS_3 became MoS_x ($3 > x > 2$). By the annealing of amorphous MoS_3 material for 1 h, crystalline MoS_x catalysts were also prepared. According to XPS and electron diffraction patterns, when amorphous MoS_3 (a-MoS_3) was annealed at 350 °C, a polycrystalline MoS_3 catalyst (MoS_3-350) was generated. At 650 °C, it resulted in single crystalline MoS_2 (MoS_2-650) phase. The activity towards HER followed the order a-MoS_3 > MoS_3-350 > MoS_2-650. This order may be explained by materials' crystallinity. Unsaturated sulfur atoms play a key role in the discharge step of HER by the hydrogen adsorption to originate a S-H bond. The quantity of these sulfur atoms in surface increase as particle size and crystallinity decrease.

Jaramillo's group also reported a simple wet chemical method to synthesize amorphous MoS_3 with no need of heating or potential application[91]. A solution containing $(NH_4)_6Mo_7O_{24}$ and H_2SO_4 was mixed to another solution containing Na_2S; resulting in a fast formation of nanoparticles which were later recovered by centrifugation. The absence of crystallinity was verified by TEM and XRD. Surface composition, investigated by XPS, confirmed the MoS_3 formation. As expected, the "pre-catalyst" material behaved differently in the first reductive cycle as compared to subsequent ones. Additionally, material showed to resemble to MoS_2 on XPS analysis after reductive cycles, albeit distinctive A_{1g} and E^1_{2g} Raman spectroscopy peaks remained undetectable; it suggests that resultant MoS_2 still has amorphous characteristic. A Tafel slope of about 60 mV dec^{-1} and $\eta_{onset} \approx 150$ mV were obtained for this material at 5 mV s^{-1} in a 0.5 M H_2SO_4 solution. Furthermore, $\eta_{10} \approx 200$ mV was obtained, showing better activity than MoS_3 catalyst synthesized by chemical route by Hu's group [90]. After 10 000 reductive cycles, the overpotential to achieve the same 10 mA

cm^{-2} was increased of 57 mV. It was verified by SEM, after stability testing, that delamination occurred and was one of reasons for its activity loss.

Chen *et al.* [71] developed a comparative study between the activity of MoS_2 and WS_2 on the HER in 0.5 M H_2SO_4 electrolyte, in which carbon cloth (CC) served as substrate. For the synthesis, CC was immersed in a solution of $(NH_4)_2MoS_4$ or $(NH_4)_2WS_4$, according to the desired sulfide, and then heated at 100 ºC for 10 min. The coated substrate was then submitted to a heat treatment at different temperatures (between 200 and 1 000 ºC) in a 20 % H_2/Ar atmosphere flowing at 100 mL min^{-1}. SEM analyses showed that pristine CC fibers presented a smooth surface which became rough after the introduction of sulfide species. Noteworthy, the roughness of these fibers increase as the temperature in heat treatment is higher due to crystallinity of resulted sulfides. From XRD analyses, the MoS_2 diffraction line was just detected for the sample heated at 1 000 ºC, none was detected for the 200, 300 and 500 ºC. In the case of WS_2, samples heated at 200 and 400 ºC already presented the main diffraction line, but the increase of temperature to 800 and 1 000 ºC led to a higher crystallinity of samples and other lines were also detected. However, these samples obtained at higher temperatures also exposed a line of WO_3 on XRD analysis. In contrast, no trace of oxidation was verified for MoS_2 samples. Raman spectra analyses were also performed, and results agreed with XRD. Other WS_2 samples were prepared by heating at 1 000 ºC in air and Ar atmosphere. According to Raman and XPS analyses, only WO_3 was detected in the sample heated in air, whereas only WS_2 was detected for sample heated in Ar. For samples synthesized in 20 % H_2/Ar at 200 and 1 000 ºC, tungsten was found with oxidations of +4, +5 and +6 and sulfur was found as S^{-2} and S_2^{-2}, which indicates the presence of crystalline and amorphous WS_2, besides WO_3. But the content of WO_3 increase in higher temperature. Besides that, sulfone specie was also identified at 1 000 ºC. In the case of MoS_2 samples, it was verified that Mo^{+5} was detected in materials synthesized at low temperature, above 300 ºC only Mo^{+4} was detected. No considerable peak corresponding to MoO_3 was detected.

From HER analysis at 5 mV s^{-1}, it was verified that the activity of MoS_2 decreased with the increase of the temperature in the heating treatment. Therefore, amorphous MoS_2 seemed to be more active than the crystalline one. The contrary trend was observed for WS_2. The WS_2 materials, synthesized in air and Ar atmosphere, were also tested and they exhibited the worst and best activity, respectively. It can be concluded that WO_3 is not active for the

HER and, consequently, crystalline WS_2 is more active than amorphous one. Finally, WS_2 prepared at 1 000 ºC showed to be stable when a potential of -0.3 V vs RHE was applied for 3 h. A current density of about 2.2 mA cm^{-2} was achieved with no relevant variations.

Xu et al. [92] reported the synthesis, and high activity towards HER in both acidic and alkaline media, of an unsaturated sulfur-enriched MoS_2 embedded into carbon nanohybrid material (SD-MoS_2@C). Initially, positively charged carbon cloth, obtained from its treatment with n-methyl-2-pyrrolidone (NMP), was immersed in a negatively charged polystyrene nanosphere aqueous solution containing glucose and ammonium thiomolybdate. After calcination at 700 ºC for 2 h under Ar atmosphere, it was produced a MoS_2@C deposited onto carbon cloth (CC) electrocatalyst. To enrich the electrocatalyst with unsaturated sulfur, MoS_2@C was used as working electrode in a sodium-ion half battery, which was charged and discharged within a window of 0.25-3.0 V at 1.0 A g^{-1} for only one cycle. In this process, Mo-S linkage is broken and generate unbound sulfur which further creates a bond with unbroken Mo-S, producing then more unsaturated sulfur sites. As result, the SD-MoS_2@C deposited onto CC electrocatalyst with a mass loading of 1.0 mg cm^{-2} was obtained and 45.3 % of this mass corresponded to carbon as suggested by TG results. SEM and TEM techniques indicated the formation of a hybrid material containing macroporous of about 200 nm and wall thickness of, approximately, 15 nm. MoS_2 nanocrystals, identified as 2H phase (also confirmed by XRD), embedded into amorphous carbon framework presented 1-3 layers with lateral dimensions in the range of 5-10 nm. Wettability of electrocatalyst surface is a parameter of paramount importance in HER, and it was shown that a droplet takes 0.05 s to be absorbed by SD-MoS_2@C, whereas a contact angle of 77º was registered for MoS_2@C. As evidenced by FTIR, CH-groups were found in MoS_2@C and none was detected for SD-MoS_2@C material, therefore, the sodiation/desodiation treatment also removed hydrophobic species; it surely contributed to the enhanced activity of SD-MoS_2@C. Additionally, conductivity of S-MoS_2@C is 130 % higher, according to four-point probe technology. XPS spectra confirmed the increase of S_2^{2-} species, associated with unsaturated sulfur, after sodiation/desodiation treatment. Yet, the presence of C-S was verified, evidencing the strong sulfide-carbon interaction. When evaluated on HER in 0.5 M H_2SO_4 at 2 mV s^{-1}, SD-MoS_2@C achieved η_{10} = 136 mV and showed Tafel slope of 78 mV dec^{-1}. On the other hand, MoS_2@C presented η_{10} = 176 mV Tafel slope about 99 mV dec^{-1}. Specifically at an overpotential of 200 mV, SD-MoS_2@C exhibited a current density of 76 mA cm^{-2},

approximately, four-fold the value obtained by MoS_2@C. Additionally, according to EIS measurements, SD-MoS_2@C showed a charge transfer resistance 3.4 times lower. Even after replacing the aforementioned electrolyte by 1 M KOH, SD-MoS_2@C showed excellent HER activity, although acidic environment results are better. It was achieved a η_{10} = 155 mV, 34 mV lower than for MoS_2@C. Moreover, SD-MoS_2@C showed a Tafel slope about 99 mV dec^{-1} and enhanced charge transfer, in comparison to MoS_2@C, in alkaline media, albeit only 1.4 times lower. The SD-MoS_2@C electrocatalyst was evaluated by chronopotentiometry at 10 mA cm^{-2} for 24 h, and also by submitting it to 10 000 consecutive LSV cycles, in acidic and alkaline environments; activity loss was negligible in all tests. In addition, the electrode was soaked in a 0.5 M H_2SO_4 or 1 M KOH solution at 60 ^oC for 12 h, and then evaluated again by LSV. The curves were not altered with these thermal treatments too. Finally, DFT calculations were performed to verify the ΔG_H^0 values in each model site of SD-MoS_2@C. As expected, the best value was obtained for the unsaturated S-edge (0.52 eV) followed by Mo-edge (- 0.94 eV), S-edge (0.97 eV) and S-basal plane (7.17 eV) sites. Therefore, this work performed by Xu and coworkers[92] presents an interesting and promising strategy to increase the quantity of active unsaturated sulfur edge sites of 2D sulfide materials.

Generally, MoS_2-based materials present a layered morphology, and each layer consists of three covalently bonded atomic sheets, S-Mo-S[45, 81]. In addition, as aforementioned, the electrical conductivity is not favored between the layers of two-dimensional sulfides. Once the transfer of electrons is mandatory on electrochemical reactions, it is desired to produce MoS_2 with a number of layers as low as possible. One strategy to achieve it is the exfoliation of the molybdenum sulfide layers. Chemical exfoliation is a methodology commonly adopted, generally through the Li intercalation of the layers[73]. Li is placed between the layers of the material and then removed by the excess of water, resulting in a few-layered material.

In addition, different arrangements of the S-Mo-S layers may originate three MoS_2 phases[74]. Figure I.6b shows the identified three phases of the bulk MoS_2 that is a hexagonally packed layered structure, similar to graphite, with a 6.15 Å Van der Waals gap separating each sheet [25]. The most common is the 2H phase which can be found naturally, since it is favored thermodynamically. Therefore, every time that no prefix is added to MoS_2 in this text, it is associated with the 2H phase, unless specified. The structure of the 2H phase is a series of S-Mo-S layers composed of edge-shared MoS_6 trigonal prisms and it has a semiconductor

behavior; whereas the 1T phase is a single S-Mo-S layer built from edge-sharing MoS_6 octahedra [25]. Because of its metallic character (*i.e.*, better electrical conductivity) and more available active sites that are mainly located in the basal plane, the 1T polymorph of MoS_2 outperform the other phases in terms of HER activities [61, 77]. Indeed, in 0.5 M H_2SO_4, the iR-corrected Tafel slopes are of 43 and 110 mV/decade for 1T-MoS_2 chemically exfoliated and 2H-MoS_2, respectively. And j = -10 mA cm^{-2} at E = -187 mV vs. RHE for 1T-MoS_2 electrode (E > -200 mV vs. RHE for 2H-MoS_2). However, the 1T phase is not naturally found in bulk MoS_2 and because it is a metastable phase, even after being generated, it can be easily converted to 2H. It also exists the 3R phase that, similarly to 2H, present a trigonal coordination. They differ by the quantity of layers per unit cell, three layers for 3R phase whereas two layers are present in the 2H phase. The 3R phase is generally not applied for catalytic purposes [77, 93]. The conversion of 2H to 1T phase is usually a consequence of the Li intercalation technique, because it occurs electron transfer from Li, which destabilizes 2H-MoS_2 structure, whereas favors 1T-MoS_2 one [73, 77].

Chemical exfoliation of bulk MoS_2 by the lithium intercalation method that consists of the intercalating of lithium compounds (e.g., methyllithium (Me-Li), n -butyllithium (n-Bu-Li) and tert-butyllithium (t-Bu-Li)) between MoS_2 layers followed by a exfoliation of Li-intercalated compounds via reacting with water is a widely used approach to obtain single- or few-layered MoS_2 [59]. Pumera's group found that, in 0.5 M H_2SO_4, the Tafel slope of bulk MoS_2 is 151 mV dec^{-1}, while the exfoliated materials gave lower Tafel slopes of 102, 96 and 94 mV dec^{-1} for MoS_2 exfoliated with Me-Li, n-Bu-Li and t-Bu-Li, respectively. Mechanistically, the experimental Tafel slope values for the exfoliated MoS_2 are situated between the Volmer mechanism (120 mV dec^{-1}) and the Heyrovsky mechanism (40 mV dec^{-1}). Thus, the *rds* for the HER on the MoS_2 exfoliated samples is the mix Volmer-Heyrovsky mechanism. It can be concluded that the efficiency of the chemical exfoliation of MoS_2 through Li intercalation follows Me- Li < n-Bu-Li < t-Bu-Li. According to the authors, this disparity can be explained by the stability of the generated anion R^- which size follows the order n-Bu-Li > t-Bu-Li > Me-Li as well as the basicity of the formed carbon anion (t-Bu-Li is one of the strongest commercially available organic base with pKa ~ 53). Hence, more stable anions provide more available Li^+ leading to a more efficient intercalation.

Through the chemical vapor deposition (CVD) method, Lukowski[77] *et al.* initially synthesized a flower-like MoS_2 nanostructure which was further exfoliated by Li

intercalation method. TEM, XRD and Raman spectroscopy were performed and the as-synthesized MoS_2, before exfoliation, was identified as a semiconducting 2H-MoS_2 phase containing, approximately, 12 layers per flake. This material was soaked in n-butyllithium solution at 60 °C for 48 h and exfoliated with addition of water in excess. New XRD analyses presented the disappearance of (00l) diffraction lines which was attributed to a monolayer structure by the authors. Besides that, Raman spectroscopy indicated a transformation from 2H-MoS_2 to 1T-MoS_2 phase.

Graphite electrode supported as-grown 2H-MoS_2 and its chemically exfoliated form (1T-MoS_2), synthesized by Lukowski et al. [77], were tested on HER in 0.5 M H_2SO_4 electrolyte at 3 mV s^{-1} and 2 000 rpm. 2H-MoS_2 presented $\eta_{onset} \approx 200$ mV, $\eta_{10} = 320$ mV and Tafel slope about 110 mV dec^{-1}, after iR correction. The onset potential has shifted to a more positive potential on 1T-MoS_2 catalyst, besides that, $\eta_{10} = 187$ mV and Tafel slope of, approximately, 43 mV dec^{-1} were obtained, after iR correction. It was revealed that phase transformation from 2H to 1T increased the density of active site in more than 10-fold and decreased charge-transfer resistance in 58-fold.

During stability test, 1T-MoS_2 nanosheets showed a loss lower than 15 % in cathodic current density after 1 000 continuous cycles, which was followed by a slight increase in charge-transfer resistance, according to EIS. Yet, to maintain a current density of 10 mA cm^{-2}, an increase of 10 mV in overpotential was requested after 9 h of operation. The authors attributed this effect to a slow return of 1T to 2H phase. This assumption was based on the loss of activity and the rise of charge-transfer resistance with the aging of 1T-MoS_2 sample. To fully confirm it, post-reaction characterizations (XRD, Raman, etc.) should be performed.

This exfoliation strategy is also effective for tungsten sulfide materials. Lukowski *et al.* [94] applied the same methodology to a previously synthesized flower-like WS_2, although the n-butyllithium solution used was maintained at 80 °C; such temperature increase was done to favor the intercalation, which is harder for WS_2 than MoS_2. In addition, the oxidation is more favorable in WS_2 nanosheets than MoS_2 ones. Aiming to deal with this issue, the authors also reported the development of a shorter exfoliation method (20 min instead of 48 h) employing a microwave device. These exfoliated materials were tested towards HER in 0.5 M H_2SO_4 at 3 mV s^{-1} using RDE operating at 2 000 rpm. Similar results were obtained for materials exfoliated by both methods (conventional and microwave-assisted). Both presented a Tafel slope about 70 mV dec^{-1}, while $\eta_{10} = 142$ and 151 mV were obtained for

conventional and microwave-assisted methods, respectively. On the other hand, 2H-WS_2 pristine material presented a Tafel slope about 85 mV dec^{-1} and did not achieve 10 mA cm^{-2} until -0.33 V vs RHE. According to EIS measurements, the exfoliation also reduced about 40 times the R_{ct}, as expected. The authors also showed evidence to state the importance of pristine material for the exfoliation process. Both processes were performed simultaneously to the CVD synthesized material (flower-like WS_2 containing ~10 layers and presenting well defined crystallinity) and commercial WS_2 bulk powder (larger particle sizes and irregular morphology). Materials exfoliated after CVD method performed much better for HER. Despite that, Voiry *et al.*[47] chemically exfoliated a commercially available WS_2 powder through Li intercalation method. It originated a highly distorted 1T-WS_2 structure with no Li impurity detected by Rutherford backscattering spectroscopy (RBS). Likewise MoS_2, 1T-WS_2 is a metastable structure and its annealing may result in relaxation of structure leading to its reconversion toward 2H-WS_2 phase, calculations suggest that the energy barrier for this transition is, approximately, 0.95 eV though. Voiry *et al.*[47] reported that even after 200 storing days at laboratory, 1T phase remained constant. The 1T-WS_2 nanosheets were evaluated towards HER in Ar-purged 0.5 M H_2SO_4 at 5 mV s^{-1} and presented η_{onset} = 80-100 mV and Tafel slope of ~55 mV dec^{-1}, after iR correction. To evaluate the stability of this catalyst, 10 000 cycles were run monitoring the current density in a continuous operation at –0.3 V vs RHE for 120 h; a fluctuation of current density was observed, although a maximum cathodic current loss of about 10 % was calculated during all operation. Noteworthy, DFT calculations suggested that tensile strains provoked by distortion on 1T phase led to a better adjust on G_H^0 (closer to zero). Better structure towards hydrogen adsorption occurs when strain percentage is between 2-3 %. Yet, it was suggested that only tensile strain improve the activity, nanosheets in compression are not active. Additionally, calculations evidenced that the strain has no influence on 2H phase. Therefore, the superior activity of these WS_2 nanosheets came from 1T phase, as already expected, but also from the highly strain feature of the material, which showed to be an important parameter to 1T-WS_2-based materials.

Contrary of what was reported by Voiry *et al.* [47] for 2H-WS_2, Tan *et al.* showed that out-of-plane strain may enhance the activity of 2H-MoS_2 for HER[95]. The authors synthesized a continuous MoS_2 monolayer on the internal surface of nanoporous gold (NPG), which contains curves. Applying Raman spectroscopy measurements, they also reported that the number of layers of MoS_2 could be controlled by adjusting the CVD time and distance

between MoO_3 and NPG substrate, besides to confirm the homogeneity of the films. Aided by STEM analyses, the authors could verify the existence of out-of-plane strains on curved regions of NPG, resulting in the increase of S-Mo-S bonding angle (α), and the absence of morphological characteristics related to the presence of uncoordinated sulfur species. This MoS_2/NPG composite was tested towards HER at 0.5 M H_2SO_4 and showed a η_{onset} = 118 mV and Tafel slope about 46 mV dec^{-1}. DFT calculations proposed by the authors suggest that the activity is result of α increasing. It was reported that when α > 140º (α = 120º for a non-distorted regular MoS_2) the band gap of 2H-MoS_2 becomes closer to zero. Additionally, it was reported that at bent regions, charge density of sulfur becomes similar to edge sulfur atoms. Therefore, this work provides evidences of out-of-plane strain effect on 2H-MoS_2 materials.

Several authors reported the development of methods which resulted in materials containing many features responsible for enhancing catalyst activity. An extensive study on the effect of crystalline phase (1T or 2H) and quantity of edge and vacancy sites in MoS_2-based material's activity was performed by Yin *et al.*[96]. A liquid-ammonia-assisted lithiation method was applied to bulk MoS_2 to generate mesoporous 1T-MoS_2 (MP-1T-MoS_2), the annealing of this sample at 550 ºC originated mesoporous 2H-MoS_2 (MP-2H-MoS_2) material, part of this was further placed in the downstream of an oven, while sulfur powder was placed in the upstream. Oven temperature was set at 550 ºC and it led to the production of sulfur-compensated mesoporous 2H-MoS_2 (MP-2H-MoS_2+S). 2H-MoS_2 and 1T-MoS_2 materials were also synthesized by liquid-exfoliation in N-methylpyrrolidone (NMP) and Li-exfoliation, respectively, of MoS_2 bulk powder. All materials presented nanosheets morphology and similar thickness of, approximately, 1-2 layers, which is important for the comparisons. MP-1T-MoS_2 materials synthesized from different Li:MoS_2 ratios were studied by TEM, and their porosity increased as this ratio rises. STEM images also revealed that thermal treatment, applied to produce MP-2H-MoS_2-based materials, does not affect the porosity when compared to the pristine MP-1T-MoS_2. Additionally, TEM, Raman and XPS analyses confirmed the existence of 1T phase in MP-1T-MoS_2 and 1T-MoS_2, approximately, 80 %.

All materials were deposited in a rotating GCE and tested for HER in 0.5 M H_2SO_4 at 5 mV s^{-1} and 2,000 rpm. The activity order registered was MP-1T-MoS_2 > 1T-MoS_2 > MP-2H-MoS_2 > MP-2H-MoS_2+S > 2H-MoS_2, exactly the same for several parameters (η_{10}, j_0, Tafel slope,

ECSA and R_{ct}). Therefore, increasing the number of edge and vacancy sites, besides the proportion of 1T phase, has a huge impact in availability of active sites for HER, enhancing then the electrocatalyst's activity. Besides that, looking deeper to EIS analysis, one may see that 1T-based material present charge-transfer resistance of one order of magnitude lower than 2H-analogous-based material, which comes from the metallic property of 1T phase, while 2H phase shows semiconductor feature. The number of S-vacancies of material was quantified by positron annihilation lifetime spectroscopy (PALS), and it was revealed that MP-1T-MoS_2 and MP-2H-MoS_2 possess similar quantity of S-vacancies, therefore, the difference of activity is associated with the difference of phase. Additionally, MP-2H-MoS_2 exhibited more S-vacancies than MP-2H-MoS_2+S, as expected, thus, since they present the same phase and similar quantities of edge sites, it shows the positive influence of S-vacancies on HER. Finally, the best electrocatalyst, MP-1T-MoS_2 exhibited η_{10} = 154 mV, j_0 = 15.8 μA cm^{-2}, R_{ct} = 16 Ω at 250 mV and Tafel slope about 43 mV dec^{-1}. This good performance is result of its crystalline phase, mainly, but also mesoporosity and S-vacancies. Finally, this electrocatalyst presented a loss of activity of 7 and 15 %, approximately, when submitted to 1 000 cycles and chronoamperometric analysis at 180 mV (initial current density of ~15 mA cm^{-2}) of overpotential for 20 000 s (~5.5 h), respectively.

Shin's group presented a unique synthesis method capable of producing MoS_2 containing several features used as strategy to enhance its activity towards HER, such as: transformation towards 1T phase, creation of defects and vacancy and expansion of interlayer distance [97]. Initially, phosphomolybdic acid (PMo_{12}) reacted with melamine (MA) at 90 °C and produced a monobasic MA-PMo_{12} complex which was subsequent reacted with thiourea at 180 °C for 20 h. During this step, an excess of ammonia is generated and part of this is lodged between the layers of MoS_2, resulting them in an ammonia-intercalated molybdenum sulfide (NH_3-MoS_2) material. According to SEM, NH_3-MoS_2 presents a nanoflower-like morphology with sharped edges formed by the aggregation of nanosheets. XRD, TEM and XPS revealed the coexistence of 2H- and 1T-phases in the material, 71 % of 1T metallic phase, with an interlayer distance equal to 8.40 Å, much higher than the standard (6.15 Å). The existence of defects and NH_3/NH_4^+ species was also verified by TEM and XPS, respectively. The NH_3-MoS_2 material was reduced under H_2 atmosphere at 500 °C for 3 h, leading to the removal of NH_3, despite not totally, and S species, which resulted in the decrease of interlayer spacing to about 6.85 Å, creation of S vacancies and reduction of 1T-

phase proportion to 34 %. However, the same morphology was verified by SEM and TEM images, albeit increased crystallinity, larger flake size and smaller holes were result of thermal treatment. Reduction temperatures of 400 and 600 °C were also tested but it resulted in less active materials.

The use of monobasic MA-PMo_{12} complex as molybdenum source is of paramount importance because the generation of octahedral structure, typical of 1T-MoS_2 phase, likely comes from the octahedral array of MoO_3 units present in PMo_{12}. In addition, melamine acts as nitrogen source to generate ammonia, responsible for interlayer expansion. MoS_2 was also synthesized in the absence of melamine and resulted in nanosheets with interlayers distance of 6.34 Å. The materials were drop-casted in a GCE and evaluated for HER in 1M KOH solution at 5 mV s^{-1} and 1 600 rpm. The reduced catalyst (R-MoS_2) showed the best activity achieving 10 mA cm^{-2} with an overpotential of 111 mV, 118 mV lower than for NH_3-MoS_2, besides η_{onset} = 20 mV, about 8 times lower than registered for NH_3-MoS_2 catalyst. Even in a mass basis, R-MoS_2 catalyst was the most active and needed only 103 mV overpotential to achieve 10 A g^{-1}. On the other hand, NH_3-MoS_2 showed a much lower Tafel slope than R-MoS_2 (66 vs 105 mV dec^{-1}) which is likely due to rapid electron transport in 1T metallic phase, more present in NH_3-MoS_2. When it comes to exchange current densities, once again R-MoS_2 shows better result than NH_3-MoS_2 (0.876 vs 0.004 mA cm^{-2}); it evidences higher intrinsic activity of reduced sample. R-MoS_2 was also tested for HER in 0.5 M H_2SO_4 and needed an overpotential equal to 184 mV to generate a 10 mA cm^{-2} current density, noteworthy, higher than in alkaline environment.

Other materials aiming the integration of R-MoS_2 to N-doped graphene (R-MoS_2@NG) or nickel foam (R-MoS_2@NF) were produced. While NG only slightly increased R-MoS_2 activity, a great improvement was verified with NF integration, exhibiting η_{onset} = 5 mV and η_{10} = 71 mV. Although R-MoS_2@NF showed, approximately, the same Tafel slope than R-MoS_2, the calculated j_0 increased to 2.27 mA cm^{-2}, closer to the value obtained for the benchmark Pt/C catalyst (2.65 mA cm^{-2}). In fact, R-MoS_2@NF performed better than Pt/C at high currents; to achieve 40 mA cm^{-2}, Pt/C requested an overpotential of 156 mV, while only 105 mV was necessary for R-MoS_2@NF. Additionally, while R-MoS_2 showed an ECSA equal to 178.5 cm^2, R-MoS_2@NF exhibited 4325.3 cm^2 and, therefore, ECSA is a very important parameter to justify the catalytic enhancement provided by NF integration. Stability tests were performed for R-MoS_2@NF and R-MoS_2 electrocatalysts. R-MoS_2@NF

showed negligible loss of performance when submitted to 5 000 successive CV cycles at 100 mV s^{-1} and chronoamperometry analysis at 100 mV overpotential for 22 h. On the other hand, R-MoS_2 showed a small loss activity in the chronoamperometric test at 100 mV for 10 h, probably due to bubble formation and loss of catalyst. Interestingly, after 5 000 successive CV cycles at 100 mV s^{-1}, R-MoS_2 has its activity improved. XPS post-reaction analyses showed a reduction on N 1s spectrum, therefore, such improvement is likely due to elimination of weekly bonded nitrogen species which remained even after reduction process.

Shaijumon's group developed a sonication-assisted synthetic method to make a hybrid nanostructure of 1 nm-sized quantum dots interspersed in few-layered MoS_2 nanosheets. The resulting hybrid nanomaterial (loaded on an Au electrode) showed excellent HER activity with a relatively low Tafel slope of ~74 mV dec^{-1} and a large j_0 of 3.2×10^{-5} A cm^{-2}, probably due to the enhanced edge-to-basal plane ratio resulting from the unique morphology of the material.

The hybridization of sulfides with other metallic-based materials was also explored and reported. The decoration of MoS_2 and WS_2 materials with gold nanoparticles was reported as a methodology to promote the catalytic activity [98]. Although the gold addition raises material price, if it is added in very small quantities and provides a relevant improvement, its use may be justified. The decoration of chemically exfoliated nanosheets of MoS_2 and WS_2 by Au nanoparticles was realized by the simple addition of $HAuCl_4$ in an aqueous dispersion of these sulfides. Chemical exfoliation promotes more defects on nanosheets when compared to physical exfoliation; this is an advantage once edges and defects are preferred places to deposit Au nanoparticles. Additionally, exfoliation method adopted resulted in partial phase transition from 2H to 1T in both MoS_2 and WS_2 materials. Quantity and size of gold particles could be increased with the increase of $HAuCl_4$ concentration.

Gold decorated sulfides by different concentrations of $HAuCl_4$ were tested towards the HER in 0.5 M H_2SO_4 at 5 mV s^{-1}. Current densities increased while Tafel slope decreased with $HAuCl_4$ concentration increase for both catalysts, although the effect was more pronounced for WS_2. It was probably a consequence of the harder formation of 1T phase for WS_2 than for MoS_2, thus, as Au nanoparticles act on the boosting of charge transfer, it became more evident for WS_2 nanosheets. However, excessive addition of Au may block catalytic active site, and consequently diminishes current densities, as could be seen for WS_2 nanosheets.

A one-pot synthesis methodology for the production of Ni_3S_2-MoS_2 heterostructure supported on nickel foam (NF) was proposed by Yang et al [99]. To accomplish it, NF was solvothermally reacted with thioacetamide (TAA) and ammonium heptamolybdate (AHM) in the presence of urea for 24 h at 240 °C. The AHM/NF mass ratio showed impact on material morphology; it varied from nanorods to nanoparticles as this ratio increased. The best catalyst was obtained from the optimal ratio AHM/NF = 0.07. From EDS results, authors reported the atomic ratios of Ni/S and Ni/Mo of 1.46 and 34.48, respectively. Therefore, the structure is composed predominantly of Ni_3S_2 decorated by MoS_2 species. Yet, according to XPS analysis, the interaction between Ni_3S_2 and MoS_2 led to a redistribution of charge, specifically an electron density reduction around Ni, which enhances the binding of H atom. Additionally, binding energies associated to S_2^{2-} and SO_4^{2-}, related to unsaturated-sulfur and oxidation by air, respectively, were also verified.

The Ni_3S_2-MoS_2/NF catalyst was tested for HER at 1 M KOH environment. After iR-drop correction, the values of η_{onset} = 31 mV, η_{10} = 98 mV, η_{100} = 191 mV and Tafel slope about 61 mV dec^{-1} were obtained. Its stability was tested and compared to commercial Pt/C by performing 10 000 continuous cycles and chronoamperometry analysis. Although Pt/C is more active, it suffers an activity loss, while negligible loss is verified for Ni_3S_2-MoS_2/NF.

Li and coworkers [100] developed a synthesis for highly active porous amorphous nickel-cobalt hydrazine complexes hybridized with 1T-MoS_2 (NCH-1T-MoS_2) materials. For that, Ni-Co hydroxides nanosheets with about 4 nm and 30-150 nm of thickness and diameter, respectively, containing a circular shape were reacted with $(NH_4)_2MoS_4$ in DMF containing hydrazine hydrate (HZH); the influence of HZH on the synthesis was evaluated by the addition of different amounts. All the materials, synthesized by the addition of 0, 0.05, 1 and 2.5 mL of HZH (resulting in 0-NCH-1T-MoS_2, 0.05-NCH-1T-MoS_2, 1-NCH-1T-MoS_2 and 2.5-NCH-1T-MoS_2, respectively), showed to maintain the nanosheet morphology. TEM analysis evidenced that the quantity and size of porous increased as more HZH was added to the synthesis, it occurred because hydrazine may decompose at high temperatures to produce N_2 and NH_3 gases which create porous during their release. As result, 2.5-NCH-1T-MoS_2 presented a specific surface area equal 91 m^2 g^{-1}, the highest among materials. Addition of 3 and 5 mL of HZH during the synthesis was also tested but it did not result in differences when compared to 2.5-NCH-1T-MoS_2. Additionally, TEM, XRD, XPS and XANES analyses evidenced that hydrazine interacted with nickel and cobalt resulting in amorphous

complexes, although small quantities of KOH were also added during the synthesis to guarantee the gases release by hydrazine decomposition as aforementioned. Besides that, bigger amounts of HZH (at least 1 mL) promoted the synthesis of 1T-MoS_2 as unique phase; in lower quantities, 1T- and 2H-MoS_2 coexisted. The transition from 2H to 1T phase depends on the existence of an electron donor, which would be the hydrazine in this case. However, the synthesis procedure was repeated without the addition of nickel and cobalt hydroxides and the resultant MoS_2 material did not present a pure 1T phase. It means that Ni-Co complexes have an important role for 1T phase stabilization.

The active materials were mixed with carbon Vulcan XC72 in a mass ratio equal 5:1, respectively, to produce the catalytic ink and deposit it onto GCE surface before being evaluated towards HER in 1 M KOH solution at 5 mV s^{-1} and 1 600 rpm. The η_{10} for 0-NCH-1T-MoS_2, 0.05-NCH-1T-MoS_2, 1-NCH-1T-MoS_2 and 2.5-NCH-1T-MoS_2 was 87, 148, 128 and 70 mV, respectively. It shows that the tuning of HZH is of paramount importance once the material synthesized in the absence of this compound showed the second-best performance. It may be associated with crystallinity of Ni, since it appears in amorphous phase for all materials, except 0-NCH-1T-MoS_2. The best performance was obtained for 2.5-NCH-1T-MoS_2 which showed a very low η_{onset}, Tafel slope about 38 mV dec^{-1} and lower reaction resistance. The stability of this catalyst was assessed by chronoamperometric analysis at an overpotential of 130 mV (initial current density of ~30 mA cm^{-2}) for 24 h. In the first 3 h, a degradation of current was verified and the current increased in the subsequent hours. The ECSA of materials was calculated and, as expected, 2.5-NCH-1T-MoS_2 exhibited higher ECSA than 0-NCH-1T-MoS_2 (807.5 vs 502.5 cm^2). Authors also proposed an alternative intramolecular mechanism for HER. In this mechanism, Ni(III)- and Co(III)-hydrazine complexes would receive 2 e-, resulting to the transition from trivalent to monovalent metal. In the sequence, protons from water molecule react with monovalent metal and the amine in the second coordination sphere, it originates back the trivalent metal and NH_3^+ specie and, finally, these hydrogen species combine between themselves to produce and release H_2, besides to regenerate the initial complex. This mechanism is better described below on Scheme 1.

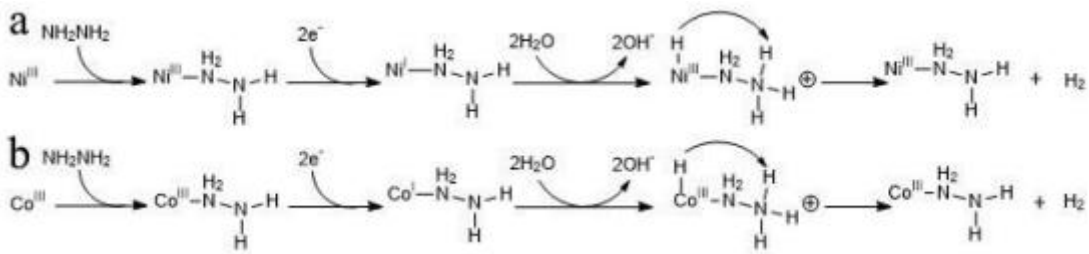

Scheme I.1. (a) and (b) Possible mechanism of intramolecular proton transfer in hydrazine coordinated Ni and Co complexes. Reprinted with permission from Ref. [100]*; Copyright 2017, Springer Nature.*

The doping of transition metal sulfides is a technique already employed with success in industrial hydrotreating catalysts [101]. Most used dopants for these sulfides are nickel and cobalt. Once both hydrotreating and HER catalysts need an optimum hydrogen adsorption, this methodology is also widely tested for HER catalysts.

Bonde et al. [70] synthesized several MoS_2 and WS_2 materials exhibiting the same structure - Co-promoted and without promoter, besides CoS_x - all supported in Toray carbon paper. All catalysts were analyzed by CV in a 0.5 M H_2SO_4 solution purged with N_2 and presented an irreversible oxidation in higher anodic potentials, which drives to loss of activity in the subsequent cathodic sweeps. MoS_2/C presented the oxidation peak at 0.98 V vs NHE, approximately. While, in WS_2/C, it appeared at 1 V vs NHE, approximately. All materials presenting cobalt (CoS_x/C, Co-MoS_2/C and Co-WS_2/C) showed oxidation peaks at, approximately, 1.1 V vs NHE. Polarization curves were performed from 0.1 to -0.4 V vs NHE at 5 mV s^{-1}. On CoS_x/C material was noticed that HER activity decreased in successive sweeps due to instability of material in sulfuric acid, which may drive to dissolution or cathodic desorption of CoS_x. Same behavior was seen to cobalt-promoted materials, however, their current density stabilized in higher values than no promoted materials, which indicates that although there was the presence of CoS_x species on them, there was also Co specie acting as promoter.

Finally, authors also investigated how Co promoter acts by calculating ΔG_H^0 for the sites of both molybdenum- and tungsten-based catalysts. In the absence of Co, HER at MoS_2 is favored in Mo-edge (ΔG_H^0 = 0.08 eV) instead of S-edge (ΔG_H^0 = 0.18 eV). On the other hand, for WS_2 material both edge-sites are equally favored (ΔG_H^0 = 0.22 eV). According to the authors, the incorporation of cobalt occurs only in the S-edges, and free energy of hydrogen

adsorption for these sites in MoS_2 and WS_2 becomes 0.10 eV and 0.07 eV, respectively. Therefore, while in MoS_2 the cobalt promoter acts increasing the number of active sites, in WS_2 it creates sites with higher activity than sites found on pristine material. It is important to highlight that, for the DFT calculations performed by Bonde *et al.* [70], hydrogen adsorption occurs always in S-sites, even in the metallic-terminated edges, therefore, W- or Mo-edges are, in fact, sulfided W- or Mo-edges, differently of the Mo-edge model used in the calculations of Xu et al. [92]. Doped tungsten sulfides were also studied elsewhere [102].

Mukherji and coworkers [103] published an extensive study on the HER activity of $Co_{1-y}Mo_yS_x$-based materials. Initially, several $Co_{0.5}Mo_{0.5}S_x$ materials were synthesized by four different methodologies and varying some parameters. In the first methodology, a SBA-15 template was submitted to an incipient wetness impregnation with a solution containing Co and Mo precursors and calcined. This calcined material was solvothermally sulfided with thioacetamide (TAA) at 160 ºC for 24 h and the resultant material was treated in alkaline medium to remove the SBA-15 template. The catalyst obtained was then labeled as "$Co_{0.50}Mo_{0.50}S_x$-SBA". In the second methodology, an ammonium thiomolybdate (ATM) aqueous solution was dropwised to another aqueous solution containing $Co(NO_3)_2 \bullet 6\ H_2O$ and polyvinylpyrrolidone (PVP) and then hydrothermally heated at 200 ºC. Hydrothermal step was tested at 6, 24 and 48 h and, consequently, catalyst synthesized were named as "$Co_{0.50}Mo_{0.50}S_x$-ATM-6", "$Co_{0.50}Mo_{0.50}S_x$-ATM-24" and "$Co_{0.50}Mo_{0.50}S_x$-ATM-48", respectively. The third methodology started with the addition of a sulfidation agent, thiourea (TU) or L-cysteine (Cys), to an aqueous solution of Mo and Co precursors. After guarantee a good dispersion of species, the resultant solution was hydrothermally heated at 200 ºC for 24 or 48 h. Catalyst samples were named according to sulfur source used and heating time, therefore, they were called "$Co_{0.50}Mo_{0.50}S_x$-TU-24", "$Co_{0.50}Mo_{0.50}S_x$-TU-48", "$Co_{0.50}Mo_{0.50}S_x$-Cys-24" and "$Co_{0.50}Mo_{0.50}S_x$-Cys-48". The fourth method was similar to the third one. Cobalt and molybdenum precursors were added to water with pH adjusted to 6 by HCl addition. An ethanolic solution containing 2-amino-thiophenol was dropwised to the previously mentioned solution. Resultant solution was then solvothermally heated at 200 ºC for 24 ºC and this synthesized catalyst was labeled as "$Co_{0.50}Mo_{0.50}S_x$-ATM".

All catalysts were deposited in a glassy carbon rotating disk electrode (0.2 mg cm^{-2}) and tested for HER in 1 M NaOH solution at 10 mV s^{-1} and 1 000 rpm. It was verified a correlation between activity and crystallinity. Materials containing amorphous character (synthesized

by first, second and fourth methods described earlier) performed worse, albeit $Co_{0.50}Mo_{0.50}S_x$-ATM-6's activity surpassed $Co_{0.50}Mo_{0.50}S_x$-TU-48's one at high overpotentials (higher than 600 mV). It is also important to highlight that carbon may be formed in the surface of $Co_{0.50}Mo_{0.50}S_x$-ATM-series of catalysts by PVP hydrothermal treatment [104], which may result in a negative impact on HER performance. The $Co_{0.50}Mo_{0.50}S_x$-Cys-48, exactly the catalyst which presented higher intensity of MoS_2 diffraction lines in XRD analyses, showed the highest activity towards HER among these catalysts, followed by $Co_{0.50}Mo_{0.50}S_x$-TU-24. As one may see, different heating times resulted in best catalysts in each class of material, 6, 24 and 48 h for ATM, TU and Cys, respectively. Authors attributed these differences for each sulfur source to their degradation kinetics.

Once $Co_{0.50}Mo_{0.50}S_x$-Cys-48 was found as the most active catalyst, its synthetic method was used to produce a new series of materials only varying the Co:Mo molar ratio. $Co_{1-y}Mo_yS_x$ materials (y = 0, 0.25, 0.40, 0.50, 0.60, 0.75 or 1) were obtained and evaluated in HER reaction at the same aforementioned conditions. Between monometallic compounds, CoS_2 showed a better activity (η_{10} = 444 mV) than MoS_2 catalyst (η_{10} = 558 mV). All bimetallic compounds showed a cathodic peak prior hydrogen evolution, which authors associated to the water dissociation in Volmer step. The $Co_{0.40}Mo_{0.60}S_x$ catalyst showed the best activity with η_{10} = 188 mV and calculated Tafel slope about 87 mV dec^{-1}. Interestingly, although CoS_2 was more active than MoS_2, which uses to be the contrary on acidic environments, a material containing higher quantities of Mo atoms than Co ones was the most active in the bimetallic series. It is possible that Co species play a key role on H_2O dissociation during Volmer step, a mandatory event on alkaline medium, but irrelevant in acidic one. However, the confirmation of this assumption requires further characterizations.

The stability of $Co_{0.40}Mo_{0.60}S_x$ was tested on a chronoamperometry (CA) analysis performed for 10 h at – 0.34 V vs RHE (~80 mA cm^{-2}), which showed a very small loss of current density. Additionally, EIS analysis at the same potential was done and showed a lower charge transfer resistance for $Co_{0.40}Mo_{0.60}S_x$ when compared to CoS_2 and MoS_2. XRD, TEM and XPS analyses evidenced the coexistence of 2H- and 1T-MoS2 phases on $Co_{0.40}Mo_{0.60}S_x$. Additionally, the existence of both Co-S and Co-O linkages was confirmed by XPS. This oxidation detected is likely due to the use of water as solvent for the sulfidation step.

A third series of materials was studied by replacing Co species on $Co_{0.40}Mo_{0.60}S_x$ by Fe or Ni species, then originating $Fe_{0.05}Co_{0.35}Mo_{0.60}S_x$, $Fe_{0.10}Co_{0.30}Mo_{0.60}S_x$, $Ni_{0.05}Co_{0.35}Mo_{0.60}S_x$ and

$Fe_{0.10}Co_{0.30}Mo_{0.60}S_x$ materials. All these replacements resulted in loss of activity compared to the bimetallic sulfide and Ni doping resulted in a still more negative effect than Fe one.

Hu's group presented a study on the doping effect of M species (M = Co, Fe, Ni, Mn, Cu or Zn) on amorphous MoS_3 film aiming the HER at pH = 0 and 7 [89]. Synthesis methodology adopted was the same as already reported in Ref. [88], the only difference consisted in the addition of MCl_2 aqueous solution containing 0.1 M $HClO_4$ to the deposit bath. A $(NH_4)_2MoS_4/MCl_2$ molar ratio equal 3 was applied during synthesis for all doping metals.

When tested towards HER in a 1 M H_2SO_4 solution at 1 mV s^{-1}, Co and Fe showed to enhance MoS_3 activity. Fe^{2+} was the best promoting since Fe-MoS_3 achieved 24.9 mA cm^{-2} at 200 mV overpotential, approximately two-fold the current density of MoS_3. Tafel analysis showed very similar Tafel slopes in the range of 39-43 mV dec^{-1} for all materials. On the other hand, addition of Co^{2+}, Fe^{2+} and Ni^{2+} increased considerably the exchange current density of the MoS_3 film; approximately, 320, 130 and 70 % after Co, Ni and Fe addition, respectively.

When 1 M H_2SO_4 electrolyte solution was replaced by a standard phosphate buffer (pH = 7), the doping effect became even more evident. Ni, Co, and Fe enhanced the MoS_3 film activity towards HER in this condition. Co^{2+} ion showed to be the best dopant, which exhibited a current of 1.05 mA cm^{-2} at 200 mV of overpotential, five-fold higher than MoS_3 film alone. Tafel slopes were calculated in the range of 86-96 mV dec^{-1} and, once more, an increase in exchange current density after Co, Ni and Fe addition was verified. But at this case, approximately, 1140, 1020 and 440 % of rising was detected, respectively.

SEM analyses indicated that the incorporation of the three aforementioned species increased the thickness and porosity of the MoS_3 film. Unpromoted, Mn-, Zn- and Cu-promoted MoS_3 films had thickness in the range 100-150 nm, even when more than 25 CV cycles were applied. In contrast, Co-, Fe- and Ni-MoS_3 contained a thickness equal 400-500, 200-300 and 150-190 nm, respectively. Elemental analysis provided by XPS showed that less than 5 % of doping metal was detected for Mn-, Zn- and Cu-MoS_3, whereas coherent values were found to other promoted materials. ICP-OES analysis reinforced that those metals were not well incorporated in the films and, for this reason, did not present relevant promoting effects. Using calculations based on C_{dl} of the films, it was shown that the ECSA of Co-, Fe- and Ni-MoS_3 increased together with their thickness, as expected.

The use of Ni as doping for MoS_2 materials was also studied by Miao et al. [105]. The authors synthesized Ni-Mo-S/C, besides MoS_2 and NiS_x, HER catalysts using carbon fiber cloth

(single fiber diameter about 10 μm) as substrate and applying the hydrothermal method at 200 °C for 24 h. L-Cysteine, Na_2MoO_4 and $NiSO_4$ were used as S, Mo, and Ni sources, respectively. For the bimetallic compounds the Ni:Mo molar ratios employed in the synthesis were 3:1, 1:1 and 1:3. SEM analyses showed that this molar ratio play a key role in the morphology of the materials. The Ni^{2+} ions inhibit MoS_2 crystal growth along the basal plane, which avoids nanosheets stacking. But the insertion of huge quantity of Ni^{2+} in the system results in bad growth of MoS_2 onto the carbon fibers. Therefore, according to SEM, the 1:1 molar ratio is the optimum one since a uniform film consisting of 8-10 nm thickness nanosheets was obtained. Additionally, EDS analyses showed that the films synthesized from 3:1, 1:1 and 1:3 Ni:Mo molar ratio present, in fact, 1:4.5, 1:8.3 and 1:11.3, therefore, they are always rich in Mo and may be considered Ni-incorporated MoS_x. According to TEM analyses, the introduction of Ni (1:1 molar ratio) resulted in a flower-like morphology, although a decreasing of crystallinity was verified when compared to MoS_2. Besides that, such insertion resulted in the increase of interlayer distance from 0.63 to 0.92 nm. Besides to aid in the identification of 2H-MoS_2, XRD analysis also confirmed the enlargement of the interlayer distance, ~0.94 nm according to this technique. Authors attributed it to the weakening in layers interaction with Ni addition. Raman spectra suggested that 1:1 Ni-Mo-S/C contained low layers stacking and the presence of defects. Molybdenum in +6 oxidation state was identified by XPS, which suggests that the reduction was not complete in hydrothermal reaction.

The catalytic materials were tested for HER in neutral solution (phosphate buffer). All bimetallic materials presented onset overpotentials in the range 130-150 mV, lower than for MoS_2/C (approximately, 200 mV). The Ni-Mo-S (1:1) showed the best activity with η_{10} = 200 mV, Tafel slope about 85 mV dec^{-1} and j_0 = 4.89 x 10^{-2} mA cm^{-2}. Additionally, MoS_2/C presented an ECSA higher than three-fold of 1:1 Ni-Mo-S/C, it suggests that the last one possesses more edge sites, probably coming from defects created, than former one. Finally, 1:1 Ni-Mo-S/C presented a faradaic efficiency of 98.2 % when HER was performed at -0.2 V vs RHE.

Non-metal doping is a strategy that has also been implemented with success to enhance electrocatalytic activity of MoS_2 materials. Liu et al. [106] synthesized phosphorus-doped molybdenum disulfide (P-MoS_2) nanosheets by a simple one-pot reaction method. A mixture containing sodium molybdate dihydrate (Na_2MoO_4 • 2 H_2O), thioacetamide

(CH_3CSNH_2) and ammonium dihydrogen phosphate ($NH_4H_2PO_4$) in water was stirred for 1 h, and then heated at 200 °C for 24 h. Different quantities of $NH_4H_2PO_4$ were added in the synthesis, resulting in materials containing different atomic percentages of phosphorus (0, 1.7, 3.4 and 5.0 %). A trend was verified, the higher was the quantity of phosphorus, the more active in HER was the catalyst. SEM analysis showed a nanoflower-like morphology for all materials, although the P-doping resulted in an enlarged interlayer spacing in (002) plane of 2H-MoS_2 phase; while 9.1 Å was measured for the most doped MoS_2 (5P-MoS_2), a distance of 6.5 Å was verified for pure MoS_2, according to TEM and XRD results. In the S 2p spectrum obtained by XPS was verified that a peak related to 1T-MoS_2 phase appears and becomes more intense with increasing the quantity of P.

The materials were tested for HER in Ar-saturated 0.5 M H_2SO_4 at 2 mV s^{-2} after the working electrode being fabricated by drop-casting a mixture containing equal mass ratio of active material and Carbon Vulcan XC72 in a GCE. The 5P-MoS_2 electrocatalyst showed the best performance with η_{onset} = 15 mV, η_{10} = 43 mV, j_0 = 0.49 mA cm^{-2} and Tafel slope about 34 mV dec^{-1}. The material also showed a good catalytic stability after being submitted to 5 000 CV cycles at 100 mV s^{-1} or 20 h of electrolysis at 100 mV of overpotential (~96 mA cm^{-2}). Further electrochemical characterizations elucidate that P-doping diminishes R_{ct} of the material and increase C_{dl}, resulting, therefore, in higher active ECSA. These features have a positive impact on HER performance.

In order to better elucidate the effects of P addition on MoS_2, DFT were performed by the authors [106]. As result of that, it was possible to verify that the P-doping introduce electronic states around the Fermi level, which did not exist in pure MoS_2, besides to promote strong hybridization of P and S p orbitals and d orbital of Mo, enhancing then charge transfer in basal plane. Hydrogen adsorption energy was also calculated for different sites and showed that for P-neighbor basal plane S sites, ΔG_H^0 is equal 0.43 eV, instead of 2.2 eV for non-doped S sites in basal plane. In addition, the P sites show a ΔG_H^0 equal 0.04 eV. The expansion of (002) plane interlayer distance also reflects a positive effect on hydrogen adsorption in MoS_2 because the ΔG_H^0 about – 0.36 eV calculated for a material containing an interlayer distance of 6.5 Å, becomes – 0.11 eV when the distance is expanded to 9.1 Å. Therefore, the P dopant provide a better tuning on MoS_2 electronic state, create new active sites, and enhance the hydrogen adsorption on already existing active sites.

Iron, nickel and cobalt were first presented as possible transition metals in the formation of catalytic active sulfides for HER by Cui's group [107]. FeS_2, CoS_2, NiS_2, $Ni_{0.68}Co_{0.32}S_2$ and $Fe_{0.43}Co_{0.57}S_2$ were synthesized, deposited onto a GCE, and evaluated towards HER in a N_2 deaerated 0.5 M H_2SO_4 solution at 2 mV s^{-1}. All of them showed to be active and achieved 4 mA cm^{-2} by applying 190-270 mV of overpotential, besides to present a Tafel slope in the range 40-70 mV dec^{-1}. They also had their stability tested by measuring their activities before and after the application of 1 000 CV cycles at 50 mV s^{-1}. Ni-based sulfides presented loss of cathodic current, whereas the others presented good stability. The $Fe_{0.43}Co_{0.57}S_2$ was the most active material achieving 10 mA cm^{-2} at less than 200 mV of overpotential and presenting a Tafel slope of ~56 mV dec^{-1}. CoS_2 was the second most active by presenting the same current density at, approximately, 250 mV overpotential, besides a Tafel slope of about 45 mV dec^{-1}.

Li et al [108] studied the activity of pyrite FeS_2 on the HER in N_2-saturated 1 M KOH solution. Material was synthesized by hydrothermal reaction at 240 ^oC for 12 h, using iron (III) chloride hexahydrate ($FeCl_3 \bullet 6\ H_2O$) and sodium diethyldithiocarbamate trihydrate ($C_5H_{10}NS_2Na \bullet 3\ H_2O$) as iron and sulfur source, respectively. Sodium diethyldithiocarbamate is decomposed and release H_2S, responsible to reduce Fe^{3+} species to originate FeS_2 compound. The synthesis of pyrite FeS_2 material was confirmed by XRD and XPS measurements. The last technique also detected binding energies related to SO_4^{2-} and Fe(III)-S species, which were attributed to the occurrence of oxidation of surface material when exposed to air. A heterogeneity of particle size (50-750 nm) was verified by TEM.

For catalytic evaluation of material, a catalytic ink was produced by mixing FeS_2, commercial carbon powder and a water/ethanol mixture containing low amount of Nafion®; this ink was deposited in Ni foam (NF) by drop-casting method. LSV curves were performed at 5 mV s^{-1} and FeS_2-C/NF exhibited η_{10} = 202 mV, Tafel slope of, approximately, 98 mV dec^{-1} and negligible loss of current after being cycled 1,000 times. A FeS_2/NF electrode, obtained from catalytic ink produced without carbon powder, was also evaluated and needed an overpotential 30 mV higher to achieve the same 10 mA cm^{-2}. It shows the importance of carbon addition on catalyst performance, however, if carbon was added in the hydrothermal synthesis step, it could act as nucleation substrate and inhibit the agglomeration of FeS_2 particles. A more homogeneous particle size distribution would be

expected, much lower than 750 nm, and, consequently, enhanced catalytic activity since more active sites would be exposed.

Hybridization has also been showed to be an interesting alternative to enhance the catalytic activity of CoS_x-based electrocatalysts. A material containing core-shell nanoparticles, Co core and CoS_2 shell, located inside sulfur- and nitrogen-doped carbon nanotubes, named as "S,N-CNTs/CoS_2@Co" by authors, was synthesized and showed excellent activity towards HER in alkaline medium [109]. Initially, $Co(NO_3)_2 \bullet 6\ H_2O$, melamine and glucose were grinded together to ensure a better contact between them and submitted to a calcination step at 800 ^oC for 2 h under N_2 atmosphere; it originated N-CNTs/Co material and cobalt was the responsible to catalyze the growth of carbon nanotubes. The as-synthesized material was then added to a boat which was placed inside an oven containing another boat filled with thiourea and the second thermal treatment at 500 ^oC for 3 h under N_2 atmosphere was performed; it resulted in the desired S,N-CNTs/CoS_2@Co material. Figure I.8a presents a representative illustration of the synthetic methodology adopted. Using SEM, TEM, XRD and XPS techniques, it was possible to confirm that carbon nanotubes encapsulated core-shell nanoparticles containing the metallic Co in the nucleus and outer layers of CoS_2. Furthermore, EDX suggested the incorporation of sulfur and nitrogen in the carbon nanotube framework which was confirmed by XPS spectra of material. Nitrogen physisorption was performed and material showed a BET specific surface area equal 149 $m^2\ g^{-1}$.

The HER activity of S,N-CNTs/CoS_2@Co catalyst was evaluated performing LSV analysis in 1 M KOH at 10 mV s^{-1}. The material was deposited in a GCE containing 0.2 mg cm^{-2}. The electrocatalyst showed η_{onset} = 81 mV, η_{10} = 112 mV and Tafel slope about 105 mV dec^{-1}. Additionally, as one may see in Figure I.8b, it was showed that to achieve very high current densities, about more than 175 mA cm^{-2}, lower overpotential is required for S,N-CNTs/CoS_2@Co when compared to Pt/C electrode, the HER benchmark electrocatalyst. To verify the catalyst stability, HER activity was evaluated before and after 1 000 CV cycles. It was noticed that to achieve 50 mA cm^{-2}, it was necessary an increase of 20 mV of overpotential after the CV cycles, whereas increase of 25 mV was necessary for Pt/C; it demonstrates that S,N-CNTs/CoS_2@Co is also more stable than Pt/C. Authors attributed the excellent performance of this catalyst to several factors. According to them, the existence of Co^{2+} species promotes the water dissociation by its combination with OH^-. Doping of

CNT's with S and N summed up to the creation of metal/semiconductor interface enhanced material's conductivity. Finally, the CNT-encapsulating effect collaborated to the catalyst stability.

Another hybrid CoS_x-based electrocatalyst was evaluated by Wu *et al.*[110], a NF-supported Ni_3S_2 nanosheets containing $Ni_xCo_{3-x}S_4$ nanoparticles ($Ni_xCo_{3-x}S_4/Ni_3S_2$/NF). Its synthesis proceeded by two simple steps; firstly, NF was added to an aqueous solution containing thiourea and heated at 150 °C for 5 h, producing then the Ni_3S_2/NF electrocatalyst. At the second step, this as-synthesized electrocatalyst was immersed into a solution of cobaltous acetate in ethylene glycol and heated at 200 °C for 12 h, resulting in the $Ni_xCo_{3-x}S_4/Ni_3S_2$/NF material. Further cationic exchange could be performed by increasing the heating time and, for comparison purposes, an additional $Ni_xCo_{3-x}S_4$/NF material was synthesized by letting the second step occur for 72 h; the two possibilities of cationic exchange extent according to the time of reaction are illustrated in Figure I.8c.

According to SEM and TEM characterization techniques, all materials showed a three-dimensional macroporous foam-like framework, due to the presence of NF, in which the surface was covered by vertically-aligned nanosheets. Specifically for $Ni_xCo_{3-x}S_4/Ni_3S_2$/NF material, it was verified the presence of $Ni_xCo_{3-x}S_4$ nanoparticles, with size varying between 3 and 5 nm, onto surface of Ni_3S_2 nanosheets with an average thickness of 20 nm. XRD analysis showed the presence of metallic nickel and Ni_3S_2 in the $Ni_xCo_{3-x}S_4/Ni_3S_2$/NF material, $Ni_xCo_{3-x}S_4$ was probably not identified because of its very small nanoparticles size. However, its presence, besides the other aforementioned species, was confirmed by selected-area diffraction pattern (SAED). Additionally, Raman spectrum of $Ni_xCo_{3-x}S_4/Ni_3S_2$/NF showed weak bands associated to $Ni_xCo_{3-x}S_4$ and Ni_3S_2. Finally, it was verified that $Ni_xCo_{3-x}S_4$/NF resembles the composition of $Ni_{0.05}Co_{2.95}S_4$/NF, therefore, it is a nickel-doped Co_3S_4-based material.

The activity of materials towards HER was tested in 1 M KOH at 0.1 mV s^{-1} and can be seen in Figure I.8d. The $Ni_xCo_{3-x}S_4/Ni_3S_2$/NF showed the best activity, if all of them are compared at 500 mV of overpotential, $Ni_xCo_{3-x}S_4/Ni_3S_2$/NF's activity is about 6 and 2.5 times better than Ni_3S_2/NF and $Ni_xCo_{3-x}S_4$/NF, respectively. A Tafel slope of, approximately, 107 mV dec^{-1} and η_{10} = 136 mV were verified for $Ni_xCo_{3-x}S_4/Ni_3S_2$/NF electrocatalyst. Additionally, this catalyst presented the smallest R_{ct} (26.1 Ω), according to EIS, and highest ECSA (350 cm^2), approximately, double of the other materials. A good

stability was also noticed, even at high current densities (as 900 mA cm^{-2}) and applying an overpotential of 136 mV (resulting in ~10 mA cm^{-2}) for 50 h. Yet, DFT calculation were performed and elucidated important features. According to calculations, Co_3S_4 presents a ΔG_H^0 closer to 0 than Ni_3S_2. Furthermore, an even more thermoneutral hydrogen adsorption was verified on Ni-doped Co_3S_4 and Co_3S_4/Ni_3S_2 interface sites, the former one presents the best value; it justifies the enhanced activity of $Ni_xCo_{3-x}S_4/Ni_3S_2$/NF electrocatalyst.

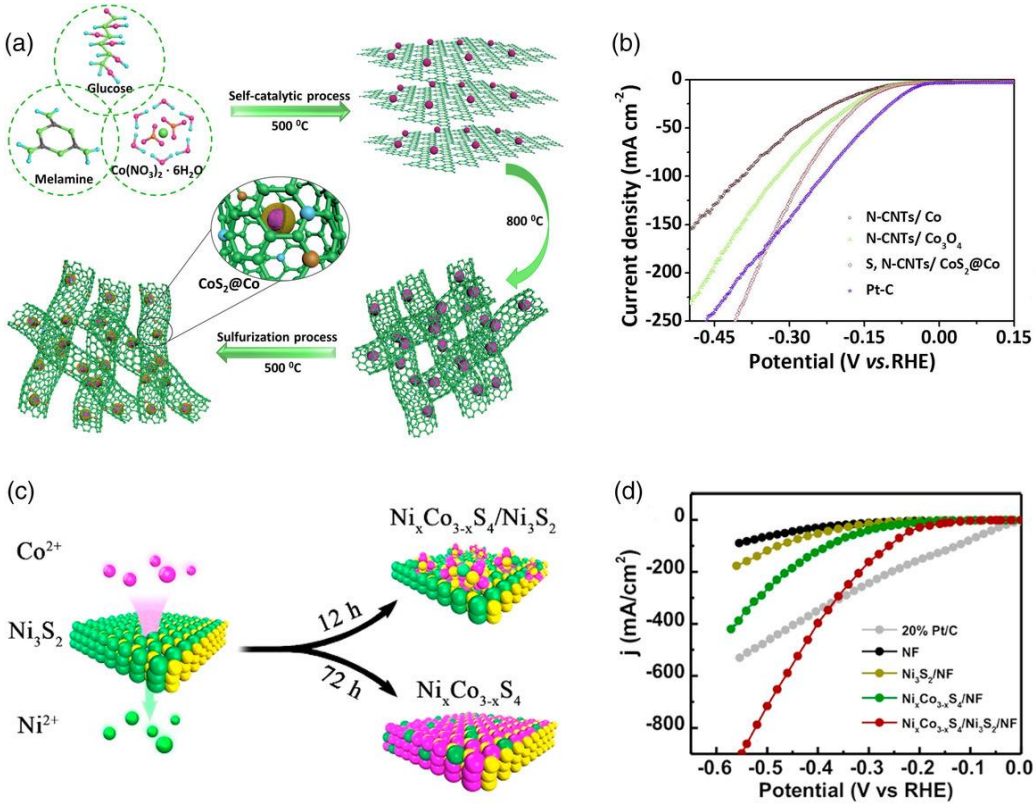

Figure I.8. (a) Growth schematic of core-shell structure S,N-CNTs/CoS_2@Co. (b) LSV curves for HER extracted from [109]. (c) Schematic illustration of the synthesis of $Ni_xCo_{3-x}S_4/Ni_3S_2$/NF and $Ni_xCo_{3-x}S_4$/NF by cation exchange reaction between Ni_3S_2/NF and Co(II) ions. (d) Steady-state current density as a function of applied potential during HER in 1 M KOH solution over NF, Ni_3S_2/NF, $Ni_xCo_{3-x}S_4$/NF, $Ni_xCo_{3-x}S_4$/ Ni_3S_2/NF and Pt/C (20 wt. %). (a-b) Reprinted and adapted with permission from Ref. [109]; Copyright 2018, Elsevier. (c-d) Reprinted and adapted with permission from Ref. [110]; Copyright 2017, Elsevier.

As aforementioned for MoS_2 material, P-doping showed to be also an interesting methodology to enhance CoS_2 performance, in this case due to stability improvement. Hybrid material consisting of cobalt phosphosulfide nanoparticles grown on carbon

nanotubes (CoS|P/CNT) was reported by Liu et al. [111] as a very active and stable catalyst for HER in acidic environment; the synthesis is divided into three steps. In first one, Co_3O_4 nanoparticles are growth onto mildly oxidized multi-walled carbon nanotubes, previously submitted to a modified Hummers method, by hydrolysis of cobalt acetate at 80 °C. An ethanol/water solvent mixture and aqueous ammonia were used to reduce hydrolysis rate and, consequently, control the size of cobalt oxide particles. According to SEM, TEM and XRD, Co_3O_4 nanoparticles with 5-10 nm of size were obtained. In the second step, Co_3O_4/CNT was converted to CoS_2/CNT by hydrothermal reaction with thioacetamide at 200 °C for 6 h. SEM, TEM and XRD evidenced a pyrite-structured CoS_2 nanoparticles with sizes between 10 and 20 nm. In third step, S atoms were replaced by P atoms during reaction of CoS_2 with PH_3 produced from thermal decomposition of $NaH_2PO_2 \bullet H_2O$ at 400 °C for 1 h. SEM, TEM, XRD and Raman suggested that P atoms only replaced S ones and no considerable change in CoS_2 structure or production of cobalt phosphide was verified. TEM and XPS also revealed a S:P atomic ratio about 1.0.

CoS|P/CNT presented high performance towards HER in 0.5 M H_2SO_4 at 5 mV s^{-1}, since it presented negligible onset overpotential, η_{10} = 48 mV, Tafel slope about 55 mV dec^{-1} and j_0 = 1.14 mA cm^{-2}. Noteworthy, CoS_2/CNT electrocatalyst was as active as CoS|P/CNT, although CoS_2/CNT presents low stability in the acidic electrolyte and in contact with air. Therefore, the P acts enhancing material stability, inhibiting the formation of sulfate groups. Finally, CoS|P/CNT showed to be stable in chronoamperometric analysis (~ 45 mA cm^{-2}) for 24 h and also after 2 000 CV's. The HER performance of CoS_2, FeS_2 and NiS_2 was also reported elsewhere[107, 112].

I.3. New trends and challenges

I.3.1. From hydrogen to system: Storage challenges

Owing to its extremely high energy density of 123 kJ g^{-1} (highest of all fuels) it is suggested that H_2 can effectively replace gasoline for NO_x- and CO_2-free clean energy generation. However, no matter H_2 is obtained from native biomass electrolysis[113] or water splitting[114-115], the use of hydrogen as a fuel for transportation and stationary applications is receiving much attention as a technical and policy issues. If the safety of hydrogen relies on its high volatility and non-toxicity, a compact, light, safe and affordable containment is mandatory

for non-board energy storage such as vehicles. A simple calculation indicates that, at room temperature and atmospheric pressure, a huge balloon of 2 m diameter is needed to store 2 kg of hydrogen (which occupies a volume of ca. 22 m^3), which is hardly a practical solution for transportation. Hence, we must therefore find little storage facilities with high security. Existing methods to store hydrogen can be divided in three main categories such as conventional hydrogen storage (using classical high-pressure tanks), hydrogen adsorption on solids of large surface area (depending on the applied pressure and the temperature) and hydrogen storage by metal hydrides (exploiting the reversible absorbing capability of metals and alloys) [116-117]. It should be noted that the hydrogenation and dehydrogenation of some aromatics such as toluene (CH_3-C_6H_6), which reversibly adsorbs 3 hydrogen molecules leading to methyl-cyclohexane (CH_3- C_6H_{12}) [118-119], also emerge as an alternative and is used in numerous chemical plants under steady-state conditions, but the on-board process under variable conditions is another matter and challenge. Recently, a decisive advance has been made in this field when Mitsushima and co-workers reported on the electrocatalytic hydrogenation of xylene in a PEM reactor for hydrogen storage [120]. Compared to hydrogen adsorption on solid materials (carbon-based materials: nanotubes, fibers, etc.), the hydrides option (metals, complexes, chemicals) is the most promising and is currently attracting much attention because of the flexibility in the choice of primary materials [116-117, 121-123]. Basically, the molecular hydrogen is dissociated at the surface before absorption into two H atoms. Then, the two H atoms recombine during the desorption process to give H_2. The thermodynamic aspects of hydride formation from gaseous hydrogen are described by pressure-composition isotherms and are a key parameter for understanding and optimizing the process [116, 123-127]. For transportable applications, the critical properties of the hydrogen storage materials should be evaluated by: (i) light weight, (ii) cost and availability, (iii) high volumetric and gravimetric density of hydrogen (>6.0 wt.%), (iv) fast kinetics, (v) ease of activation, (vi) low temperature of dissociation or decomposition (operate below 100 °C for H_2 delivery), (vii) appropriate thermodynamic properties (30-55 kJ mol^{-1} H_2), (viii) long-term cycling stability, and (ix) high degree of reversibility (about 1 000 cycles) [117].

I.3.2. Instruction for designing new generation of robust and low cost electrocatalysts

Water splitting by electrochemical or photochemical approach, could in principle, conveniently provide clean hydrogen fuel and avoid the greenhouse gases. However, existing catalytic materials are too inefficient in practice: either weak binding interactions between the reaction intermediates and the catalyst give rise to high overpotentials (requiring more energy to make the reaction), or slow electron transfer kinetics result in low exchange current densities (poor kinetics for drawing high current densities). Fundamental multidisciplinary investigations demonstrated that both metrics depend not only on the intrinsic electronic properties of the catalyst, but also on the solvent and the catalyst morphology. Thus, the success in water electrolysis for large-scale production of hydrogen fuel from renewable energy sources will require materials that are highly active, cost-effective, and durable with facile/affordable synthesis scaling up capability. Two main reactions (HER and OER) simultaneously occur during the electrochemical water splitting, so-called water electrolysis. The first instruction is to pursue the search of both activity and stability descriptors in aqueous medium. Then, particular attention should be paid to replacing expensive and rare noble metal electrocatalysts with inexpensive and earth-abundant ones. To this end, more options for robust catalysts that work at varying pHs should be promoted to provide more springiness in terms of cost. Furthermore, efforts should be allocated to the scalability of the synthesis processes for the large-scale production of catalysts. To mimic practical applications in industrial plants, the glassy carbon electrode that is an excellent support for testing catalyst should be gradually replaced by suitable convenient supports which are able to afford high current density of amps per square centimeter. Finally, the search for innovative materials with high hydrogen-storage capacity should have a primordial attention. It is worth noting that the standardization of testing conditions, i.e., establishing standardized testing to compare different materials obtained by different researchers, and to screen the optimal catalysts is very mandatory. Concretely, researchers should provide as much information as possible so that the results comparison with each other is easy, reliable, and really trustworthy. Should be provided: (i) electrode performance (Tafel slope, exchange current density, catalytic activities normalized by both mass and electrode area, overpotential at specific activity of 10 milliamps per square

centimeter, Faradaic efficiency, potentiostatic and galvanostatic stabilities, both pristine and iR-corrected polarization curves), and (ii) testing conditions (electrolyte, temperature, electrochemical methods, loading amount of catalyst, electrode surface: extremely small electrode area and metal loading should be avoided since they do not reflect the reality and practicability at all).

I.4. Conclusions and Outlooks

Up to now, most real systems to produce hydrogen do not employ the elegant electrochemical water splitting. The integration of electrochemical method is confronted to poor and conflicting understanding of fundamental processes that occur during the operation. That is why the twofold target exposed within this review was to provide tips for the analysis of the electrochemical hydrogen and oxygen evolution reactions by the assessment of the entire fundamental parameters and discuss the recent advances that have been made in these fields within the last ten years. The identified main reaction performance (activity and stability) descriptors from the so-called volcano relations ultimately reflect the Sabatier principle, which accounts for optimal surfaces as ones that exhibit moderate binding energies of reaction intermediates, hydrogen adsorption in the case of the hydrogen evolution reaction (mostly in acidic medium) and adsorbed hydroxyl in the case of the oxygen evolution reaction. Since noble and rare-earth metals are economically and strategically inaccessible, an ideal material for either the electrochemical hydrogen evolution reaction or oxygen evolution reaction electrocatalyst should meet several standards: (1) high efficiency similar to that of the state-of-the-art material; (2) good durability over a period of at least several cycles; (3) high chemical/catalytic stability over a wide pH (even at all pH values) and temperature ranges; (4) low cost to ensure inexpensive hydrogen production; and (5) scalability of the catalysts preparation methods to ensure a wide range of commercial uses. Based on theoretical predictions and experimental data, the designed and synthesized earth-abundant noble metal free materials based on nitrogen, phosphorus, molybdenum, sulfur, iron, nickel, manganese, carbon, etc. electrocatalysts for the sustainable and efficient water splitting half-cell reactions lead to the conclusion that these heteroatoms affect the valence orbital energy levels each other to induce a synergistically enhanced electrocatalytic performance. Efforts in this direction as well as the development of advanced materials for hydrogen storage should be pursued.

Chapter II: Experimental Part

This chapter presents the methodology for the synthesis of electrocatalysts studied herein, besides the fundamentals and protocols applied in their physicochemical and electrochemical characterizations.

II.1. Electrocatalysts preparation

Transition metal sulfide (TMS) catalysts were prepared according to the hydrothermal method reported by Li *et al.*[108] with modifications. Initially, an aqueous solution of the metallic precursor was prepared and let stirring. The cobalt, nickel and molybdenum precursors employed herein were cobalt chloride hexahydrate ($CoCl_2 \cdot 6\ H_2O$, Alfa Aesar, 99.9 % metals basis), nickel chloride hexahydrate ($NiCl_2 \cdot 6\ H_2O$, Sigma-Aldrich, 99.999 % trace metals basis) and ammonium heptamolybdate tetrahydrate ($(NH_4)_6Mo_7O_{24} \cdot 4\ H_2O$, Alfa Aesar, 99 %), respectively. Simultaneously, sodium diethyldithiocarbamate trihydrate ($C_5H_{10}NNaS_2 \cdot 3\ H_2O$, Alfa Aesar, 98 %) was added to 20 mL of ultrapure water (Milli-Q, 18.2 MΩ cm at 20 ºC) and the solution was stirred until the complete dissolution of the sulfur precursor. In the sequence, the sulfur precursor solution was slowly dripped (about one droplet per second) into the metallic one, which was under vigorous stirring. During this dripping, solids started emerging in the metallic solution. For CoS_x and NiS_x syntheses, it was evidenced the appearance of green solids, while for MoS_x yellow solids were seen initially, but it started becoming orange as more droplets were added. The final mixture, containing ca. 60 mL, was then transferred to a 100 mL Teflon-lined stainless-steel autoclave which was posteriorly heated at 240 ºC during 24 h. It is noteworthy that the autoclave was always introduced in the oven already at 240 ºC. Afterwards, the autoclave was let cooling down naturally before opening until a temperature close to ambient one was achieved; this step used to take around 1.5 h. The material was collected after various centrifugation (six times applying 9000 rpm during 20 min) and washing steps. The first centrifugation step was done with the mixture resulting from hydrothermal reaction. The two subsequent steps and last three ones were performed after ultrapure water and absolute ethanol (VWR Chemicals) washing, respectively. Centrifugation was performed in the Hettich Universal 320 R centrifuge set up at 5 ºC with the use of 85 mL Thermo Scientific™ Nalgene™ Oak Ridge High-Speed Polycarbonate centrifuges tubes. To avoid catalyst loss during washing,

one centrifuge tube was filled with the catalyst and respective solvents of each washing step, while a second tube was filled only with the same solvent. This second tube was filled until have a similar solvent volume verified in the tube containing the catalyst and it served to equilibrate the mass on the centrifuge system. Hence, the second tube was positioned diametrically opposite to the first tube in the centrifuge equipment. Resultant solids from centrifugation were then dried at 50 ºC in vacuum (50-200 mbar) overnight. Finally, they were collected and stocked, inside a desiccator under vacuum, to be applied in the characterizations thereafter. Particularly, during the bimetallic sulfides syntheses, the metallic solution was prepared by the direct addition of cobalt/nickel chloride solution to ammonium heptamolybdate (AHM) solution, followed by vigorous stirring. Once the solution containing the sulfur precursor was dripped into the metallic solution containing both metals, green solids started appearing as well as in CoS_x and NiS_x syntheses. The precursor amounts and volumes applied in the synthesis of monometallic and equimolar bimetallic transition metal sulfides (i.e., $Co_{0.5}Mo_{0.5}S_x$ and $Ni_{0.5}Mo_{0.5}S_x$) are evidenced in **Table II.1**.

Table II.1. *Quantities of precursors and volumes applied in the synthesis of unsupported monometallic and equimolar bimetallic transition metal sulfides.*

Catalyst	CoS_x	NiS_x	MoS_x	$Co_{0.5}Mo_{0.5}S_x$	$Ni_{0.5}Mo_{0.5}S_x$
n_{CC} (mmol)	2.00	0	0	1.00	0
n_{NC} (mmol)	0	2.00	0	0	1.00
n_{AHM} (mmol)	0	0	0.28	0.14	0.14
n_{SDEDTC} (mmol)	2.00	2.00	2.00	2.00	2.00
V_{CC} (mL)	40	0	0	20	0
V_{NC} (mL)	0	40	0	0	20
V_{AHM} (mL)	0	0	40	20	20
V_{SDEDTC} (mL)	20	20	20	20	20

*n_X = quantity of compound "X", V_X = volume of solution "X", CC = cobalt chloride, NC = nickel chloride, AHM = ammonium heptamolybdate and SDEDTC = sodium diethyldithiocarbamate.

Furthermore, precursor amounts, and volumes used in the synthesis of cobalt molybdenum sulfides, $Co_yMo_{1-y}S_x$ (y = 0.15, 0.25, 0.40, 0.50 and 0.75), aiming the verification of the better Co:Mo ratio in Chapter III, are shown in Table II.2.

Table II.2. *Quantities of precursors and volumes applied in the synthesis of the unsupported bimetallic cobalt molybdenum metal sulfides.*

Catalyst	$Co_{0.15}Mo_{0.85}S_x$	$Co_{0.25}Mo_{0.75}S_x$	$Co_{0.4}Mo_{0.6}S_x$	$Co_{0.5}Mo_{0.5}S_x$	$Co_{0.75}Mo_{0.25}S_x$
n_{CC} (mmol)	0.30	0.50	0.80	1.00	1.50
n_{AHM} (mmol)	0.24	0.21	0.17	0.14	0.07
n_{SDEDTC} (mmol)	2.00	2.00	2.00	2.00	2.00
V_{CC} (mL)	6	10	16	20	30
V_{AHM} (mL)	34	30	24	20	10
V_{SDEDTC} (mL)	20	20	20	20	20

*n_X = quantity of compound "X", V_X = volume of solution "X", CC = cobalt chloride, AHM = ammonium heptamolybdate and SDEDTC = sodium diethyldithiocarbamate.

II.2. Physicochemical characterizations

II.2.1. Inductively Coupled Plasma Optical Emission Spectrometry (ICP-OES)

The inductively coupled plasma optical emission spectrometry (ICP-OES) is a technique applied in many catalysis laboratories, including IC2MP, with the goal of detecting and quantifying different elements. However, samples can only be directly injected in the equipment at liquid or gas states. Therefore, when the matrix analysis consists of solid sample, e.g., catalyst powders, a pretreatment is mandatory. Acid digestion is commonly applied to release the analytes (elements of interest in the analyses) to the final solution.[128] In addition, liquid samples need to pass through a device called "nebulizer", which is responsible to convert them into an aerosol; this one is further transported to the plasma. The production of plasma occurs because of the collision of argon atoms, flowing through a torch, with ions and electrons generated in argon gas by a spark produced from Tesla coil, which is radiofrequency (RF) powered. The plasma is kept with the continuous addition of energy provided by RF-induced collisions, achieving 10 000 K in its core. This plasma

sustaining methodology is known as "inductive coupling" and originates the terminology "ICP".[128]

The aerosol is instantaneously dried when it comes into contact in with the plasma, then the particles go into the gaseous state; decomposition can also take place. Finally, atoms are generated and subsequently excited and ionized. The relaxation of excited electrons to ground states release photons that contain characteristic energies. With the use of optical instruments, these photons are focused on the entrance aperture of a wavelength selection device.[128] As the number of photons is proportional to the quantity of analyte, a calibration curve of an element can be constructed by using a standard sample. Such curve must present a linear profile and can be used for quantification analyses.

ICP-OES analyses were performed with an Agilent 5110 VDV device. Catalyst powder was first submitted to a mineralization procedure, which consisted in the addition of 5 mL of HNO_3 solution (> 68 %) and 3 mL of HCl solution (34-37 %), and further heating in an Anton-Paar Multiwave PRO microwave reaction system. Ultrapure water was added to the resultant solution until a final volume of 50 mL was achieved. The final solution was sampled five times to be used in the analysis to obtain a good precision of the results.

II.2.2. X-ray Diffraction (XRD)

The X-ray diffraction (XRD) is a technique widely applied in material science to study materials containing crystalline phases. A crystal is derived from a periodic repetition of unit cells, which is the smallest cell containing all structural and chemical information necessary to describe it. Normally, if an X-ray beam achieves a sample, scattering in all directions takes place. However, in the presence of diffraction effect, the scattered waves are aligned into specific directions. For the occurrence of such diffraction some conditions are necessary. Firstly, the incident beam must have wavelength in the same order of magnitude of interatomic distances (i.e., order of Angstroms), and the second condition is the arising of constructive interference of waves. In brief, the electric field of X-ray wave interacts with electrons present in an atom, which will then emit a wave with the same wavelength of incident one. Hence, the intensity of diffraction peaks in the diffractograms has a strong relation with the atomic number (Z) of the atom associated to the diffraction phenomenon; light elements scatters less than heavy elements. Considering two parallel

planes, a constructive interference occurs when the difference of the sums of paths taken by incident and emitted waves that interacted with an atom present in the upper plane and bottom planes is equal an integer multiple of the wavelength; it describes the Bragg's law (Eq. II.1)[129-130].

$$n \times \lambda = 2 \times d \times \sin(\theta) \qquad \text{(Eq. II.1)}$$

In which:

- n corresponds to diffraction order;
- λ corresponds to X-ray wavelength;
- d is the interplanar distance;
- θ is the angle between the plane and incident X-ray wave, also known as Bragg angle.

The previous statement concerning the Bragg's law is illustrated in Figure II.1.

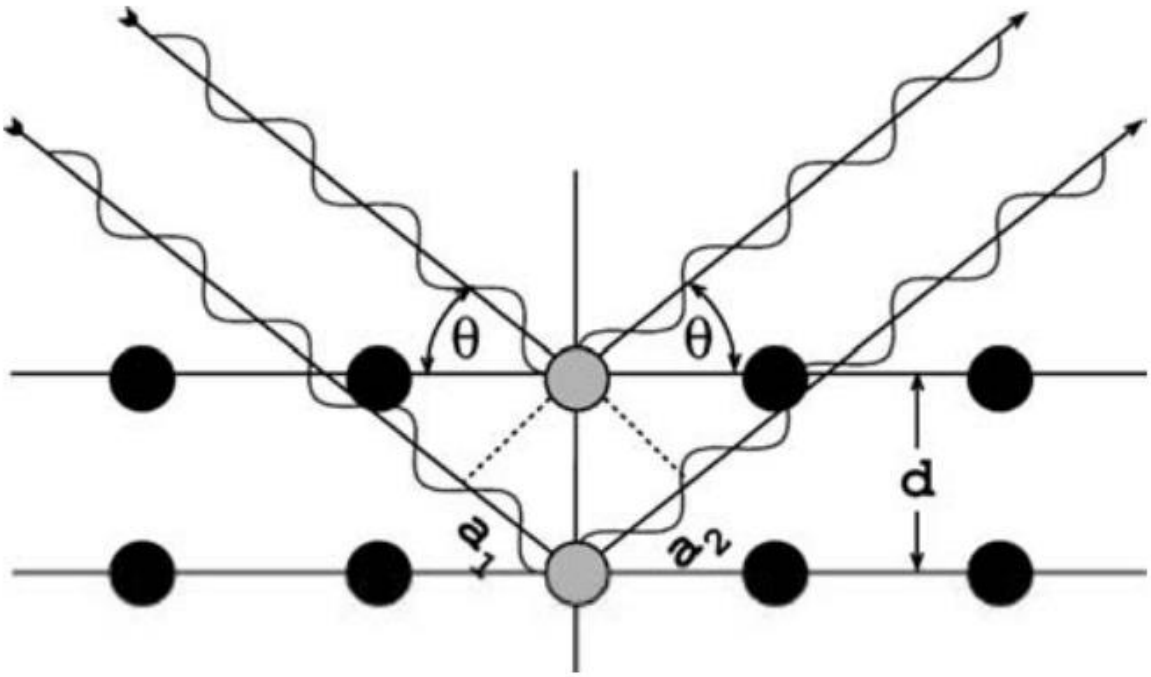

Figure II.1. Illustration of Bragg's law. Reprinted with permission from Ref.[130]; Copyright 2004, Springer Nature.

The variable "a_1" corresponds to the additional path of incident wave, while "a_2" corresponds to the additional path of emitted wave. Using simple geometry concepts, one may deduce that $a_1 = a_2 = d \times \sin(\theta)$.

Despite that, for small crystals in particular, a constructive interference, at some extent, can also occurs for small deviations of Bragg angle. The same doesn't take place for big crystals because at some position will be originated a wave with a phase delay of $\lambda/2$, which originates a destructive interference. On the other hand, the bigger is the crystal, more unit cells it contains and, consequently, the diffraction intensity will be higher for a given Bragg angle. Thus, samples containing high crystallinity exhibit sharp peaks in the diffractograms, while the peaks for low crystallinity samples are broadened[130]. Additionally, it is important to bear in mind that Figure II.1 shows a very simple representation of a crystal. In more complex structures, the phase delay between waves scattered from atoms at different positions can originate interferences. Hence, the diffraction peaks present different relative intensities which depends on crystal structure and are very useful for identification of phases.

The characteristics of X-ray source also plays a role in the analysis result. X-rays containing lower wavelength, also known as hard X-ray, are less susceptible to interference and absorption, therefore, results with the sources show high intensity of signal. However, their use leads to loss of Bragg angle resolution, mainly in lower interplanar distances, once 2θ axis is contracted in the diffractogram. For this reason, most laboratories use a Cu kα radiation ($\lambda = 1.542$ angstroms), since it shows a good compromise between loss of intensity and Bragg angle resolution. Nonetheless, its interaction with some atoms may originate a fluorescence effect, responsible to increase the baseline of diffractogram which difficult the analyses. Nowadays, there are devices that can be added to the diffractometer to reduce, or even eliminate, this effect.

X-ray diffraction (XRD) analyses were performed with the use of a diffractometer EMPYREAN from MALVERN PANalytical equipped with Cu K radiation source (45 kV and 40 mA) and the linear detector PIXcel1D which works with energy discrimination; it allows not only eliminate the fluorescence effect but also delete the K-beta contribution without the use of a nickel filter. The device was operated with divergence slit and primary anti-scatter slit sizes of $1/16^{o}$ and $1/8^{o}$, respectively, and the detector was used at its

maximum aperture (*i.e.*, 3.35º). Additionally, it was applied a step size of 0.078º and time per step of 600 seconds.

II.2.3. Vibrational Raman Spectroscopy

Raman spectroscopy is a technique of interest to study the structure of materials. It consists of the incidence of a monochromatic light with known characteristics (near infrared, visible or ultraviolet) that when interacting with a sample leads to changes in its vibrational energy levels, which originates inelastic scattered light. When hit by a photon, the sample in an initial vibrational energy level accesses an intermediate virtual state and then goes to the final vibrational energy level[131]; this is illustrated in Figure II.2.

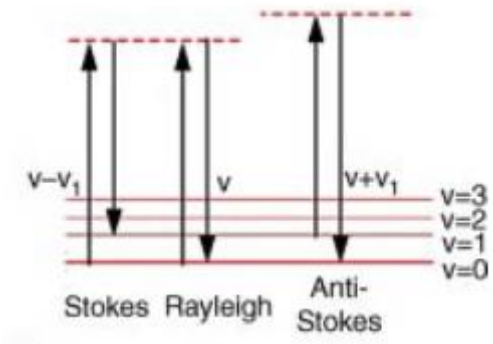

Figure II.2. Possibilities of energy transition in vibrational Raman spectroscopy. Reprinted with permission from Ref.[131]; Copyright 2012, John Wiley and Sons.

For elastic scattering, i.e., when initial and final energy of photon are the same, the phenomenon is called Rayleigh scattering. On the contrary, when an inelastic scattering takes place, the phenomenon is called Raman scattering and photon initial and final energy are different (Raman shift). Raman spectroscopy can also be classified as Stokes or anti-Stokes. The former one involves a light scattered with lower energy than the incident one, while the second one is related to the scattering of light with higher energy. Although Raman scattering is much rarer than Rayleigh one since only, approximately, 1 out of 10^8 photons are Raman scattered, Raman spectroscopy can give valuable information about vibrational modes of material[131].

Raman spectroscopy measurements of catalyst powders were carried out at room temperature using a HORIBA JOBIN YVON Labram HR800UV Raman confocal microscope, specifically an Olympus BXM confocal microscope which enabled the operation in backscattering mode, equipped with a CCD detector cooled by the Peltier effect. For all measurements, it was applied the excitation wavelength of 532 nm, supplied by a diode-pumped solid state (DPSS) green laser from Oxxius, and the laser power delivered to the samples was 0.2 mW, aided by an optical density filter. In addition, 600 grooves mm^{-1} grating and the confocal pinhole diameter of 200 μm were used, resulting in a spectral resolution of 1.5 cm^{-1}. Finally, the spectrometer was calibrated with a silicon standard and the LabSpec v.5 software was used for the acquisition and treatment of data.
Raman spectroscopy measurements of GDE materials, which results are present in Chapter IV, were obtained with the same parameters, in general. The exception was the application of 1 800 grooves mm^{-1} grating, resulting in a spectral resolution of 0.5 cm^{-1}. To perform the analysis, the MEA samples were directly placed under the microscope objective, which focused to a spot size corresponding to 2 μm^2 of the sample, and many spectra were registered at different points of cathode GDE surface.
Finally, the spectrometer was calibrated with a silicon standard and the LabSpec v.5 software was used for the acquisition and treatment of data.

II.2.4. X-ray Photoelectron Spectroscopy (XPS)

The X-ray photoelectron spectroscopy (XPS) is a technique based on the photoelectric effect. It consists in the emission of low-energy electrons, called photoelectrons, when an electromagnetic radiation hits a material. In the XPS analysis, the electromagnetic radiation comes from an X-ray source with known energy. It hits the material, which emits photoelectrons that have their kinetic energy further measured in the equipment. For solid materials, e.g., catalyst powders, the contact between the sample and the spectrometer leads their Fermi level to equalize and their vacuum levels to become different. Therefore, to guarantee the energy balance of the system, the work function of spectrometer needs to be considered. The correction with this function is unnecessary when the object of analysis is in gas phase[132]. Figure II.3 illustrated the energies involved in the XPS analysis.
The meanings of the variables are as follow:

- hυ is the incident photon energy;
- E_B is the binding energy of electron;
- E_{kin} is the kinetic energy of the photoelectron;
- $E\varphi_{spec}$ is the work function of spectrometer, which can be calibrated.

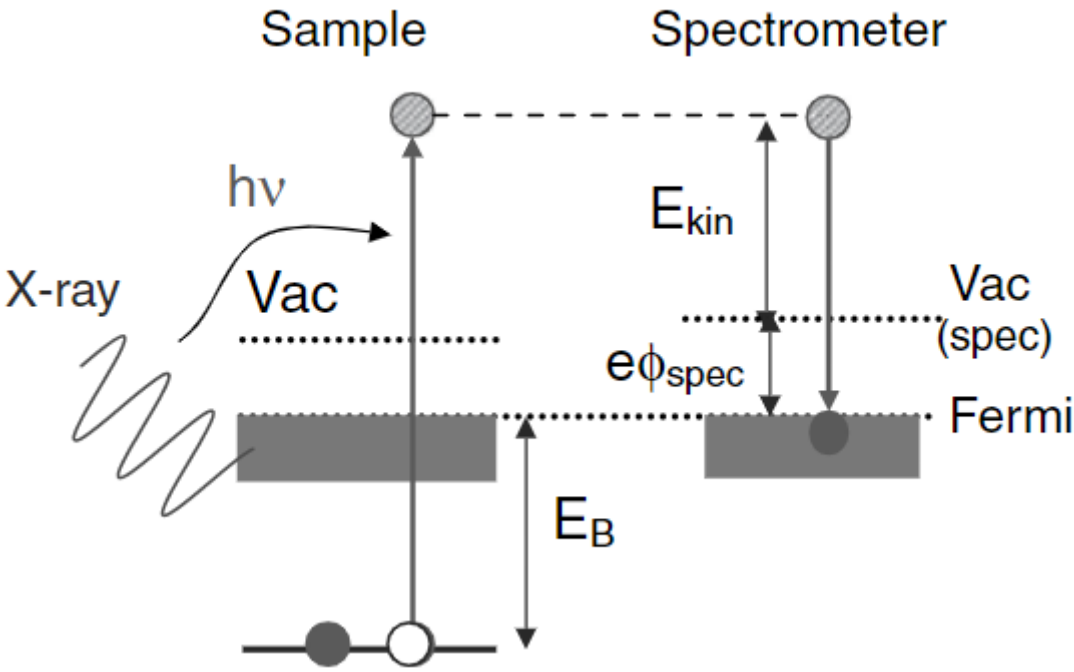

Figure II.3. Energies involved in the XPS analysis. Reprinted and adapted with permission from Ref.[132]; Copyright 2012, John Wiley and Sons.

Therefore, Eq. II.2 is obtained by applying an energy balance to the system.

$$E_B = h\upsilon - E_{kin} - e\varphi_{spec} \qquad \text{(Eq. II.2)}$$

Contrary to kinetic energy, the binding energy is an intrinsic property of the electron, and its value can give information concerning the emitting element, ionized level, and oxidation state; depending on the situation, data related to coordination of the element can also be extracted. Since the photoelectrons have a strong interaction with matter, only the electrons of atoms near to the surface can leave the sample without suffering inelastic collisions. Hence, XPS analysis must be performed in ultra-high vacuum (UHV) and is restricted to

probe the surface of materials[132]. This is not necessarily a drawback since the study of materials' surface is of paramount importance in many fields as catalysis. The aforementioned inelastic collisions also influence spectra backgrounds.

During analysis, material's surface can be positively charged, mainly for non-conductive samples, which results in the shift of kinetic energy. Since this is the measurable variable, miscalculation of binding energy is a consequence. Such problem may be identified using an internal standard and circumvented by the injection of low-energy electrons, aided by flood-gun device. The C 1s line coming from adventitious carbon is commonly applied as internal standard in many laboratories. Therefore, C 1s spectrum is generally acquired in the beginning and final of analyzes to verify their positions; if they don't match, the surface was charged during analysis.

Except for electrons from orbitals s, photoemission lines are doublets due to the coupling between angular momentum and spin[132]. The difference in binding energy and intensity of doublets are typical of the atom and orbital, respectively; it doesn't depend on chemical states. Such differences are very important for data treatment.

Although XPS has become the most common technique for surface analysis due to its very sensitive character, many details can influence result spectra. Therefore, thorough data treatment is necessary to avoid misinterpretations[133]. If the goal is to analyze complex samples, it is very recommended to perform the analysis also for simpler similar samples which can serve as standards and aid in result interpretation. Furthermore, it is recommended to have some previous knowledge of the sample before analysis. Hence, information obtained from other characterizations can be valuable. Nonetheless, one must ever remember that XPS result is restricted to surface, which may not be the case for another technique. Thus, a perfect match shouldn't be pursued blindly.

X-ray photoelectron spectroscopy (XPS) analyses were carried out with a Kratos Axis Ultra DLD spectrometer using a monochromatic Al Kα source (1486.6 eV) operating at 180 W (12 mA, 15 kV). The device was operated at 9×10^{-8} Pa and the charge neutralizer system was applied to all samples containing an isolating feature. High-resolution spectra were recorded using an analysis area of 300 µm x 700 µm, step size of 0.1 eV and 40 eV pass energy, which corresponds to Ag $3d_{5/2}$ full width at half maximum (FWHM) of 0.55 eV. The binding energy was calibrated using C 1s binding energy fixed at 284.8 eV as an internal

reference. Data were treated with Casa XPS software (version 2.3.24) applying Gaussian-Lorentzian profiles (Lorentzian 30%).

II.2.5. Electron Microscopy

Electrons are elementary particles that exhibit wave-particle duality and present strong interaction with matter, even higher than X-rays. Due to their lower wavelengths, in comparison to optical light, more details and higher resolutions of material's structure can be assessed by using electron microscopy instead of light microscopy. Additionally, the generation of electrons beam is an easy task, and their wavelengths can be tuned by only varying the beam acceleration voltage. Figure II.4 shows the electromagnetic spectrum comparing wavelengths of electrons used in SEM and TEM with other electromagnetic radiations[134-135].

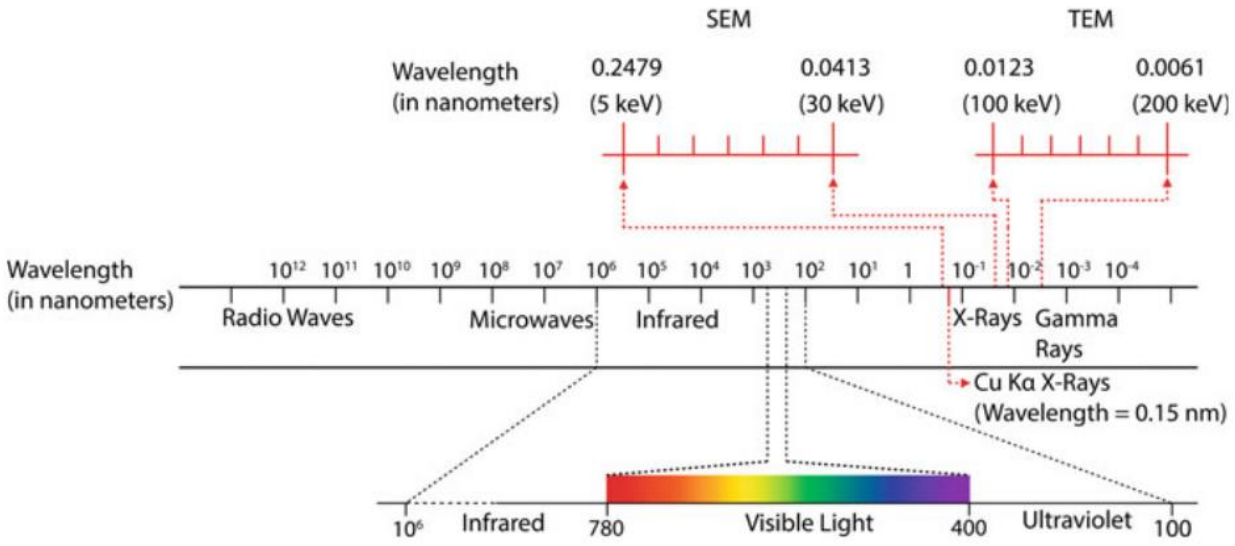

Figure II.4. Wavelengths of typical electromagnetic radiations. Reprinted with permission from Ref.[134]; Copyright 2018, Springer Nature.

When the electron hits the analyzed sample, various phenomena occur leading to the generation of many signals[135] as illustrated in Figure II.5.

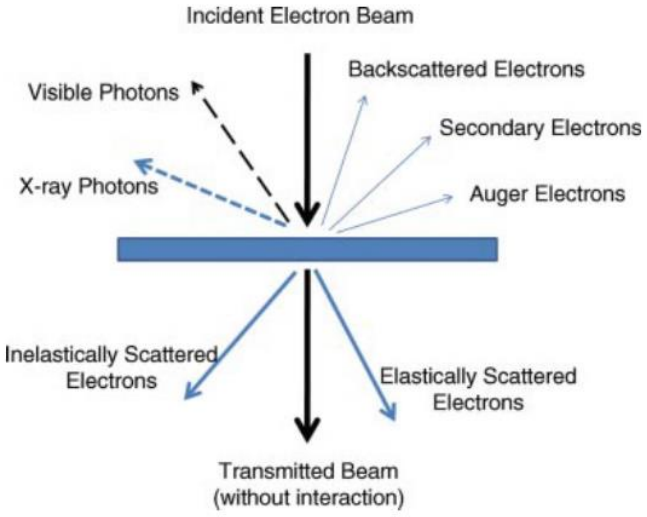

Figure II.5. Main signals generated in the interaction of electron beam with analyzed sample. Reprinted with permission from Ref.[135]; Copyright 2012, John Wiley and Sons.

The backscattered and secondary electrons are the most common signals for imaging reconstruction in scanning electron microscopy (SEM), while the signals crossing the samples are the ones applied for imaging reconstruction in transmission electron microscopy (TEM) and scanning transmission electron microscopy (STEM). The X-ray photons detected are used for chemical analysis by energy dispersive X-ray spectroscopy (EDS). Further details of these mentioned techniques are given below.

II.2.5.1. Scanning Electron Microscopy (SEM)

This technique allows to acquire surface, or near surface, information about structure, composition, and defects of materials. The electron beam penetrates fairly the sample (only few micrometers), interact with it, and generate different signals which are detected and further processed to generate images and chemical composition of the sample[134].

During analysis different detectors may be chosen to favor the detection of a desired signal. Most of signal coming from the sample accrues from backscattered electrons (BSE). This group is originally composed of electrons coming from incident electron beam which suffered elastic scattering after interacting with the sample. As said in the section II.2.2, heavy elements scatters better than light ones. It also impacts the BSE signal, therefore, the higher the atomic number of an element, the higher will be the BSE signal collected. For this

reason, images collected in BSE mode present the so-called "Z contrast", since the brightness of some region of the sample will depend on the atomic number of elements involved in such region; brighter regions contain heavier elements[134].

The most common analyzed signal in SEM comes from secondary electrons (SE). These are electrons from the outer shell of atoms in sample's surface, which once hit by the incident electron beam suffer an inelastic scattering but have enough energy to leave the sample; these SE are characteristically low-energy electrons. This inelastic scattering has no influence of atom's atomic number; hence, no Z-contrast is obtained by SE mode. On the other hand, since SE electrons are originated from material's surface, it provides topography contrast. Therefore, the use of BSE or SE signal depends on the sample analyzed and, mainly, the desired information[134].

Moreover, by the interaction of the electron beam with sample, X-rays containing characteristic energy related to each atom are released and collected by a detector operating very close to the sample. Besides the proximity, the detector also contains a collimator in its front end; both features are responsible to eliminate X-ray signals emanating from other parts of analysis environment. Thus, elements can be identified and quantified in specific spots, and this is the so-called EDS technique. This technique can be applied to numerous spots and, with the spectra of each spot, reconstruct images based on the presence or absence of elements (quantities also influence the final image), this type of image is called "elemental mapping". EDS is very useful to identify heterogeneities and segregations[134].

Field emission gun scanning electron microscopy (FEG-SEM) analyzes were performed in a JEOL 7900F microscope, equipped with Brucker QUANTAX FlatQUAD energy dispersive X-ray spectroscopy (EDS) microanalysis system. Samples were directly observed in the microscope without any particular preparation.

II.2.5.2. Transmission Electron Microscopy (TEM) and Scanning Transmission Electron Microscopy (STEM)

To obtain images in transmission mode, samples must have low thickness, therefore, some samples that can be directed analyzed by SEM must follow some special preparation for TEM/STEM applications. In addition, electron beam must be formed by electrons containing higher energy than the ones for SEM (Figure II.4). Hence, some materials can suffer damage in long analysis time due to elevated radiation doses. TEM/STEM analyses

give access to information related morphology, size, and spatial distribution of the sample[135].

The differences between TEM and STEM are mainly attributed to illumination strategy, incident beam geometry and detection approach, as evidenced in Figure II.6.

Both TEM and STEM allow to obtain image in bright-field (BF) mode, in which the signal accrues from the central unscattered beam. It generated a mass thickness contrast. On the contrary, dark-field (DF) images, collected only by STEM, comes from electrons scattered to specific regions. For example, when the microscopy is adjusted to analyze only electrons that suffered high scattering effect, the analysis is called HAADF-STEM ("HAADF" = high-angle annular dark-field). The contrast obtained in DF mode is based on diffraction effects.

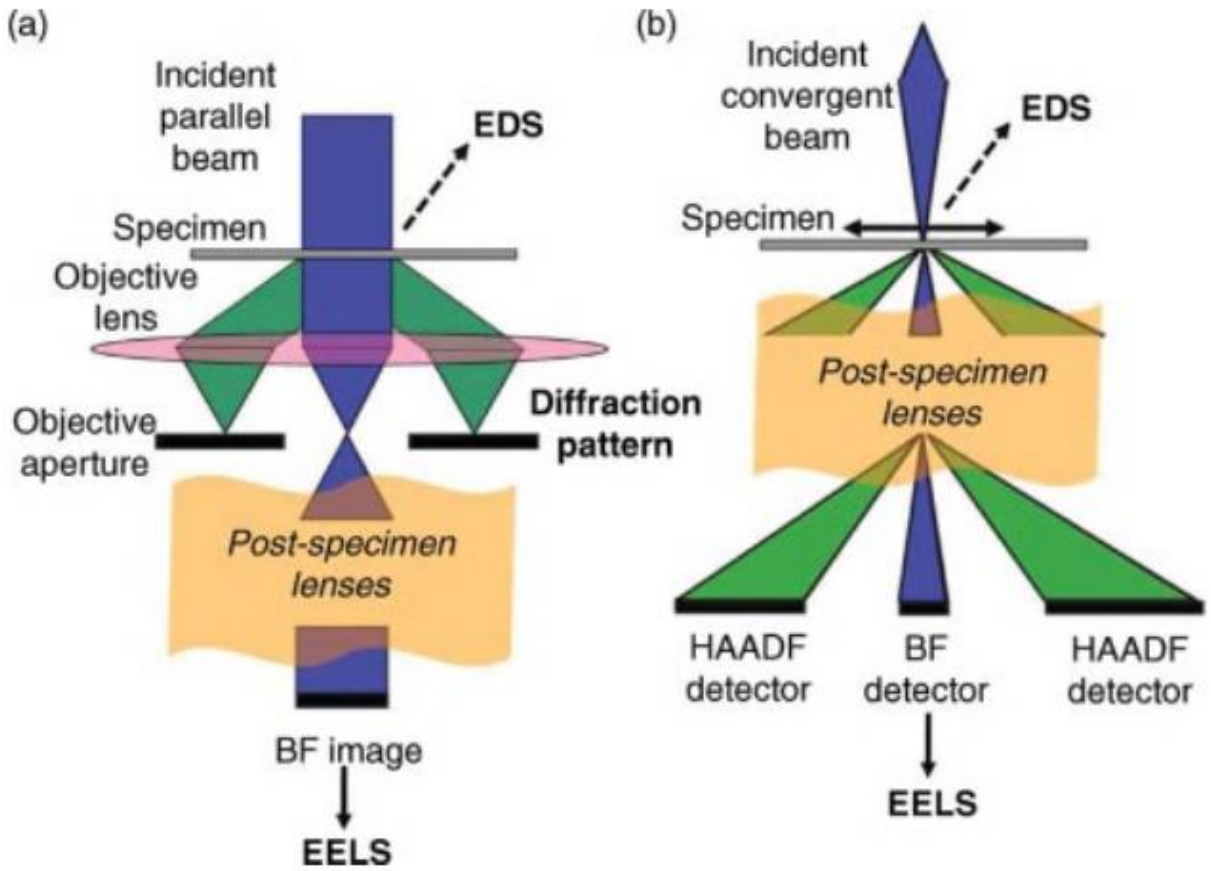

Figure II.6. Main differences of TEM and STEM techniques. Reprinted with permission from Ref.[135]; Copyright 2012, John Wiley and Sons.

Transmission electron microscopy (TEM) analyses were performed in a JEOL JEM-2100 device, operated in bright field mode at 200 kV with a LaB_6 source, coupled with an energy-

dispersive X-ray spectrometer containing a JEOL JED-2200 detector (30 mm^2 SiLi), enabling then the application of energy-dispersive X-ray spectroscopy (EDS) analysis. STEM characterization was performed with the use of a JEOL STEM operated at 200 kV. Images were collected with a nano probe (between 0.5 and 2.4 nm) and using an annular dark field (ADF) detector in high-angle annular dark field (HAADF) camera length, which allowed to collect mostly high-angles diffracted electrons. To prepare the sample for analysis, the catalyst powder was dispersed in ethanol aided by an ultrasound equipment. Subsequently, few drops of the dispersion were immediately drop-casted on a carbon-coated, holey carbon, copper TEM grid (300 mesh) and dried under vacuum.

II.3. Electrochemical characterizations

II.3.1. Types of electrochemical measurements

II.3.1.1. Linear Sweep Voltammetry (LSV) and Cyclic Voltammetry (CV)

In three-electrode configuration, both linear sweep voltammetry (LSV) and cyclic voltammetry (CV) are techniques in which potential values applied to the working electrode are varied by a constant rate, called "scan rate". The applied potential is controlled by voltage application between the working and reference electrodes, the last one must be very stable in the electrochemical environment. As result, the current flowing between working and counter electrode is measured and plot in function of the applied potential to working electrode. Noteworthy, current is always positive, however, it can have different sense. To simply elucidate the sense, signals are added to the current value. As standard, when a cathodic process occurs in the working electrode, it receives a negative value while positive values are attributed to anodic processes. In electrolyzer configuration, reference electrode does not exist, therefore, the controlled variable in the LSV measurement is the voltage between the anode and cathode.

While in the LSV the potential is uniformly swept between two potentials in only one direction, in the CV potentials are swept in both directions, forward and reverse, as much as desired. Generally, CV provides more information about the electrochemical processes

involved in an analysis. It is possible to distinguish between capacitive or faradaic process, its reversibility feature, etc.

II.3.1.2. Chronoamperometry (CA)

Chronoamperometry (CA) is a method in which voltage is also applied and the generated current in function of time is registered. However, this is not a voltametric method, but a step-potential method. In other words, instead of sweeping the voltage, it is instantaneously changed. Due to possible abrupt voltage change, as typical in transient processes, some electrochemical processes may occur in short time. Initially, double-layer charging takes place followed by convection phenomena before a new steady-state is achieved. As a matter of fact, this steady-state is, in fact, a "quasi steady-state" since processes are continuously happening and variations related to blockage of active sites, electrocatalyst degradation and so on, are unavoidable; they may occur to a small extent or be reversible though. Chronoamperometry is very useful to evaluate the stability of an electrochemical system[136].

II.3.1.3. Electrochemical Impedance Spectroscopy (EIS)

In the electrochemical impedance spectroscopy (EIS), potential or current containing small amplitude sinusoidal behavior is applied the working electrode and the resultant current or potential, not the controlled variable, is measured. Generally, many frequencies for the sinusoidal signal are evaluated. The main goal of this technique is to measure the link between potential and current in the frequency domain[137]. The impedance value for each frequency is obtained by Eq. II.3.

$$Z(f) = \frac{E}{I} \qquad \text{(Equation II.3)}$$

In which:

- Z(f) corresponds to the impedance value and depends on the frequency;
- E is the potential applied/measured;

- I is the current applied/measured.

Therefore, the impedance is calculated according to the amplitude ratio and phase lag between potential and current. By obtaining a set of impedance values according to the frequencies employed, the transfer function related to independent and dependent variables (E and I) may be estimated and its deeper analysis can provide interesting information about the electrochemical system, such as phenomena involved, values of capacitances and/or resistances, diffusion coefficients, chemical reaction rates, etc.[137]
Undoubtedly, EIS is a powerful tool to understand electrochemical systems, nonetheless, some conditions must be attended to guarantee meaningful results in this technique. First, the system must be stable because otherwise changes with time, containing no relation with applied variable, will be erroneously taken into consideration for impedance calculation. Second, perturbation must be linear and, hence, small amplitudes are applied in this technique; such feature can be confirmed by the Lissajous plot. Third, it must exist a causality relation between potential and current, i.e., the variation of measured variable must be result of controlled variable only and no other external factor[137-138].

II.3.2. Adopted electrochemical methodology

II.3.2.1. Three-electrode system

Potentiostat device (Autolab, PGSTAT 302N) was connected to a homemade three-electrode cell composed of Kel-F® material and containing a PTFE top (**Figure II.7)**, due to the use of alkaline electrolyte. Glassy carbon slab and Hg/HgO (RE-61AP Reference electrode, ALS Co., Ltd) filled with 1 M KOH (Sigma-Aldrich, reagent grade, 90 %, flakes) solution, were applied as counter- and reference electrodes, respectively. The working electrode was composed of a commercial rotating disk electrode (RDE) system (Metrohm Autolab) containing 5 mm diameter glassy carbon as substrate, which served as surface for the deposition of the evaluated electrocatalysts.
The materials were attached to the electrode by preparing a catalytic ink, which was deposited onto the glassy carbon substrate and let drying for some minutes, while the electrode was stirred at 700 rpm. For the inks prepared by implementing Nafion® as

ionomer, the composition consisted of 475 μL of ultrapure water, 475 μL of isopropanol (VWR Chemicals, HiPerSolv CHROMANORM® for HPLC), 50 μL of Nafion® perfluorinated resin suspension (5 wt. % in lower aliphatic alcohols and water, containing 15-20 % water, Sigma-Aldrich) and 14 mg of the catalyst (or physical mixture) analyzed, except for the commercial 40 % Pt/C (Sigma-Aldrich); in this case, 8 mg was added. For the inks prepared with Dioxide Materials™ Sustainion® XB-7 (5 % in ethanol) as ionomer (**Chapter V**), a variation of ink compositions was tested, the added catalyst amount was the same of the aforementioned Nafion® application though. Despite that, Eq. II.4, in which V_{H2O}, V_{ISO} and V_{IONO} correspond, respectively, to the volumes (in μL) of water, isopropanol and ionomer suspension, was respected in all ink preparations. More importantly, it was introduced the variable R_{solv}, evidenced in Eq. II.5, which brings the information about water/isopropanol volume ratio.

$$V_{H2O} + V_{ISO} + V_{IONO} = 1000 \quad \text{(Eq. II.4)}$$

$$R_{solv} = \frac{V_{H2O}}{V_{ISO}} \quad \text{(Eq. II.5)}$$

Figure II.7. Electrochemical cell designed with Kel-F and PTFE top.

As methodology adopted to the ink production, initially, only water, isopropanol and ionomer suspension were added to a sample vial, which was ultrasonicated in a bath for 15 min. Subsequently, the solid material was added to the produced suspension, which was further put in ultrasound bath once more until the homogenization of the ink was achieved (approximately, 30 min). To perform the electrochemical analyses, 7 µL of ink was added to the glassy carbon substrate, therefore, the theoretical mass loading of 40 % Pt/C used in the present study was 0.28 mg cm^{-2}, while 0.50 mg cm^{-2} was applied for all other materials. Noteworthy, these values consider the geometrical surface area of the electrode.

Although all measurements were performed with Hg/HgO reference electrode, the potential values reported in this document are referenced to reversible hydrogen electrode (RHE); to do so, a methodology to calibrate the Hg/HgO electrode was performed. Initially, 40% Pt/C was deposited on the working electrode glassy carbon substrate with a mass loading of 0.28 mg cm^{-2}. Then CV analysis was performed between -0.93 and 0.40 V vs Hg/HgO in H_2-saturated 1 M KOH at 100 mV s^{-1} until a reproducible profile in current density vs potential plot was achieved. Consecutively, a new CV analysis was performed between -1.03 and -0.83 V vs Hg/HgO at 10 mV s^{-1}; the result is presented in **Figure II.8**. The average of potentials in which the curve crosses the value of 0 mA cm^{-2} in both anodic and cathodic directions was considered the theoretical potential of HOR/HER (0 V vs RHE). Based on this analysis, it was stated that for the reference electrode used during three-electrode cell measurements, -0.940 V vs Hg/HgO is equivalent to 0 V vs RHE. Therefore, such value was used for all potential conversions towards V vs RHE unit.

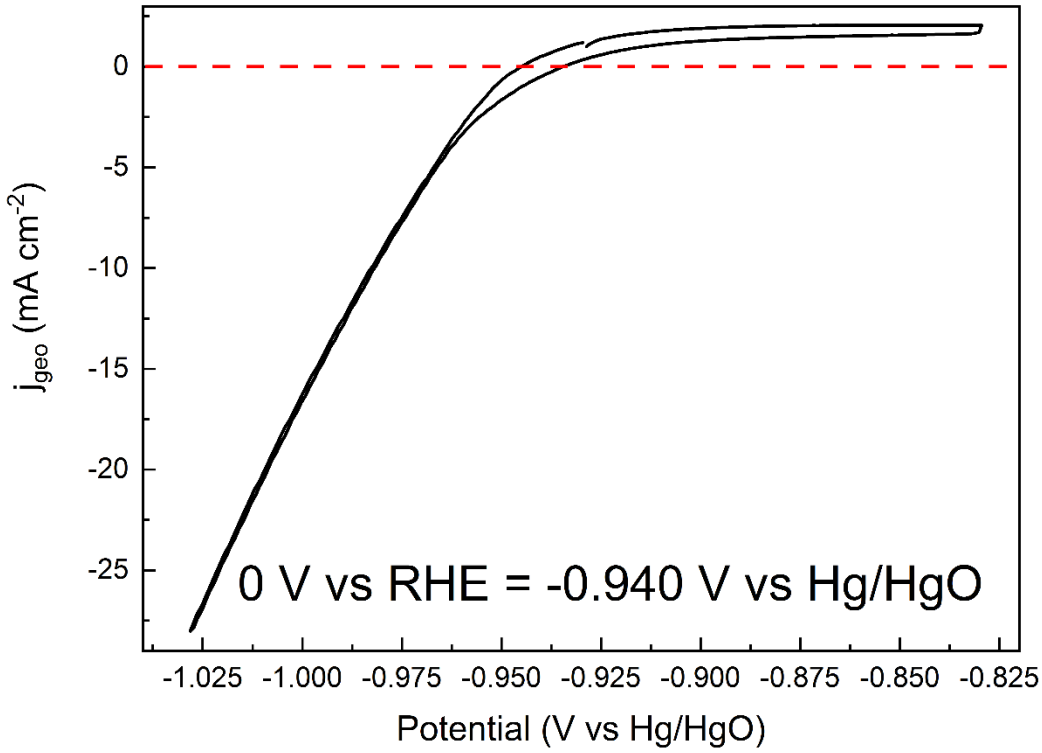

Figure II.8. CV of 40% Pt/C in H_2-saturated 1 M KOH at 10 mV s^{-1} in a potential window of HER/HOR.

Linear sweep voltammetry (LSV) analyses were performed in 1 M KOH by scanning the potential between 0.14 V and -0.56 V vs RHE at 10 mV s^{-1}, besides applying a rotation speed of 1600 rpm in the working electrode. Before any LSV measurement, electrochemical impedance spectroscopy (EIS) was performed at open-circuit potential (OCP) to obtain the solution resistance (R_s) value, which was used when ohmic drop compensation was applied. The Tafel plots were constructed with the same data obtained from LSV analyses, but only selecting the interval in which a linear behavior relationship between overpotential (η) and the logarithm of absolute value of current density (log |j|) was verified, besides to be the data associated with the beginning of the hydrogen evolution reaction (HER). The resultant curve could be fitted with the Tafel equation: $\eta = a + b \log |j|$. The variable "b" corresponds to the Tafel slope, and the exchange current density (j_0) corresponds to the value of "j" when η is assumed to be zero.

EIS analyses in the region of HER were performed at various DC potentials with an AC perturbation of 10 mV amplitude in frequency range between 100 kHz and 1,10 or 100 Hz (according to the linearity verified by potential and current in Lissajous diagram) and applying 10 points per decade. Finally, all previous reported electrochemical measurements, including reference electrode calibration, were performed at room temperature.

II.3.2.2. Anion Exchange Membrane Water Electrolyzer (AEMWE) system

A BioLogic VSP Potentiostat (20 V/4 A) was connected to a single AEMWE cell composed of two titanium-based polar plates containing three parallel straight channels each (length, width, and depth equal 15, 2 and 2 mm, respectively), two porous titanium, which plays a role as porous transport layer (PTL) and was applied in both anodic and cathodic compartments, besides the membrane electrode assembly (MEA). This last one comprised a Sustainion® X37-50 Grade RT (Dioxide Material™) membrane sandwiched by two gas diffusion electrodes (GDE) of 1.8 cm^2, which were directly assembled in the cell. However, before being inserted in the cell, the membrane was soaked in 1 M KOH overnight and the electrodes were soaked in 0.1 M KOH for 1 h, followed by vigorous rinsing. The anode GDE was obtained by depositing 2 mg cm^{-2} of commercial Iridium black (Sigma-Aldrich) onto Bekaert Bekipor® ST 40 BL3 stainless steel (alloy: 316 L, thickness = 0.23 mm, and porosity = 84 %), while each cathode GDE was obtained by depositing the transition metal sulfide onto AvCarb® MGL370 (thickness = 0.37 mm, and porosity = 78 %) carbon paper with a mass loading target of 3.5 mg cm^{-2}. All catalysts were in a powder form and, therefore, to deposit them on the gas diffusion layers (GDL) by spray-coating method, catalytic inks were prepared. Inks were produced by mixing the catalyst with Sustainion® XB-7 ionomer and solvent (50 % v/v ethanol in water). The homogenization was obtained by the application of pulsed sonication, i.e., 1 s of sonication followed by 4 s of ultrasound absence repeated during 5 min, with an ultrasonic probe (power = 280 W) from Qsonica. When it came to the anode, a proportion of 97 and 3 wt.% of Ir black and XB-7, respectively was respected, while for the cathodes such proportion was altered to 90 and 10 wt.%; the catalyst was maintained as major component though. As previously mentioned, the mass loading target was 3.5 mg

cm^{-2} for each TMS, however, real mass loading, presented in **Table II.3**, was obtained by the mass difference of AvCarb® MGL370 before and after catalysts deposition.

Table II.3. *Mass loading obtained for each GDE cathode.*

Catalyst	Mass loading (mg cm^{-2})
CoS_x	3.6
MoS_x	3.4
$Co_{0.5}Mo_{0.5}S_x$	3.9* / 3.4#

Mass loadings in the activity* (represented by **Figure IV.2**) and stability# (represented by **Figures IV.3** and **B3**) tests.

During analysis, the cell, maintained at 50 ºC, was fed only in the anodic compartment by 2 mL min^{-1} of 0.1 M KOH solution, also stocked at 50 ºC, in a closed loop. **Figure II.9** presents images of AEMWE setup. For performance tests, the LSV curves were registered at 10 mV s^{-1}. The stability test was divided in many steps. Initially, a LSV was recorded at 5 mV s^{-1} between OCV and 2 V, then the cell was maintained at 2 V during 10 h. Thereafter, it was repeated three more times until achieve 40 h of chronoamperometry analysis.

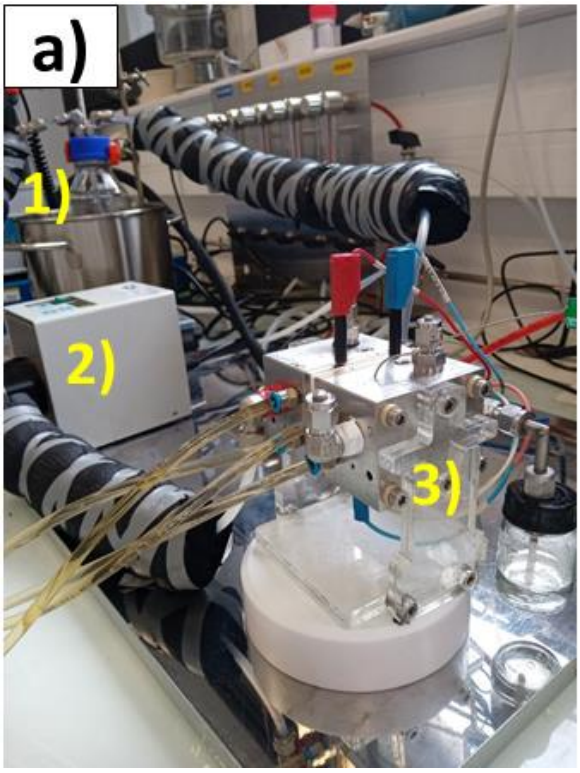

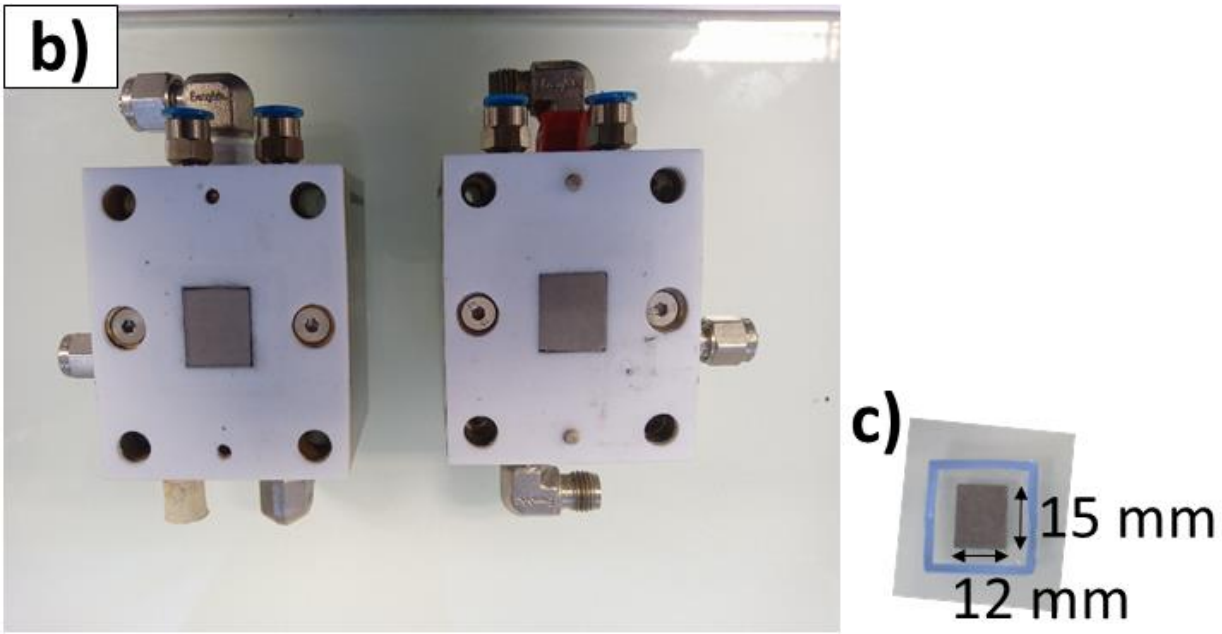

Figure II.9. Anion exchange membrane water electrolysis setup used for the obtained results reported herein. a) Image of complete setup comprising 1) oil bath with temperature controlled by thermostat for electrolyte heating, 2) pump for electrolyte recirculation and 3) AEMWE cell. b) Cell gaskets and c) MEA images.

In addition, the value of specific energy consumption is given by **Eq. II.6.**

$$\varepsilon\ (\mathrm{kWh\ Nm^{-3}}) = \frac{2 \times F}{3600 \times V_m\ (\mathrm{m^3\ mol^{-1}}) \times 10^3} \times U(j) \qquad \textbf{(Eq. II.6)}$$

Assuming that H_2 behaves as ideal gas, V_m can be calculated by **Eq. II.7**.

$$V_m = \frac{R \times T}{P} \qquad \textbf{(Eq. II.7)}$$

Therefore, by combining **Eqs. II.6 and II.7**, the **Eq. II.8**, which was used to plot curves of **Figure IV.2**, was obtained.

$$\varepsilon\ (\mathrm{kWh\ Nm^{-3}}) = \frac{2 \times F \times P}{3600 \times R \times T \times 10^3} \times U(j) \qquad \textbf{(Eq. II.8)}$$

For the calculations, voltage unit adopted was Volt. Furthermore, all parameters' values applied are presented below.

- F = 96,485 C mol^{-1};
- P = 101,325 Pa;
- R = 8.314 Pa m^3 mol^{-1} K^{-1};
- T = 323.15 K.

The calculation of reversible current decay, irreversible current decay, and current decay rate were done according to the **Eqs. II.9, II.10 and II.11**, respectively.

$$\text{Reversible current decay of } n^{th} \text{ interval } (\%) = \frac{j_b^{n+1} - j_f^n}{j_b^n - j_f^n} \times 100 \qquad \textbf{(Eq. II.9)}$$

$$\text{Irreversible current decay of } n^{th} \text{ interval } (\%) = \frac{j_b^n - j_b^{n+1}}{j_b^n - j_f^n} \times 100 \qquad \textbf{(Eq. II.10)}$$

$$\text{Current decay rate } (\%\ h^{-1}) = \frac{\left(\sum_{i=1}^{n} \frac{j_b^n - j_f^n}{j_b^n}\right) \times \frac{100}{10}}{n} \qquad \textbf{(Eq. II.11)}$$

For the calculations, the meaning of the variables is presented below.

- **j** corresponds to current density;
- **n** corresponds to the number of the interval;
- **b** corresponds to the beginning of the interval, i.e., first value in the interval;
- **f** corresponds to the final of the interval, i.e., last value in the interval.

Chapter III: Taking Advantage of Teamwork: Unsupported Cobalt Molybdenum Sulfide as an Active HER Electrocatalyst in Alkaline Media

This chapter is based on the following publication: *"Taking Advantage of Teamwork: Unsupported Cobalt Molybdenum Sulfide as an Active HER Electrocatalyst in Alkaline Media"*. C.V.M. Inocêncio, J. Rosseau, N. Guignard, C. Canaff, S. Morisset, C. Comminges, C. Morais, K.B. Kokoh, J. Electrochem. Soc. **2022**, 169, 054524.

https://doi.org/10.1149/1945-7111/ac6b59

Abstract

A bimetallic cobalt molybdenum sulfide ($Co_{0.5}Mo_{0.5}S_x$) material was studied as candidate electrocatalyst to replace platinum-based cathode for HER reaction in alkaline media. The $Co_{0.5}Mo_{0.5}S_x$was obtained from a hydrothermal synthesis methodology employing sodium diethyldithiocarbamate as sulfurizing agent, a non-conventional compound. The recovered sulfide material was physicochemically characterized by XRD, Raman spectroscopy, TEM and XPS measurements. Analogous monometallic sulfides were also synthesized to compare their HER activities to that of $Co_{0.5}Mo_{0.5}S_x$. Such electrochemical characterization was performed by the application of polarization and EIS analyzes in 1 M KOH. An evident synergistic effect emerged in the bimetallic sulfide and it was associated with the design of a catalyst less susceptible to air-oxidation added to the roles performed by cobalt- and molybdenum-based species in the HER mechanism. Finally, a physical mixture of $Co_{0.5}Mo_{0.5}S_x$ and Carbon Vulcan was prepared aiming to enhance the electronic conductivity of the electrode. As result, an overpotential of 131 mV was requested to achieve −10 mA cm^{-2}. In addition, to achieve −200 mA cm^{-2}, this electrode only needed an overpotential 66 mV higher than the one necessary for the benchmarking 40% Pt/C electrocatalyst.

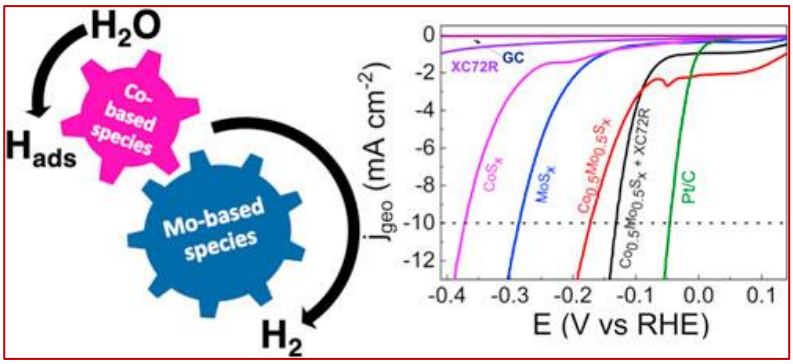

III.1. Introduction

Hydrogen already plays a key role in many industrial processes and the interest in this compound has recently increased since it is pointed-out as a promising future energy carrier. Besides to present a high energy yield, no greenhouse gas is produced during its oxidation[139]. However, most of current hydrogen production still comes from fossil feedstock and, due to environmental concerns, methods aiming the renewable, cleaner, and economically suitable production of hydrogen are being developed[11, 140].

Hydrogen production from water, in the so-called "water electrolysis" process, has been receiving great attention because if it is coupled to a renewable energy source, it results in zero carbon emission[141]. In this process, water is split to originate two gases, hydrogen (H_2) at the cathode and oxygen (O_2) at the anode, both containing high purity. The reactions responsible for their production in each half-cell are called hydrogen evolution reaction (HER) and oxygen evolution reaction (OER), respectively[4, 142].

To minimize the overpotential of aforementioned reactions and, consequently, increase process efficiency, the utilization of active catalysts is required[142-144]. Noble metal-based materials, mainly Pt, Ru and Ir, remain state-of-the-art catalysts of these reactions, but their high-cost and scarcity are responsible for limiting their application in large scale[145]. These concerns can be overcome with the development and design of new candidate catalysts which should not only be active, stable and selective, but also cheap and earth-abundant. Molybdenum (MoS_2) and cobalt (CoS_2) sulfides have been extensively investigated as HER active materials[4-5, 90, 109, 146-149]. Besides they are arousing much interest owing to their low cost, these metal sulfides are representative of transition metal dichalcogenides for the water reduction. Moreover, some authors stated that CoS_2 exhibits in acidic environment evident advantages over layered metal sulfides such as MoS_2 and WS_2 due to its intrinsically metallic or conductive features[150-151]. Alkaline HER medium brings an additional step of water dissociation which provides the adsorbed hydrogen species required for the HER to proceed; such step may increase energy consumption of reaction. Furthermore, lower binding energy of water compared to hydronium and the interaction of hydroxyl groups, abundant in high pH's, with the catalytic sites may play a key role in catalysts' activity. As result, the mechanism of HER in alkaline electrolyte is more complex. Despite that, the

alkaline environment allows the application of wider range of materials, including non-noble metal-based ones, in HER and OER[97, 152-153]. This, summed up to new developments in alkaline exchange membranes[154-155], makes it worth to search for materials that may be applied in alkaline exchange membrane water electrolyzers (AEMWE). Once it has been described elsewhere[109, 152] that cobalt-based species perform well the water dissociation, our strategy was to synthesize bimetallic cobalt molybdenum sulfide ($Co_{0.5}Mo_{0.5}S_x$) catalyst to take advantage of both cobalt and molybdenum sulfide species characteristics and, consequently, obtain a synergistic effect.

III.2. Results and Discussion

III.2.1. Physicochemical characterizations

The synthesized materials were analyzed by the XRD technique and results are presented in **Figure III.1a**. The CoS_x sample presented well-defined peaks in the same positions of CoS_2 pattern (ICSD collection code: 624848) and other peaks of low intensity, still apparent though, in Bragg angles corresponding to the $CoSO_4 \cdot H_2O$ phase (PDF: 01-074-1330). Therefore, cobalt sulfide was successfully synthesized, though part of it was oxidized to sulfate, probably due to the contact of CoS_2 with air. Both MoS_x and $Co_{0.5}Mo_{0.5}S_x$ showed diffraction peaks that can be associated with hexagonal MoS_2 phase (ICSD collection code: 601647), also known as 2H-MoS_2. The peak shift towards lower angles in (002) line, present in both MoS_x and $Co_{0.5}Mo_{0.5}S_x$, is generally associated with enlargement of the MoS_2 interlayer distance[156]. For the 2H-MoS_2 pattern, (002) line appears at $2\theta = 14.4^o$ and the standard interlayer distance of the material is 6.15 Å. On the other hand, (002) line is observed at 13.9^o for MoS_x and $Co_{0.5}Mo_{0.5}S_x$. By applying the Bragg equation, it is expected MoS_2 sheets with interlayer distance (d(002)) of about 6.36 Å. Another feature verified for MoS_x and $Co_{0.5}Mo_{0.5}S_x$ is the absence of peaks corresponding to (103) and (105) crystallographic planes of MoS_2 and the existence of broad bands in those regions instead. Since the (002) line exists for both samples, such feature is associated to turbostratic disorder[157-158]. In addition, the broadening of peaks associated to (100) and (110) planes, seen in MoS_x and $Co_{0.5}Mo_{0.5}S_x$, mainly the first one, had been reported elsewhere as characteristic

of MoS_2 defect-rich structure[159]. In order to compare, **Figure A1** shows the XRD profile of commercial MoS_2, in which the aforementioned deviations from the MoS_2 pattern do not exist. Thus, disordered and defect-rich 2H-MoS_2 phase is likely to be present in the herein synthesized Mo-based catalysts. Additional peaks, others than related to MoS_2 phase, were verified for $Co_{0.5}Mo_{0.5}S_x$. The peaks present at 2θ, nearly 30.9º, 35.4º, 46.9º and 55.0º, are indexed respectively to (010), (011), (012) and (110) planes of CoS pattern (ICSD collection code: 624857). Consequently, XRD unveiled that, besides MoS_2, hexagonal CoS specie is also present in the composition of $Co_{0.5}Mo_{0.5}S_x$.

Raman spectroscopy analyses were also performed to further characterize the materials and the obtained spectra are plotted in **Figure III.1b**. As stated previously, XRD results evidenced the existence of pyrite CoS_2 phase in CoS_x. In this structure sulfur atoms are presented as S_2^{2-} ion forming a dumbbell-shape arrangement and the peaks present in 250-450 cm^{-1} range of CoS_x Raman spectrum are related to the vibration modes of these sulfur atoms in the dumbbells[160]. The most intense peak at 391 cm^{-1} is the result of in-phase stretching vibration, (A_g). The peak at 414 cm^{-1} also comes from pure stretching vibration mode, out-of-phase though ($T_g(2)$). Differently, the peak at 287 cm^{-1} is derived from pure librational vibration mode (E_g), while the peak at 315 cm^{-1} is related to the combination of several librational and stretching vibration modes ($T_g(1)$)[160]. Another peak at 1025 cm^{-1} is also observed for CoS_x and it can be related to υ_1 symmetric stretching vibration mode of sulfate group. To the best of our knowledge, there are no records of Raman spectrum of $CoSO_4 \cdot H_2O$, the phase encountered by XRD (**Figure III.1a**), in the literature. Nevertheless, this υ_1 mode of sulfate group has been reported at 1024 cm^{-1} in $CoSO_4 \cdot 7\ H_2O$ sample[161]. Thus, it is believed that the peak at 1025 cm^{-1} is associated with the sulfate groups, although we are aware that the vicinity of sulfate may influence the Raman shift and further analyses would be necessary to confirm such assumption. So, the obtained Raman spectrum corroborates the XRD result found for CoS_x.

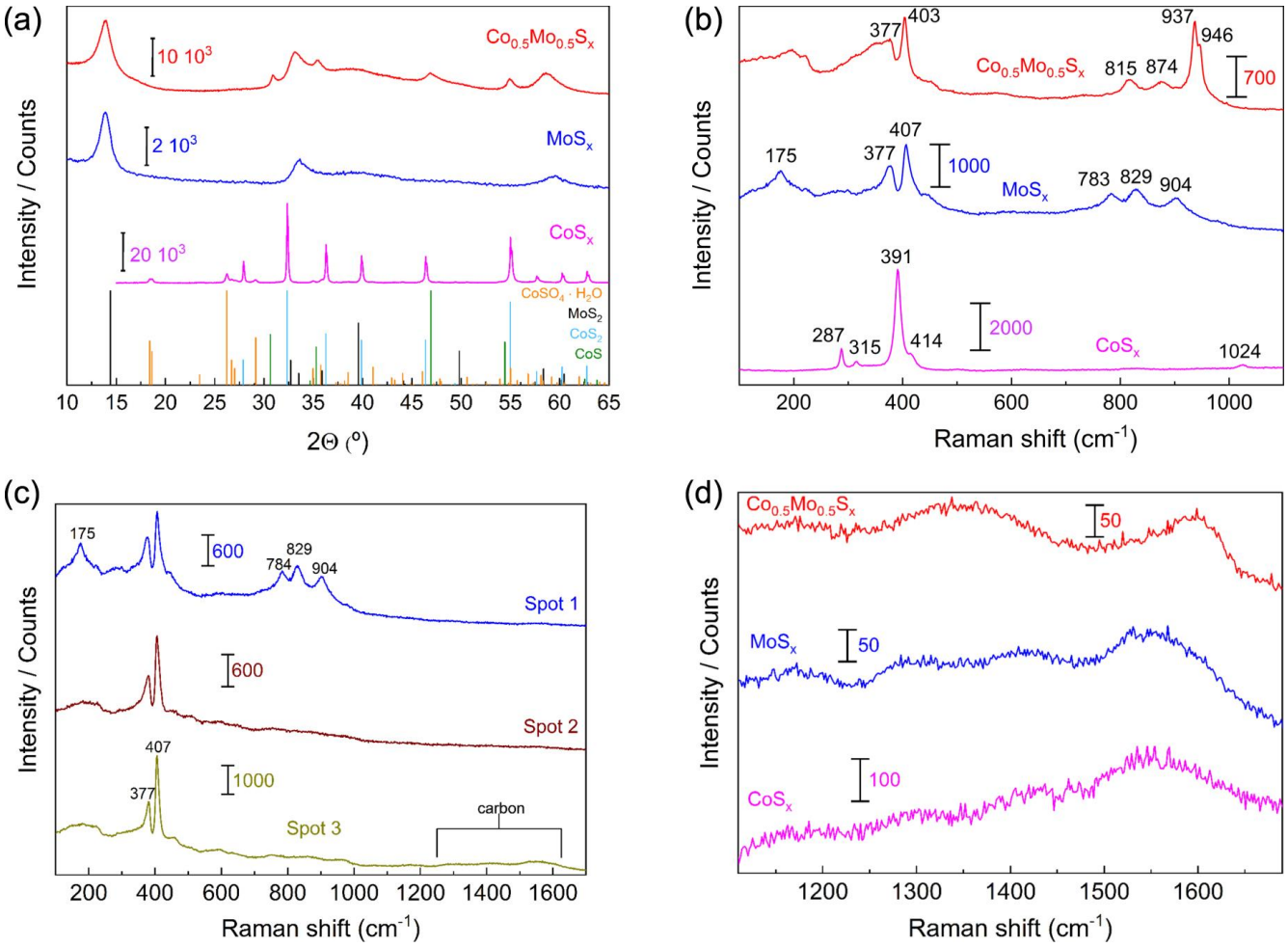

Figure III.1. XRD (a) and Raman spectroscopy (b) results of CoS_x, MoS_x and $Co_{0.5}Mo_{0.5}S_x$ materials. (c) Profiles obtained from the application of Raman spectroscopy analysis to different spots of the synthesized MoS_x catalyst. (d) Raman spectra of the synthesized transition metal sulfides in the region related to vibration modes of carbonaceous materials.

In the MoS_x Raman spectrum presented in **Figure III.1b**, three peaks are present in the range 750-950 cm^{-1}. These three peaks, summed up to the one at 175 cm^{-1}, resemble the most intense peaks of η-Mo_4O_{11}, as reported by Zoller *et al.*[162] and Pham *et al.*[163], and are associated with the vibration modes of linkages between molybdenum and oxygen[164]. Since heptamolybdate ($(NH_4)_6Mo_7O_{24}$) was used as Mo precursor at this work, it is believed that those peaks in MoS_x spectrum reveal the incomplete consumption of molybdates during the synthesis. Noteworthy, the Raman spectroscopy analysis was performed in different spots of MoS_x sample to verify the homogeneity of the material. **Figure III.1c** shows three representative spectra and evidence that the Mo-O linkages are not throughout the material, which confirms that they correspond to a residue of synthesis. On the other hand, the peaks

verified at 377 and 407 cm^{-1}, related to the well-known in-plane (E^1_{2g}) and out-of-plane (A^1_g) Mo-S phonon modes of MoS_2 material[165], respectively, were detected throughout the material.

The aforementioned E^1_{2g} and A^1_g Raman active modes of MoS_2 were also detected in $Co_{0.5}Mo_{0.5}S_x$ spectrum at 377 and 403 cm^{-1}, respectively, confirming the existence of molybdenum disulfide as already stated by XRD (**Figure III.1a**). An additional ensemble of peaks appeared at 352, 815, 874, 937 and 946 cm^{-1}, which can be assigned to $CoMoS_4$ Raman profile[166]. This compound cannot be identified by XRD due to its amorphous character[166-167].

Noteworthy, for CoS_x and $Co_{0.5}Mo_{0.5}S_x$, Raman spectra were also taken in different spots of the materials, similar profiles were obtained though. Therefore, it is believed that the kinetics of sulfide synthesis is slower in the absence of cobalt, hence, MoS_x lacks homogeneity, probably, due to incomplete reaction in 24 h. Furthermore, in some spots of all synthesized sulfides reported here, it was evidenced the presence of carbon-based compounds, as shown in **Figure III.1d**. This carbon is likely a residue of sulfur precursor (sodium diethyldithiocarbamate) employed in the synthesis. Li *et al.*[168] also showed the presence of carbon in CoS_2-FeS_2 nanosheets synthesized hydrothermally when using the same sulfur precursor as the one used in this work and a very similar synthesis methodology.

Figure III.2 depicts the electron microscopy images of synthesized materials. **Figure III.2a** is an image derived from high-angle annular dark-field scanning transmission electron microscopy (HAADF-STEM) technique applied to the CoS_x catalyst. One can see two patterns of particles, bigger and brighter ones and smaller particles containing less brightness. This technique is well-known to evidence Z-contrast in the samples, *i.e.*, the intensity of signal increases with the atomic number of each atom ($I \alpha Z^{\upsilon}$, $1.6 \leq \upsilon \leq 1.9$)[169]. Once XRD and Raman spectroscopy results unveiled the existence of cobalt sulfide and cobalt sulfate species, it is assumed that the big particles correspond to the cobalt sulfide phase since it is richer in cobalt, while the smaller particles are related to cobalt sulfate. Such assumption is further corroborated by EDS, which detected oxygen in the small particles but not in the big ones, as can be seen in the elemental mapping presented in **Figure III.3**.

TEM images of the MoS_x sample are shown in **Figures III.2b-d**. The presence of agglomerated sheets, a morphology typical of MoS_2 materials, containing different patterns

of lateral size and dispersion can be seen in **Figure III.2b**. There are some zones of MoS_x which contain large sheets and many stacked layers, as observed in **Figure III.2c**, while in other zones few-layers nanosheets are noticed in **Figure III.2d**. This last pattern is generally the goal for HER applications because the active sites reside in the edges of 2H-MoS_2[149]. Besides that, the resistivity between the layers is much higher than along the same layer[148, 165].

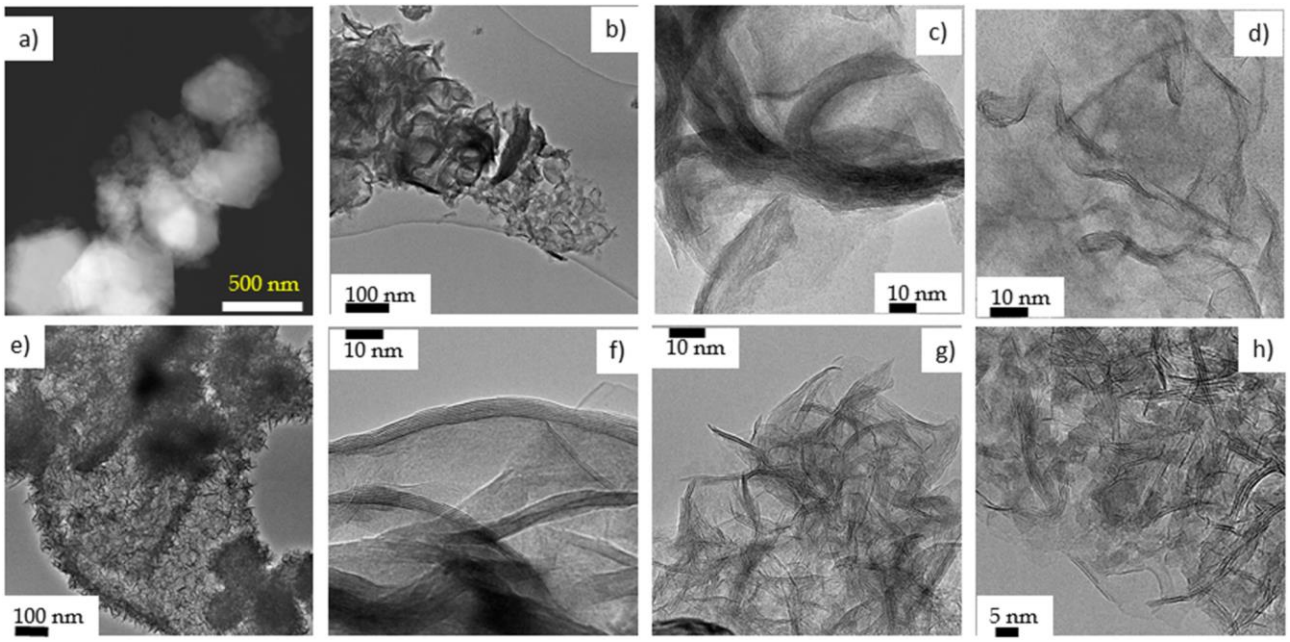

Figure III.2. STEM image of (a) CoS_x and TEM images of (b, c, d) MoS_x and (e, f, g, h) $Co_{0.5}Mo_{0.5}S_x$.

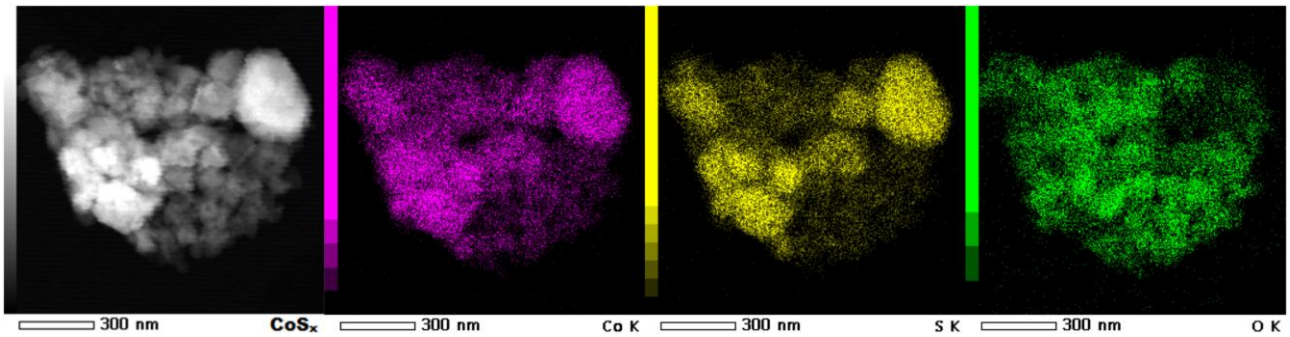

Figure III.3. Elemental mapping constructed from the application of EDS in a HAADF-STEM image of CoS_x.

TEM images of $Co_{0.5}Mo_{0.5}S_x$ sample are depicted in **Figures III.2e-h**. Similarly to MoS_x, when a lower magnification is applied for $Co_{0.5}Mo_{0.5}S_x$, as in **Figure III.2e**, two patterns of sheets are found in the image. There are zones containing high degrees of agglomeration, darker

zones in the image, where larger and more stacked sheets are present, see **Figure III.2f**, but there are also zones containing more dispersed and shorter few-layer nanosheets, as shown in **Figure III.2g**. Additionally, crystallized nanoparticles with sizes between 5 and 10 nm are observed in $Co_{0.5}Mo_{0.5}S_x$ as verified in the **Figure III.2h**. By performing EDS analyses, whose results are shown in **Table III.1**, it was noticed that such nanoparticles are rich in Co and S, therefore, after also considering the XRD result of $Co_{0.5}Mo_{0.5}S_x$, these nanoparticles are likely cobalt sulfide species. Interestingly, EDS results (**Table III.1**) also revealed that the zones containing the few-layer nanosheets are richer in Co than the zones containing more stacked sheets. In addition, Tang *et al.*[170] reported that CoS_2 may serve as backbone for MoS_2 growth on hydrothermal reaction. Therefore, it can be assumed herein that Co may also play a role on the growth of molybdenum sulfide nanosheets in the synthesis.

Table III.1. Co/Mo atomic ratio obtained by EDS applied to different zones of $Co_{0.5}Mo_{0.5}S_x$ catalyst analyzed by TEM.

Zone	Characteristic[#]	Co/Mo atomic ratio
1	F	0.54
2	F	1.00
3	F	0.98
4	S	0.26
5	S	0.22
6	S	0.27
7	F + P	3.02
8	F + P	4.26

[#]F = few-layer nanosheets, S = stacked nanosheets, P = nanoparticles rich in Co and S.

The XPS analysis was performed for CoS_x, MoS_x and $Co_{0.5}Mo_{0.5}S_x$ aiming to better understand the chemical state at their surfaces; results are presented in **Figure III.4**. Based on the Co 2p spectrum of CoS_x (**Figure III.4a**), it is evident that most of Co species are associated to oxidized species as cobalt sulfate and cobalt oxide, although a small amount is still identified as CoS_2. The S 2p spectrum of CoS_x is also presented in **Figure III.4e** and the sulfur species are also mostly present in oxidized form, in this case as sulfate. These results are in line with those of HAADF-STEM, which showed that the bigger particles corresponded to the cobalt sulfide phase, while smaller particles were related to cobalt

sulfate. Although, XRD and Raman showed that CoS_x is composed mostly of CoS_2, it is necessary to consider that the XPS is a technique to probe the surface of the material, even lower depth than Raman analysis. Therefore, due to dispersion issues the surface of cobalt sulfate becomes more representative than the cobalt sulfide one.

In **Figure III.4c** four peaks are shown, the one between 224 and 228 eV is, in fact, related to the S 2s contribution, while the other three are associated with the Mo 3d spectrum of the MoS_x catalyst. These three peaks can be decomposed in three doublets containing the Mo $3d_{5/2}$ and Mo $3d_{3/2}$ contributions of molybdenum species involving oxidation states equal to +4, +5 and +6. The Mo^{4+} contribution, the most present for MoS_x, is associated with the MoS_2 phase identified by XRD and Raman analyses. Mo^{5+} and Mo^{6+} states, present in similar quantities, are related to oxidized species as MoS_yO_x and MoO_3, respectively. The first one is reported as an intermediate phase between molybdenum oxide and molybdenum sulfide. Therefore, it can be associated with a residue of the synthesis or even with a light oxidation of MoS_2 at the surface due to the contact with air. On the other hand, MoO_3 is likely to be result of the oxidation of MoS_2 at the surface due to the contact with air. In fact, the detection of these Mo^{5+} and Mo^{6+} chemical states by XPS for molybdenum sulfides, related to oxidized phases, is a common feature that has been reported by many authors[91, 171-172]. Noteworthy, the same commercial MoS_2 material, supplied by Sigma-Aldrich, reported in **Figure A1** was analyzed by XPS, and the result also showed the existence of Mo^{6+} species. The S 2p spectrum of MoS_x (**Figure III.4f**) showed mostly the contribution of MoS_2 doublet, although some contributions of other sulfur-based species as bridging S_2^{2-} ligands were also revealed. Finally, although detected, this sample exhibited very low intensity of peaks related to sulfate species.

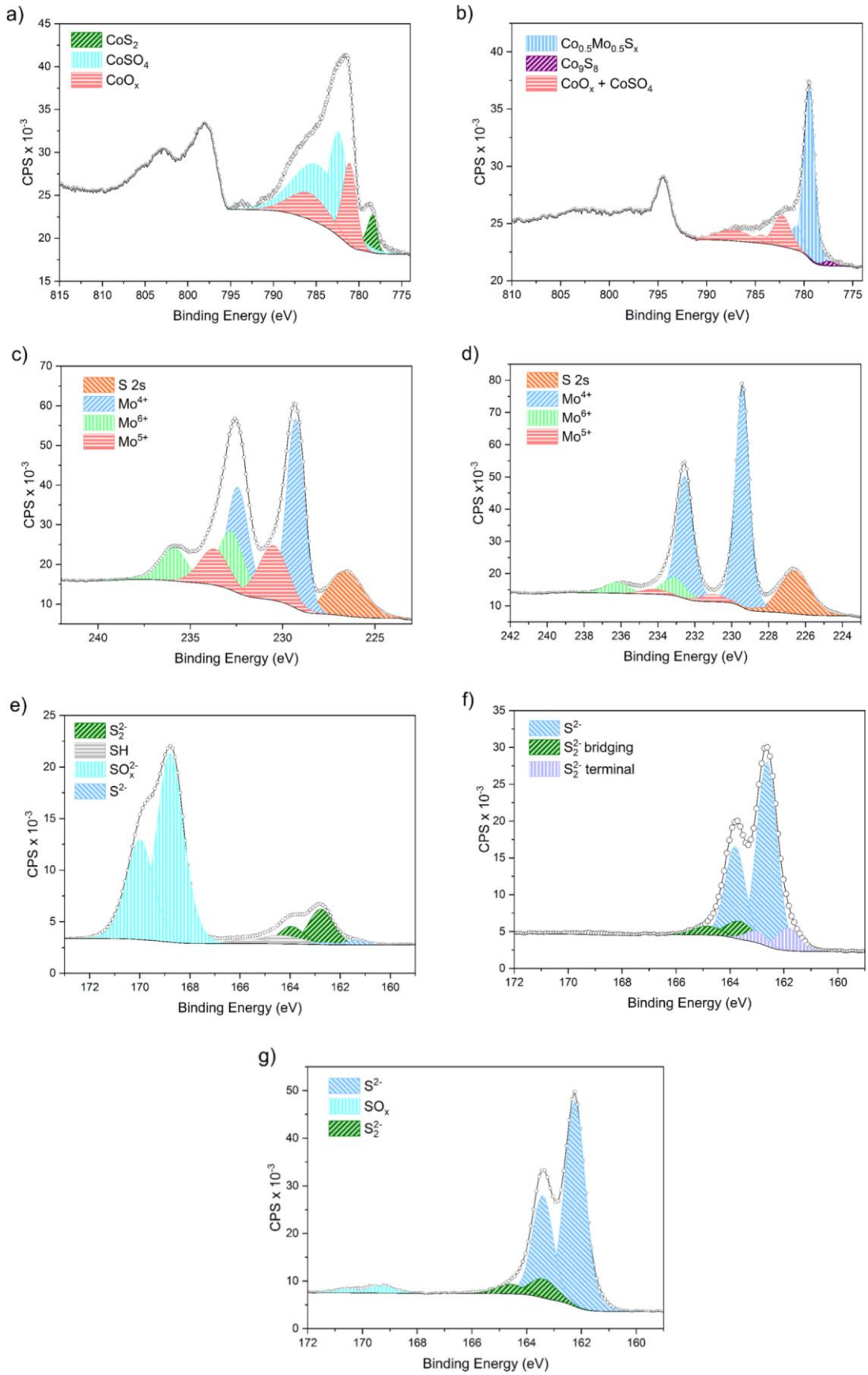

Figure III.4. Co 2p spectra of (a) CoS_x and (b) $Co_{0.5}Mo_{0.5}S_x$, Mo 3d of (c) MoS_x and (d) $Co_{0.5}Mo_{0.5}S_x$ and S 2p spectra of (e) CoS_x, (f) MoS_x and (g) $Co_{0.5}Mo_{0.5}S_x$.

The Co 2p spectrum of $Co_{0.5}Mo_{0.5}S_x$ (**Figure III.4b**) shows an intense peak associated with cobalt in the structure of a tertiary sulfide, *i.e.*, cobalt molybdenum sulfide. In addition, a smaller peak related to cobalt sulfide specie is revealed, which showed the existence of a segregation of cobalt from the bimetallic sulfide structure. The Mo 3d spectrum for $Co_{0.5}Mo_{0.5}S_x$ (**Figure III.4d**) evidenced the existence of molybdenum in three oxidation states (+4, +5 and +6). The Mo^{4+} is the most representative one and it is related to the molybdenum sulfide (MoS_2) species. The Mo^{6+} was found in smaller amounts and can be associated to the $CoMoS_4$ structure verified by Raman, although the presence of MoO_3 due to oxidation of molybdenum sulfide in presence of air should not be discarded. In even lower quantities can be found Mo^{5+}, which is probably a result of molybdenum surrounded by oxysulfidic species, commonly reported as intermediates in the transition of molybdenum oxide to molybdenum sulfide[173].

On the S 2p spectrum of CoS_x (**Figure III.4e**) can be verified that most of sulfur is associated with sulfate species, which is in line with the Co 2p spectrum of the same material (**Figure III.4a**). Only a small amount of sulfur is associated with sulfide in its surface. On the other hand, based on S 2p spectrum for $Co_{0.5}Mo_{0.5}S_x$ (**Figure III.4g**), very low amount of sulfur is related to the sulfate species; in fact, sulfur is present almost totally as S^{2-}. Additionally, a small contribution related to bridging S_2^{2-} ligands, generally present in molybdenum sulfides containing low degree of crystallinity, is also present in $Co_{0.5}Mo_{0.5}S_x$. Once XRD result of $Co_{0.5}Mo_{0.5}S_x$ (**Figure III.1a**) evidenced a MoS_2 structure containing defects, such ligands were already expected to be present in the catalyst.

XPS results suggest that in the monometallic cobalt sulfide (CoS_x), the surface is highly oxidized resulting in the formation of cobalt sulfate and cobalt oxide structures. The same is not verified for the bimetallic sulfide ($Co_{0.5}Mo_{0.5}S_x$), in this case cobalt is mostly incorporated to the structure of tertiary sulfide, *i.e.*, cobalt molybdenum sulfide, although part of cobalt also segregates in a cobalt sulfide structure. For MoS_x, the sulfate contribution is even lower, although it was evidenced the existence of MoO_3 and MoS_yO_x phases, which is a common feature for molybdenum sulfide. These species were also present in $Co_{0.5}Mo_{0.5}S_x$, in much less quantity though. Therefore, the use of Co and Mo on the design of a bimetallic sulfide leads to a more stable surface that is not easily oxidized, preserving then the sulfide species at the catalyst surface. Besides that, the tertiary sulfide structure

may enhance the activity towards HER, once a better interaction between cobalt and molybdenum is expected and a synergistic effect can be derived.

III.2.2. Electrochemical characterizations

The monometallic and bimetallic sulfides were tested towards the HER by applying the linear sweep voltammetry (LSV) technique in 1 M KOH at 10 mV s^{-1} and results are shown in **Figure III.5a**; while the main graph presents uncompensated polarization curves recorded before any voltammetric cycling in wide range of current density, the inset graph shows iR-drop compensated polarization curves at small values of current density ($|j_{geo}| \leq$ 13 mA cm^{-2}). The bare glassy carbon electrode (GCE) used as substrate for the deposition of catalytic inks was also evaluated and it can be easily seen that it does not present any HER activity, even at -0.5 V vs. RHE. Thus, it is confirmed that it only plays a role as inert electrode substrate and the HER activities verified in the polarization curves are the result of catalysts' activity. On the contrary, MoS_x and CoS_x showed to be active for the reaction, presenting values of overpotential to achieve -10 mA cm^{-2} (η_{10}) equal to 285 and 372 mV, respectively, after iR-compensation. The $Co_{0.5}Mo_{0.5}S_x$ catalyst also presented a better HER activity than the monometallic sulfides, since a current density of -10 mA cm^{-2} was obtained at an overpotential of 172 mV, lower than the value of 241 mV reported by Mukherji *et al.*[103] for $Co_{0.5}Mo_{0.5}S_x$ material synthesized in 48 h of hydrothermal reaction applying L-cysteine as sulfur precursor; these differences on the choice of the sulfur precursor and time of reaction may certainly affect the characteristics of the obtained materials and, consequently, their activities. Other authors have also reported the enhancement of HER activity by the coexistence of cobalt and molybdenum in sulfide-based materials[89, 103]. It has been known for over ten years that edge sites of MoS_2 are very active for the H_2 production by reduction of proton species[5, 149], but when it comes to the HER applied at alkaline media, the availability of protons is extremely reduced. Hence, the additional step of water dissociation becomes relevant for the reaction mechanism at this condition. Cobalt-based species are reported as good catalysts for this additional step[109]; therefore, their presence leads to an acceleration of the Volmer step and their coexistence with molybdenum sulfide results in a synergistic effect as the one verified herein. In the insets of **Figs III.5a and III.5b**, one can observe a cathode current above 0 V vs. RHE which is most likely due to the capacitance of

a such material (for $Co_{0.5}Mo_{0.5}S_x$ a value 22 μF cm^{-2} is obtained). A cyclic voltammogram of $Co_{0.5}Mo_{0.5}S_x$ is presented in **Figure A2**. **Figure III.5b** presents polarization curves obtained with a physical mixture of CoS_x and MoS_x (50 wt.% of each) and it shows a better activity than both monometallic sulfides. It corroborates therefore the idea that each one plays a role in the reaction and together a synergistic effect is obtained. But the $Co_{0.5}Mo_{0.5}S_x$ still performs better than the physical mixture of CoS_x and MoS_x, which is likely in reason of a better interaction between cobalt sulfide and molybdenum sulfide species in the bimetallic compound; a possible electronic effect cannot be discarded though. It can be noticed that the activity trend does not change whatever the normalization of the current densities with mass loading or geometric surface (**Figures III.5b** and **A3**). An additional investigation of Co/Mo ratio effect, based on the quantity of precursors added in the synthesis, on cobalt molybdenum sulfide HER activity was performed. As verified in **Figure A4**, the best result was obtained for equimolar quantities of the metals, i.e., $Co_{0.5}Mo_{0.5}S_x$.

A commercial 40% Pt/C catalyst was also tested in the same conditions to compare the activity of the synthesized sulfides with a benchmarking material for HER. It showed to be much more active than all synthesized materials. For example, as reported in **Table III.2**, to achieve -100 mA cm^{-2}, $Co_{0.5}Mo_{0.5}S_x$ needed an overpotential 168 mV higher than 40% Pt/C. In addition, this last one only needed an overpotential of 46 mV to achieve -10 mA cm^{-2}.

Tafel plot curves, shown in **Figure III.5c**, were constructed by using the same data presented in the inset graph of **Figure III.5a**. It is possible to verify that, although MoS_x presents a Tafel slope lower than Co-containing sulfides, all synthesized transition metal sulfides (TMS) show Tafel slope values much higher than 40% Pt/C. The Tafel slope is a well-established tool to evaluate the kinetics of electrochemical reactions. However, it is important to consider that when the Tafel plot is constructed from LSV data, it is impossible to isolate the influence of charge-transfer kinetics from catalyst resistance issues[29]. There are several works reporting MoS_2 with good electronic conductivity, specifically the 1T-MoS_2 phase[61, 174], however, TMS materials contain commonly semiconductive nature[109, 175].

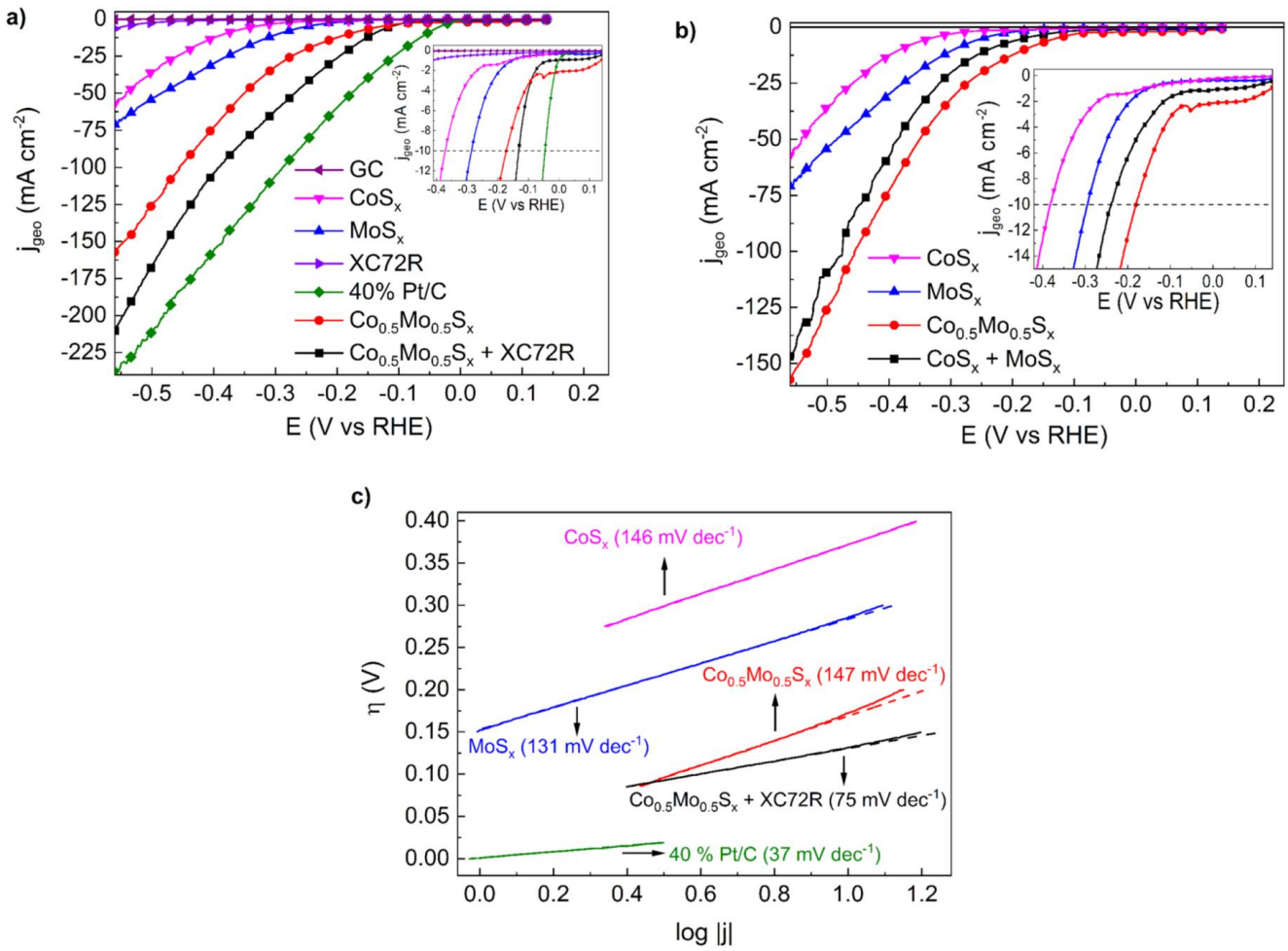

Figure III.5. (a) Ohmic drop uncompensated HER LSV curves in 1 M KOH at 10 mV s^{-1} and 1600 rpm. Inset: Curves after iR-compensation at low current densities window. (b) Polarization curves of monometallic, bimetallic and physical mixed sulfides in 1 M KOH at 10 mV s^{-1} and 1600 rpm without iR-drop correction (c) Tafel plot derived from iR-compensated polarization curves.

Table III.2. Parameters values obtained from LSV analyses in HER region.*

Catalyst	CoS_x	MoS_x	$Co_{0.5}Mo_{0.5}S_x$	$Co_{0.5}Mo_{0.5}S_x$ + XC72R	40% Pt/C
η_{10} (mV)	372	285	172	131	46
η_{100} (mV)	-	-	456	392	288
η_{200} (mV)	-	-	-	547	481
b (mV dec^{-1})	146	131	147	75	37
j_0 (mA cm^{-2})	0.03	0.07	0.43	0.19	0.95

*η_{10}, b and j_0 were obtained after iR-compensation, while η_{100} and η_{200} are related to non-compensated results.

Based on this information, a physical mixture of $Co_{0.5}Mo_{0.5}S_x$ and Carbon Vulcan XC72R, mass ratio of 1:1, was prepared during the catalytic ink formulation and such ink was deposited onto the GCE to be evaluated towards the HER. The total mass loading was maintained, the mass loading of $Co_{0.5}Mo_{0.5}S_x$ was halved when compared to this material used in absence of Carbon Vulcan though. From **Figure III.5a**, one can see that the physical mixture shows onset overpotential similar to $Co_{0.5}Mo_{0.5}S_x$, but the increase of cathodic current promoted by the reduction of potential is more relevant in the presence of Carbon Vulcan; thus, the physical mixture presents higher activity than $Co_{0.5}Mo_{0.5}S_x$. Carbon Vulcan XC72R was also evaluated alone as HER catalyst and showed negligible activity, which discarded any possibility of the activity enhancement, verified by coupling $Co_{0.5}Mo_{0.5}S_x$ and XC72R, be result of a superior catalytic activity coming from the carbon. By evaluating the Tafel plot (**Figure III.5c**), it can be observed that the Tafel slope calculated for $Co_{0.5}Mo_{0.5}S_x$ (~147 mV dec^{-1}) significantly decreases with the addition of Carbon Vulcan (~75 mV dec^{-1}). Therefore, we assume that Carbon Vulcan plays a role as conductive additive by enhancing the electron transport in the electrode. This strategy of adding a carbon-based material into the catalytic ink formulation has already been reported elsewhere[90, 100, 108]. To achieve a current density of -10 mA cm^{-2}, the physical mixture only requested an overpotential of 131 mV after iR-drop compensation. So, this electrocatalyst generated by the deposition of the physical mixture, comprising $Co_{0.5}Mo_{0.5}S_x$ and XC72R, onto GCE is, at least, very competitive with other non-noble-metal-based electrocatalysts, mainly when it comes to unsupported materials and by applying GCE as substrate instead of three-dimensional substrates, e.g., nickel foam and carbon cloth. Although the physical mixture is still less active than 40% Pt/C, the difference of overpotential to achieve -100 ($\Delta\eta_{100}$) and -200 ($\Delta\eta_{200}$) mA cm^{-2} is 104 and 66 mV, respectively. Bearing in mind the cost and, mainly, the earth-abundance factors, the physical mixture appears as a promising candidate to replace Pt-based materials as cathode of anion exchange membrane water electrolyzers (AEMWE), once the $\Delta\eta$ at elevated current densities is small.

Table III.2 reports the values of exchange current densities (j_0) calculated from Tafel plot. At first, it is seen that MoS_x shows a higher exchange current density than CoS_x. Additionally, one may verify that j_0 of both aforementioned catalysts is one order of magnitude lower than for $Co_{0.5}Mo_{0.5}S_x$. This result further confirms the synergistic effect of the existence of both cobalt and molybdenum given that it is known that j_0 is related to the

intrinsic activity of the catalyst. When Carbon Vulcan is added in the $Co_{0.5}Mo_{0.5}S_x$ catalytic ink preparation, j_0 decreases from 0.43 to 0.19 mA cm^{-2}. This decrease to about half of value is coherent because the exchange current density varies linearly with the number of active sites[149], and the mass loading of $Co_{0.5}Mo_{0.5}S_x$ in the GCE containing the physical mixture is half than on the GCE containing only $Co_{0.5}Mo_{0.5}S_x$. It is important to highlight that the previously mentioned linearity accrues from the use of geometrical surface area to normalize the exchange current density. If the surface of active sites would be used instead, no variation of j_0 with mass loading should be expected. Yet, it is interesting to highlight that j_0 calculated for $Co_{0.5}Mo_{0.5}S_x$ is in the same order of magnitude than 40% Pt/C, which reinforces the potential of $Co_{0.5}Mo_{0.5}S_x$ for future applications in AEMWE.

EIS analysis at HER potential (-0.3 V vs RHE) was applied to all sulfide-based electrocatalysts, besides the benchmarking 40% Pt/C, to have deeper comprehension of their activities towards the reaction; such results are present in **Figure III.6a-c**. At first, based on impedance (|Z|) values at high frequencies, where the phase angle is about 0°, the solution resistance (R_s) is lower than 1 Ω cm^2 for all materials reported herein. The Nyquist plot (**Figure III.6a**) evidences an obvious semi-circle shape, which can be associated with hydrogen evolution reaction, for the curves of 40% Pt/C and the physical mixture containing $Co_{0.5}Mo_{0.5}S_x$ and Carbon Vulcan XC72R. According to the diameter of the semi-circles, their charge-transfer resistances (R_{ct}) at η = 300 mV are, approximately, 0.4 and 3.2 Ω cm^2, respectively. Additionally, for the physical mixture this value decays to, approximately, 1.2 Ω cm^2 when 400 mV of overpotential is applied (**Figure III.6d**). Although not complete, it is possible to notice the semi-circle trend for the curve related to CoS_x. The R_{ct} for CoS_x at η = 300 mV cannot be directly inferred from the curve, but by an extrapolation it is expected a value much higher than the one obtained for the physical mixture of cobalt molybdenum sulfide and Carbon Vulcan XC72R. According to the Bode plot (**Figures III.6b,c**), while the maximum of the peak related to HER in the phase angle curve for 40% Pt/C takes place between 100 Hz and 1 kHz, for both CoS_x and the physical mixture it only appears around 10 Hz. However, for the MoS_x electrocatalyst, a noise arises in the EIS measurement around 10 Hz, which may prevent the appearance of the semi-circle trend. This noise also appears around 10 Hz when the EIS is applied at -0.4 V vs RHE (**Figure III.6d-f**), however, due to the shift of the phase angle peak to higher frequencies as result of overpotential increase, at such potential the semi-circle behavior is verified for MoS_x.

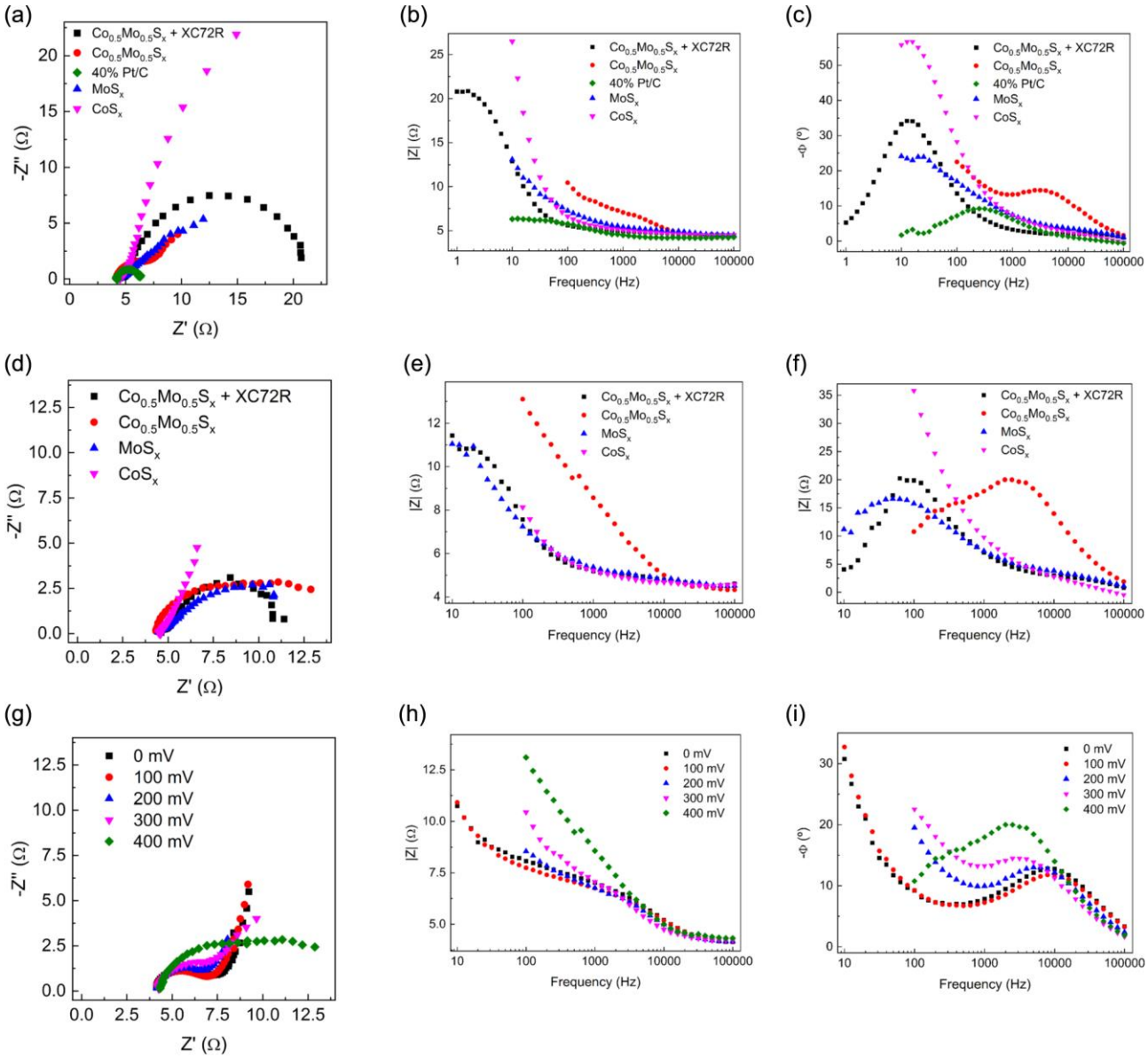

Figure III.6. (a) Nyquist and (b,c) Bode plots obtained from EIS analysis of the electrocatalysts at -0.3 V vs RHE applying an amplitude of 10 mV and probing 10 points per decade. (d) Nyquist and (e,f) Bode plots obtained by the application of 400 mV of overpotential towards the HER in 1 M KOH with an amplitude of 10 mV and 10 points per decade. (g) Nyquist and (h,i) Bode plots obtained for $Co_{0.5}Mo_{0.5}S_x$ catalyst at different overpotentials towards the HER in 1 M KOH with an amplitude of 10 mV and 10 points per decade.

At first sight, one may believe that the small semi-circle at high-frequencies of Nyquist plot (**Figure III.6a**) and its correspondent phase angle peak between 1 and 10 kHz of Bode plot (**Figures III.6b,c**) for $Co_{0.5}Mo_{0.5}S_x$ can be associated with the HER. However, such charge-

transfer process may be verified at various applied DC potentials, including the ones in which HER do not take place, e.g., 0 V vs RHE (**Figure III.6g-i**). Therefore, it is certainly consequence of another process. We suggest that this process is related to the water adsorption and further dissociation, favored by the existence of Co^{2+} species[152], which results in the generation of hydrogen adsorbed intermediate species in the catalyst, mainly in the molybdenum sulfide sites. Such process seems to be more evident in the coexistence of cobalt and molybdenum, which reinforces the bifunctionality of $Co_{0.5}Mo_{0.5}S_x$. The charge transfer process related to HER for $Co_{0.5}Mo_{0.5}S_x$ may not be seen in **Figure III.6a-c** because the points at frequencies lower than 100 Hz do not present a good linearity between current and potential according to their Lissajous diagrams. As seen in **Figure III.6g-i**, at η = 400 mV the HER process becomes evident even at frequencies higher than 100 Hz, although it appears superimposed with the aforementioned process.

III.3. Conclusion

Monometallic (CoS_x and MoS_x) and bimetallic ($Co_{0.5}Mo_{0.5}S_x$) sulfides were hydrothermally synthesized by using sodium diethyldithiocarbamate as sulfurizing agent, a non-conventional precursor. Disulfides, *i.e.*, CoS_2 and MoS_2, were the major phases obtained for each monometallic catalyst, in accordance with the stoichiometry applied in the syntheses. Although, the XRD analysis showed the presence of MoS_2 and CoS phases for the $Co_{0.5}Mo_{0.5}S_x$, XPS results revealed the existence of a tertiary cobalt molybdenum sulfide at the surface. Besides that, MoS_x and CoS_x showed to be more easily oxidized than $Co_{0.5}Mo_{0.5}S_x$, therefore, the interaction of cobalt- and molybdenum-based phases resulted in the prevention of material's oxidation. The monometallic sulfides showed to be active for the HER, but the use of both metals led to a superior activity as result of a synergistic effect, as evidenced by the exchange current density calculated values. EIS results exposed a faradaic process for $Co_{0.5}Mo_{0.5}S_x$ which was absent for CoS_x and MoS_x. This process is likely the responsible for accelerating the HER, and we attributed it to the water dissociation step. Carbon Vulcan (XC72R) was physically mixed to $Co_{0.5}Mo_{0.5}S_x$ in an attempt of enhancing the electronic conductivity. Polarization analysis showed the increase of HER kinetics with

this strategy obtaining η_{10} = 131 mV and reducing the Tafel slope in half of value. Noteworthy, in order to achieve a current density of 200 mA cm^{-2}, the physical mixture only requested an overpotential 66 mV higher than a commercial 40% Pt/C catalyst. Considering the earth-abundance and cost features of both materials, the aforementioned physical mixture emerges as an interesting candidate to be tested as cathode catalyst in an AEMWE.

Appendix A. Supporting Information Chapter III

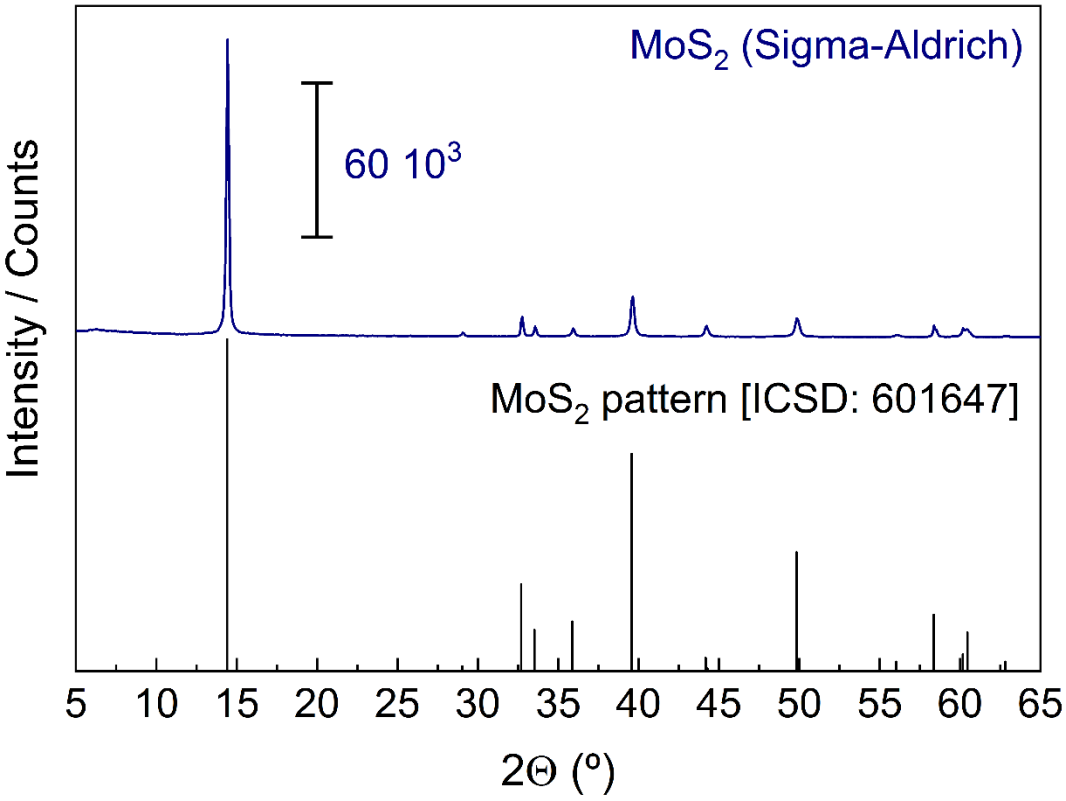

Figure A1. *X-ray diffractogram of a commercial MoS_2 powder supplied by Sigma-Aldrich.*

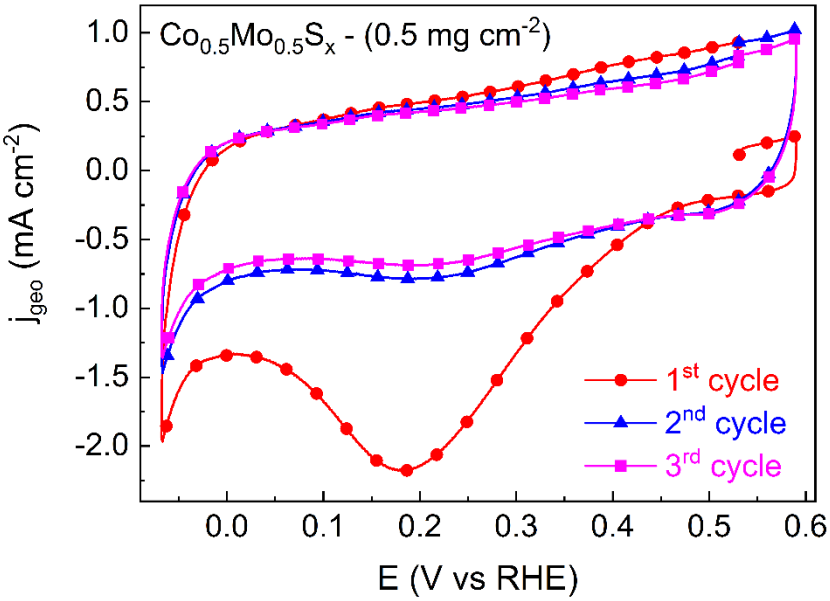

Figure A2. *Cyclic voltammetry registered for $Co_{0.5}Mo_{0.5}S_x$ (0.5 mg cm^{-2}) in 1 M KOH at 10 mV s^{-1}. It can be noticed an important variation between the first cycle and the following ones. This modification, which is probably due to the surface modification through the faradaic contribution (first cycle), affects the capacitive properties of electrode material. The capacitance was found to be 22 μF cm^{-2} after surface stabilization (third cycle).*

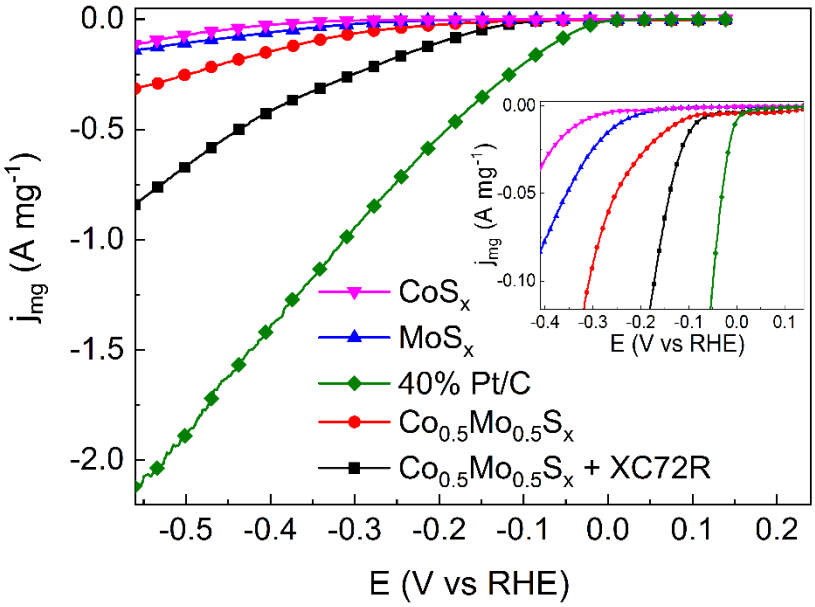

Figure A3. *Polarization curves of monometallic, bimetallic, and physical mixed sulfides in 1 M KOH at 10 mV s^{-1} without iR-drop correction normalized with mass loading. Inset: Ohmic-drop compensated curves at lower cathodic current density region.*

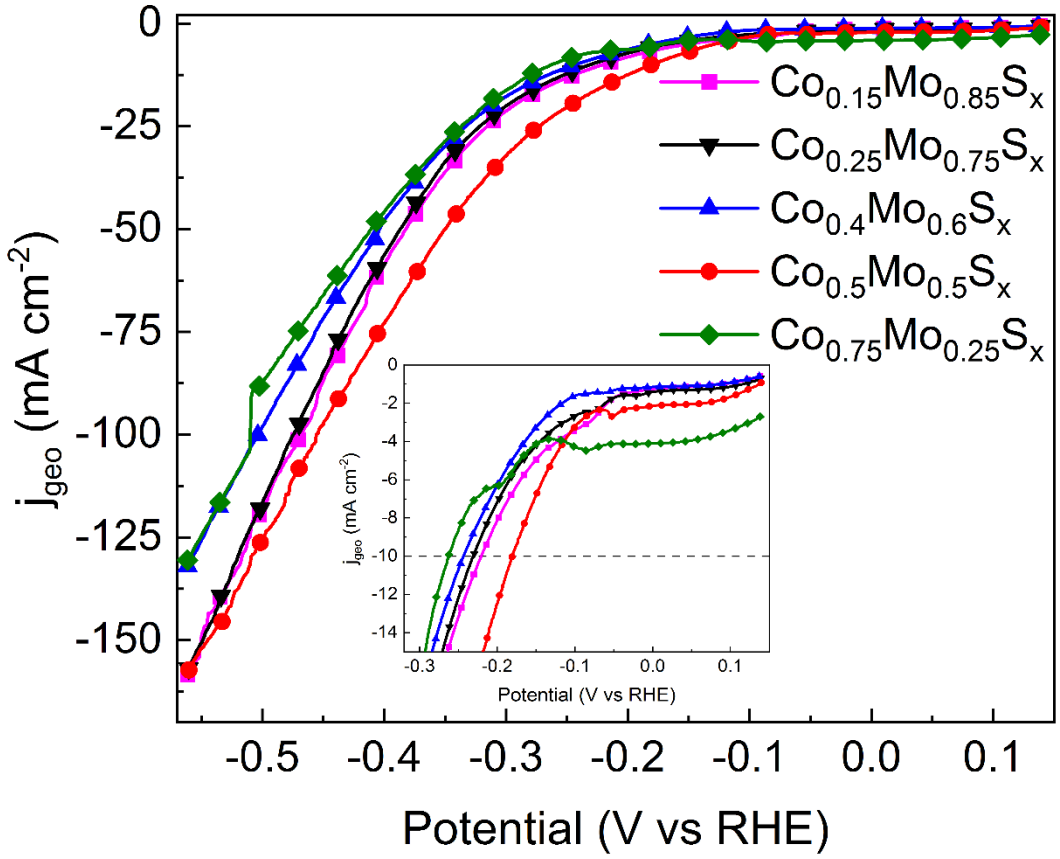

Figure A4. *Uncompensated polarization curves of cobalt molybdenum sulfides containing different Co:Mo compositions in 1 M KOH at 10 mV s^{-1}.*

Chapter IV. A Step Forward: Hydrogen Production on Cobalt Molybdenum Sulfide Electrocatalyst in Anion Exchange Membrane Water Electrolyzer

This chapter is based on the following publication: *"A Step Forward: Hydrogen Production on Cobalt Molybdenum Sulfide Electrocatalyst in Anion Exchange Membrane Water Electrolyzer"*. C.V.M. Inocêncio, F. Fouda-Onana, J. Rosseau, N. Guignard, T. Napporn, C. Morais, K.B. Kokoh, ACS Appl. Energy Mater. **2022**, 5, 10396.

https://doi.org/10.1021/acsaem.2c02270

ABSTRACT

Cobalt molybdenum sulfide ($Co_{0.5}Mo_{0.5}S_x$) was evaluated, as an alternative cathode catalyst for hydrogen large scale production in an anion exchange membrane water electrolyzer (AEMWE). Performance testing in a $Co_{0.5}Mo_{0.5}S_x$//Ir single cell fed with 0.1 mol L^{-1} KOH exhibited the best activity reported to date for transition metal sulfide cathodes in alkaline media. The aforementioned cell presented good stability during 40 h of operation at 2 V; in addition, it had most of its current density degradation recovered in the beginning of the subsequent 10 h interval.

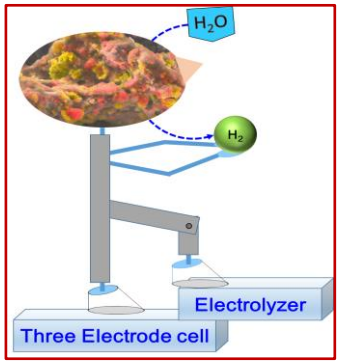

Hydrogen (H_2) is expected to play an important role to enable the energy transition to clean energy since its oxidation leads to the release of energy and only generates water as a byproduct[4]. In contrast, most of industrial hydrogen production still utilizes fossil sources as feedstock[11, 140]. Therefore, to really achieve the goal of a carbon footprint decrease, while hydrogen acts as energy carrier, alternative processes for its production must be further developed. Water electrolysis emerges as the most promising process for this purpose once it demands energy, which can be derived from renewable sources, e.g., wind and solar, to split water toward high purity hydrogen and oxygen in the cathode and anode compartments, respectively[4, 141-142]. Water electrolyzers may exist in several configurations. Specifically, the one known as the anion exchange membrane water electrolyzer (AEMWE), though still in research stages, has the potential to operate at high current densities; in addition, it avoids the use of platinum-group metal (PGM) catalysts[176]. These are both very relevant features. Hence, the goal of this work is to propose new electrocatalysts to be applied as cathodes in AEMWEs.

It was reported, by theoretical calculations and experimental studies, that transition metal sulfides (TMS) are effective catalysts for the hydrogen evolution reaction (HER) when the sulfur atoms are present at the edge of the structure[54]. Hence this group, (Mo, Co)-based sulfides, was synthesized by a methodology described recently[177].

The results obtained for monometallic and bimetallic cobalt- and molybdenum-based sulfides are presented herein. The main phases obtained for monometallic catalysts were disulfides, i.e., CoS_2 and 2H-MoS_2, which is in accordance with the stoichiometry applied during their syntheses. The bimetallic sulfide consisted mostly of CoS and MoS_2 hexagonal phases, though its surface characterization also unveiled the existence of a sulfide structure containing both cobalt and molybdenum. Furthermore, it was noticed that both molybdenum disulfide phases for the referenced Mo-containing catalysts were defect-rich; this feature was revealed to be very relevant for the enhancement of MoS_2 activity toward the hydrogen evolution reaction (HER)[97]. A deeper investigation, aided by XRD, Raman spectroscopy, TEM, HAADF-STEM, and XPS, and interpretation of the physicochemical nature of the electrocatalysts was previously reported and may be found in a previous publication[177].

In addition, the elemental composition of $Co_{0.5}Mo_{0.5}S_x$ was investigated by ICP-OES and XPS analyses, mainly to ascertain if the Co:Mo atomic ratio followed the stoichiometry applied in the synthesis; the results are summarized in **Table IV.1**. One may notice that, according to ICP-OES data, the Co:Mo ratio agreed with targeted values, i.e., the equimolarity of metals was preserved. Likewise, the S:Mo ratio around 3 also indicated a coherence in the coexistence of CoS and MoS_2 phases. A different proportionality was obtained by XPS quantitative analysis, but nevertheless, the results are not necessarily antagonistic as XPS results are restricted to its surface while ICP-OES provides a global information on the sample. Therefore, it may be stated that the $Co_{0.5}Mo_{0.5}S_x$ surface is poorer in cobalt than its bulk. The former statement was confirmed by Raman spectroscopy, which is also restricted to the surface, although this technique can probe deeper regions of the sample than XPS. Indeed, in the catalyst's Raman spectrum (**Figure B1**) bands associated with tertiary sulfides were identified, but no band related to CoS_x species could be detected, although the CoS phase was clearly identified in $Co_{0.5}Mo_{0.5}S_x$.

Table IV.1. *Atomic ratio of elements in $Co_{0.5}Mo_{0.5}S_x$, normalized with the molybdenum amount obtained by ICP-OES and XPS techniques.*

Element ratio*	ICP-OES	XPS
$\frac{n_{Co}}{n_{Mo}}$	1.09	0.15
$\frac{n_{S}}{n_{Mo}}$	3.07	1.74

*n_X = quantity, in mol, of element "X".

The electrocatalysts' performance for HER was first evaluated in a three-electrode configuration at room temperature; it used a homemade cell produced with Kel-F polymer to avoid Pyrex glass cell corrosion in an alkaline medium. A glassy carbon slab and $Hg/HgO/HO^-$ were used as counter and reference electrodes, respectively, while a rotating disk electrode (RDE) containing a glassy carbon substrate, onto which the cathode catalyst was deposited, was employed as a working electrode. After a simple conversion, results were plotted in potential referenced to the reversible hydrogen electrode (RHE); to do this, reference electrode calibration was accomplished. Further details concerning the cell configuration, ink preparation, and reference calibration are provided in the **Section II.3.2.1**.

Polarization curves (**Figure IV.1**) were obtained by LSV analysis in N_2-saturated 1 M KOH at 10 mV s^{-1} and 1 600 rpm. Molybdenum sulfide exhibited better HER performance than cobalt sulfide throughout the applied potential range. Indeed, molybdenum sulfide has been pointed out as a promising HER catalyst by theoretical and experimental studies over the past two decades[45, 54, 149]. However, its activity is reduced once acidic electrolytes are replaced by alkaline ones because of its poor water dissociation ability as well as the strong adsorption of generated hydroxyl to its surface[178]. Nonetheless, these characteristics may be tuned by the incorporation of Co-based species to derive a catalyst with superior activity[103, 178]. The synergistic effect existing in the bimetallic sulfide is highlighted in the polarization curve (**Figure IV.1**) as it exhibits less negative onset potential, in addition to generating more than twice the current density of monometallic sulfides at −0.56 V vs RHE. To reach 10 mA cm^{-2}, the overpotential was 181 mV, which set $Co_{0.5}Mo_{0.5}S_x$ among the best electrocatalysts for HER in alkaline medium, especially the unsupported ones. Different Co:Mo ratios were previously tested, and the equimolar one showed the best result[177].

Due to the promising character of $Co_{0.5}Mo_{0.5}S_x$ as an earth-abundant cathode for water electrolysis, it was further tested in an AEMWE configuration. The activity of monometallic sulfides was also investigated to evaluate the relevance of the bimetallic composition. Sustainion® X37-50 grade RT (Dioxide Material) and Ir black (Sigma-Aldrich), with mass loading of about 2 mg cm^{-2}, were used as an anion exchange membrane and anode for all measurements. Despite iridium being a scarce element and a noble metal, it has been widely used in water electrolyzers[179-181], and therefore, it plays a role herein as a reference anode to evaluate the cathode's activity, the main goal of this chapter.

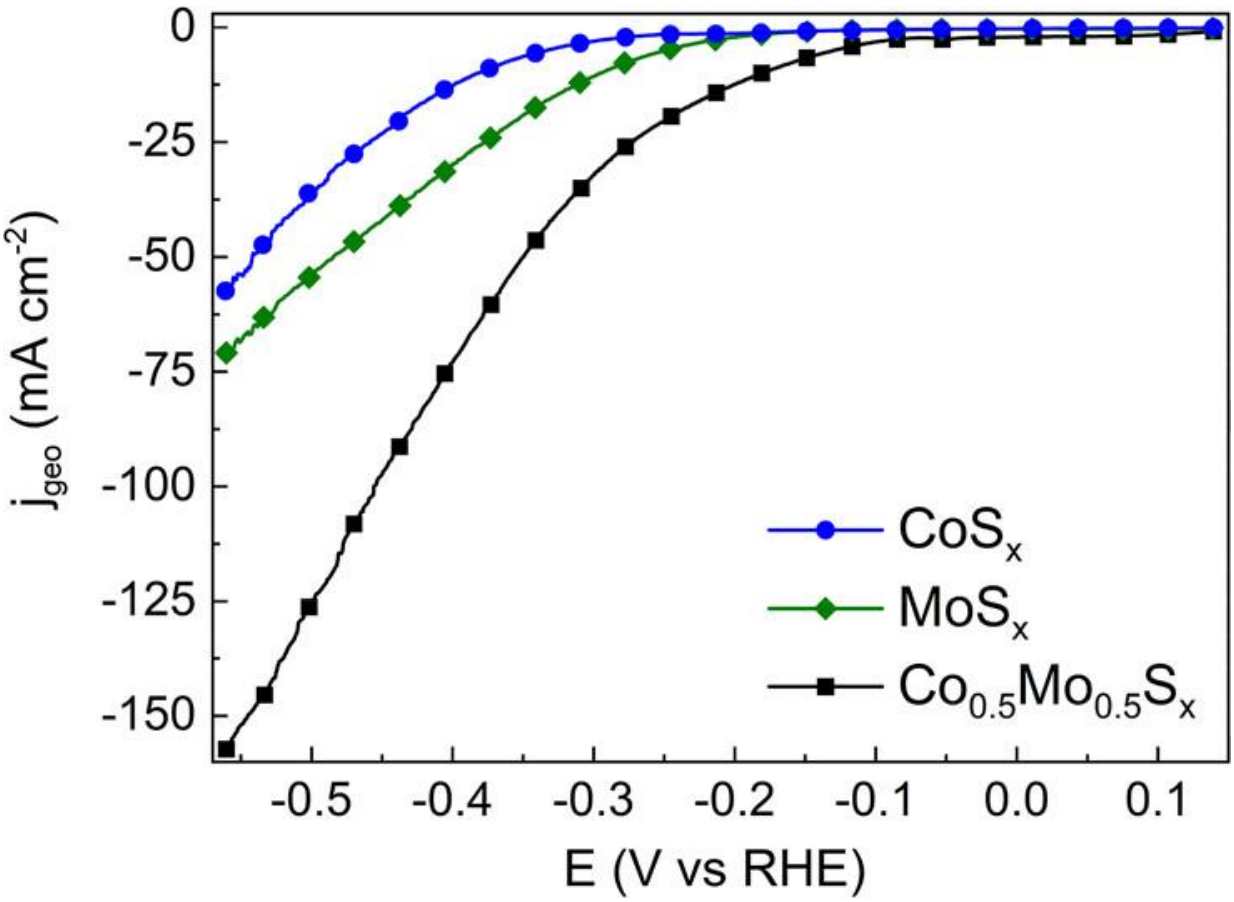

Figure IV.1. *Polarization curves acquired with RDE system (1 600 rpm) in N2-saturated 1 mol L^{-1} KOH at 10 mV s^{-1}, and room temperature.*

Polarization curves, presented in **Figure IV.2**, were recorded at 50 °C by applying a 10 mV s^{-1} scan rate in an AEMWE cell, 1.8 cm^2 electrodes' geometrical surface area, fed with 2 mL min^{-1} of 0.1 M KOH. More experimental details are given in **Section II.3.2.2**. At a low current density, between 0 and 0.1 A cm^{-2}, CoSx presented the highest activity. It may be related to its superior water dissociation ability when compared to Mo-based sulfides, though the same trend was not verified in the three-electrode cell configuration. Conversely, in the region where polarization curves assume a linear profile, i.e., at high current densities, CoS_x becomes less active than molybdenum-based catalysts. In fact, polarization profiles of MoS_x and $Co_{0.5}Mo_{0.5}S_x$ are very similar, and the major difference comes from the onset voltage of water splitting, lower for the bimetallic sulfide. While the similarity is prone to be a consequence of the $Co_{0.5}Mo_{0.5}S_x$ surface being rich in molybdenum, the difference probably arises from faster water dissociation promoted by cobalt species. The cell composed by $Co_{0.5}Mo_{0.5}S_x$ and Ir black as cathode and anode ($Co_{0.5}Mo_{0.5}S_x$//Ir), respectively, achieved ca. 1.2 A cm^{-2} at 2 V; a current density about 28% higher than the one obtained once $Co_{0.5}Mo_{0.5}S_x$

was replaced by MoS_x. A comparison of activity normalized by cathode mass can be verified in **Figure B2**.

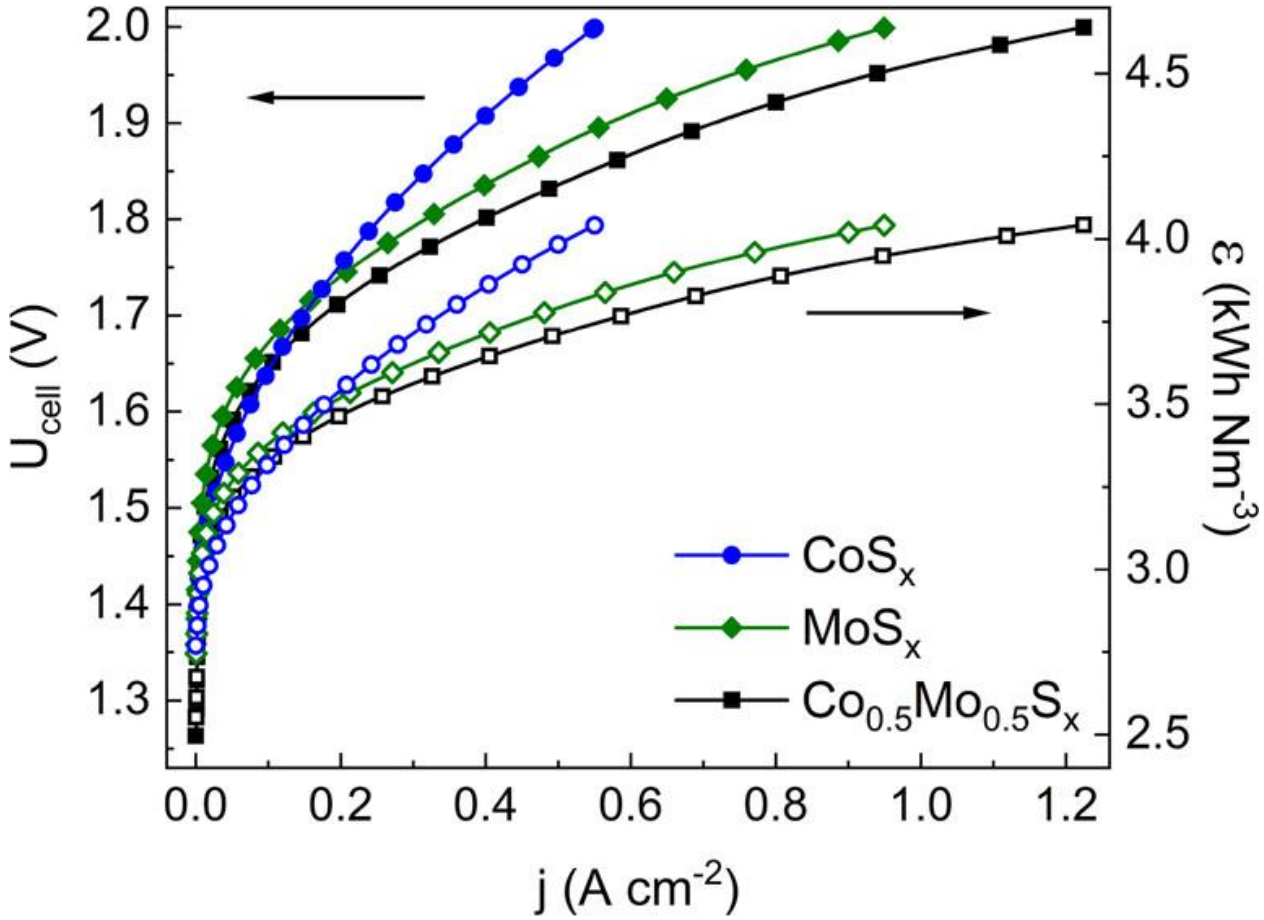

Figure IV.2. *Polarization (left) and specific energy consumption (right) curves obtained from analysis in an AEMWE device fed by 0.1 M KOH. Ir black and Sustainion® X37-50 were applied as anode catalyst and membrane, respectively, for all measurements.*

To the best of our knowledge, there are only two articles reporting the use of TMS materials as cathode of AEMWE, specifically Co-[180, 182] and Ni-based[180] sulfides. At 2 V, Guo *et al.*[180] reported a current density about 0.5 A cm^{-2} for the Ni–Co–S//IrO_2 configuration operated at 50 °C, while the value obtained by Park *et al.*[182] was 0.431 A cm^{-2} for Co_3S_4//$Cu_{0.81}Co_{2.19}O_4$ cell; both systems were fed with 1 M KOH. Both results revealed a performance lower than those measured in this work with a KOH concentration 10-fold diluted, i.e., $Co_{0.5}Mo_{0.5}S_x$ (or MoS_x)//Ir systems. Although different metal sulfides have been investigated as HER catalysts, molybdenum sulfide is the most representative one and has been widely researched as a PGM-free alternative catalyst during the last three decades[4]. Despite that,

the application of Mo-based sulfides electrocatalysts in the cathodic compartment of AEMWE device is reported for the first time herein.

Ni-containing materials for AEMWE were also investigated using 0.1 M KOH concentration for increasing the ionic conductivity. Under conditions that are the same as ours (50 °C and Ir as anode), current densities of 0.5 and 1 A cm^{-2} at 2 V were obtained with NiMo/C and NiCu MMO/C cathodes, respectively[179, 181]. Interestingly, both cells were also tested with a higher electrolytic concentration (1 M KOH), which led to the best performance. Although the increase of electrolyte concentration boosts cell performance, it brings technological disadvantages, and therefore, the goal is, in fact, to reduce it until the technology reaches maturity as verified for proton exchange membrane water electrolyzers (PEMWEs), which are only fed with water[176]. So far, most studies in AEMWE operate with 1 M KOH feeding[183], making the result reported herein even more relevant since an excellent cell performance was obtained with a KOH concentration 10-fold lower than those commonly reported. **Table IV.2** summarizes the performance of the mentioned AEMWE cells.

Table IV.2. *Performance comparison of different AEMWE cells at 2 V and operated at 50 ºC.*

Cathode	Anode	j (A cm^{-2})	KOH concentration (mol L^{-1})	Reference
CoS_x	Ir	0.55	0.1	This work
MoS_x	Ir	0.95	0.1	This work
$Co_{0.5}Mo_{0.5}S_x$	Ir	1.22	0.1	This work
NiCu MMO/C	Ir	1.0	0.1	179
Ni-Co-S	IrO_2	0.5	1.0	180
NiMo/C	Ir	0.5	0.1	181
Co_3S_4	$Cu_{0.81}Co_{2.19}O_4$	0.431	1.0	182

Figure IV.2 also reports values of specific energy consumption derived from polarization curves. Genuinely, such a parameter varies with cell voltage (U_{cell}); however, current density has a linear relation to quantity of hydrogen produced, assuming 100% of faradaic efficiency, and the function $U_{cell}(j)$ depends on the applied catalyst. Therefore, by assuming an operational consumption of 4 kWh per Nm^{-3} of H_2, for example, the use of $Co_{0.5}Mo_{0.5}S_x$ as a cathode would result in a H_2 production of about 27% and 112% higher than those of

MoS_x and CoS_x, respectively. These differences would certainly have a huge impact on hydrogen market price.

Undoubtedly, stability, which is still a bottleneck in AEMWE applications[176], is one of the main aspects to be evaluated in cell performance since the economical suitability of the process depends on its long-term operation. Hence, such a feature was evaluated for a $Co_{0.5}Mo_{0.5}S_x$//Ir cell by applying 2 V for 40 h. Stability analysis was divided in different steps. The 40 h were uniformly prorated in 4 intervals, and polarization analyses at 5 mV s^{-1} were performed before the stability test and after each interval. Results associated with the 4 intervals are depicted in **Figure IV.3,** while polarization curves are exhibited in **Figure B3**. In the $j \times t$ graph (**Figure IV.3a**), the current density decay profile for the $Co_{0.5}Mo_{0.5}S_x$//Ir electrolysis cell can be observed. Most of the current density lost during each interval is recovered in the beginning of the following one. An investigation of Ni–Co–S//IrO_2 stability was performed by Guo *et al.*[180] by applying 0.4 A cm^{-2} for 8 h. Regrettably, no numerical value nor discussion was provided by the authors, and the resultant graph containing a large cell voltage scale makes data analysis difficult. Furthermore, IrO_2 is deposited onto carbon paper, whereas carbon-based materials are known for being unstable in the anodic compartment due to corrosion issues. The system proposed by Park *et al.*[182] (Co_3S_4//$Cu_{0.81}Co_{2.19}O_4$) was submitted to a 12 h stability test at 500 mA cm^{-2} (applied continuously). The authors reported a good stability once an initial cell voltage of 2 V was registered and about 0.05 V of increase was verified during operation.

Figure IV.3b provides further details on current density decay during $Co_{0.5}Mo_{0.5}S_x$//Ir stability testing. As shown, the absolute value of current density decay was, approximately, the same during each interval, about 70 mA cm^{-2}. However, part of this decay is reversible from one interval to another, and the reversibility percentage varied in each interval; the percentage of irreversible current decay diminished during the first three intervals and was maintained below 10% from the third interval onward. Irreversible activity losses are likely related to catalysts degradation, but modifications of cell components may not be discarded though. The reversible decay is credited to the blocking of either catalyst surface or fluids channels due to hydrogen bubbles formation; these bubbles can be released once the 2 V application is interrupted to perform the LSV measurement.

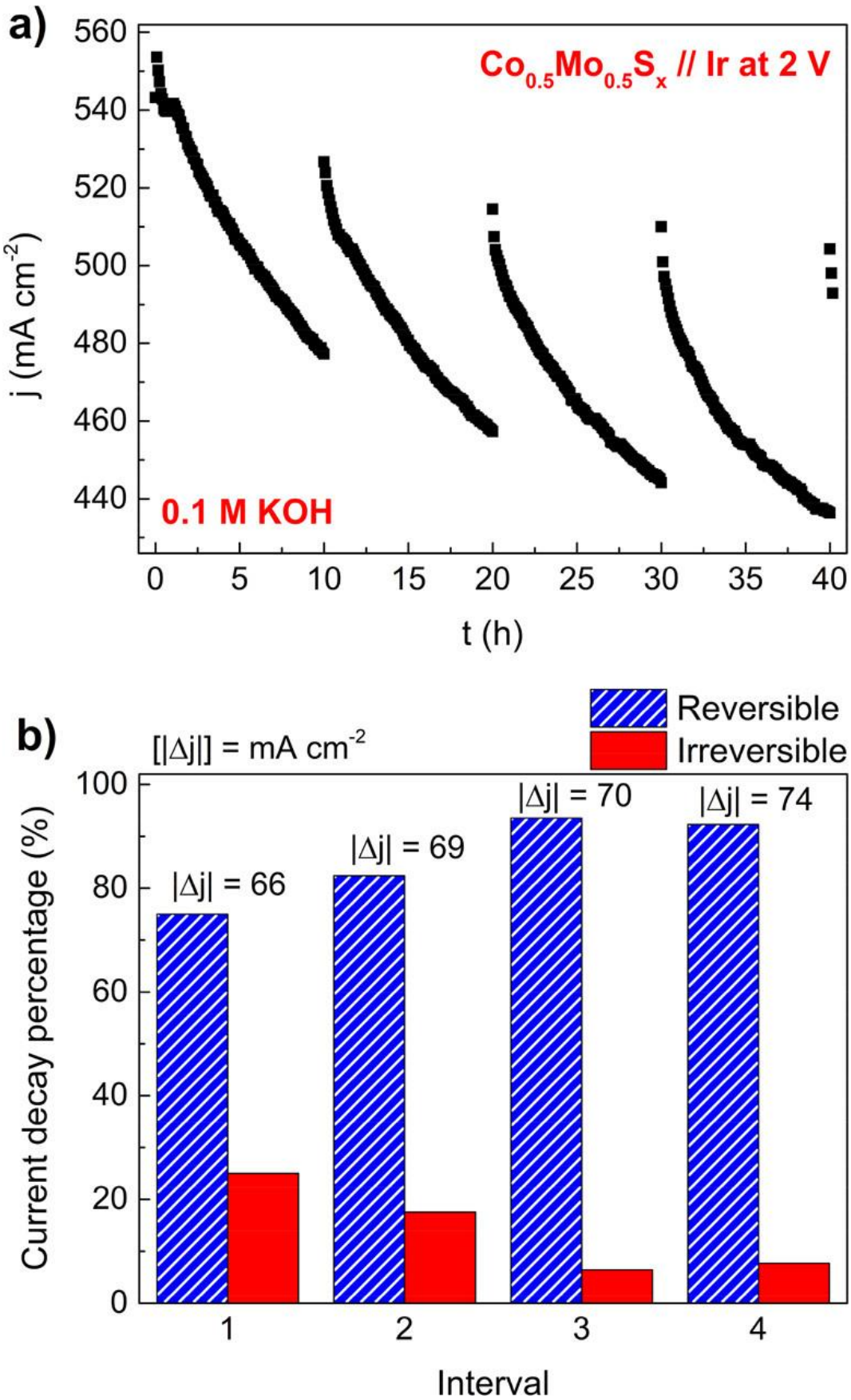

Figure IV.3. *(a) Chronoamperometry analysis applied to the $Co_{0.5}Mo_{0.5}S_x$//Ir system, fed by 0.1 M KOH, at 2 V during 40 h, divided in four intervals of 10 h. (b) Details of current density decay during stability testing and its reversibility aspect.*

Raman spectroscopy and field emission gun scanning electron microscopy (FEG-SEM) analyses of $Co_{0.5}Mo_{0.5}S_x$, submitted to the 40 h test, were performed to comprehend the irreversible activity decay; results are presented in **Figure IV.4**. One may see that Raman spectra (**Figure IV.4a**) were obtained by probing different points of GDE, comprising both the center and corner of MEA. Another $Co_{0.5}Mo_{0.5}S_x$//Ir MEA, which was not submitted to any test, was prepared following the same protocol to provide information on $Co_{0.5}Mo_{0.5}S_x$ GDE before reaction; its Raman spectra are exhibited in **Figure B4**. In general, Raman spectra before and after electrolysis are very similar. It is verified that the characteristic E^1_{2g} and A^1_g phonon modes[177] of MoS_2 were preserved during the reaction. The major difference comes from the appearance of a band at 691 cm^{-1} in one corner spectrum after reaction. This may be associated with the oxidation of cobalt[184] after the MEA was exposed to air. The application of the energy dispersive X-ray spectroscopy (EDS) technique during FEG-SEM analyses provided deeper information (**Figure IV.4b-e**). **Figures IV.4c,e** unveiled the occurrence of segregation between cobalt and molybdenum during the stability test; **Figure B5** illustrates the good dispersion before reaction. This segregation is likely the irreversible activity loss reason, once superior HER activity of cobalt molybdenum sulfide arises from its bifunctionality[177].

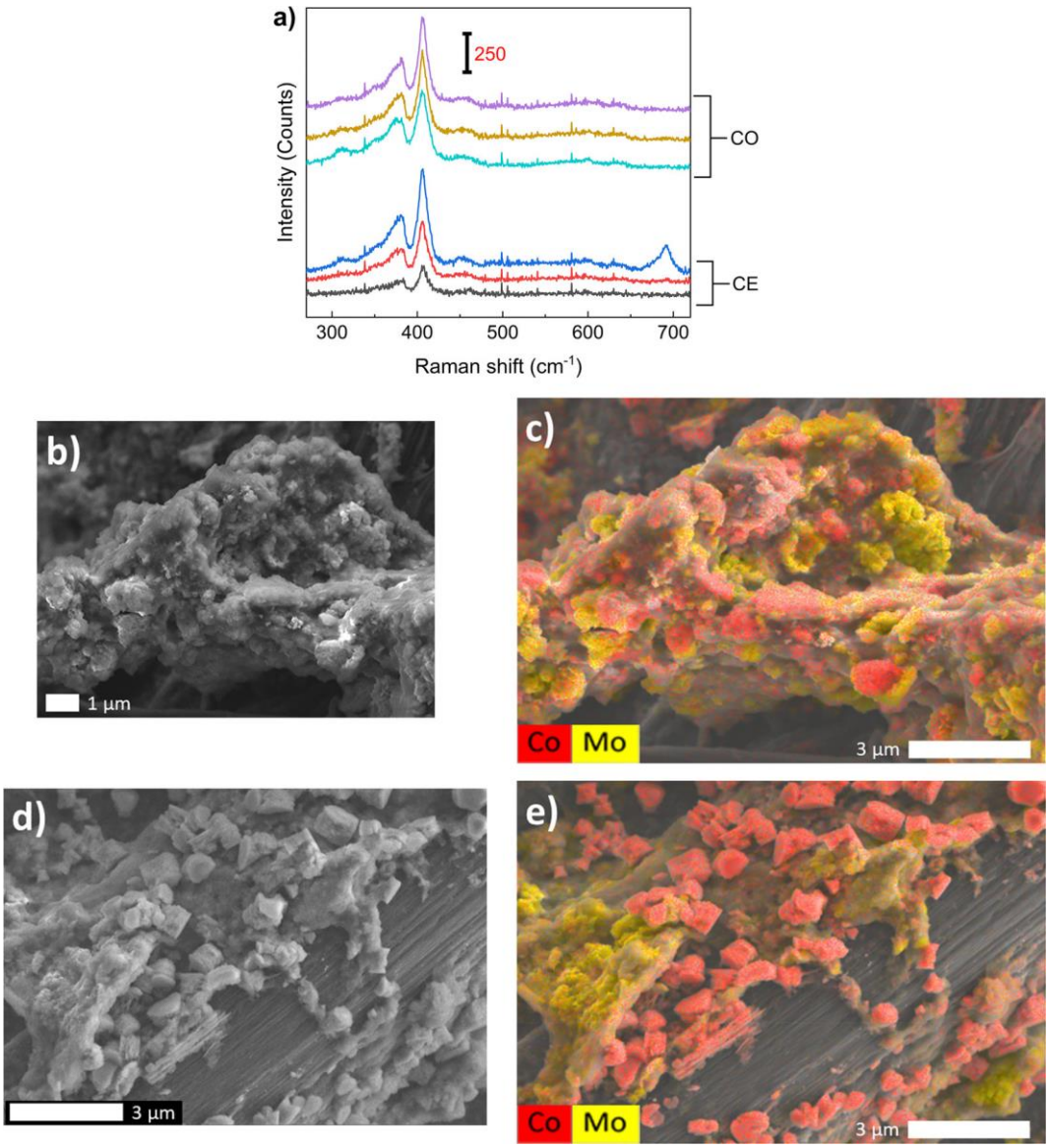

Figure IV.4. *(a) Raman spectroscopy of aged $Co_{0.5}Mo_{0.5}S_x$ applied to different points of the GDE. "CO" and "CE" indicate positions at the corner and center of GDE, respectively. (b, d) FEG-SEM images of aged $Co_{0.5}Mo_{0.5}S_x$ recorded in secondary electron mode. (c, e) Cobalt and molybdenum elemental mapping obtained by EDS technique.*

In summary, the $Co_{0.5}Mo_{0.5}S_x$//Ir cell delivered 1.22 A cm^{-2} at 2 V in LSV analysis, a value higher than any other TMS cathode. This cell also showed good stability during 40 h of operation at 2 V with current density degradation of ca. 1.4%/h. It is noteworthy that most of such degradation could be recovered by releasing the bubbles from the electrolyzer once the 2 V application is interrupted; 75% was recovered after the first 10 h, while from 30 h onward this recovery surpassed 90%. The FEG-SEM technique demonstrated that the small irreversible activity loss arose from cobalt segregation during the HER process. Results

presented herein become even more relevant when considering that the AEMWE cell was fed with 0.1 M KOH in electrochemical analyzes, 10 times lower than usually applied in the literature.

Appendix B. Supporting Information Chapter IV

Raman spectrum of $Co_{0.5}Mo_{0.5}S_x$ catalyst powder:

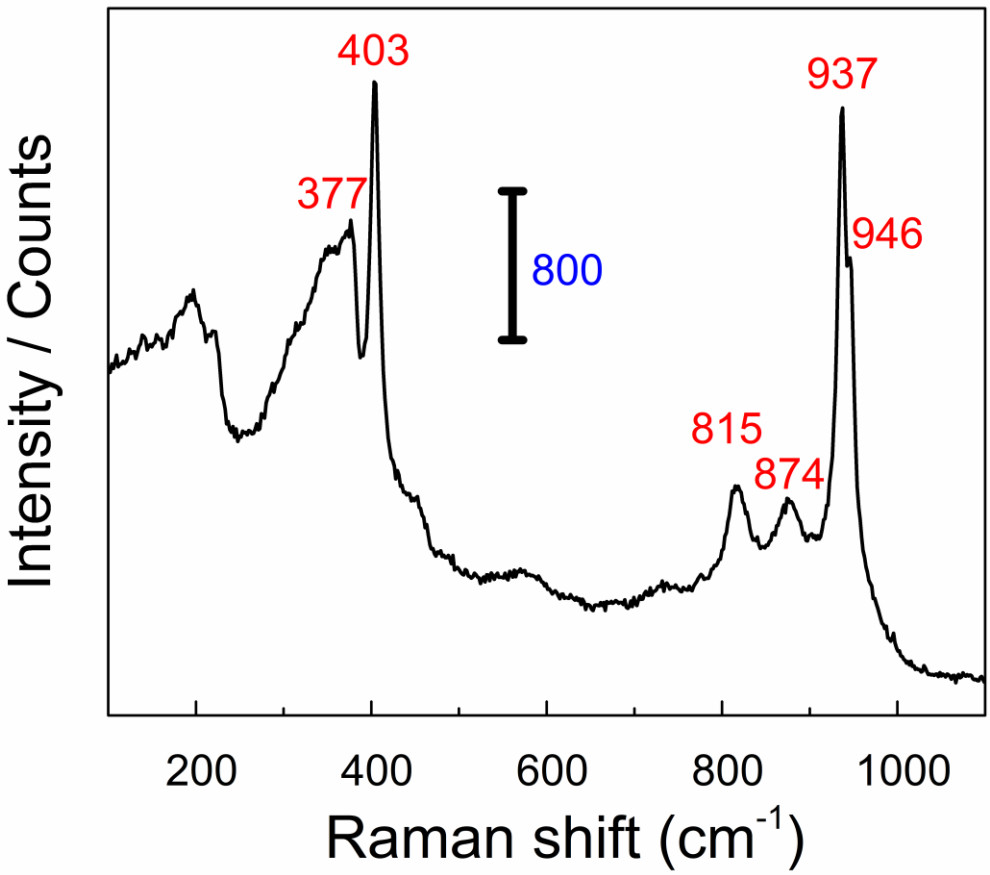

Figure B1. *Raman spectrum of $Co_{0.5}Mo_{0.5}S_x$ powder.*

Performance test result with mass loading normalization:

Although the aim during cathode deposition was to obtain a mass loading equal 3.5 mg cm^{-2}, this value can suffer experimental deviation, which is natural in the spray-coating method. As verified in **Table II.3**, each GDE cathode had a different mass loading. Once $Co_{0.5}Mo_{0.5}S_x$ mass loading was the highest one, **Figure IV.2** was replotted but with mass loading normalization, as may be seen in **Figure B2**, in order to elucidate that its highest activity does not accrue from its higher quantity in the analysis.

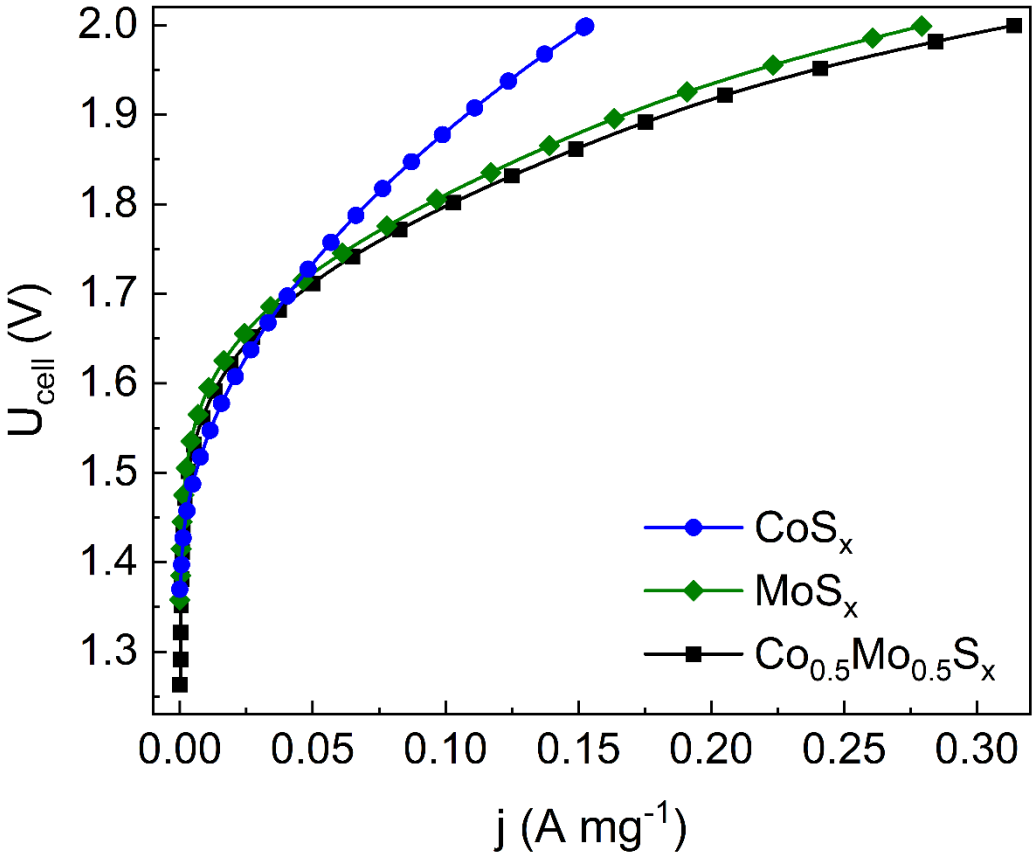

Figure B2. *Mass loading normalized polarization curves obtained from analysis in AEMWE device at 50 °C fed by 0.1 M KOH. Ir black and Sustainion® X37-50 were applied as anode catalyst and membrane, respectively, for all measurements.*

Polarization curves recorded during stability test:

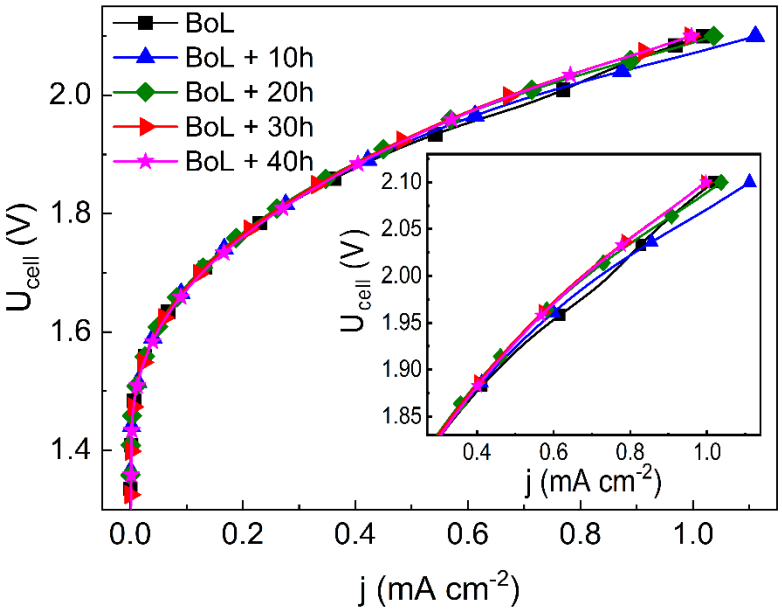

Figure B3. *Polarization curves, at 5 mV s^{-1}, obtained before and after each chronoamperometry interval of stability test. BoL = "Beginning of life", i.e., fresh $Co_{0.5}Mo_{0.5}S_x$.*

Raman spectra of fresh $Co_{0.5}Mo_{0.5}S_x$ GDE:

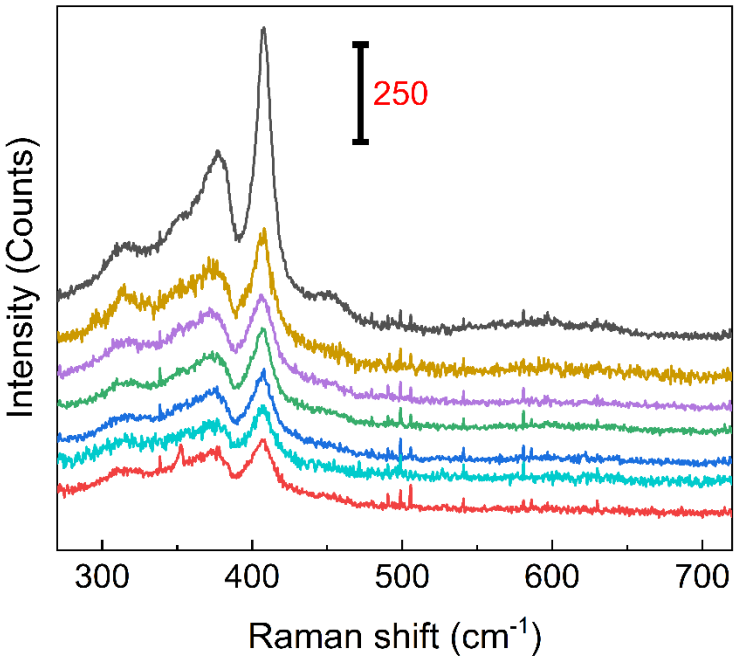

Figure B4. *Raman spectra of fresh $Co_{0.5}Mo_{0.5}S_x$ GDE probed at both center and corner of MEA.*

Cobalt and molybdenum elemental mapping for a fresh $Co_{0.5}Mo_{0.5}S_x$ GDE:

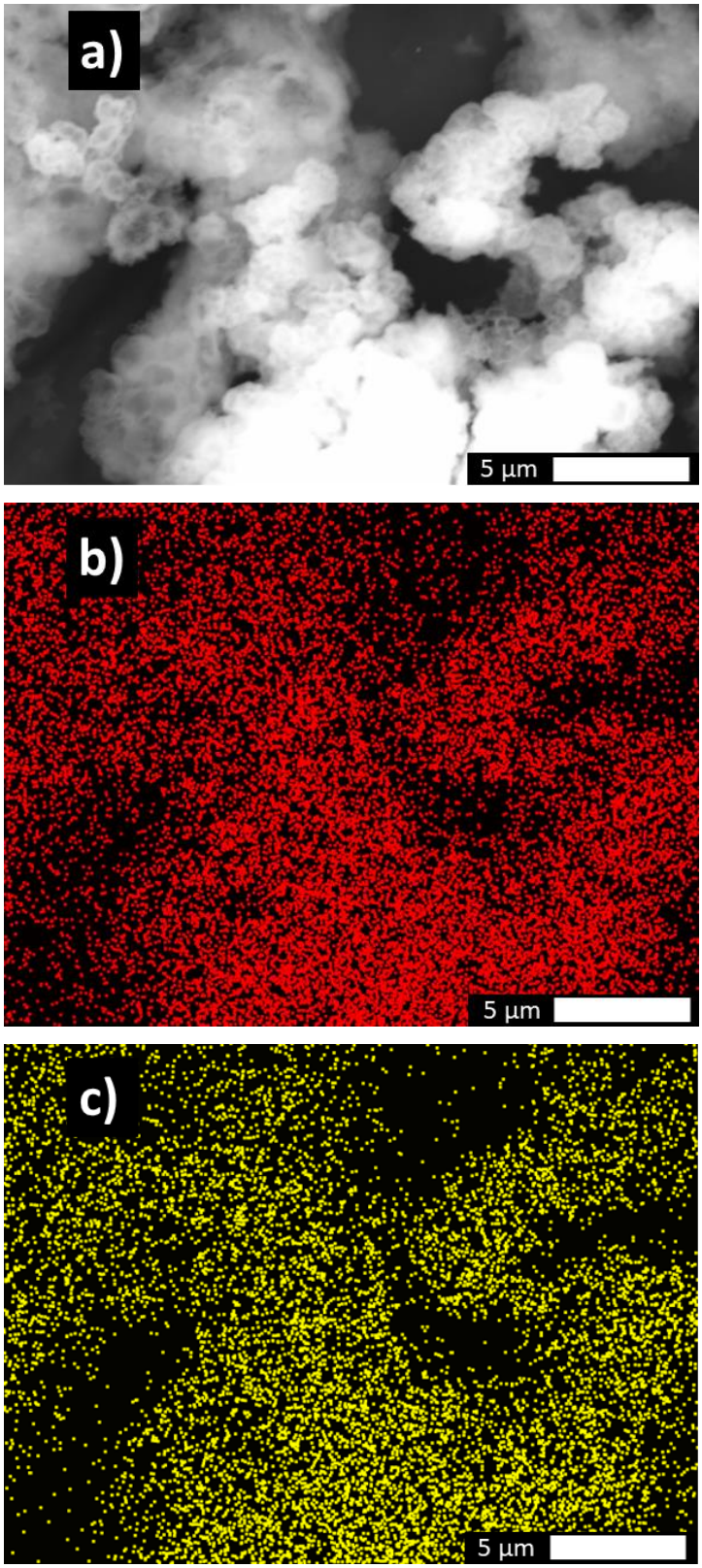

Figure B5. *a) FEG-SEM image of a fresh $Co_{0.5}Mo_{0.5}S_x$ recorded in backscattered electron mode. b) Cobalt and c) Molybdenum elemental mapping obtained by the application of EDS analysis.*

Chapter V: HER Activity of Nickel Molybdenum Sulfide Electrocatalyst as Function of the Ionomer in the Ink Formulation

This chapter is based on the following publication: *"HER Activity of Nickel Molybdenum Sulfide Electrocatalyst as Function of the Ionomer in the Ink Formulation"*. C.V.M. Inocêncio, J. Rosseau, N. Guignard, C. Canaff, S. Morisset, T. Napporn, C. Morais, K.B. Kokoh, Int. J. Hydrog. Energy, 2022. Accepted.

https://doi.org/10.1016/j.ijhydene.2022.10.138

Abstract

Transition metal sulfides (NiS_x, MoS_x and $Ni_{0.5}Mo_{0.5}S_x$) are synthesized and have their HER performance evaluated in three-electrode cell setup by applying LSV analyzes in 1 M KOH. XRD, Raman, TEM and XPS characterizations are applied aiming to correlate physicochemical properties/electrocatalytic activity. It is evidenced a synergistic effect in which nickel oxide, present in the surface of $Ni_{0.5}Mo_{0.5}S_x$, accelerates the water dissociation, while molybdenum sulfide catalyzes the reduction of adsorbed hydrogen species. When physically mixed with Carbon Vulcan, $Ni_{0.5}Mo_{0.5}S_x$ only needs 60 mV higher overpotential to achieve -200 mA cm^{-2} than 40 % Pt/C. Furthermore, $Ni_{0.5}Mo_{0.5}S_x$ activity is assessed in interaction with different ionomers (Nafion® or Sustainion® XB-7). It is shown by an exploratory study that, when Nafion® is replaced by XB-7, the amount of ionomer and water to isopropanol volume ratio must be diminished in the ink formulation to, at least, maintain a comparable activity of the electrode material.

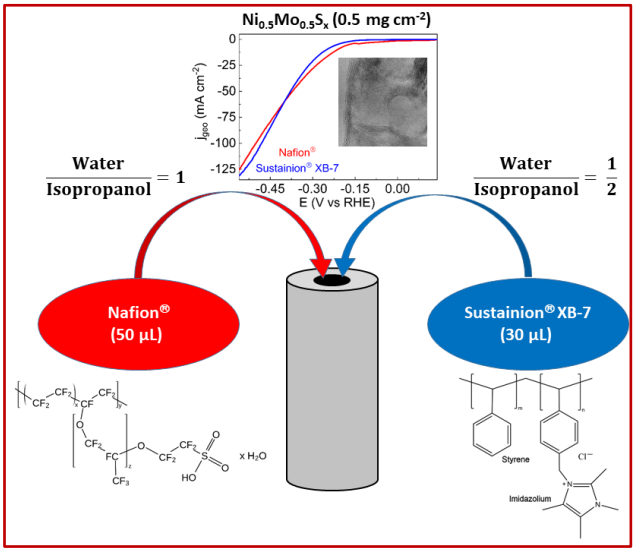

V.1. Introduction

The Sixth Assessment Report provided by IPCC in 2021 makes it clear that changes in energy sector are mandatory to envisage the control of climate change; hydrogen is pointed-out as an important energy carrier in this transition [93, 185]. However, most of industrial hydrogen production still comes from processes using fossil feedstocks, such as the steam reforming of hydrocarbons and coal gasification [141, 186]. Due to their carbon fingerprints, those processes must be replaced by decarbonized ones.

The solid polymer electrolyte water electrolysis (SPEWE) is an interesting alternative process, since if it is coupled to clean energy sources, it results in zero carbon emission. In this process, energy is supplied to the electrolyzer device, which splits water in hydrogen (H_2) and oxygen (O_2) released at the cathode and the anode compartments, respectively. These reactions are known as hydrogen evolution reaction (HER) and oxygen evolution reaction (OER), and both need the use of electrocatalysts to accelerate them, resulting in the increase of process efficiency. Noble-metal-based materials are the benchmarking catalysts for those reactions, but their high-cost and, mainly, scarcity make their use prohibitive in large-scale applications [4]. Hence, it is very important to work on the design of alternative earth-abundant catalysts that must be active, selective, and stable for the reaction.

While many catalysts produced from earth-abundant elements are not stable in acidic environment, many researchers have been devoting their attention to the development of water electrolysis in alkaline media [152-153, 187-188]. However, the hydrogen evolution in high pH's has some drawbacks as the additional energy-consuming step called water dissociation, besides the interaction of generated hydroxyl groups with active sites that can play a negative role in the reaction [97, 152-153]. Thus, a good HER electrocatalyst in alkaline media must not only show a good performance for the reduction of adsorbed hydrogen species, but also present good water dissociation skills. Previously studies reported the ability of MoS_2 to reduce protons towards molecular hydrogen [5, 55], but it lacks activity in alkaline media due to its low water dissociation performance.

In SPEWE systems, the reaction takes place in the membrane electrode assembly (MEA), which is, because of this, known as the "heart of the process". Therefore, aiming to reduce the cost of green hydrogen production and boost the desired energetic transition, many

studies are devoted to the construction of MEA increasingly efficient and at lower cost. To do so, it is important to pay attention at each part of this component. The MEA is consisted of an electrolyte membrane sandwiched by two catalyst layers, one layer responsible to perform the HER, while the other is responsible for the OER. The catalyst layers must contain the catalyst particles in good contact with ionomer because the latter one, besides to play a role as a binder, is responsible for ionic conductivity [189-190].

Many articles show the evaluation and comparison of different membranes [154-155, 191] and catalysts [4, 141, 188, 192] performances as main topic, however, lower attention has been addressed to the ionomer or even the interaction between the ionomer and the catalyst [190], although there are manuscripts that report its impact on catalysts activity [193-195]. Nafion® is the unanimous ionomer for applications in acidic media and, although it has its efficiency decreased in alkaline conditions [141], it is still widely used in analysis at high pH's [86, 97, 103]. Sustainion® XB-7 ionomer, called hereafter "XB-7", was developed to be used at alkaline conditions and its good behavior on water electrolysis has already been reported elsewhere [196].

Therefore, a bimetallic nickel molybdenum sulfide was synthesized herein and tested towards the HER to profit from reduction capability of molybdenum sulfide, and Ni^{2+} water dissociation skills due to its unpaired electrons in e_g orbitals [152]. Besides that, both Nafion® and XB-7 ionomers were applied in this study to investigate the influence of their use in $Ni_{0.5}Mo_{0.5}S_x$ HER performance. To the best of our knowledge, this is the first time that the electrochemical performance of a transition metal sulfide electrocatalyst in association with Sustainion® XB-7 ionomer is reported; not only considering HER, but any reaction. It was revealed that, when it replaces Nafion®, the ink must be produced with lower quantity of ionomer and the solvent must be mostly isopropanol; the complete removal of water also decreases HER activity.

V.2. Results and Discussion

The structures of the materials were investigated by applying the XRD technique and the results are shown in **Figure V.1a**. For NiS_x catalyst, well-defined sharp peaks were observed; it indicates a good crystallinity of the material. The peaks at 2θ equal 16.3°, 26.6°, 38.0°, 50.0°, 54.7° and 64.4° are related to the Ni_3S_4 phase (PDF: 43-1469), while the peaks at 27.2°, 35.3°, 38.8°, 45.1°, 53.4°, 56.0°, 58.5° and 60.9° are associated with the NiS_2 phase (ICSD: 646347).

Although the most intense peak of NiS_x has its maximum at 31.5º, such peak starts to be formed at 31.0º and only finishes at 31.8º. A zoom of this peak region is presented in **Figure C1** and the appearance of a contribution from two distinct peaks may be noticed, although they are superimposed. In fact, the two peaks can be associated with the most intense diffraction lines of Ni_3S_4 and NiS_2 patterns at 31.3º and 31.5º, respectively. Therefore, besides the NiS_2 phase (in agreement with synthesis stoichiometry), Ni_3S_4, a phase poorer in sulfur, has also been detected by XRD. Both molybdenum-based sulfides presented herein showed profiles that resemble to defect-rich 2H-MoS_2 with slightly expanded (002) plane, d(002) about 6.36 Å, and containing turbostratic disorder [65, 157-158]. Indeed, the XRD profiles of MoS_x and $Ni_{0.5}Mo_{0.5}S_x$ don't match perfectly well with 2H-MoS_2 pattern (ICSD: 601647) due to aforementioned features. The expansion of interlayer distance of (002) planes results in a shift of (002) diffraction peak and the existence of turbostratic disorder leads to the absence of (103) and (105) diffraction, replaced by large bands in those regions [177]. The XRD profile of a commercial MoS_2 well crystallized and containing none of previously mentioned characteristics is shown in **Figure A1**. Furthermore, additional sharp peaks, which may be associated with monoclinic nickel (II) sulfate hexahydrate (PDF: 33-955), are verified for $Ni_{0.5}Mo_{0.5}S_x$ material.

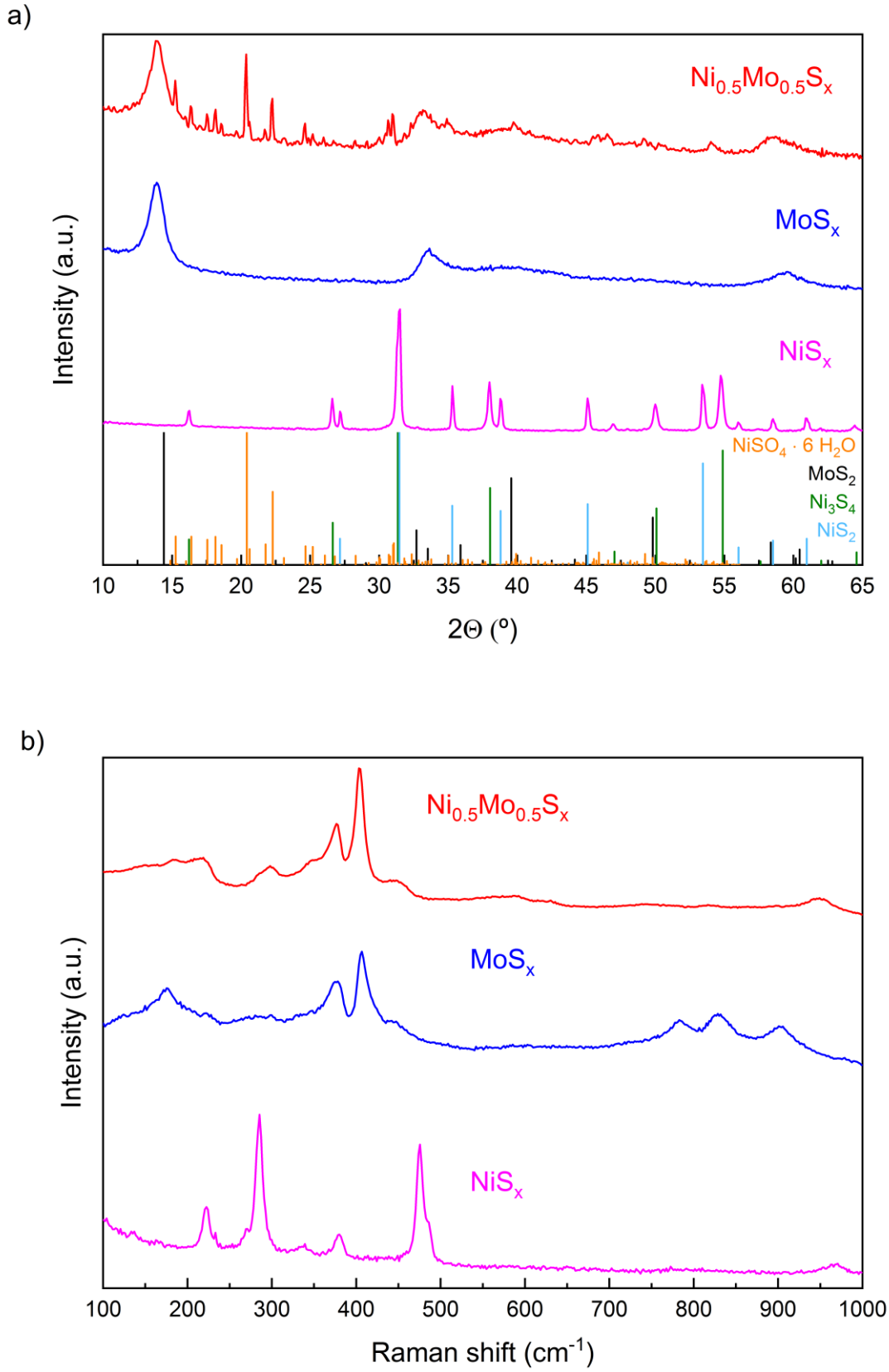

Figure V.1. *(a) X-ray diffractograms and (b) Raman spectra of synthesized monometallic and bimetallic sulfides.*

Ulbrich *et al.* [197] provided an interesting study on the phase evolution of synthesized nickel sulfide species by applying XRD technique. It was shown that, even in ambient temperature, high humidity ambient accelerated the transformation of nickel sulfide toward nickel sulfate. Therefore, it is likely that the sulfide to sulfate transformation in $Ni_{0.5}Mo_{0.5}S_x$ was boosted by the high temperature and pressure conditions applied in the hydrothermal synthesis reported herein. Nonetheless, the nickel sulfate phase was not identified in the X-ray diffractogram of NiS_x. Another point highlighted by Ulbrich *et al.* [197] is that the smaller are nickel sulfide species, the faster are their bulk oxidation. As indicated by TEM results (**Figure V.2**), Ni-containing species are much bigger in NiS_x than in $Ni_{0.5}Mo_{0.5}S_x$. Hence, in NiS_x, sulfate formation is limited to its surface as evidenced by XPS (**Figure V.5e**). For MoS_x, no sulfate is produced at all due to the high stability of MoS_2 sulfur species against oxidation [198].

The structures of the materials were also investigated by Raman spectroscopy and the results are presented in **Figure V.1b**. The bands at 222, 285, 339 and 379 cm^{-1} are attributed to Ni_3S_4 [199], while those at 270, 476, 486 and 971 cm^{-1} are assigned to NiS_2 [200-201]. The Raman analyses were applied to different spots of NiS_x to evaluate the homogeneity of the catalyst. **Figure C2(a)**, which evidences these spectra, shows that different proportions of aforementioned phases are identified according to the zone of the material where the analysis is applied, therefore, there is a lack of homogeneity for NiS_x. Raman spectrum of MoS_x (**Figure V.1b**) evidenced remaining molybdate synthesis residue due to the presence of the band at 175 cm^{-1} and the three other bands which appear in the 750-950 cm^{-1} range [162-164]. It is important to highlight that such residue is not present throughout the material. As one may see in **Figure C2(b)**, there are spots of the material in which those bands are not observed in the corresponding Raman spectra. In addition, the well-known E^1_{2g} and A^1_g phonon modes of MoS_2 are present at 377 and 407 cm^{-1}, respectively [165]. These bands are also present for $Ni_{0.5}Mo_{0.5}S_x$, although in this case the A^1_g mode shifts towards 403 cm^{-1}. Raman spectrum of $Ni_{0.5}Mo_{0.5}S_x$ also exhibited a band at 298 cm^{-1}, which is assigned to E_{1g} mode of MoS_2 [202-203], and bands in the range of 120-240 cm^{-1} containing a profile which appears for molybdenum sulfide materials containing high density of defects [204]. Therefore, both XRD and Raman analyses show features related to defect-rich MoS_2 for the bimetallic sulfide. Finally, it can also be verified a band at 949 cm^{-1} associated with the $NiMoS_4$ phase, which cannot be detected by XRD due to its amorphous character [205]. It is noteworthy that

the Raman analysis was also performed in different spots of $Ni_{0.5}Mo_{0.5}S_x$, however, no change in the spectra were detected for this compound. Thus, the association of Ni and Mo leads to a catalyst more homogeneous in micrometric scale.

The materials were also characterized by transmission electron microscopy (TEM) to investigate their morphologies; the resulting micrographies are presented in **Figure V.2**. NiS_x presented two distinct morphologies, three- (**Figure V.2a**) and two-dimensional (**Figure V.2b**) crystals. Negligible amount of oxygen was detected in this material by the application of energy-dispersive X-ray spectroscopy (EDS) analysis. The MoS_x material presented sheet morphology, typical of MoS_2 (**Figure V.2c**). Besides that, the sheets can be divided into two groups, one containing very stacked large MoS_2 sheets (**Figure V.2d**) and another corresponding to well-dispersed few-layer MoS_2 nanosheets (**Figure V.2e**), which is the most interesting morphology for HER application. $Ni_{0.5}Mo_{0.5}S_x$ exhibited a similar trend of MoS_x. In **Figure V.2f**, it can be seen the sheets containing different agglomeration and stacking degrees. The larger sheets containing elevated stacking degree are evidenced in **Figure V.2g**, while the few-layer nanosheets are shown in **Figure V.2h**. Additionally, $Ni_{0.5}Mo_{0.5}S_x$ contains crystallized larger particles (**Figure V.2i**) which are rich in nickel and sulfur according to EDS analysis. Such particles were attributed to the existence of nickel sulfate species detected by XRD.

In addition, HRTEM images of molybdenum-based sulfides were acquired and interplanar spacings were measured. **Figure V.3** shows distances of 0.63 and 0.62 nm in MoS_x and $Ni_{0.5}Mo_{0.5}S_x$ nanosheets, respectively. These distances are associated with (002) plane distance of 2H-MoS_2 phase, also identified by XRD. Yet, these distances are close, bearing in mind the equipment resolution, to the calculated by XRD taking into consideration the diffraction peak of (002) plane. An interplanar spacing of 0.26 nm is also verified for the $Ni_{0.5}Mo_{0.5}S_x$ HRTEM micrograph (**Figure V.3b**), which is related to the (100) plane of 2H-MoS_2. Therefore, HRTEM micrographs provide more evidence about the presence of 2H-MoS_2 in molybdenum-containing catalysts. HRTEM image of NiS_x was also obtained and d-spacings were measured as shown in **Figure C4**. However, due to the similarity between distances of NiS_2 and Ni_3S_4 planes [206], it is not possible to distinguish which of the phases are present in the image.

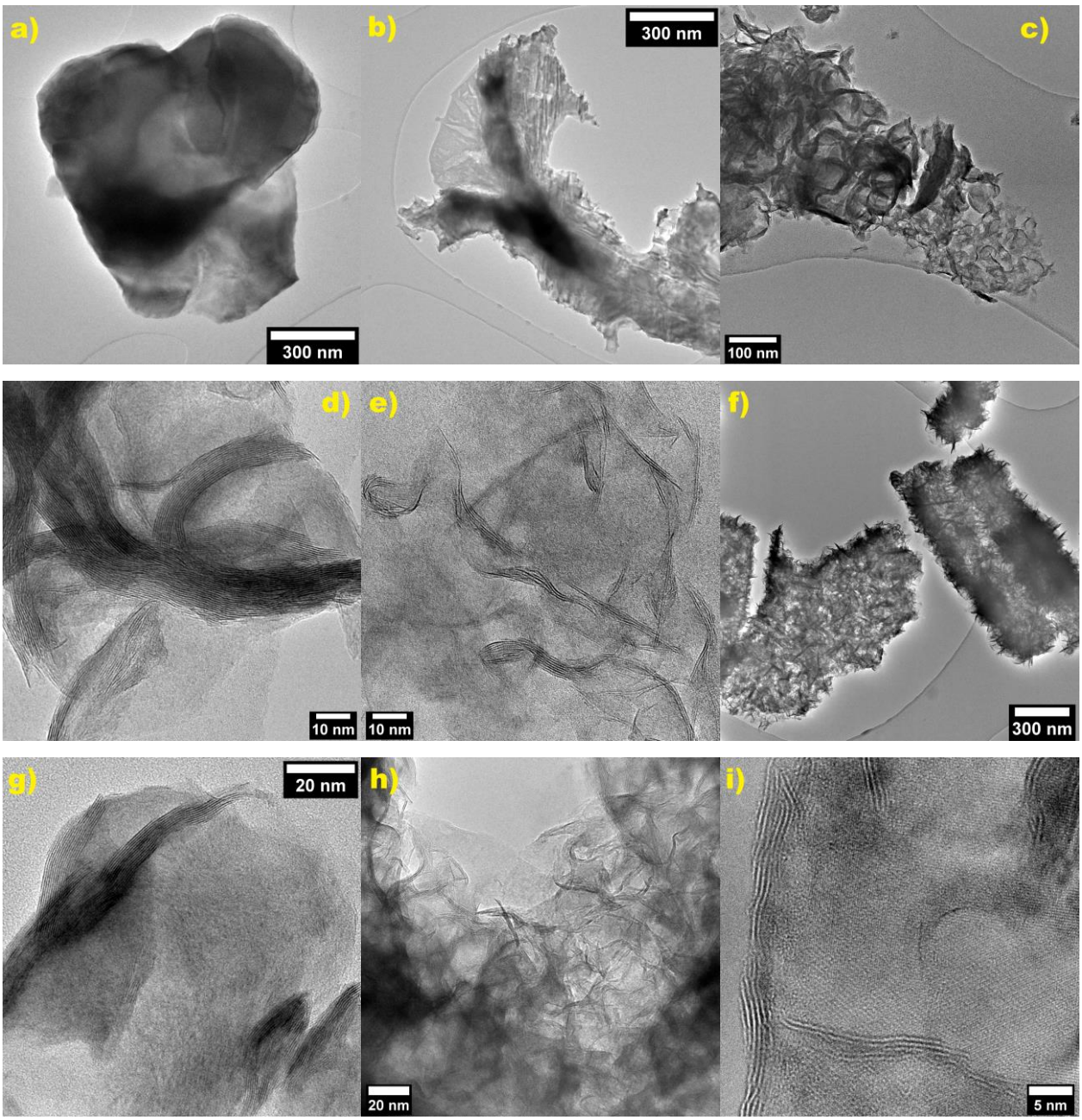

Figure V.2. *TEM images of (a,b) NiS_x, (c, d,e) MoS_x and (f, g, h,i) $Ni_{0.5}Mo_{0.5}S_x$.*

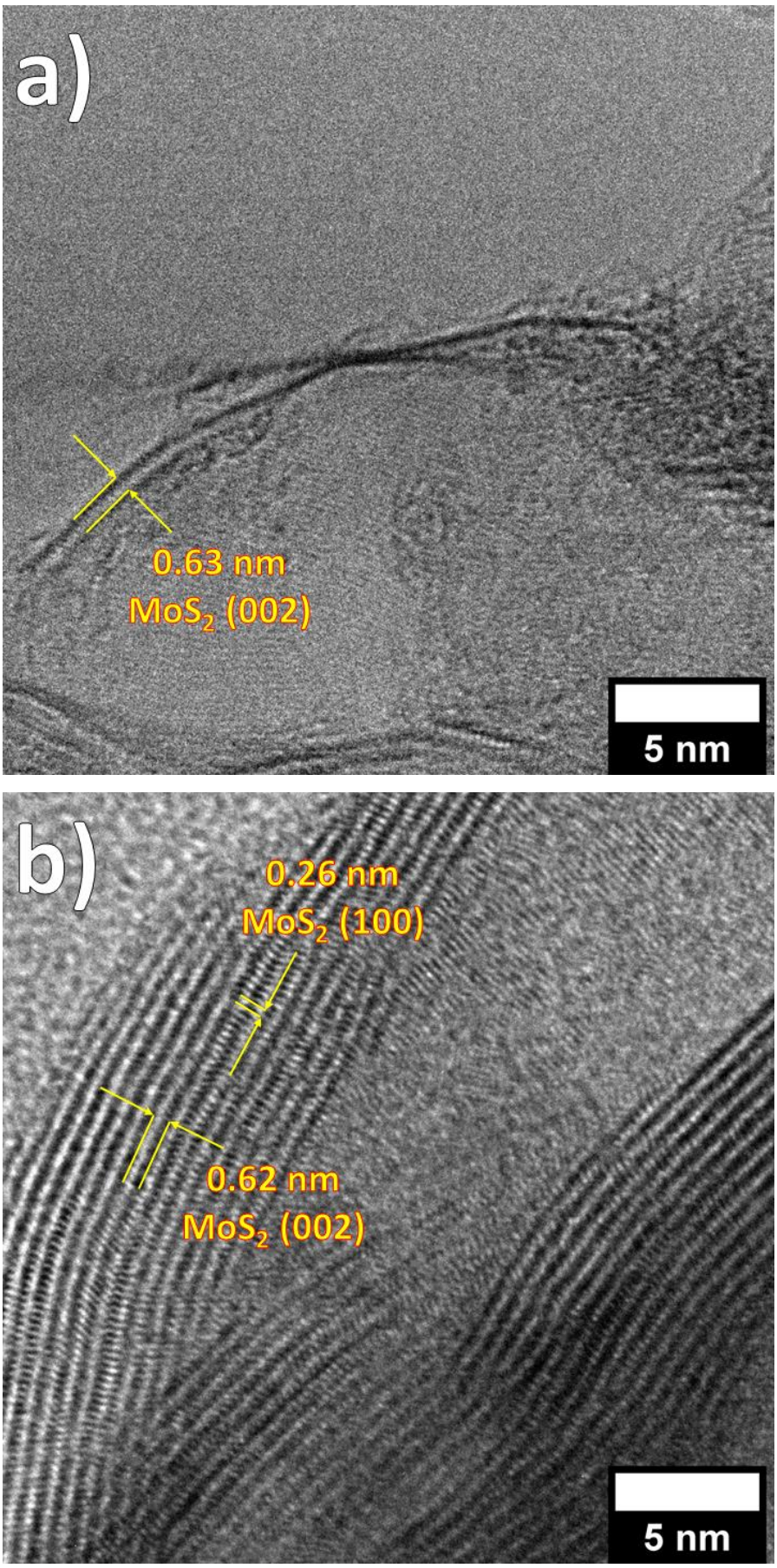

Figure V.3. *HRTEM micrographs of (a) MoS_x and (b) $Ni_{0.5}Mo_{0.5}S_x$.*

To investigate the dispersion of elements in $Ni_{0.5}Mo_{0.5}S_x$, an elemental mapping was generated from applying EDS technique in transmission electron microscope; resultant images are shown in **Figure V.4**. As one may see, all elements, including oxygen (as expected due to the presence of sulfate), are well dispersed in this bimetallic sulfide. Such analysis was also extended to NiS_x and MoS_x materials and the results are presented in **Figures C5** and **C6**, respectively. Interestingly, nickel and sulfur also showed good dispersion for NiS_x, however, less oxygen is detected in this material when compared to $Ni_{0.5}Mo_{0.5}S_x$; this trend matches with results obtained by XRD. On the contrary, good dispersion of molybdenum, sulfur and oxygen was registered for MoS_x. This result is not surprising since the existence of molybdate residues in MoS_x was verified by Raman spectroscopy.

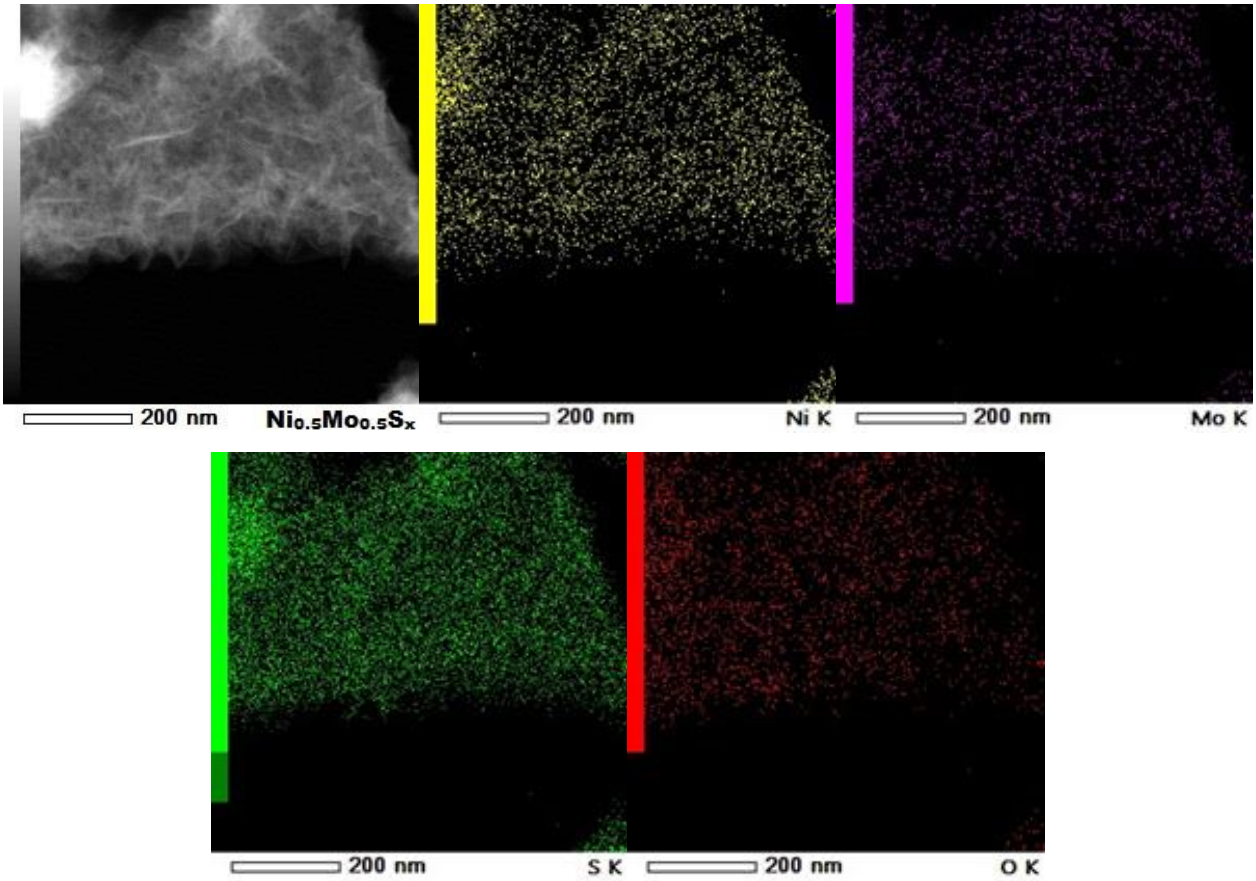

Figure V.4. *Elemental mapping of $Ni_{0.5}Mo_{0.5}S_x$. Gray scale image represents the original figure, while the images in yellow, violet, green and red were generated according to the spots where nickel, molybdenum, sulfur, and oxygen, respectively, were identified.*

The chemical nature at the surface of the catalysts was studied by XPS and the resulting spectra are depicted in **Figure V.5**. The Ni 2p spectrum of NiS_x (**Figure V.5a**) exhibited three peaks that could be deconvoluted by the contribution of three doublets. The major contribution came from the NiS_2 species [207] which were also verified by XRD and Raman results. The contact with air led to an oxidation of the NiS_x surface resulting in the formation of nickel oxide [208] and, in less quantity, nickel sulfate species. The existence of nickel sulfate in the surface was also clearly revealed by the analysis of S 2p spectrum of NiS_x (**Figure V.5e**). Besides that, contributions related to S_2^{2-} and S^{2-} species were also detected [209]. To unveil the contributions of nickel sulfate in Ni 2p and S 2p spectra, a commercial nickel sulfate heptahydrate was analyzed by XPS measurements and their spectra are presented in **Figure C7**.

As seen in **Figure V.5c**, molybdenum was present in three oxidation states at the surface of MoS_x. The highest contribution came from Mo^{4+}, typical of MoS_2 species; Mo^{5+} and Mo^{6+} were also present in similar quantities [208]. MoS_2 may also suffer oxidation derived from the air-contact which leads to the formation of MoO_3, in which molybdenum is present with an oxidation state equal +6. It is noteworthy that Raman analysis also identified remaining Mo-O linkages which can also be related to the state +6. It has already been reported that the existence of Mo^{5+} can be attributed to existence of molybdenum oxysulfide. It is, in fact, an intermediate specie between molybdenum sulfide and molybdenum oxide and, therefore, its presence can be associated with molybdate that was not completely sulfurized [173] or MoS_2 which has been only partially oxidized. The S 2p spectrum of MoS_x (**Figure V.5f**) exhibited negligible contribution from sulfates and the existence of S_2^{2-} [173] in low quantities. This latter specie is generally associated with molybdenum sulfides containing low degree of crystallinity. In fact, for this spectrum, the major contribution came from S^{2-} as expected for MoS_2 [173].

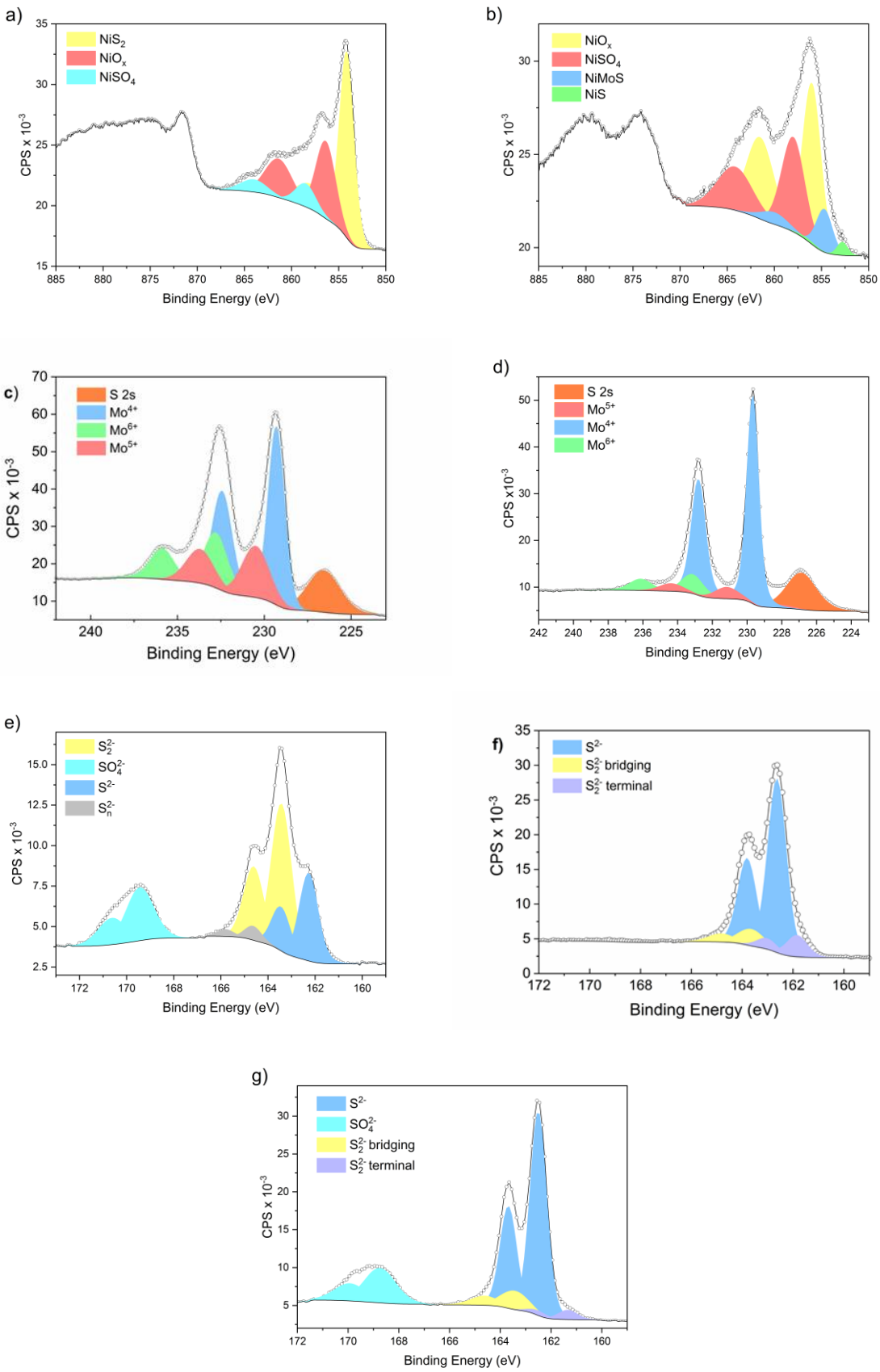

Figure V.5. *Ni 2p spectra of (a) NiS_x and (b) $Ni_{0.5}Mo_{0.5}S_x$, Mo 3d of (c) MoS_x and (d) $Ni_{0.5}Mo_{0.5}S_x$ and S 2p spectra of (e) NiS_x, (f) MoS_x and (g) $Ni_{0.5}Mo_{0.5}S_x$.*

Contrary to NiS_x, according to Ni 2p spectrum of $Ni_{0.5}Mo_{0.5}S_x$ (**Figure V.5b**), most of nickel in this compound was present in an oxidized form; mostly as oxide [208], but also as sulfate. Despite that, although in lower quantity, a tertiary sulfide containing nickel, molybdenum and sulfur was also verified [208], which is likely associated with the $NiMoS_4$ phase also detected by Raman spectroscopy. **Figure V.5d**, which shows the Mo 3d spectrum of $Ni_{0.5}Mo_{0.5}S_x$, elucidates that, as well as for MoS_x, the curve can be fitted by the contribution of Mo^{4+}, Mo^{5+} and Mo^{6+} species [208]. However, in the bimetallic sulfide, the contribution from the Mo^{4+} oxidation state, typical of MoS_2 materials, is even higher. Small contribution of Mo^{6+} may be associated with the existence of the previously cited $NiMoS_4$ phase, but the possibility of MoO_3 coexistence due to molybdenum oxidation in contact with air may not be discarded. As explained above, the Mo^{5+} oxidation state is related to molybdenum surrounded by oxysulfidic species [173]. Finally, the S 2p spectrum of $Ni_{0.5}Mo_{0.5}S_x$, presented in **Figure V.5g**, showed that most sulfur species were present as S^{2-} ligands, as expected for MoS_2 phase [173]. The presence of sulfate groups was also evident, in agreement with the Ni 2p spectrum (**Figure V.5b**). In minority, the S_2^{2-} ligands, bridging and terminal [173], were also present, although in lower quantity than that detected for a MoS_x material.

Therefore, according to XPS results, nickel present in the bimetallic sulfide was more susceptible to oxidation than in NiS_x. Despite that, the existence of a tertiary sulfide phase (likely $NiMoS_4$) was verified for $Ni_{0.5}Mo_{0.5}S_x$. Another important point is that, although the nickel oxides and sulfates were extensively present on the surface of $Ni_{0.5}Mo_{0.5}S_x$, the incorporation of nickel in the synthesis led to MoS_2 phase less oxidized than the one obtained to MoS_x, which contained higher contents of Mo^{5+} and Mo^{6+}.

The materials have their activities towards HER tested by LSV measurement in 1 M KOH at 10 mV s^{-1} and 1 600 rpm; the resulting curves are depicted in **Figure V.6a**. It became evident that the glassy carbon (GC) electrode is not active at all, and it was only used as a substrate to deposit the active materials. The monometallic sulfides, MoS_x and NiS_x, showed to be active for the reaction and requested 285 and 300 mV of overpotential to achieve -10 mA cm^{-2}. In addition, while the first one could not achieve -100 mA cm^{-2} during the experiment, i.e., at overpotentials lower than 560 mV, the second one delivered this value at 513 mV. By the inset graph in **Figure V.6a**, containing iR-drop corrected curves by using R_s values acquired in OCP (**Figure C8**), one may see that MoS_x started the HER at slightly lower overpotential

than NiS_x. However, considering the Tafel plot (**Figure V.6b**) derived from the polarization curve, it may be inferred that NiS_x presents a better HER kinetics than MoS_x, once the former exhibited a Tafel slope about 112 mV dec^{-1} and the calculated value for the latter was about 131 mV dec^{-1}. For this reason, NiS_x presented a better activity at higher current densities. The bimetallic $Ni_{0.5}Mo_{0.5}S_x$ also showed to be active towards the HER and presented an onset overpotential lower than both monometallic sulfides. Furthermore, the values of η_{10} and η_{100} registered on the polarization curve for $Ni_{0.5}Mo_{0.5}S_x$ were 203 mV and 500 mV, respectively. It is important to highlight that the water dissociation step is of paramount importance for HER in alkaline media. MoS_2 is well-known for being an excellent electrocatalyst for proton reduction, but it presents low performance for water dissociation [178, 210]. Additionally, XPS measurements evidenced a higher concentration of nickel oxide on the surface of $Ni_{0.5}Mo_{0.5}S_x$ when compared to NiS_x. Generally, the oxidation of sulfides is an undesired process, however, Boettcher group [211] showed that nickel oxide, which is hydroxylated in alkaline environment, is an excellent water dissociation catalyst. Therefore, in fact, the nickel oxide at the surface of $Ni_{0.5}Mo_{0.5}S_x$ is responsible for the water dissociation and, consequently, for producing the hydrogen adsorbed specie that will be further reduced to H_2 on molybdenum sulfide active sites. The lower overpotentials registered for $Ni_{0.5}Mo_{0.5}S_x$ can clearly be explained, compared to those observed on the surface of the monometallic sulfides. It can be noticed that the beginning of hydrogen evolution is overlaid with a reduction process for $Ni_{0.5}Mo_{0.5}S_x$. This reduction only appears in the first cycle of LSV analysis and is attributed to the reduction of oxidized species at the surface of the electrocatalyst. Therefore, to obtain the Tafel plot for $Ni_{0.5}Mo_{0.5}S_x$, the necessary data were extracted from the second scan polarization curve shown in **Figure C9**. **Figure V.6b** displays the Tafel plots of the different investigated electrode materials; among them the Tafel slope (b) of $Ni_{0.5}Mo_{0.5}S_x$ is 78 mV dec^{-1}. This is the only material reported herein in which the second polarization curve was used for the calculations, all the others had their data extracted from the first scan. By applying only η_{10}, η_{100} and b as activity descriptors, it could be concluded that the $Ni_{0.5}Mo_{0.5}S_x$ cathode is more active than both NiS_x and MoS_x. Nonetheless, at -0.56 V vs RHE the NiS_x electrocatalyst delivered 133 mA cm^{-2} current density, while at the same potential the current density obtained on $Ni_{0.5}Mo_{0.5}S_x$ was 126 mA cm^{-2}; this activity inversion is noticed from -0.54 V vs. RHE onwards.

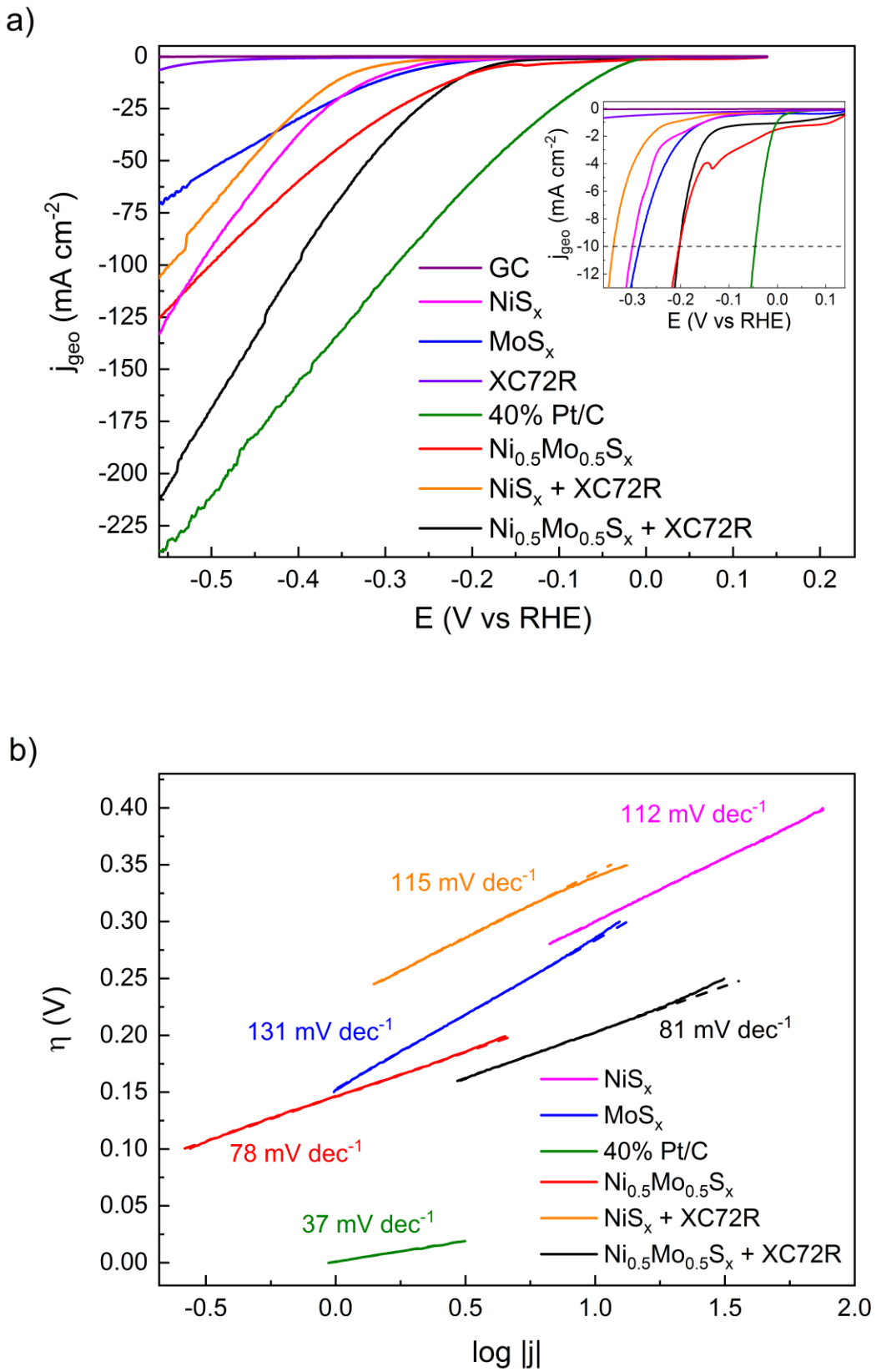

Figure V.6 – *(a) Uncompensated polarization curves for HER in 1 M KOH at 1 600 rpm. Inset: iR-drop compensated curves at low current densities. (b) Tafel plot derived from the iR-corrected polarization curves. *The Tafel plot of $Ni_{0.5}Mo_{0.5}S_x$ was obtained from 2nd scan.*

Despite the synthesized sulfide materials are active for the HER, their performance is still far from the one verified for the commercial (Sigma Aldrich) 40% Pt/C, which was also analyzed during the work as a reference electrocatalyst for HER. From the polarization curve (**Figure V.6a**), the values of η_{10}, η_{100} and η_{200} were equal 46 mV, 288 mV and 481 mV for this material; in addition, it was verified a Tafel slope about 37 mV dec^{-1} (**Figure V.6b**). The aforementioned descriptors of 40% Pt/C showed values much lower than the ones obtained for the sulfides, however, it is necessary to keep in mind the influence of electrocatalysts conductivity on their activity [212]. Although some metal sulfides may present metallic properties, e.g. the 1T-MoS_2 phase [61, 174], all the transition metal sulfide (TMS) phases identified herein exhibit semiconductive nature [175, 200-201, 213]. Such conductivity issue may be overcome by mixing physically the semiconductor catalyst with Carbon Vulcan XC72R material, which acts as a conduction additive. Thus, this physical association of materials was tested for NiS_x and $Ni_{0.5}Mo_{0.5}S_x$ since they presented the best activities at elevated current density values. Although the onset potential of NiS_x was maintained in the physical mixture with Carbon Vulcan XC72R, its activity was reduced as evidenced in **Figure V.6a**. This physical mixture needed overpotentials 39 mV and 33 mV higher than only NiS_x to achieve -10 mA cm^{-2} and -100 mA cm^{-2}, respectively. Moreover, no relevant alteration on the value of Tafel slope was noticed as result of Carbon Vulcan addition (**Figure V.6b**). Concerning the Tafel slope, the same behavior was noticed for the addition of Carbon Vulcan to the ink formulation of $Ni_{0.5}Mo_{0.5}S_x$. From **Figure V.6a**, it is evident that the value of η_{10} for $Ni_{0.5}Mo_{0.5}S_x$ is the same in the presence and absence of Carbon Vulcan and the onset overpotential also seems to be equal; nonetheless, the reduction process observed in the curve registered in the absence of Carbon Vulcan becomes an inconclusive admeasurement. Therefore, a graph was plotted with the results of the second scans with LSV technique and it is exhibited in **Figure C9**. This figure allows to confirm the maintenance of the same overpotential; therefore, it does not depend on the presence of Carbon Vulcan. Despite the aforementioned descriptors did not alter with the use of Carbon Vulcan, its addition effect became clear at high current densities, exactly in the operation condition that conductivity feature is even more relevant. A reduction of 98 mV in overpotential to achieve -100 mA cm^{-2} was obtained with the conduction additive. Furthermore, it should be noted that this physical mixture containing $Ni_{0.5}Mo_{0.5}S_x$ and

Carbon Vulcan, with mass ratio equal 1:1, only requested an overpotential 60 mV higher than the 40% Pt/C catalyst to achieve a current density of 200 mA cm^{-2}. Thus, bearing in mind the cost of catalyst production, this physical mixture emerges as an interesting electrocatalyst candidate to be applied on the cathode of anion exchange membrane water electrolyzer (AEMWE) devices. The Carbon Vulcan was also evaluated on HER, but it presented negligible activity as shown in **Figure V.6a**. Hence, it can be concluded that even in the physical mixtures, the activity keeps coming from the sulfides and the Carbon Vulcan aids by enhancing the electroconductivity. The values of η_{10}, η_{100}, η_{200} and *b* for all materials are summarized in **Table V.1**.

Table V.1. *Parameters values obtained from LSV analyses in HER region.*

Catalyst	NiS_x	MoS_x	$Ni_{0.5}Mo_{0.5}S_x$	NiS_x + XC72R	$Ni_{0.5}Mo_{0.5}S_x$ + XC72R	40% Pt/C
η_{10} (mV)	300	285	203	339	203	46
η_{100} (mV)	513	-	500	548	402	288
η_{200} (mV)	-	-	-	-	541	481
b (mV dec^{-1})	112	131	78[a]	115	81	37

*η_{10} and b were obtained after iR-compensation, while η_{100} and η_{200} are related to non-compensated results.

[a]Value calculated from the second scan of LSV analysis.

An interesting aspect of the use of Carbon Vulcan in the ink preparation was the fact that it worked very well for $Ni_{0.5}Mo_{0.5}S_x$, although it reduced the activity when combined with NiS_x. It is of paramount importance to consider that, once the mass loading of material was maintained constant in the analyses, the addition of Carbon Vulcan led to a reduction of the quantity of TMS in the electrode, which are the real active species for the reaction. Thus, it may be assumed that the enhancement of conductivity provoked by the Carbon Vulcan addition was not enough to compensate the lower quantity of NiS_x HER active sites. On the other hand, such conductivity enhancement on the combination with $Ni_{0.5}Mo_{0.5}S_x$ was likely more relevant than the decrease of available active sites. Despite the sulfide species highlighted in this work present semiconductive nature, it does not mean that they possess the same conductivity. We hypothesize that the Ni content may play a role in the conductivity; the more nickel, the more conductive. Such behavior has already been noticed

and reported by Xu *et al.* [212] for oxides containing iron group elements. In this study, $NiCoO_x$ and $NiCoFeO_x$ showed much higher conductivity than Co_3O_4 and $CoFeO_x$. Since a conduction additive would impact the catalytic behavior more as less conductive is the material, assuming that the reaction kinetics is limited by the conductivity in the absence of the aforementioned additive, the previously hypothesis may justify the improvement of performance for $Ni_{0.5}Mo_{0.5}S_x$ and not for NiS_x. Nonetheless, the increase of activity by the association of NiS_x and Carbon Vulcan is not verified in **Figure V.6a** because current density is obtained by geometrical surface normalization. In **Figure C10** the same results were plotted, but at this time normalizing the current by the mass of active compounds (carbon-based species were not considered). At elevated overpotentials the physical mixture (NiS_x + XC72R) exhibited higher absolute values of current density than NiS_x. Since the number of active sites is proportional to the mass loading of NiS_x, it is evident that the reaction became faster in the NiS_x sites for the physical mixture.

Due to the importance of a good interaction between catalyst and ionomer species, additional electrochemical experiments were done with XB-7 ionomer and these results were compared to the ones obtained by applying Nafion®. Because of the benchmark status attributed to Pt as HER catalyst, it was decided to initiate this comparison with the reference 40% Pt/C electrocatalyst. The catalytic ink was prepared with the same methodology, even same volumes, only replacing the Nafion® suspension by the XB-7 one. LSV analysis was then applied once more and a comparison of activity with each ionomer is presented in **Figure V.7a**. Although the onset overpotential of 40% Pt/C kept unaltered, it is clear that XB-7 led to higher current densities than Nafion®. The use of XB-7 reduced the values of η_{100} and η_{200} in 50 and 73 mV, respectively. Before the LSV analyses, cyclic voltammetry (CV) technique was applied and the results for the use of Nafion and XB-7 are presented in **Figure C11(a)**. The charge associated with the electrochemical oxidation of monolayers of hydrogen adsorbed species (Q_H) [214] were calculated. The ratio of charges (Q_H^{XB-7}/Q_H^{Nafion}) verified was equal 1.21, therefore, the interaction between 40% Pt/C and XB-7 resulted in an increase of Pt active sites' availability of around 21% in comparison with Nafion® application; it may justify the activity enhancement.

The same methodology was applied to $Ni_{0.5}Mo_{0.5}S_x$ electrocatalyst once it was the most interesting synthesized material reported herein. **Figure V.7b** exhibits the uncompensated polarization curves for the electrodes prepared from inks containing 50 μL of ionomer and

water to propanol volume ratio (R_{solv}) equal 1. Unexpectedly, the material prepared with the ink containing XB-7 performed worse than the electrode containing the Nafion® ionomer. A current density of -126 mA cm^{-2} could be achieved at -0.56 V vs. RHE, while, approximately, half of this values was obtained at the same potential for the electrode containing XB-7. Once there are a large variety of ink recipes and their effectiveness depends on the type of catalyst in use [195], it was decided to vary some parameters on the catalytic ink recipe containing XB-7 to investigate their effect on HER activity of $Ni_{0.5}Mo_{0.5}S_x$.

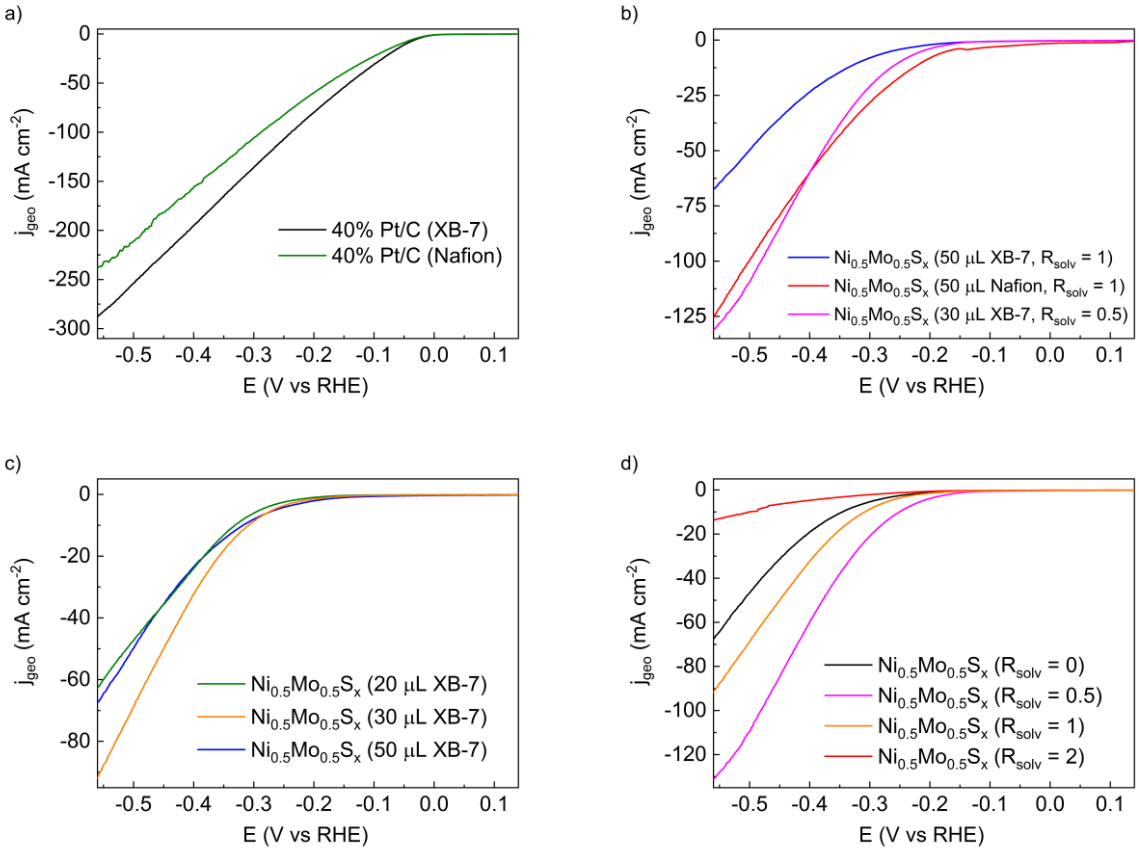

Figure V.7 *– Uncompensated polarization curves for HER in 1 M KOH at 1 600 rpm. (a) Comparison of 40% Pt/C electrocatalysts activity according to the ionomer suspension applied; catalytic ink prepared with 50 µL of ionomer suspension and R_{solv} = 1. (b) Comparison of $Ni_{0.5}Mo_{0.5}S_x$ activity using different ionomer suspensions. (c) The influence of XB-7 suspension volume added to the ink containing R_{solv} = 1 on the activity of $Ni_{0.5}Mo_{0.5}S_x$. (d) Influence of R_{solv} parameter on the activity of $Ni_{0.5}Mo_{0.5}S_x$ electrocatalysts prepared from inks produced with the addition of 30 µL of XB-7 suspension.*

Figure V.7c exhibits the results obtained for electrodes, in which the deposited inks were prepared with different volumes of XB-7 suspension. The graph shows that the electrode prepared with 20 and 50 µL of XB-7 presented similar activity, however, for the intermediate value of 30 µL, a better HER activity was achieved. The variation of activity as function of the ionomer content was also reported by Faid *et al.* [194] for Ni/C HER catalyst, although the variation of the same ionomer content, Fumatech Fumion FAA-3, had no major impact on the activity of NiO catalyst toward OER. In that study, the variation was attributed to the agglomeration of Ni/C on the electrode surface as verified by scanning electron microscopy (SEM).

Different recipes containing 30 µL of XB-7 and varying the R_{solv} parameter were prepared aiming to investigate the effect of this last one on $Ni_{0.5}Mo_{0.5}S_x$; results are depicted in **Figure V.7d**. It may be seen that, when water is present in more quantity (R_{solv} = 2) on the ink composition, $Ni_{0.5}Mo_{0.5}S_x$ presented the lowest activity. Furthermore, when isopropanol was applied as the only solvent (R_{solv} = 0), the activity was lower than for the ink prepared from equal volumes of water and isopropanol (R_{solv} = 1). However, the catalytic ink prepared from the addition of double of isopropanol in relation to water (R_{solv} = 0.5) showed the best activity. Such behavior, i.e., higher activities for electrodes prepared from ink containing low water/alcohol ratio, is typical of hydrophobic catalysts [195]. This interaction among water, isopropanol, ionomer and the catalyst is very important because it will directly impact the quality of catalyst layer deposited onto the electrode substrate and, consequently, the dispersion of the catalyst, which is an important parameter in catalysis.

By looking back to **Figure V.7b**, one may see that, at potentials lower than -0.4 V vs. RHE, the electrode prepared from the deposition of an ink containing 30 µL of XB-7 and R_{solv} = 0.5 achieved slightly higher current densities than the one obtained from the use aforementioned Nafion-containing ink. Despite that, from the CV measurements (varying scan rate from 20 to 60 mV s^{-1}) registered in the capacitive region of these electrodes, shown in **Figures C11(b)** and **C11(c)**, respectively, the capacitances were calculated. Interestingly, the electrode prepared with the Nafion ionomer showed a capacitance about 7 times higher than that with XB-7. Considering the relationship between capacitance and electrochemical surface area (ECSA), it can be concluded that the electrode containing XB-7 showed a similar activity, although it had a lower availability of active sites. Besides the effects already mentioned here, sometimes the ionomer may act by changing the chemical nature of the

catalyst at the surface [193] or even may poison the catalyst by blocking its active sites [215-216]. Further characterizations must be performed to better understand the $Ni_{0.5}Mo_{0.5}S_x$/XB-7 interaction.

This is an exploratory study of the influence of some parameters of ink preparation in HER activity, which is intended to continue aiming the optimization of catalytic ink for $Ni_{0.5}Mo_{0.5}S_x$. The aim of its exposition is to elucidate the relevance of studying catalyst/ionomer interactions to achieve superior activities. It is expected that these results can encourage the research community to investigate deeper the catalyst/ionomer interface, which can bring essential information to consolidate the AEMWE technology.

V.3. Conclusion

Monometallic (NiS_x and MoS_x) and bimetallic ($Ni_{0.5}Mo_{0.5}S_x$) sulfides were synthesized by applying a hydrothermal synthetic methodology in which sodium diethyldithiocarbamate was used as sulfur source. All of them showed to be HER active electrocatalysts, although lower overpotential descriptors were obtained for $Ni_{0.5}Mo_{0.5}S_x$. This behavior was attributed to the existence of nickel oxide species on the surface, according to XPS results, as well as molybdenum sulfide containing lower oxidation degree. While the first is an excellent water dissociation catalyst, MoS_x is one of the most active catalysts for the reduction of adsorbed hydrogen species to molecular hydrogen; therefore, a synergy effect emerges from their combination. Furthermore, $Ni_{0.5}Mo_{0.5}S_x$ performance at high overpotentials was boosted by physically mixing it with Carbon Vulcan XC72R, which played a role as conduction additive. As result, this physical mixture requested an overpotential only 60 mV higher than the benchmarking 40 % Pt/C electrocatalyst to achieve 200 mA cm^{-2}. Therefore, $Ni_{0.5}Mo_{0.5}S_x$ is presented herein as an interesting candidate to replace Pt-based catalysts in the cathode of anion exchange membrane water electrolyzers, due to its earth-abundance and low cost. Finally, $Ni_{0.5}Mo_{0.5}S_x$ HER performance was studied in function of catalytic ink formulation using two different ionomers, more precisely Nafion® and XB-7. The exploratory study showed that, when $Ni_{0.5}Mo_{0.5}S_x$ is applied as HER catalyst, to improve catalyst's performance by replacing Nafion by XB-7, it is necessary to reduce the amount of ionomer and water/isopropanol volume ratio; the same adjustment was not necessary for 40 % Pt/C. It reveals that the interaction between a catalyst and an ionomer is unique, and it also

depends on ink's production methodology. Therefore, this work sheds light on the importance of specific ink formulations' development according to the electrocatalyst employed, which requires a deep understanding of electrocatalyst/ionomer interface.

Appendix C. Supporting Information Chapter V

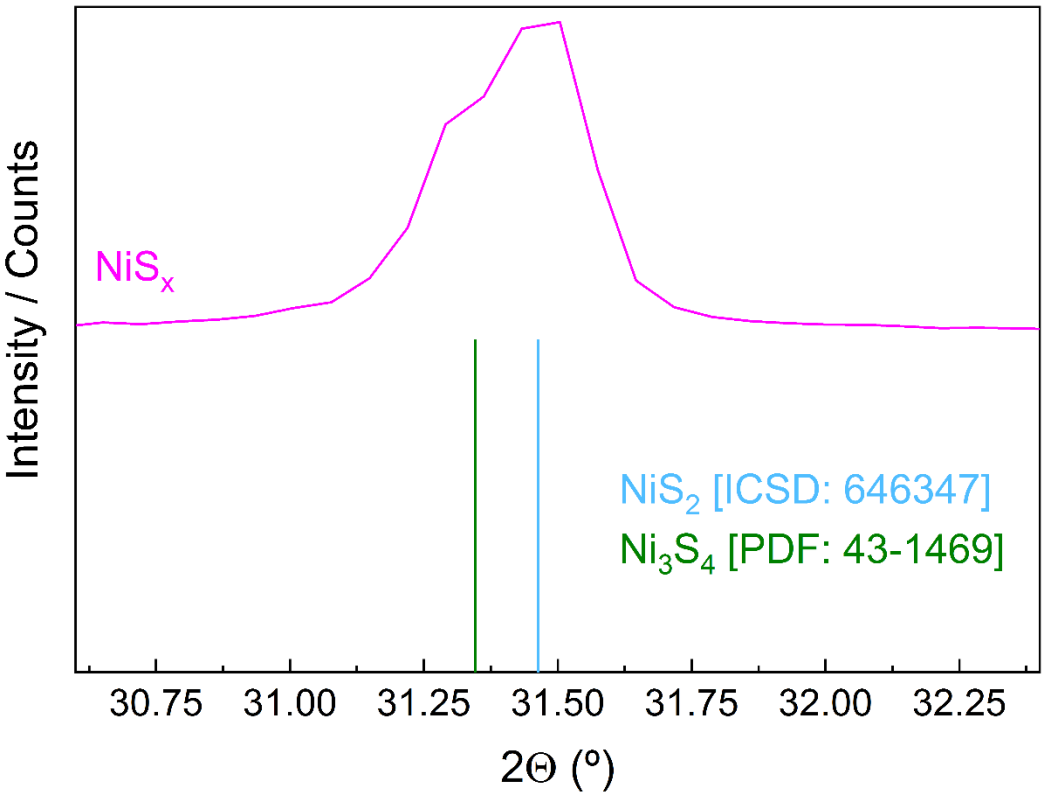

Figure C1. *X-ray diffractogram of NiS_x with a zoom in the region of the most intense peak.*

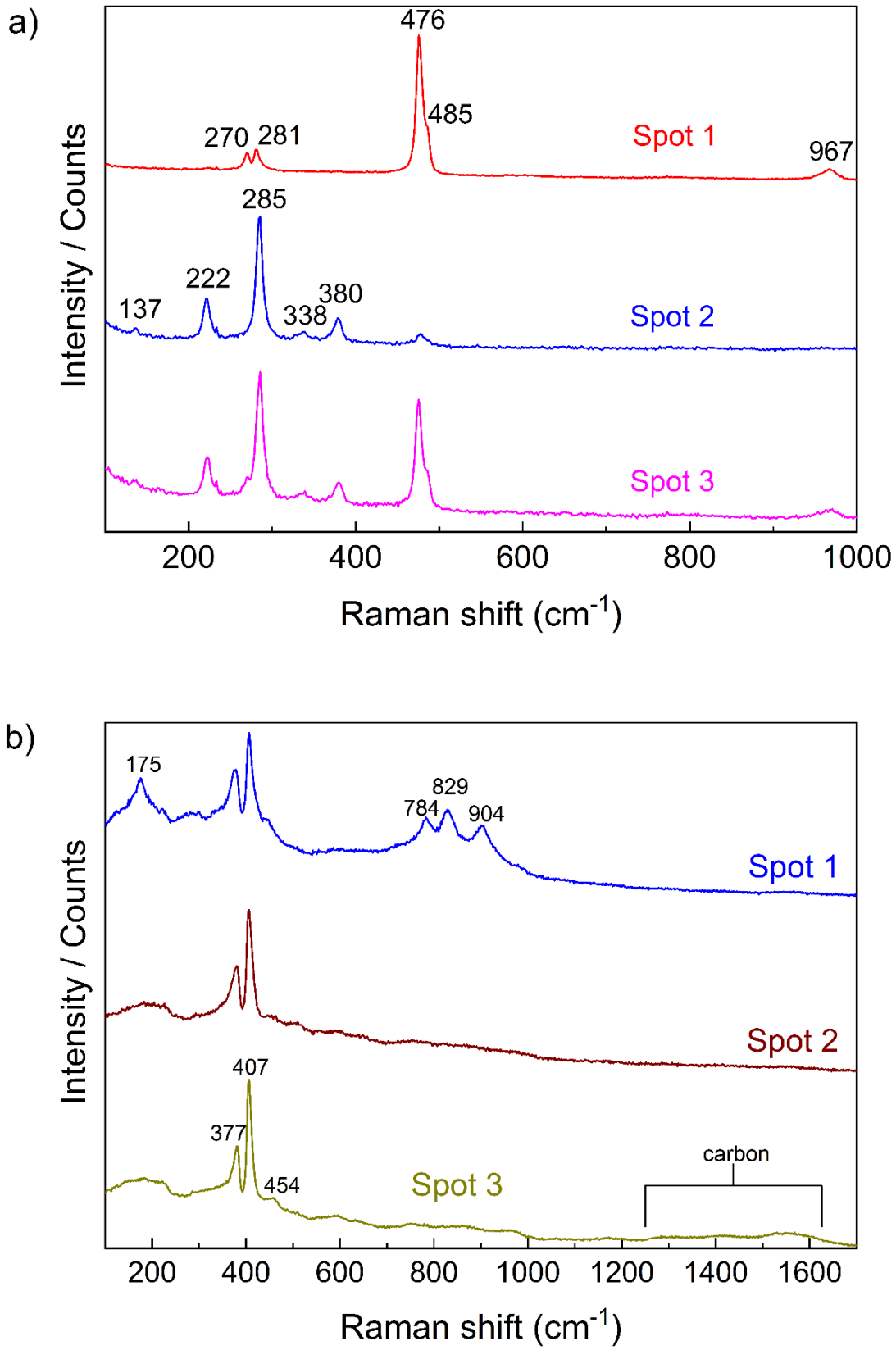

Figure C2. *Profiles obtained from the application of Raman spectroscopy analysis to different spots of (a) NiS_x and (b) MoS_x catalysts.*

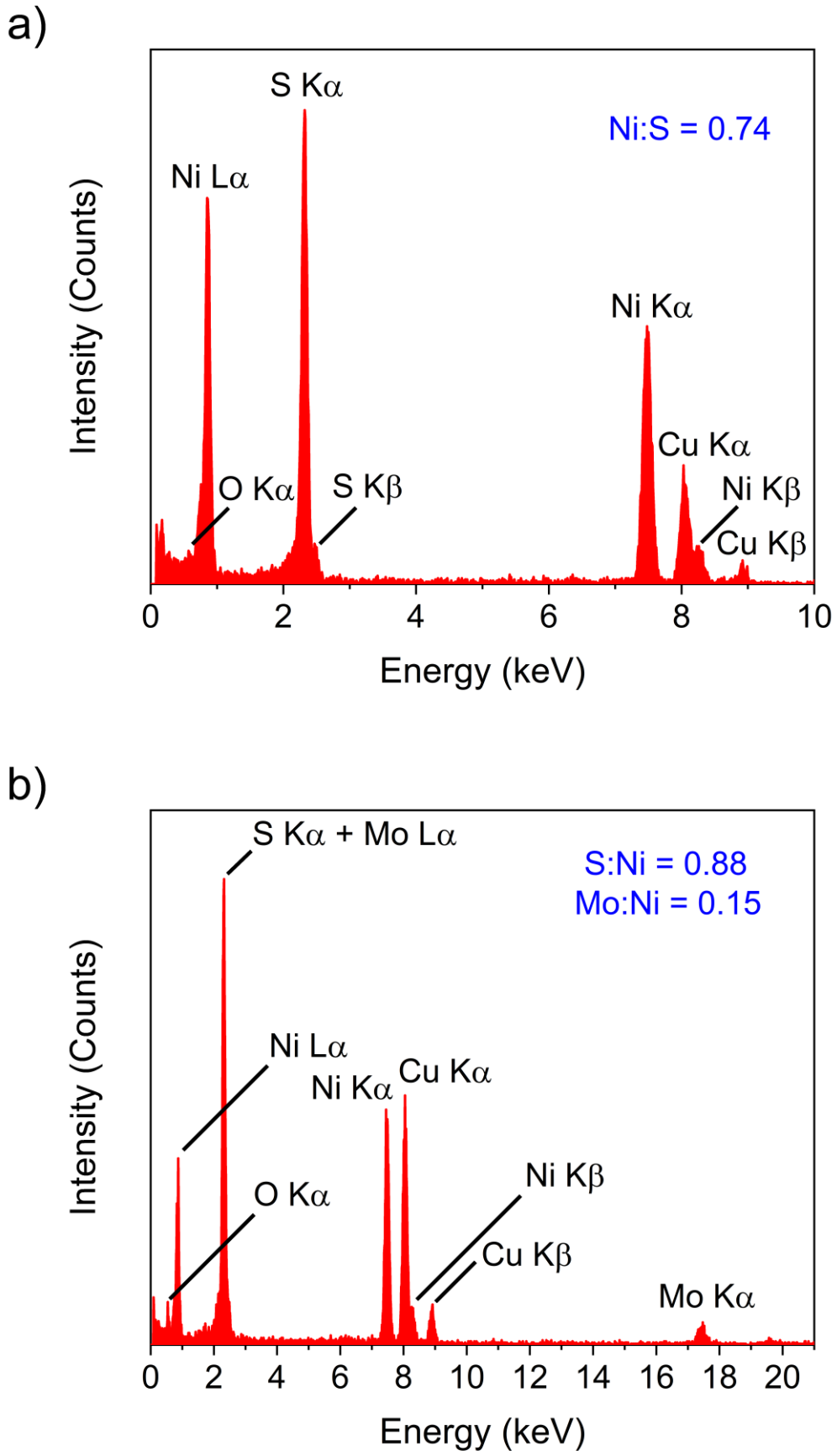

Figure C3. *EDS spectra of (a) NiS_x and (b) crystallized particles present in $Ni_{0.5}Mo_{0.5}S_x$, as illustrated in Figure V.2i.*

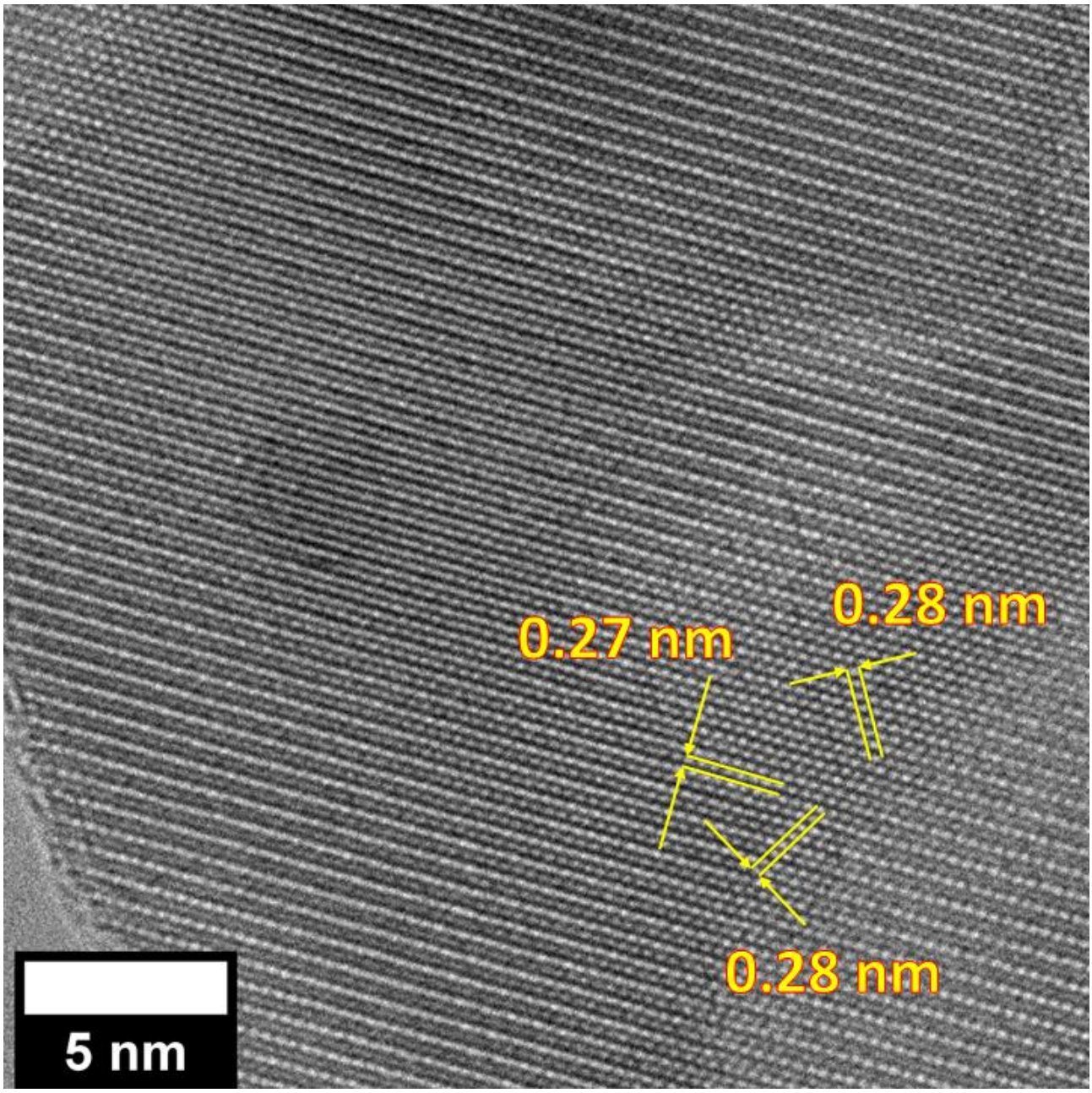

Figure C4. *HRTEM micrograph of* NiS_x.

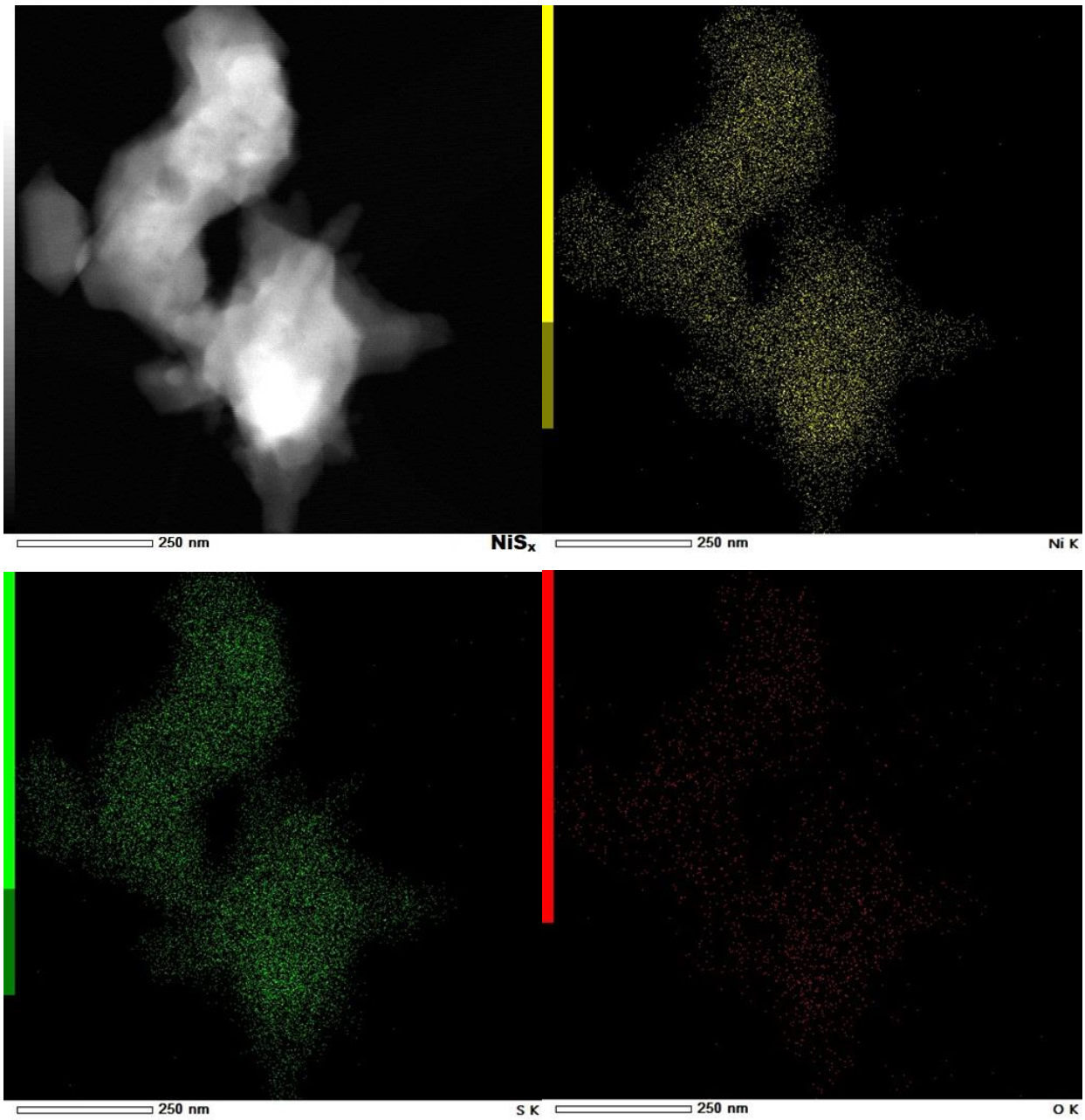

Figure C5. *Elemental mapping of NiS_x. Gray scale image represents the original figure, while the images in yellow, green, and red were generated according to the spots where nickel, sulfur, and oxygen, respectively, were identified.*

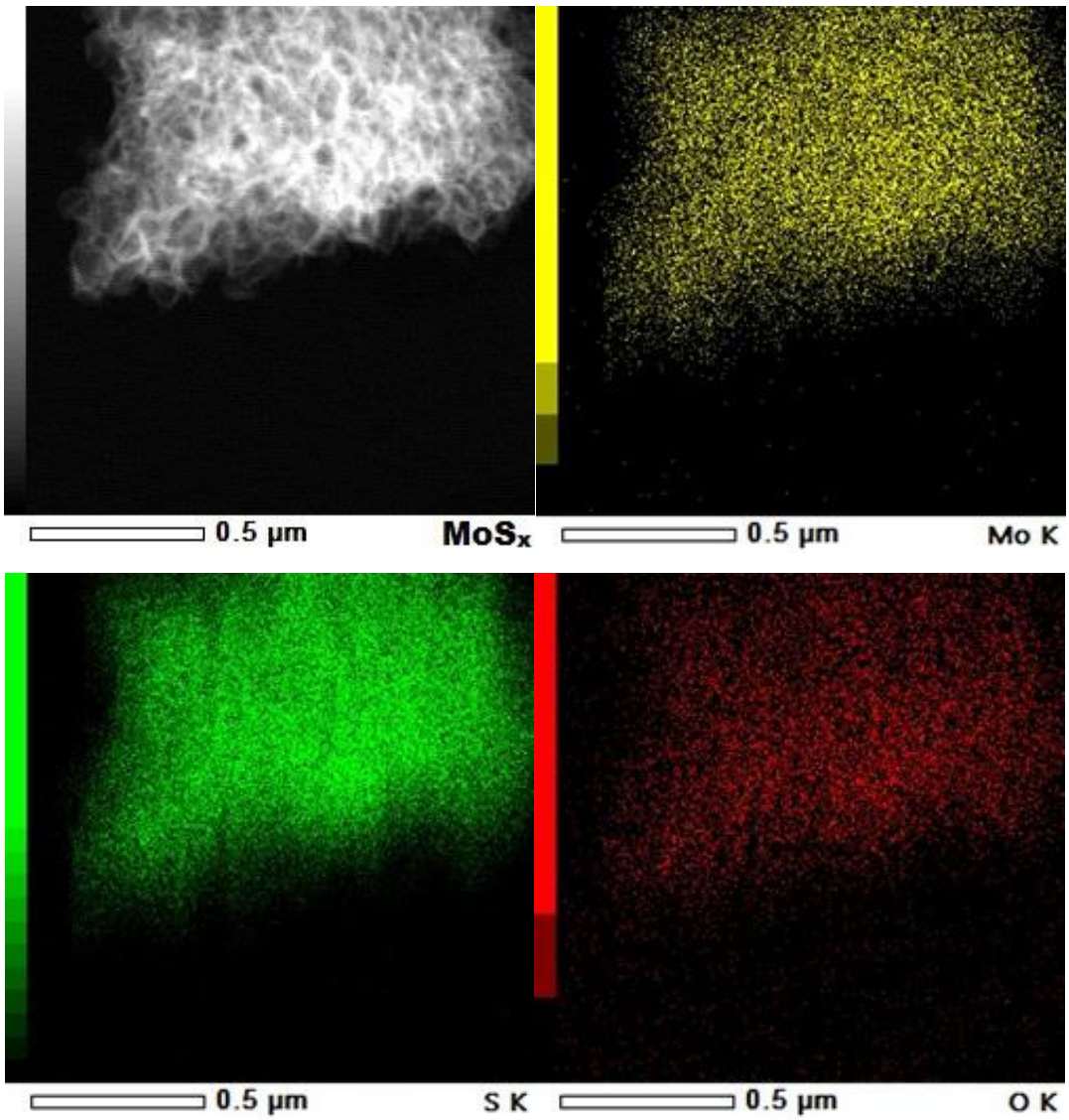

Figure C6. *Elemental mapping of MoS_x. Gray scale image represents the original figure, while the images in yellow, green, and red were generated according to the spots where molybdenum, sulfur and oxygen, respectively, were identified.*

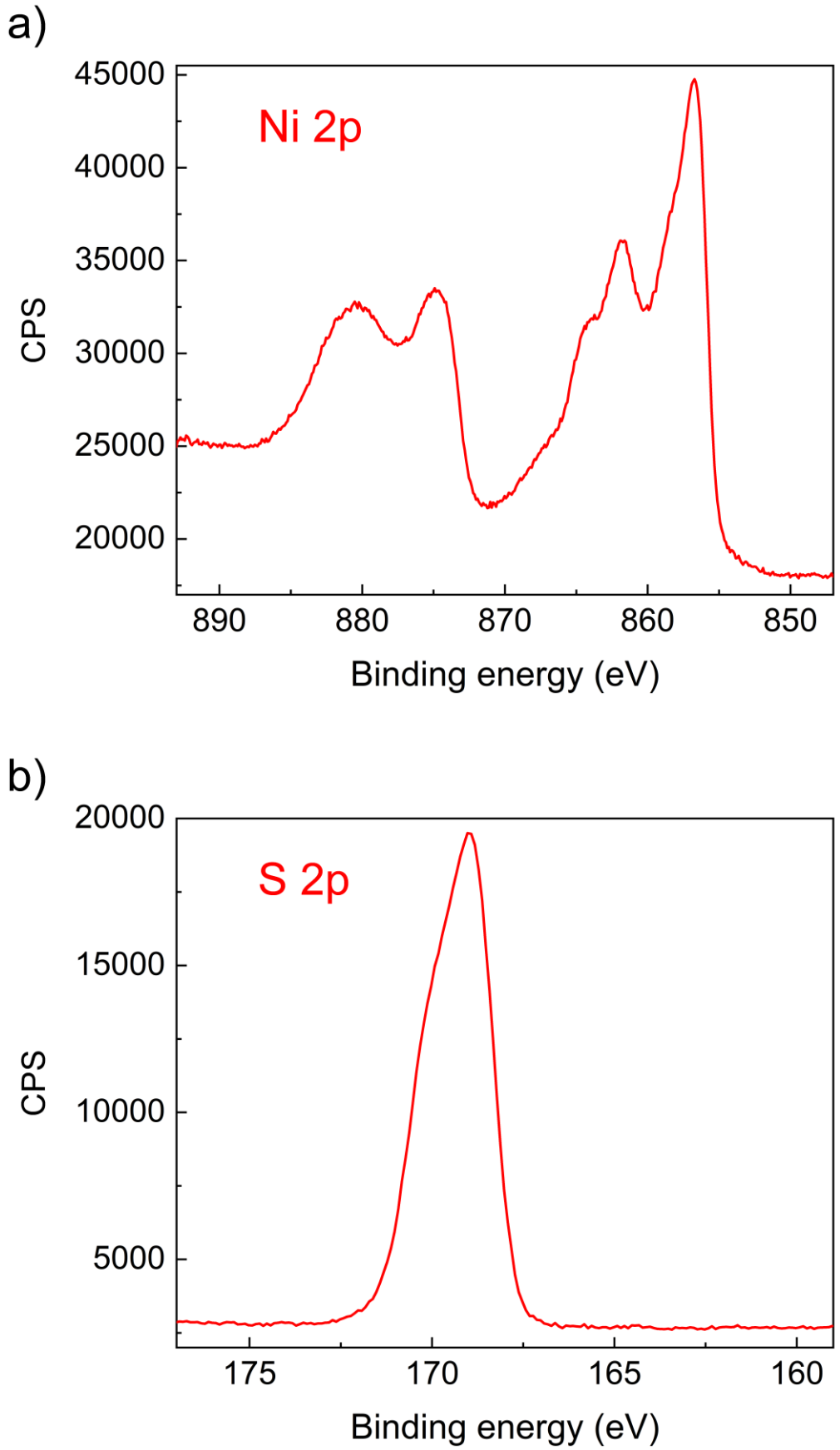

Figure C7. *(a) Ni 2p and (b) S 2p spectra of a commercial nickel sulfate heptahydrate.*

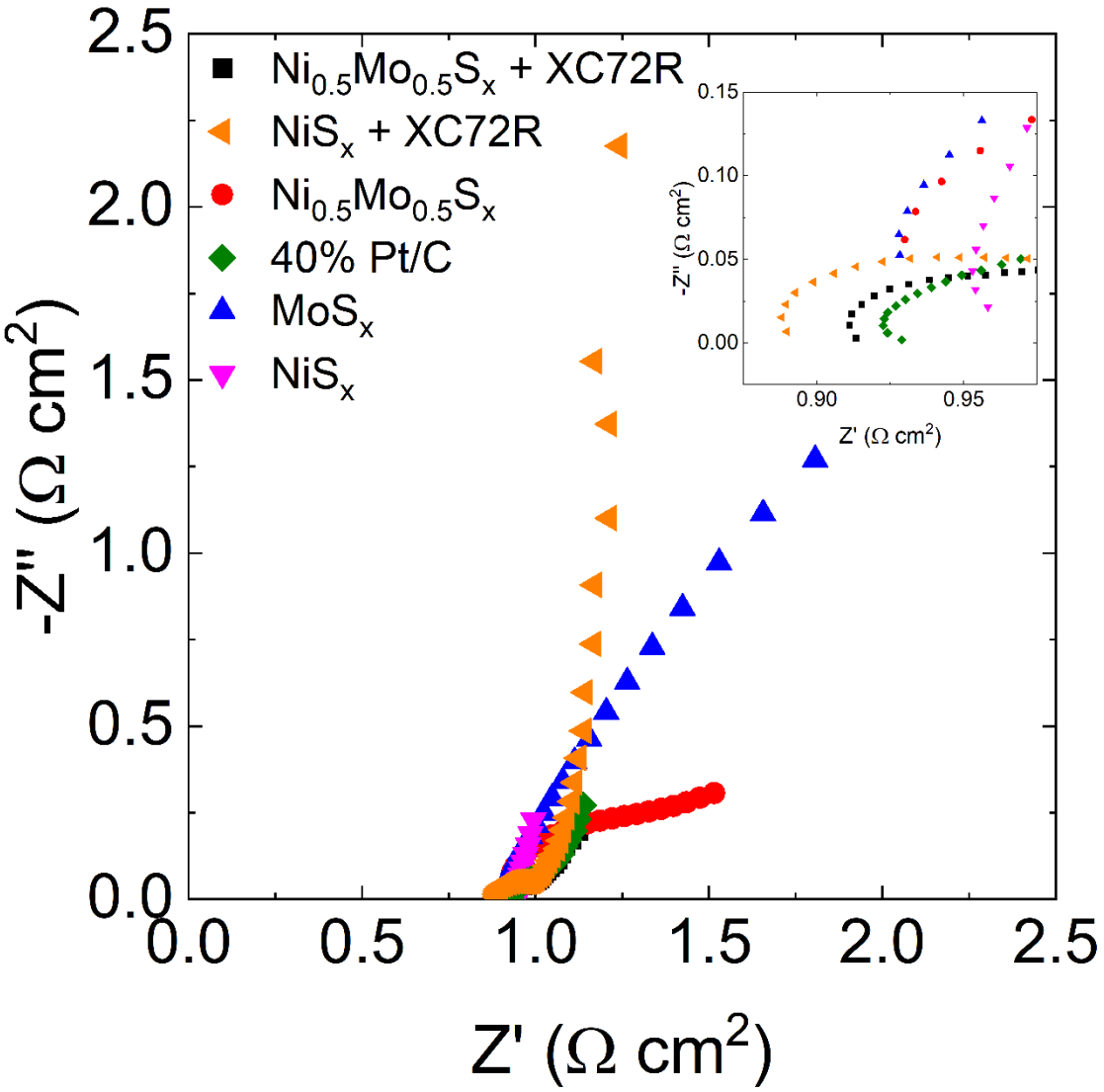

Figure C8. *Nyquist plot from data collected by the application of electrochemical impedance spectroscopy at open circuit potential. It was applied an amplitude of 10 mV and analyzed 10 points per decade.*

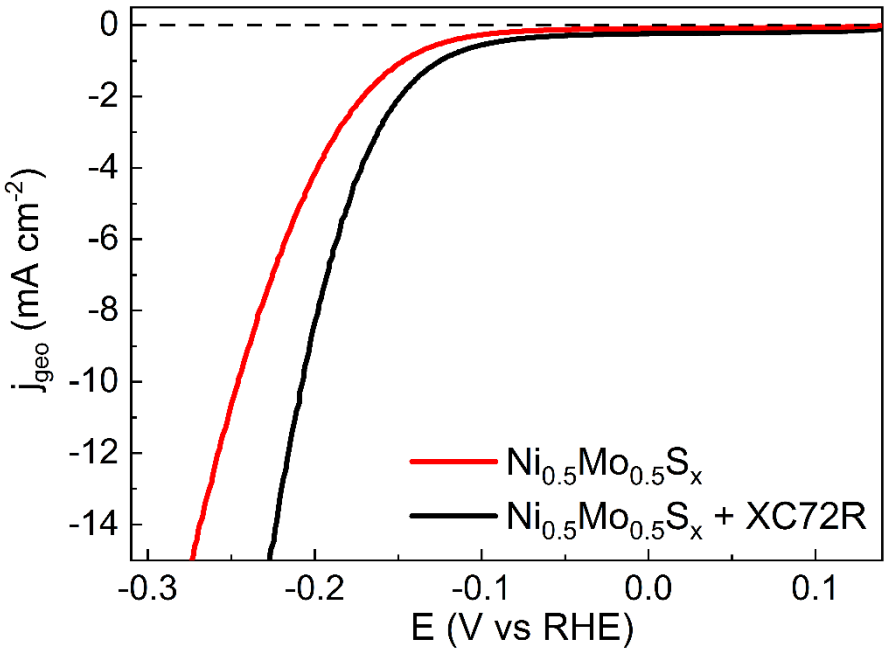

Figure C9. *Ohmic-drop compensated polarization curves obtained from the second scan of LSV technique analysis for $Ni_{0.5}Mo_{0.5}S_x$ and its physical mixture with Carbon Vulcan XC72R.*

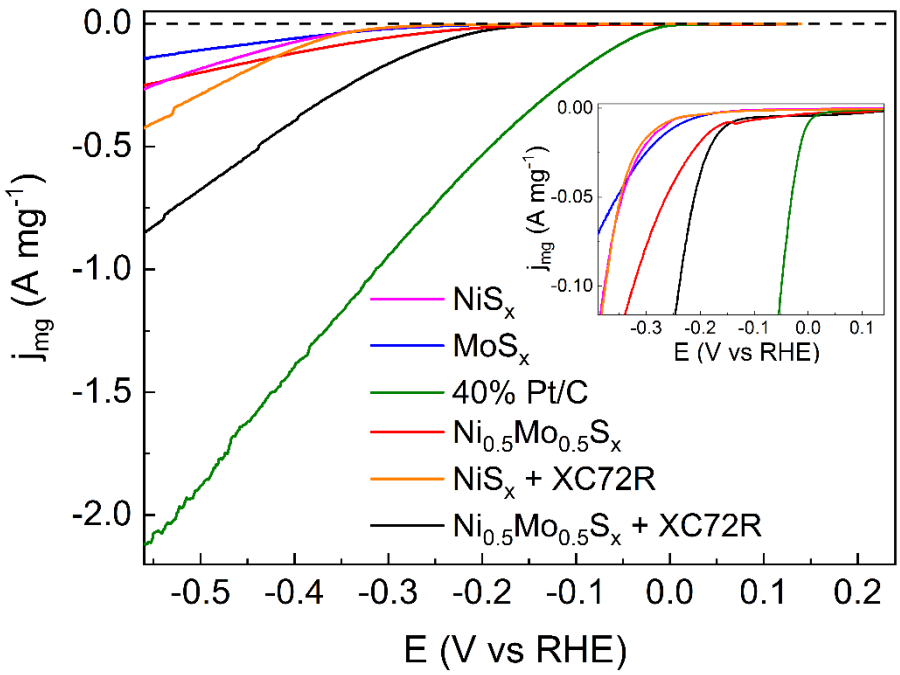

Figure C10. *Uncompensated polarization curves obtained by catalyst mass loading normalization. Inset: iR-drop compensated polarization curves at low current region.*

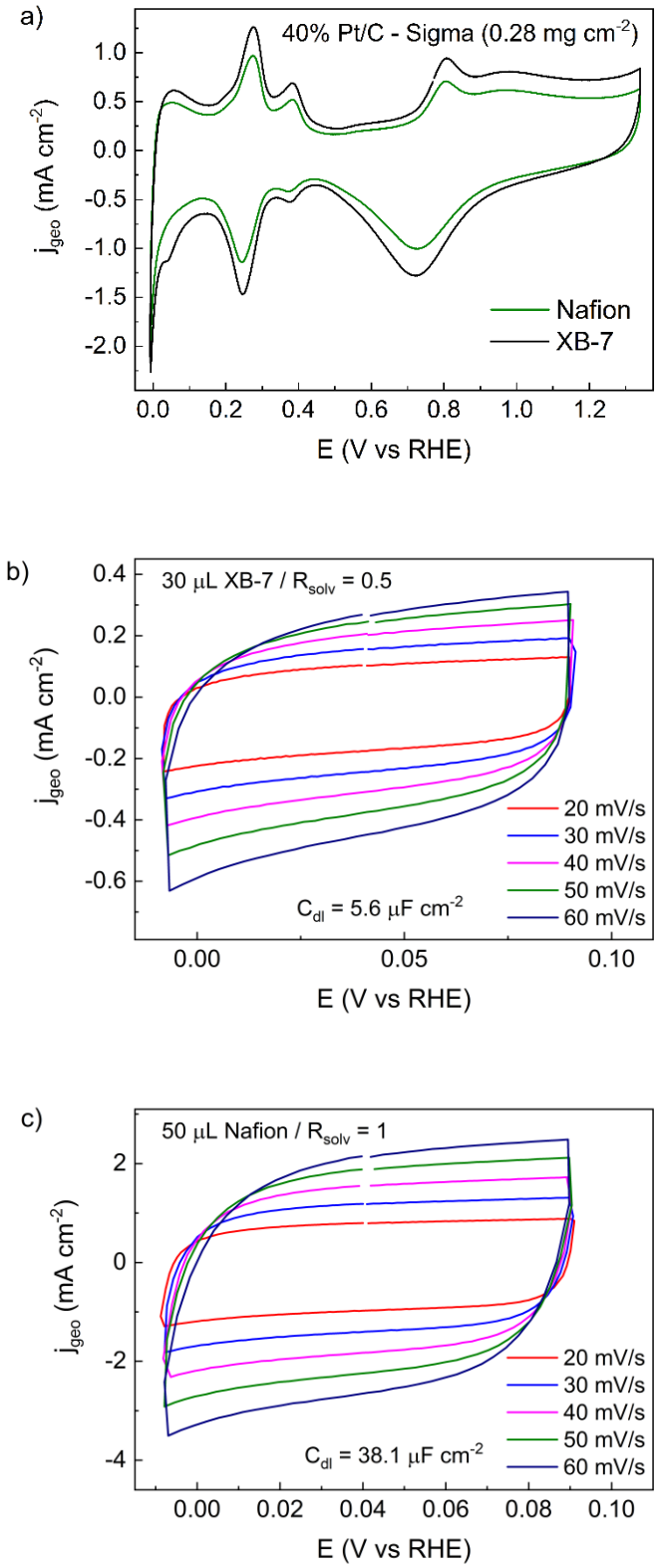

Figure C11. *CV analyses performed in N_2 saturated 1 M KOH for (a) 40% Pt/C in association with Nafion and XB-7 at 20 mV s^{-1} and $Ni_{0.5}Mo_{0.5}S_x$ obtained from inks containing (b) 30 µL of XB-7 and R_{solv} = 0.5 and (c) 50 µL of Nafion and R_{solv} = 1 at varying scan rates (20-60 mV s^{-1}).*

General Conclusion and Perspectives

The replacement of most traditional processes for hydrogen generation by its electrochemical production, supplied by green energies, is considered an important step in the fight against climate change. Such production occurs by the water electrolysis reaction, in which hydrogen is produced in cathodic compartment and oxygen is generated in the anodic one. The half-reaction at the cathode (HER) needs the use of a catalyst to perform with a higher efficiency, and the benchmark catalysts are platinum-based materials. Nonetheless, the high cost of these materials increases the capital cost of the process, besides to have their application limited due to the very low availability of platinum in earth. Hence, the aim of the work presented in this manuscript was to propose low-cost and earth-abundant catalysts that can replace platinum as HER catalyst, overcoming then the aforementioned limitations for consolidation of water electrolysis in worldwide hydrogen production.

Given that alkaline media allows the use of non-noble metals in operation and alkaline water electrolyzers using diaphragm as compartments separator can't operate at high current densities, AEMWE technology, although not so close to its maturity, was chosen as the focus of electrocatalysts application. The extensive bibliographic study allowed the identification of molybdenum sulfide species as promising class of materials for the replacement of platinum. Despite that, HER in alkaline environments requires the additional step of water dissociation which limits molybdenum sulfide HER kinetics.

The strategy applied to surpass this hindrance concerning the water activation was the combination of molybdenum sulfide with another phase, which was responsible to accelerate the water dissociation. Therefore, a sulfide formulation containing Co and Mo was developed. Since the conception of the work involved the development of catalyst for large scale application in future, a simple synthesis methodology was adopted on purpose, envisaging a simpler scaling up. Catalysts were synthesized by a hydrothermal method, i.e., using water as solvent, and without the use of any surfactant. Physicochemical characterizations revealed the existence of 2H-MoS_2 nanosheets, some regions containing them with bigger lateral size and stacking degree than others, associated to CoS phase; ternary cobalt molybdenum sulfides were also identified. Electrochemical characterizations showed that $Co_{0.5}Mo_{0.5}S_x$ presented a superior catalytic activity due to a bifunctional system,

in which, water dissociation was boosted by cobalt, while 2H-MoS_2 performed its role as good hydrogen evolution catalyst. Nonetheless, it cannot be neglected neither that cobalt sulfide also showed HER activity alone nor that electronic effects arising from a possible cobalt doping in molybdenum sulfide can enhance its activity.

This promising $Co_{0.5}Mo_{0.5}S_x$ catalyst, as well as CoS_x and MoS_x, was applied as a cathode of an AEMWE device, assembled with a Sustainion® X37-50 membrane and Ir black anode, which played a role as benchmark OER catalyst. The same activity trend verified in three-electrode cell was reproduced in AEMWE configuration. Interestingly, the cell was set at 50 ^{o}C and operated with a 0.1 mol L^{-1} KOH solution recirculation in the anode compartment, a concentration ten times lower than commonly applied in the literature. The $Co_{0.5}Mo_{0.5}S_x$ // Ir single cell delivered a current density of 1.22 A cm^{-2} at 2 V. As far as we know, this is the best performance for an earth-abundant cathode in a system operating with such diluted concentration of supporting electrolyte; besides to be the first report of molybdenum-based sulfide catalyst applied to AEMWE system. The $Co_{0.5}Mo_{0.5}S_x$ // Ir cell was submitted to 40 h of stability testing at 2 V. It was verified that most of current decay was reversible by stopping voltage application, which was attributed to the release of bubbles from catalyst surface and cell channels. On the other hand, the irreversible current decay accrued from the segregation between cobalt and molybdenum, which certainly impacts the catalyst activity once the bifunctional behavior is expected to be favored with a better contact of phases.

An expansion of the study was performed by replacing cobalt by nickel. Nickel molybdenum sulfide was synthesized by the same methodology and evaluated as HER catalyst. Contrary to cobalt, instead of nickel sulfide, nickel sulfate was identified in the bimetallic sulfide, although the expected nickel sulfide phases were encountered in monometallic nickel sulfide. Such oxidation degree of nickel phases during synthesis was attributed to the particle size parameter; being smaller particle more susceptible to oxidation. Furthermore, surface analysis indicated the presence of nickel oxides at the surface of bimetallic catalyst, which is interesting once this phase has already been proved to perform well the water dissociation. As consequence, the synergy effect derived from a good water dissociation catalyst and 2H-MoS_2 was again verified. Nonetheless, it was revealed that only replacing Nafion® by Sustainion® XB-7 ionomer in $Ni_{0.5}Mo_{0.5}S_x$ ink formulation led to a decrease of electrocatalyst performance; the opposite of 40 % Pt/C.

Then, a study of catalytic ink formulation comprising a transition metal sulfide, specifically $Ni_{0.5}Mo_{0.5}S_x$, and Sustainion® XB-7 was performed for the first time herein. It was unveiled that the amount of ionomer must be reduced when replacing Nafion® by Sustainion® to maintain a comparable activity. In addition, the solvent ratio played an important role in $Ni_{0.5}Mo_{0.5}S_x$ activity, which became better with higher volume of isopropanol than water, although the complete removal of water also decreases the electrocatalyst performance. This study demonstrated how important is the study of catalyst/ionomer interaction to avoid a misevaluation of catalyst performance.

This work open venues to many possible studies, some of them already in progress, others envisaged. First, a better understanding of the synthesis can be obtained to have the possibility of tuning the electrocatalysts. Thermal gravimetric analysis coupled to a mass spectrometer (TGA-MS), to identify generated gases during heat treatment, has been applied to the solid precipitated during addition of the sulfur precursor to the metallic solution. The results are being used to determine the solid obtained during monometallic sulfide synthesis, besides to evaluate the influence of a second metal in this solid precipitation. Furthermore, some aliquots of resultant solutions, obtained from hydrothermal treatment stopped at specific times below 24 h, have been collected and investigated in UV-visible spectroscopy. It allows the identification of intermediates, besides to give clues whether or not the mechanism of crystal growth of some phases can be influenced by additional species in the synthetic environment.

Another aspect that has been investigated is the influence of hydrothermal synthesis time on $Co_{0.5}Mo_{0.5}S_x$ characteristics and activity. To do so, XRD, Raman, XPS, LSV and CV analyses have been applied. The last one is very low explored for transition metal sulfides for researchers, although a good correlation between CV and physicochemical characterizations can advance the comprehension of sulfides behavior. Some attempts of supporting cobalt molybdenum sulfide in carbon-based materials were also done and continue to be envisaged. It could be also interesting to test carbon with different morphologies, which may play a role in sulfide characteristics (e.g., introduction of strain) and bubbles release ability. The study of trimetallic sulfide, comprising Ni, Co, and Mo, can also be interesting.

Additional tests in AEMWE have been performed, including with Ni-based catalysts. Besides that, the expansion of post-mortem analysis alternatives and the analysis of

supporting electrolyte used during stability testing are envisaged. Benchmark materials have also been analyzed to promote an extended comparison of catalysts activity and stability. Finally, the replacement of Ir black by a non-noble-based anode in AEMWE single cell is envisaged, to fill out a system completely free of noble metals.

Scientific Production List

Peer-reviewed journal publications:

- INOCÊNCIO, C.V.M.; ROUSSEAU, J.; GUIGNARD, N.; CANAFF, C.; MORISSET, S.; NAPPORN, T.; MORAIS, C.; KOKOH, K.B. HER activity of nickel molybdenum sulfide electrocatalyst as function of the ionomer in the ink formulation. INTERNATIONAL JOURNAL OF HYDROGEN ENERGY, 2022. Accepted. (DOI: 10.1016/j.ijhydene.2022.10.138)

- INOCÊNCIO, C.V.M.; FOUDA-ONANA, F.; ROUSSEAU, J.; GUIGNARD, N.; NAPPORN, T.; MORAIS, C.; KOKOH, K.B. A step forward: Hydrogen production on cobalt molybdenum sulfide electrocatalyst in anion exchange membrane water electrolyzer. ACS APPLIED ENERGY MATERIALS, 5, 10396, 2022.

- INOCÊNCIO, C.V.M.; ROUSSEAU, J.; GUIGNARD, N.; CANAFF, C.; MORISSET, S.; COMMINGES, C.; MORAIS, C.; KOKOH, K.B. Taking advantage of teamwork: Unsupported cobalt molybdenum sulfide as an active HER electrocatalyst in alkaline media. JOURNAL OF THE ELECTROCHEMICAL SOCIETY, 169, 054524, 2022.

- INOCÊNCIO, C.V.M.; HOLADE, Y.; MORAIS, C.; KOKOH, K.B; NAPPORN, T. Electrochemical hydrogen generation technology: Challenges in electrodes materials for a sustainable energy. ELECTROCHEMICAL SCIENCE ADVANCES, e2100206, 2022. In press. (DOI: 10.1002/elsa.202100206)

Oral Communications:

- Cobalt molybdenum sulfide as alternative cathode for anion exchange membrane water electrolyzer. **3rd International Conference on Materials Science & Nanotechnology**, 2022. Rome, Italy.

- A step forward: Hydrogen production on cobalt molybdenum sulfide electrocatalyst in anion exchange membrane water electrolyzer. **HYPOTHESIS XVII**, 2022.

- Earth-abundant electrocatalysts for water electrolysis: application in alkaline media. **HYPOTHESIS XVI**, 2021.

- Taking advantage of teamwork: Unsupported cobalt molybdenum sulfide as an active HER electrocatalyst in alkaline media. **1ère REUNION PLENIERE de la FRH2 du CNRS**, 2021.

- Transition metal sulfide-based electrocatalysts for hydrogen evolution reaction in alkaline environment. **239th ECS Meeting**, 2021.

REFERENCES

1. Arrhenius, S., On the Influence of Carbonic Acid in the Air upon the Temperature of the Ground. *Philosophical Magazine and Journal of Science* **1896,** *41*, 237-276.
2. Callendar, G. S., The artificial production of carbon dioxide and its influence on temperature. *Quarterly Journal of the Royal Meteorological Society* **1938,** *64*, 223-240.
3. Chatenet, M.; Pollet, B. G.; Dekel, D. R.; Dionigi, F.; Deseure, J.; Millet, P.; Braatz, R. D.; Bazant, M. Z.; Eikerling, M.; Staffell, I.; Balcombe, P.; Shao-Horn, Y.; Schafer, H., Water electrolysis: from textbook knowledge to the latest scientific strategies and industrial developments. *Chemical Society Reviews* **2022,** *51* (11), 4583-4762.
4. Inocêncio, C. V. M.; Holade, Y.; Morais, C.; Kokoh, K. B.; Napporn, T. W., Electrochemical Hydrogen Generation Technology: Challenges in electrodes materials for a Sustainable Energy. *Electrochemical Science Advances* **2022**, In Press. Track.
5. Hinnemann, B.; Moses, P. G.; Bonde, J.; Jørgensen, K. P.; Nielsen, J. H.; Horch, S.; Chorkendorff, I.; Nørskov, J. K., Biomimetic hydrogen evolution: MoS2 nanoparticles as catalyst for hydrogen evolution. *Journal of the American Chemical Society* **2005,** *127*, 5308-5309.
6. Meng, C.; Chen, X.; Gao, Y.; Zhao, Q.; Kong, D.; Lin, M.; Chen, X.; Li, Y.; Zhou, Y., Recent Modification Strategies of MoS2 for Enhanced Electrocatalytic Hydrogen Evolution. *Molecules* **2020,** *25*, 1136.
7. Seo, B.; Joo, S. H., Recent advances in unveiling active sites in molybdenum sulfide-based electrocatalysts for the hydrogen evolution reaction. *Nano convergence* **2017,** *4* (1), 19.
8. Yan, Y.; Xia, B.; Xu, Z.; Wang, X., Recent development of molybdenum sulfides as advanced electrocatalysts for hydrogen evolution reaction. *ACS Catalysis* **2014,** *4*, 1693-1705.
9. Lewis, N. S., Aspects of science and technology in support of legal and policy frameworks associated with a global carbon emissions-control regime. *Energy & Environmental Science* **2016,** *9* (7), 2172-2176.
10. Yu, E. H.; Wang, X.; Krewer, U.; Li, L.; Scott, K., Direct oxidation alkaline fuel cells: from materials to systems. *Energy & Environmental Science* **2012,** *5* (2), 5668-5680.
11. Holladay, J. D.; Hu, J.; King, D. L.; Wang, Y., An overview of hydrogen production technologies. *Catalysis Today* **2009,** *139* (4), 244-260.
12. Zheng, Y.; Jiao, Y.; Qiao, S. Z., Engineering of Carbon-Based Electrocatalysts for Emerging Energy Conversion: From Fundamentality to Functionality. *Advanced Materials* **2015,** *27* (36), 5372-5378.
13. Shi, Y.; Zhang, B., Recent advances in transition metal phosphide nanomaterials: synthesis and applications in hydrogen evolution reaction. *Chemical Society Reviews* **2016,** *45* (6), 1529-1541.
14. Zou, X.; Zhang, Y., Noble metal-free hydrogen evolution catalysts for water splitting. *Chemical Society Reviews* **2015,** *44* (15), 5148-5180.
15. Turner, J. A., A Realizable Renewable Energy Future. *Science* **1999,** *285* (5428), 687-689.

16. Walter, M. G.; Warren, E. L.; McKone, J. R.; Boettcher, S. W.; Mi, Q.; Santori, E. A.; Lewis, N. S., Solar Water Splitting Cells. *Chemical Reviews* **2010,** *110* (11), 6446-6473.

17. Lewis, N. S.; Nocera, D. G., Powering the planet: Chemical challenges in solar energy utilization. *Proceedings of the National Academy of Sciences* **2006,** *103* (43), 15729-15735.

18. Cook, T. R.; Dogutan, D. K.; Reece, S. Y.; Surendranath, Y.; Teets, T. S.; Nocera, D. G., Solar Energy Supply and Storage for the Legacy and Nonlegacy Worlds. *Chemical Reviews* **2010,** *110* (11), 6474-6502.

19. Bard, A. J.; Faulkner, L. R., *Electrochemical Methods: Fundamentals and Applications*. 2nd ed.; John Wiley & Sons, Inc.: USA, 2001; p 850.

20. Norskov, J. K.; Bligaard, T.; Rossmeisl, J.; Christensen, C. H., Towards the computational design of solid catalysts. *Nat Chem* **2009,** *1* (1), 37-46.

21. Faber, M. S.; Jin, S., Earth-abundant inorganic electrocatalysts and their nanostructures for energy conversion applications. *Energy & Environmental Science* **2014,** *7* (11), 3519-3542.

22. Sheng, W.; Zhuang, Z.; Gao, M.; Zheng, J.; Chen, J. G.; Yan, Y., Correlating hydrogen oxidation and evolution activity on platinum at different pH with measured hydrogen binding energy. *Nat Commun* **2015,** *6*, Article number: 5848.

23. Chen, W. F.; Wang, C. H.; Sasaki, K.; Marinkovic, N.; Xu, W.; Muckerman, J. T.; Zhu, Y.; Adzic, R. R., Highly active and durable nanostructured molybdenum carbide electrocatalysts for hydrogen production. *Energy & Environmental Science* **2013,** *6* (3), 943-951.

24. Greeley, J.; Jaramillo, T. F.; Bonde, J.; Chorkendorff, I.; Norskov, J. K., Computational high-throughput screening of electrocatalytic materials for hydrogen evolution. *Nat Mater* **2006,** *5* (11), 909-13.

25. Benck, J. D.; Hellstern, T. R.; Kibsgaard, J.; Chakthranont, P.; Jaramillo, T. F., Catalyzing the Hydrogen Evolution Reaction (HER) with Molybdenum Sulfide Nanomaterials. *ACS Catalysis* **2014,** *4* (11), 3957-3971.

26. Luo, J.; Im, J.-H.; Mayer, M. T.; Schreier, M.; Nazeeruddin, M. K.; Park, N.-G.; Tilley, S. D.; Fan, H. J.; Grätzel, M., Water photolysis at 12.3% efficiency via perovskite photovoltaics and Earth-abundant catalysts. *Science* **2014,** *345* (6204), 1593-1596.

27. Nørskov, J. K.; Bligaard, T.; Logadottir, A.; Kitchin, J. R.; Chen, J. G.; Pandelov, S.; Stimming, U., Trends in the Exchange Current for Hydrogen Evolution. *Journal of The Electrochemical Society* **2005,** *152* (3), J23-J26.

28. Liao, L.; Wang, S.; Xiao, J.; Bian, X.; Zhang, Y.; Scanlon, M. D.; Hu, X.; Tang, Y.; Liu, B.; Girault, H. H., A nanoporous molybdenum carbide nanowire as an electrocatalyst for hydrogen evolution reaction. *Energy and Environmental Science* **2014,** *7*, 387-392.

29. Vrubel, H.; Moehl, T.; Grätzel, M.; Hu, X., Revealing and accelerating slow electron transport in amorphous molybdenum sulphide particles for hydrogen evolution reaction. *ChemComm* **2013,** *49*, 8985-8987.

30. Kozuch, S.; Martin, J. M. L., "Turning Over" Definitions in Catalytic Cycles. *ACS Catalysis* **2012,** *2* (12), 2787-2794.

31. Lente, G., Comment on "'Turning Over' Definitions in Catalytic Cycles". *ACS Catalysis* **2013**, 381-382.

32. Choi, J.-H.; Park, K.-W.; Kwon, B.-K.; Sung, Y.-E., Methanol Oxidation on Pt/Ru, Pt/Ni, and Pt/Ru/Ni Anode Electrocatalysts at Different Temperatures for DMFCs. *Journal of The Electrochemical Society* **2003,** *150* (7), A973-A978.

33. Paulus, U. A.; Wokaun, A.; Scherer, G. G.; Schmidt, T. J.; Stamenkovic, V.; Markovic, N. M.; Ross, P. N., Oxygen reduction on high surface area Pt-based alloy catalysts in comparison to well defined smooth bulk alloy electrodes. *Electrochimica Acta* **2002,** *47* (22–23), 3787-3798.

34. Zhang, Y.; Gu, Y.-e.; Lin, S.; Wei, J.; Wang, Z.; Wang, C.; Du, Y.; Ye, W., One-step synthesis of PtPdAu ternary alloy nanoparticles on graphene with superior methanol electrooxidation activity. *Electrochimica Acta* **2011,** *56* (24), 8746-8751.

35. Subbaraman, R.; Tripkovic, D.; Chang, K.-C.; Strmcnik, D.; Paulikas, A. P.; Hirunsit, P.; Chan, M.; Greeley, J.; Stamenkovic, V.; Markovic, N. M., Trends in activity for the water electrolyser reactions on 3d M(Ni,Co,Fe,Mn) hydr(oxy)oxide catalysts. *Nat Mater* **2012,** *11* (6), 550-557.

36. Trasatti, S., Work function, electronegativity, and electrochemical behaviour of metals. *Journal of Electroanalytical Chemistry and Interfacial Electrochemistry* **1972,** *39* (1), 163-184.

37. Greeley, J.; Nørskov, J. K.; Kibler, L. A.; El-Aziz, A. M.; Kolb, D. M., Hydrogen Evolution Over Bimetallic Systems: Understanding the Trends. *ChemPhysChem* **2006,** *7* (5), 1032-1035.

38. Yoon, D.; Seo, B.; Lee, J.; Nam, K. S.; Kim, B.; Park, S.; Baik, H.; Hoon Joo, S.; Lee, K., Facet-controlled hollow Rh2S3 hexagonal nanoprisms as highly active and structurally robust catalysts toward hydrogen evolution reaction. *Energy & Environmental Science* **2016,** *9* (3), 850-856.

39. Dessources, S.; Morais, C.; Napporn, T. W.; Kokoh, K. B., Reversible Electrocatalytic Activity of Carbon Supported PtxNi1-x on Hydrogen Reactivity. *ChemPhysChem* **2016**, 17 (23), 3964-3973.

40. Holade, Y.; Morais, C.; Arrii-Clacens, S.; Servat, K.; Napporn, T. W.; Kokoh, K. B., New Preparation of PdNi/C and PdAg/C Nanocatalysts for Glycerol Electrooxidation in Alkaline Medium. *Electrocatalysis* **2013,** *4* (3), 167-178.

41. Lee, S. C.; Holm, R. H., Speculative synthetic chemistry and the nitrogenase problem. *Proceedings of the National Academy of Sciences* **2003,** *100* (7), 3595-3600.

42. Rees, D. C.; Howard, J. B., The Interface Between the Biological and Inorganic Worlds: Iron-Sulfur Metalloclusters. *Science* **2003,** *300* (5621), 929-931.

43. Le Goff, A.; Artero, V.; Jousselme, B.; Tran, P. D.; Guillet, N.; Métayé, R.; Fihri, A.; Palacin, S.; Fontecave, M., From Hydrogenases to Noble Metal–Free Catalytic Nanomaterials for H2 Production and Uptake. *Science* **2009,** *326* (5958), 1384-1387.

44. Kibsgaard, J.; Chen, Z.; Reinecke, B. N.; Jaramillo, T. F., Engineering the surface structure of MoS2 to preferentially expose active edge sites for electrocatalysis. *Nat Mater* **2012,** *11* (11), 963-969.

45. Kong, D.; Wang, H.; Cha, J. J.; Pasta, M.; Koski, K. J.; Yao, J.; Cui, Y., Synthesis of MoS_2 and $MoSe_2$ Films with Vertically Aligned Layers. *Nano Letters* **2013,** *13* (3), 1341-1347.

46. Wang, H.; Kong, D.; Johanes, P.; Cha, J. J.; Zheng, G.; Yan, K.; Liu, N.; Cui, Y., $MoSe_2$ and WSe_2 Nanofilms with Vertically Aligned Molecular Layers on Curved and Rough Surfaces. *Nano Letters* **2013,** *13* (7), 3426-3433.

47. Voiry, D.; Yamaguchi, H.; Li, J.; Silva, R.; Alves, D. C. B.; Fujita, T.; Chen, M.; Asefa, T.; Shenoy, V. B.; Eda, G.; Chhowalla, M., Enhanced catalytic activity in strained chemically exfoliated WS2 nanosheets for hydrogen evolution. *Nat Mater* **2013,** *12* (9), 850-855.

48. Wang, X.-D.; Xu, Y.-F.; Rao, H.-S.; Xu, W.-J.; Chen, H.-Y.; Zhang, W.-X.; Kuang, D.-B.; Su, C.-Y., Novel porous molybdenum tungsten phosphide hybrid nanosheets on carbon cloth for efficient hydrogen evolution. *Energy & Environmental Science* **2016,** *9* (4), 1468-1475.

49. Popczun, E. J.; McKone, J. R.; Read, C. G.; Biacchi, A. J.; Wiltrout, A. M.; Lewis, N. S.; Schaak, R. E., Nanostructured Nickel Phosphide as an Electrocatalyst for the Hydrogen Evolution Reaction. *Journal of the American Chemical Society* **2013,** *135* (25), 9267-9270.

50. Cao, B.; Veith, G. M.; Neuefeind, J. C.; Adzic, R. R.; Khalifah, P. G., Mixed Close-Packed Cobalt Molybdenum Nitrides as Non-noble Metal Electrocatalysts for the Hydrogen Evolution Reaction. *Journal of the American Chemical Society* **2013,** *135* (51), 19186-19192.

51. Kong, D.; Wang, H.; Lu, Z.; Cui, Y., $CoSe_2$ Nanoparticles Grown on Carbon Fiber Paper: An Efficient and Stable Electrocatalyst for Hydrogen Evolution Reaction. *Journal of the American Chemical Society* **2014,** *136* (13), 4897-4900.

52. Chhetri, M.; Maitra, S.; Chakraborty, H.; Waghmare, U. V.; Rao, C. N. R., Superior performance of borocarbonitrides, BxCyNz, as stable, low-cost metal-free electrocatalysts for the hydrogen evolution reaction. *Energy & Environmental Science* **2016**.

53. Tributsch, H.; Bennett, J. C., Electrochemistry and photochemistry of MoS2 layer crystals. I. *Journal of Electroanalytical Chemistry and Interfacial Electrochemistry* **1977,** *81* (1), 97-111.

54. Hinnemann, B.; Moses, P. G.; Bonde, J.; Jørgensen, K. P.; Nielsen, J. H.; Horch, S.; Chorkendorff, I.; Nørskov, J. K., Biomimetic Hydrogen Evolution: MoS_2 Nanoparticles as Catalyst for Hydrogen Evolution. *Journal of the American Chemical Society* **2005,** *127* (15), 5308-5309.

55. Jaramillo, T. F.; Jørgensen, K. P.; Bonde, J.; Nielsen, J. H.; Horch, S.; Chorkendorff, I., Identification of Active Edge Sites for Electrochemical H_2 Evolution from MoS_2 Nanocatalysts. *Science* **2007,** *317* (5834), 100-102.

56. Gopalakrishnan, D.; Damien, D.; Shaijumon, M. M., MoS2 Quantum Dot-Interspersed Exfoliated MoS2 Nanosheets. *ACS Nano* **2014,** *8* (5), 5297-5303.

57. Karunadasa, H. I.; Montalvo, E.; Sun, Y.; Majda, M.; Long, J. R.; Chang, C. J., A Molecular MoS_2 Edge Site Mimic for Catalytic Hydrogen Generation. *Science* **2012,** *335* (6069), 698-702.

58. Yan, Y.; Xia, B.; Xu, Z.; Wang, X., Recent Development of Molybdenum Sulfides as Advanced Electrocatalysts for Hydrogen Evolution Reaction. *ACS Catalysis* **2014,** *4* (6), 1693-1705.

59. Ambrosi, A.; Sofer, Z.; Pumera, M., Lithium Intercalation Compound Dramatically Influences the Electrochemical Properties of Exfoliated MoS2. *Small* **2015,** *11* (5), 605-612.

60. Gholamvand, Z.; McAteer, D.; Harvey, A.; Backes, C.; Coleman, J. N., Electrochemical Applications of Two-Dimensional Nanosheets: The Effect of Nanosheet Length and Thickness. *Chemistry of Materials* **2016,** *28* (8), 2641-2651.

61. Voiry, D.; Salehi, M.; Silva, R.; Fujita, T.; Chen, M.; Asefa, T.; Shenoy, V. B.; Eda, G.; Chhowalla, M., Conducting MoS2 Nanosheets as Catalysts for Hydrogen Evolution Reaction. *Nano Letters* **2013,** *13* (12), 6222-6227.

62. Laursen, A. B.; Kegnaes, S.; Dahl, S.; Chorkendorff, I., Molybdenum sulfides-efficient and viable materials for electro - and photoelectrocatalytic hydrogen evolution. *Energy & Environmental Science* **2012,** *5* (2), 5577-5591.

63. Zhang, L.; Wu, H. B.; Yan, Y.; Wang, X.; Lou, X. W., Hierarchical MoS2 microboxes constructed by nanosheets with enhanced electrochemical properties for lithium storage and water splitting. *Energy & Environmental Science* **2014,** *7* (10), 3302-3306.

64. Wu, Z.; Fang, B.; Wang, Z.; Wang, C.; Liu, Z.; Liu, F.; Wang, W.; Alfantazi, A.; Wang, D.; Wilkinson, D. P., MoS2 Nanosheets: A Designed Structure with High Active Site Density for the Hydrogen Evolution Reaction. *ACS Catalysis* **2013,** *3* (9), 2101-2107.

65. Xie, J.; Zhang, H.; Li, S.; Wang, R.; Sun, X.; Zhou, M.; Zhou, J.; Lou, X. W.; Xie, Y., Defect-Rich MoS2 Ultrathin Nanosheets with Additional Active Edge Sites for Enhanced Electrocatalytic Hydrogen Evolution. *Advanced Materials* **2013,** *25* (40), 5807-5813.

66. Lu, Z.; Zhu, W.; Yu, X.; Zhang, H.; Li, Y.; Sun, X.; Wang, X.; Wang, H.; Wang, J.; Luo, J.; Lei, X.; Jiang, L., Ultrahigh Hydrogen Evolution Performance of Under-Water "Superaerophobic" MoS2 Nanostructured Electrodes. *Advanced Materials* **2014,** *26* (17), 2683-2687.

67. Chung, D. Y.; Park, S.-K.; Chung, Y.-H.; Yu, S.-H.; Lim, D.-H.; Jung, N.; Ham, H. C.; Park, H.-Y.; Piao, Y.; Yoo, S. J.; Sung, Y.-E., Edge-exposed MoS2 nano-assembled structures as efficient electrocatalysts for hydrogen evolution reaction. *Nanoscale* **2014,** *6* (4), 2131-2136.

68. Yu, Y.; Huang, S.-Y.; Li, Y.; Steinmann, S. N.; Yang, W.; Cao, L., Layer-Dependent Electrocatalysis of MoS2 for Hydrogen Evolution. *Nano Letters* **2014,** *14* (2), 553-558.

69. Shi, J.; Ma, D.; Han, G.-F.; Zhang, Y.; Ji, Q.; Gao, T.; Sun, J.; Song, X.; Li, C.; Zhang, Y.; Lang, X.-Y.; Zhang, Y.; Liu, Z., Controllable Growth and Transfer of Monolayer MoS2 on Au Foils and Its Potential Application in Hydrogen Evolution Reaction. *ACS Nano* **2014,** *8* (10), 10196-10204.

70. Bonde, J.; Moses, P. G.; Jaramillo, T. F.; Norskov, J. K.; Chorkendorff, I., Hydrogen evolution on nano-particulate transition metal sulfide. *Faraday Discussions* **2008,** *140*, 219-231.

71. Chen, T. Y.; Chang, Y. H.; Hsu, C. L.; Wei, K. H.; Chiang, C. Y.; Li, L. J., Comparative study on MoS2 and WS2 for electrocatalytic water splitting. *International Journal of Hydrogen Energy* **2013,** *38*, 12302-12309.

72. Cheng, L.; Huang, W.; Gong, Q.; Liu, C.; Liu, Z.; Li, Y.; Dai, H., Ultrathin WS2 nanoflakes as a high-performance electrocatalyst for the hydrogen evolution reaction. *Angewandte Chemie - International Edition* **2014,** *53*, 7860-7863.

73. Yang, J.; Shin, H. S., Recent advances in layered transition metal dichalcogenides for hydrogen evolution reaction. *Journal of Materials Chemistry A* **2014,** *2*, 5979-5985.

74. Chen, Z.; Cummins, D.; Reinecke, B. N.; Clark, E.; Sunkara, M. K.; Jaramillo, T. F., Core-shell MoO3-MoS2 nanowires for hydrogen evolution: A functional design for electrocatalytic materials. *Nano Letters* **2011,** *11*, 4168-4175.

75. Jaegermann, W.; Schmeisser, D., Reactivity of layer type transition metal chalcogenides towards oxidation. *Surface Science* **1986,** *165*, 143-160.
76. Lauritsen, J. V.; Bollinger, M. V.; Lægsgaard, E.; Jacobsen, K. W.; Nørskov, J. K.; Clausen, B. S.; Topsøe, H.; Besenbacher, F., Atomic-scale insight into structure and morphology changes of MoS 2 nanoclusters in hydrotreating catalysts. *Journal of Catalysis* **2004,** *221*, 510-522.
77. Lukowski, M. A.; Daniel, A. S.; Meng, F.; Forticaux, A.; Li, L.; Jin, S., Enhanced Hydrogen Evolution Catalysis from Chemically Exfoliated Metallic MoS2 Nanosheets. *Journal of the American Chemical Society* **2013,** *135* (28), 10274-10277.
78. Ge, P.; Scanlon, M. D.; Peljo, P.; Bian, X.; Vubrel, H.; O'Neill, A.; Coleman, J. N.; Cantoni, M.; Hu, X.; Kontturi, K.; Liu, B.; Girault, H. H., Hydrogen evolution across nano-Schottky junctions at carbon supported MoS 2 catalysts in biphasic liquid systems. *Chemical Communications* **2012,** *48*, 6484-6486.
79. Liao, L.; Zhu, J.; Bian, X.; Zhu, L.; Scanlon, M. D.; Girault, H. H.; Liu, B., MoS2 formed on mesoporous graphene as a highly active catalyst for hydrogen evolution. *Advanced Functional Materials* **2013,** *23*, 5326-5333.
80. Wang, H.; Liang, Y.; Li, Y.; Dai, H., Co1-xS-graphene hybrid: A high-performance metal chalcogenide electrocatalyst for oxygen reduction. *Angewandte Chemie - International Edition* **2011,** *50*, 10969-10972.
81. Hu, J.; Huang, B.; Zhang, C.; Wang, Z.; An, Y.; Zhou, D.; Lin, H.; Leung, M. K. H.; Yang, S., Engineering stepped edge surface structures of MoS2 sheet stacks to accelerate the hydrogen evolution reaction. *Energy and Environmental Science* **2017,** *10*, 593-603.
82. Wu, Z.; Fang, B.; Bonakdarpour, A.; Sun, A.; Wilkinson, D. P.; Wang, D., WS 2 nanosheets as a highly efficient electrocatalyst for hydrogen evolution reaction. *Applied Catalysis B: Environmental* **2012,** *125*, 59-66.
83. Li, Y.; Wang, H.; Xie, L.; Liang, Y.; Hong, G.; Dai, H., MoS2 nanoparticles grown on graphene: An advanced catalyst for the hydrogen evolution reaction. *Journal of the American Chemical Society* **2011,** *133*, 7296-7299.
84. Bian, X.; Zhu, J.; Liao, L.; Scanlon, M. D.; Ge, P.; Ji, C.; Girault, H. H.; Liu, B., Nanocomposite of MoS 2 on ordered mesoporous carbon nanospheres: A highly active catalyst for electrochemical hydrogen evolution. *Electrochemistry Communications* **2012,** *22*, 128-132.
85. Yang, J.; Voiry, D.; Ahn, S. J.; Kang, D.; Kim, A. Y.; Chhowalla, M.; Shin, H. S., Two-dimensional hybrid nanosheets of tungsten disulfide and reduced graphene oxide as catalysts for enhanced hydrogen evolution. *Angewandte Chemie - International Edition* **2013,** *52*, 13751-13754.
86. Benchakar, M.; Natu, V.; Elmelegy, T. A.; Sokol, M.; Snyder, J.; Comminges, C.; Morais, C.; Célérier, S.; Habrioux, A.; Barsoum, M. W., On a Two-Dimensional MoS2/Mo2CTx Hydrogen Evolution Catalyst Obtained by the Topotactic Sulfurization of Mo2CTx MXene. *Journal of The Electrochemical Society* **2020,** *167*, 124507.
87. Jaramillo, T. F.; Bonde, J.; Zhang, J.; Ooi, B. L.; Andersson, K.; Ulstrup, J.; Chorkendorff, I., Hydrogen evolution on supported incomplete cubane-type [Mo 3S4]4+ electrocatalysts. *Journal of Physical Chemistry C* **2008,** *112*, 17492-17498.

88. Merki, D.; Fierro, S.; Vrubel, H.; Hu, X., Amorphous molybdenum sulfide films as catalysts for electrochemical hydrogen production in water. *Chemical Science* **2011,** *2*, 1262-1267.

89. Merki, D.; Vrubel, H.; Rovelli, L.; Fierro, S.; Hu, X., Fe, Co, and Ni ions promote the catalytic activity of amorphous molybdenum sulfide films for hydrogen evolution. *Chemical Science* **2012,** *3*, 2515-2525.

90. Vrubel, H.; Merki, D.; Hu, X., Hydrogen evolution catalyzed by MoS 3 and MoS 2 particles. *Energy and Environmental Science* **2012,** *5*, 6136-6144.

91. Benck, J. D.; Chen, Z.; Kuritzky, L. Y.; Forman, A. J.; Jaramillo, T. F., Amorphous molybdenum sulfide catalysts for electrochemical hydrogen production: Insights into the origin of their catalytic activity. *ACS Catalysis* **2012,** *2*, 1916-1923.

92. Xu, Q.; Liu, Y.; Jiang, H.; Hu, Y.; Liu, H.; Li, C., Unsaturated Sulfur Edge Engineering of Strongly Coupled MoS2 Nanosheet–Carbon Macroporous Hybrid Catalyst for Enhanced Hydrogen Generation. *Advanced Energy Materials* **2019,** *9*, 3-10.

93. Zhu, J.; Hu, L.; Zhao, P.; Lee, L. Y. S.; Wong, K. Y., Recent Advances in Electrocatalytic Hydrogen Evolution Using Nanoparticles. *Chemical Reviews* **2020,** *120*, 851-918.

94. Lukowski, M. A.; Daniel, A. S.; English, C. R.; Meng, F.; Forticaux, A.; Hamers, R. J.; Jin, S., Highly active hydrogen evolution catalysis from metallic WS2 nanosheets. *Energy and Environmental Science* **2014,** *7*, 2608-2613.

95. Tan, Y.; Liu, P.; Chen, L.; Cong, W.; Ito, Y.; Han, J.; Guo, X.; Tang, Z.; Fujita, T.; Hirata, A.; Chen, M. W., Monolayer MoS2 films supported by 3D nanoporous metals for high-efficiency electrocatalytic hydrogen production. *Advanced Materials* **2014,** *26*, 8023-8028.

96. Yin, Y.; Han, J.; Zhang, Y.; Zhang, X.; Xu, P.; Yuan, Q.; Samad, L.; Wang, X.; Wang, Y.; Zhang, Z.; Zhang, P.; Cao, X.; Song, B.; Jin, S., Contributions of Phase, Sulfur Vacancies, and Edges to the Hydrogen Evolution Reaction Catalytic Activity of Porous Molybdenum Disulfide Nanosheets. *Journal of the American Chemical Society* **2016,** *138*, 7965-7972.

97. Anjum, M. A. R.; Jeong, H. Y.; Lee, M. H.; Shin, H. S.; Lee, J. S., Efficient Hydrogen Evolution Reaction Catalysis in Alkaline Media by All-in-One MoS2 with Multifunctional Active Sites. *Advanced Materials* **2018,** *30*, 1-9.

98. Kim, J.; Byun, S.; Smith, A. J.; Yu, J.; Huang, J., Enhanced electrocatalytic properties of transition-metal dichalcogenides sheets by spontaneous gold nanoparticle decoration. *Journal of Physical Chemistry Letters* **2013,** *4*, 1227-1232.

99. Yang, Y.; Zhang, K.; Lin, H.; Li, X.; Chan, H. C.; Yang, L.; Gao, Q., MoS2-Ni3S2 Heteronanorods as Efficient and Stable Bifunctional Electrocatalysts for Overall Water Splitting. *ACS Catalysis* **2017,** *7*, 2357-2366.

100. Li, H.; Chen, S.; Jia, X.; Xu, B.; Lin, H.; Yang, H.; Song, L.; Wang, X., Amorphous nickel-cobalt complexes hybridized with 1T-phase molybdenum disulfide via hydrazine-induced phase transformation for water splitting. *Nature Communications* **2017,** *8*, 1-11.

101. Eijsbouts, S.; Mayo, S. W.; Fujita, K., Unsupported transition metal sulfide catalysts: From fundamentals to industrial application. *Applied Catalysis A: General* **2007,** *322*, 58-66.

102. Tran, P. D.; Chiam, S. Y.; Boix, P. P.; Ren, Y.; Pramana, S. S.; Fize, J.; Artero, V.; Barber, J., Novel cobalt/nickel-tungsten-sulfide catalysts for electrocatalytic hydrogen generation from water. *Energy & Environmental Science* **2013,** *6* (8), 2452-2459.

103. Mukherji, A.; Bal, R.; Srivastava, R., Understanding the Co : Mo Compositional Modulation and Fe-Interplay in Multicomponent Sulfide Electrocatalysts for Oxygen and Hydrogen Evolution Reactions. *ChemElectroChem* **2020,** *7*, 2740-2751.

104. Sun, Y.; Wang, C.; Ding, T.; Zuo, J.; Yang, Q., Fabrication of amorphous CoMoS 4 as a bifunctional electrocatalyst for water splitting under strong alkaline conditions. **2016**, 18887-18892.

105. Miao, J.; Xiao, F. X.; Bin Yang, H.; Khoo, S. Y.; Chen, J.; Fan, Z.; Hsu, Y. Y.; Ming Chen, H.; Zhang, H.; Liu, B., Hierarchical Ni-Mo-S nanosheets on carbon fiber cloth: A flexible electrode for efficient hydrogen generation in neutral electrolyte. *Science Advances* **2015,** *1*.

106. Liu, P.; Zhu, J.; Zhang, J.; Xi, P.; Tao, K.; Gao, D.; Xue, D., P Dopants Triggered New Basal Plane Active Sites and Enlarged Interlayer Spacing in MoS2 Nanosheets toward Electrocatalytic Hydrogen Evolution. *ACS Energy Letters* **2017,** *2*, 745-752.

107. Kong, D.; Cha, J. J.; Wang, H.; Lee, H. R.; Cui, Y., First-row transition metal dichalcogenide catalysts for hydrogen evolution reaction. *Energy & Environmental Science* **2013,** *6* (12), 3553-3558.

108. Li, Z.; Xiao, M.; Zhou, Y.; Zhang, D.; Wang, H.; Liu, X.; Wang, D.; Wang, W., Pyrite FeS2/C nanoparticles as an efficient bi-functional catalyst for overall water splitting. *Dalton Transactions* **2018,** *47*, 14917-14923.

109. Wang, J. Y.; Ouyang, T.; Li, N.; Ma, T.; Liu, Z. Q., S, N co-doped carbon nanotube-encapsulated core-shelled CoS2@Co nanoparticles: efficient and stable bifunctional catalysts for overall water splitting. *Science Bulletin* **2018,** *63*, 1130-1140.

110. Wu, Y.; Liu, Y.; Li, G. D.; Zou, X.; Lian, X.; Wang, D.; Sun, L.; Asefa, T.; Zou, X., Efficient electrocatalysis of overall water splitting by ultrasmall Ni x Co 3−x S 4 coupled Ni 3 S 2 nanosheet arrays. *Nano Energy* **2017,** *35*, 161-170.

111. Liu, W.; Hu, E.; Jiang, H.; Xiang, Y.; Weng, Z.; Li, M.; Fan, Q.; Yu, X.; Altman, E. I.; Wang, H., A highly active and stable hydrogen evolution catalyst based on pyrite-structured cobalt phosphosulfide. *Nature Communications* **2016,** *7*, 1-9.

112. Faber, M. S.; Lukowski, M. A.; Ding, Q.; Kaiser, N. S.; Jin, S., Earth-Abundant Metal Pyrites (FeS_2, CoS_2, NiS_2, and Their Alloys) for Highly Efficient Hydrogen Evolution and Polysulfide Reduction Electrocatalysis. *The Journal of Physical Chemistry C* **2014,** *118* (37), 21347-21356.

113. Chen, L.; Dong, X.; Wang, F.; Wang, Y.; Xia, Y., Base-acid hybrid water electrolysis. *Chemical Communications* **2016,** *52* (15), 3147-3150.

114. Symes, M. D.; Cronin, L., Decoupling hydrogen and oxygen evolution during electrolytic water splitting using an electron-coupled-proton buffer. *Nat Chem* **2013,** *5* (5), 403-409.

115. Kokoh, K. B.; Mayousse, E.; Napporn, T. W.; Servat, K.; Guillet, N.; Soyez, E.; Grosjean, A.; Rakotondrainibé, A.; Paul-Joseph, J., Efficient multi-metallic anode catalysts in a PEM water electrolyzer. *International Journal of Hydrogen Energy* **2014,** *39* (5), 1924-1931.

116. Schlapbach, L.; Zuttel, A., Hydrogen-storage materials for mobile applications. *Nature* **2001,** *414* (6861), 353-358.

117. Niemann, M. U.; Srinivasan, S. S.; Phani, A. R.; Kumar, A.; Goswami, D. Y.; Stefanakos, E. K., Nanomaterials for Hydrogen Storage Applications: A Review. *Journal of Nanomaterials* **2008,** *2008*, 1-9.

118. Mitsushima, S.; Takakuwa, Y.; Nagasawa, K.; Sawaguchi, Y.; Kohno, Y.; Matsuzawa, K.; Awaludin, Z.; Kato, A.; Nishiki, Y., Membrane Electrolysis of Toluene Hydrogenation with Water Decomposition for Energy Carrier Synthesis. *Electrocatalysis* **2016,** *7* (2), 127-131.

119. Nagai, K.; Nagasawa, K.; Mitsushima, S., OER Activity of Ir-Ta-Zr Composite Anode as a Counter Electrode for Electrohydrogenation of Toluene. *Electrocatalysis* **2016**, 1-4.

120. Takano, K.; Tateno, H.; Matsumura, Y.; Fukazawa, A.; Kashiwagi, T.; Nakabayashi, K.; Nagasawa, K.; Mitsushima, S.; Atobe, M., Electrocatalytic Hydrogenation of o-Xylene in a PEM Reactor as a Study of a Model Reaction for Hydrogen Storage. *Chemistry Letters* **2016**, DOI: 10.1246/cl.160766.

121. McLellan, R.; Harkins, C. G., Hydrogen interactions with metals. *Materials Science and Engineering* **1975,** *18* (1), 5-35.

122. Murphy, D. W.; Zahurak, S. M.; Vyas, B.; Thomas, M.; Badding, M. E.; Fang, W. C., A new route to metal hydrides. *Chemistry of Materials* **1993,** *5* (6), 767-769.

123. Li, G.; Kobayashi, H.; Taylor, J. M.; Ikeda, R.; Kubota, Y.; Kato, K.; Takata, M.; Yamamoto, T.; Toh, S.; Matsumura, S.; Kitagawa, H., Hydrogen storage in Pd nanocrystals covered with a metal–organic framework. *Nat Mater* **2014,** *13* (8), 802-806.

124. Shegai, T.; Langhammer, C., Hydride Formation in Single Palladium and Magnesium Nanoparticles Studied By Nanoplasmonic Dark-Field Scattering Spectroscopy. *Advanced Materials* **2011,** *23* (38), 4409-4414.

125. Baldi, A.; Narayan, T. C.; Koh, A. L.; Dionne, J. A., In situ detection of hydrogen-induced phase transitions in individual palladium nanocrystals. *Nat Mater* **2014,** *13* (12), 1143-1148.

126. Bardhan, R.; Hedges, L. O.; Pint, C. L.; Javey, A.; Whitelam, S.; Urban, J. J., Uncovering the intrinsic size dependence of hydriding phase transformations in nanocrystals. *Nat Mater* **2013,** *12* (10), 905-912.

127. Syrenova, S.; Wadell, C.; Nugroho, F. A. A.; Gschneidtner, T. A.; Diaz Fernandez, Y. A.; Nalin, G.; Switlik, D.; Westerlund, F.; Antosiewicz, T. J.; Zhdanov, V. P.; Moth-Poulsen, K.; Langhammer, C., Hydride formation thermodynamics and hysteresis in individual Pd nanocrystals with different size and shape. *Nature Materials* **2015,** *14*, 1236–1244.

128. Hou, X.; Amais, R. S.; Jones, B. T.; Donati, G. L., Inductively Coupled Plasma Optical Emission Spectrometry. *Encyclopedia of Analytical Chemistry: Applications, Theory and Instrumentation* **2016**, Edition John Wiley & Sons, Ltd.

129. Behrens, M.; Schlögl, R., X-Ray Diffraction and Small Angle X-Ray Scattering. *Characterization of Solid Materials and Heterogeneous Catalysts: From Structure to Surface Reactivity* **2012,** *Chapter 15*, 609-653.

130. Stanjek, H.; Häusler, W., Basics of X-ray Diffraction. *Hyperfine Interactions* **2004,** *154*, 107-119.

131. Fan, F.; Feng, Z.; Li, C., Raman and UV-Raman Spectroscopies. *Characterization of Solid Materials and Heterogeneous Catalysts: From Structure to Surface Reactivity* **2012,** *Chapter 2*, 49-87.

132. Grünert, W., Auger Electron, X ray and UV Photoelectron Spectroscopies. *Characterization of Solid Materials and Heterogeneous Catalysts: From Structure to Surface Reactivity* **2012,** *Chapter 13*, 537-583.

133. Greczynski, G.; Hultman, L., A step-by-step guide to perform x-ray photoelectron spectroscopy. *Journal of Applied Physics* **2022,** *132* (1), 011101.

134. Ul-Hamid, A., A Beginners' Guide to Scanning Electron Microscopy. **2018**, 1st Edition, Springer.

135. Thomas, J. M.; Ducati, C., Transmission Electron Microscopy. *Characterization of Solid Materials and Heterogeneous Catalysts: From Structure to Surface Reactivity* **2012,** *Chapter 16*, 655-701.

136. Sawyer, D. T.; Sobkowiak, A.; Roberts, J. L., Electrochemistry for Chemists. **1995,** *2nd Edition*.

137. Ciucci, F., Modeling electrochemical impedance spectroscopy. *Current Opinion in Electrochemistry* **2019,** *13*, 132-139.

138. Ribeiro, J., Electrochemical Impedance Spectroscopy: a tool on the electrochemical investigations. *Revista Virtual de Química* **2020,** *12*, 1-16.

139. Kong, D.; Cha, J. J.; Wang, H.; Lee, H. R.; Cui, Y., First-row transition metal dichalcogenide catalysts for hydrogen evolution reaction. *Energy and Environmental Science* **2013,** *6*, 3553-3558.

140. Sharma, S.; Ghoshal, S. K., Hydrogen the future transportation fuel: From production to applications. *Renewable and Sustainable Energy Reviews* **2015,** *43*, 1151-1158.

141. Anantharaj, S.; Ede, S. R.; Sakthikumar, K.; Karthick, K.; Mishra, S.; Kundu, S., Recent Trends and Perspectives in Electrochemical Water Splitting with an Emphasis on Sulfide, Selenide, and Phosphide Catalysts of Fe, Co, and Ni: A Review. *ACS Catalysis* **2016,** *6*, 8069-8097.

142. Lasia, A., Mechanism and kinetics of the hydrogen evolution reaction. *International Journal of Hydrogen Energy* **2019,** *44*, 19484-19518.

143. Xi, F.; Bogdanoff, P.; Harbauer, K.; Plate, P.; Ho, C.; Rappich, J.; Wang, B.; Han, X.; Krol, R. V. D.; Fiechter, S., Structural Transformation Identification of Sputtered Amorphous MoSx as an Efficient Hydrogen-Evolving Catalyst during Electrochemical Activation. **2019**.

144. Ding, Q.; Song, B.; Xu, P.; Jin, S., Efficient Electrocatalytic and Photoelectrochemical Hydrogen Generation Using MoS2 and Related Compounds. *Chem* **2016,** *1*, 699-726.

145. Yu, F.; Zhou, H.; Huang, Y.; Sun, J.; Qin, F.; Bao, J.; Goddard, W. A.; Chen, S.; Ren, Z., High-performance bifunctional porous non-noble metal phosphide catalyst for overall water splitting. *Nature Communications* **2018,** *9*, 1-9.

146. Rong, J.; Ye, Y.; Cao, J.; Liu, X.; Fan, H.; Yang, S.; Wei, M.; Yang, L.; Yang, J.; Chen, Y., Restructuring electronic structure via W doped 1T MoS2 for enhancing hydrogen evolution reaction. *Applied Surface Science* **2022,** *579*, 152216.

147. Jiang, J.; Sun, R.; Huang, X.; Cong, H.; Tang, J.; Xu, W.; Li, M.; Chen, Y.; Wang, Y.; Han, S.; Lin, H., CoS2 quantum dots modified by ZIF-67 and anchored on reduced graphene oxide as an efficient catalyst for hydrogen evolution reaction. *Chemical Engineering Journal* **2022,** *430*, 132634.
148. Laursen, A. B.; Kegnæs, S.; Dahl, S.; Chorkendorff, I., Molybdenum sulfides - Efficient and viable materials for electro - and photoelectrocatalytic hydrogen evolution. *Energy and Environmental Science* **2012,** *5*, 5577-5591.
149. Jaramillo, T. F.; Jørgensen, K. P.; Bonde, J.; Nielsen, J. H.; Horch, S.; Chorkendorff, I., Identification of active edge sites for electrochemical H2 evolution from MoS2 nanocatalysts. *Science* **2007,** *317*, 100-102.
150. Zhang, J.; Liu, Y.; Sun, C.; Xi, P.; Peng, S.; Gao, D.; Xue, D., Accelerated Hydrogen Evolution Reaction in CoS2 by Transition-Metal Doping. *ACS Energy Letters* **2018,** *3* (4), 779-786.
151. Fang, L.; Zhang, Y.; Guan, Y.; Zhang, H.; Wang, S.; Wang, Y., Specific synthesis of CoS2 nanoparticles embedded in porous Al2O3 nanosheets for efficient hydrogen evolution and enhanced lithium storage. *Journal of Materials Chemistry A* **2017,** *5* (6), 2861-2869.
152. Anantharaj, S.; Noda, S.; Jothi, V.; Yi, S.; Driess, M.; Menezes, P., Strategies and Perspectives to Catch the Missing Pieces in Energy-Efficient Hydrogen Evolution Reaction in Alkaline Media. *Angewandte Chemie - International Edition* **2021,** *60*, 18981-19006.
153. Mahmood, N.; Yao, Y.; Zhang, J. W.; Pan, L.; Zhang, X.; Zou, J. J., Electrocatalysts for Hydrogen Evolution in Alkaline Electrolytes: Mechanisms, Challenges, and Prospective Solutions. *Advanced Science* **2018,** *5*.
154. Motealleh, B.; Liu, Z.; Masel, R. I.; Sculley, J. P.; Richard Ni, Z.; Meroueh, L., Next-generation anion exchange membrane water electrolyzers operating for commercially relevant lifetimes. *International Journal of Hydrogen Energy* **2021,** *46*, 3379-3386.
155. Liu, Z.; Sajjad, S. D.; Gao, Y.; Yang, H.; Kaczur, J. J.; Masel, R. I., The effect of membrane on an alkaline water electrolyzer. *International Journal of Hydrogen Energy* **2017,** *42*, 29661-29665.
156. Gao, M. R.; Chan, M. K.; Sun, Y., Edge-terminated molybdenum disulfide with a 9.4-A interlayer spacing for electrochemical hydrogen production. *Nat Commun* **2015,** *6*, 7493.
157. Niefind, F.; Bensch, W.; Deng, M.; Kienle, L.; Cruz-Reyes, J.; Del Valle Granados, J. M., Co-promoted MoS2 for hydrodesulfurization: New preparation method of MoS2 at room temperature and observation of massive differences of the selectivity depending on the activation atmosphere. *Applied Catalysis A: General* **2015,** *497*, 72-84.
158. Joensen, P.; Crozier, E. D.; Alberding, N.; Frindt, R. F., A study of single-layer and restacked MoS_2 by x-ray diffraction and x-ray absorption spectroscopy. *Journal of Physics C: Solid State Physics* **1987,** *20*, 4043-4053.
159. Xie, J.; Zhang, H.; Li, S.; Wang, R.; Sun, X.; Zhou, M.; Zhou, J.; Lou, X. W.; Xie, Y., Defect-rich MoS2 ultrathin nanosheets with additional active edge sites for enhanced electrocatalytic hydrogen evolution. *Advanced Materials* **2013,** *25*, 5807-5813.
160. Lyapin, S. G.; Utyuzh, A. N.; Petrova, A. E.; Novikov, A. P.; Lograsso, T. A.; Stishov, S. M., Raman studies of nearly half-metallic ferromagnetic CoS2. *Journal of Physics Condensed Matter* **2014,** *26*, 1-6.

161. Buzgar, N.; Buzatu, A.; Sanislav, I. V., The Raman study on certain sulfates. *Analele Stiintifice ale Universitatii " Al. I. Cuza" din Iasi , Geologie* **2009,** *55*, 5-23.

162. Zoller, M.; Bubnova, R.; Biryukov, Y.; Haussühl, E.; Pöttgen, R.; Janka, O.; Penner, S.; Praty, C.; Fitzek, H.; Winkler, J.; Filatov, S.; Huppertz, H., Elucidating the physical properties of the molybdenum oxide Mo4O11 and its tantalum substituted variant Mo2Ta2O11. *Zeitschrift für Kristallographie - Crystalline Materials* **2020,** *235* (4-5), 143-155.

163. Pham, D. V.; Patil, R. A.; Lin, J. H.; Lai, C. C.; Liou, Y.; Ma, Y. R., Doping-free bandgap tuning in one-dimensional Magneli-phase nanorods of Mo4O11. *Nanoscale* **2016,** *8* (10), 5559-66.

164. Dieterle, M.; Mestl, G., Raman spectroscopy of molybdenum oxides. *Physical Chemistry Chemical Physics* **2002,** *4* (5), 822-826.

165. Kong, D.; Wang, H.; Cha, J. J.; Pasta, M.; Koski, K. J.; Yao, J.; Cui, Y., Synthesis of MoS2 and MoSe2 films with vertically aligned layers. *Nano Letters* **2013,** *13*, 1341-1347.

166. Xu, X.; Liu, Q.; Liang, L.; Gu, H.; Zhao, Y.; Xing, X.; Zhang, X.; Hu, Y., Well-designed nanosheet-constructed porous CoMoS4 arrays for ultrahigh-performance supercapacitors. *Ceramics International* **2020,** *46*, 4878-4888.

167. Xu, X.; Song, Y.; Xue, R.; Zhou, J.; Gao, J.; Xing, F., Amorphous CoMoS4 for a valuable energy storage material candidate. *Chemical Engineering Journal* **2016,** *301*, 266-275.

168. Wang, W.; Xu, Y.; Yao, J.; Liu, X.; Yin, Z.; Li, Z., Enhanced oxygen and hydrogen evolution performance by carbon-coated CoS2-FeS2 nanosheets. *Dalton Transactions* **2020,** *49* (38), 13352-13358.

169. Hartel, P.; Rose, H.; Dinges, C., Conditions and reasons for incoherent imaging in STEM. *Ultramicroscopy* **1996,** *63* (2), 93-114.

170. Tang, Y. J.; Zhang, A. M.; Zhu, H. J.; Dong, L. Z.; Wang, X. L.; Li, S. L.; Han, M.; Xu, X. X.; Lan, Y. Q., Polyoxometalate precursors for precisely controlled synthesis of bimetallic sulfide heterostructure through nucleation-doping competition. *Nanoscale* **2018,** *10* (18), 8404-8412.

171. Palencia-Ruiz, S.; Uzio, D.; Legens, C.; Laurenti, D.; Afanasiev, P., Stability and catalytic properties of 1T-MoS2 obtained via solvothermal synthesis. *Applied Catalysis A: General* **2021,** *626*, 118355.

172. Vrubel, H.; Hu, X., Growth and Activation of an Amorphous Molybdenum Sul fi de Hydrogen Evolving Catalyst. *ACS Catalysis* **2013,** *3*, 2002-2011.

173. Muijsers, J. C.; Weber, T.; van Hardeveld, R. M.; Zandbergen, H. W.; Niemantsverdriet, J. W. H., Sulfidation study of molybdenum oxide using MoO3/SiO2/Si(100) model catamysts and Mo3(IV)-sulfur cluster compounds. *Journal of Catalysis* **1995,** *157*, 698-705.

174. Lukowski, M. A.; Daniel, A. S.; Meng, F.; Forticaux, A.; Li, L.; Jin, S., Enhanced hydrogen evolution catalysis from chemically exfoliated metallic MoS2 nanosheets. *Journal of the American Chemical Society* **2013,** *135*, 10274-10277.

175. Benck, J. D.; Hellstern, T. R.; Kibsgaard, J.; Chakthranont, P.; Jaramillo, T. F., Catalyzing the hydrogen evolution reaction (HER) with molybdenum sulfide nanomaterials. *ACS Catalysis* **2014,** *4*, 3957-3971.

176. Santoro, C.; Lavacchi, A.; Mustarelli, P.; Di Noto, V.; Elbaz, L.; Dekel, D. R.; Jaouen, F., What is Next in Anion-Exchange Membrane Water Electrolyzers? Bottlenecks, Benefits, and Future. *ChemSusChem* **2022**, e202200027.

177. Inocêncio, C. V. M.; Rousseau, J.; Guignard, N.; Canaff, C.; Morisset, S.; Comminges, C.; Morais, C.; Kokoh, K. B., Taking Advantage of Teamwork: Unsupported Cobalt Molybdenum Sulfide as an Active HER Electrocatalyst in Alkaline Media. *Journal of The Electrochemical Society* **2022,** *169* (5), 054524.

178. Zhang, J.; Wang, T.; Liu, P.; Liu, S.; Dong, R.; Zhuang, X.; Chen, M.; Feng, X., Engineering water dissociation sites in MoS2 nanosheets for accelerated electrocatalytic hydrogen production. *Energy and Environmental Science* **2016,** *9*, 2789-2793.

179. Faid, A. Y.; Barnett, A. O.; Seland, F.; Sunde, S., NiCu mixed metal oxide catalyst for alkaline hydrogen evolution in anion exchange membrane water electrolysis. *Electrochimica Acta* **2021,** *371*, 137837.

180. Guo, W.; Kim, J.; Kim, H.; Ahn, S. H., Direct electrodeposition of Ni-Co-S on carbon paper as an efficient cathode for anion exchange membrane water electrolysers. *International Journal of Energy Research* **2021,** *45* (2), 1918-1931.

181. Faid, A.; Oyarce Barnett, A.; Seland, F.; Sunde, S., Highly Active Nickel-Based Catalyst for Hydrogen Evolution in Anion Exchange Membrane Electrolysis. *Catalysts* **2018,** *8* (12), 614.

182. Park, Y. S.; Lee, J. H.; Jang, M. J.; Jeong, J.; Park, S. M.; Choi, W.-S.; Kim, Y.; Yang, J.; Choi, S. M., Co3S4 nanosheets on Ni foam via electrodeposition with sulfurization as highly active electrocatalysts for anion exchange membrane electrolyzer. *International Journal of Hydrogen Energy* **2020,** *45* (1), 36-45.

183. Raja Sulaiman, R. R.; Wong, W. Y.; Loh, K. S., Recent developments on transition metal–based electrocatalysts for application in anion exchange membrane water electrolysis. *International Journal of Energy Research* **2021,** *46* (3), 2241-2276.

184. Gallant, D.; Pézolet, M.; Simard, S., Optical and Physical Properties of Cobalt Oxide Films Electrogenerated in Bicarbonate Aqueous Media. *The Journal of Physical Chemistry B* **2006,** *110*, 6871-6880.

185. Zhang, H.; Maijenburg, A. W.; Li, X.; Schweizer, S. L.; Wehrspohn, R. B., Bifunctional Heterostructured Transition Metal Phosphides for Efficient Electrochemical Water Splitting. *Advanced Functional Materials* **2020,** *30* (34), 2003261.

186. Zou, X.; Zhang, Y., Noble metal-free hydrogen evolution catalysts for water splitting. *Chemical Society Reviews* **2015,** *44*, 5148-5180.

187. Hu, C.; Zhang, L.; Gong, J., Recent progress made in the mechanism comprehension and design of electrocatalysts for alkaline water splitting. *Energy and Environmental Science* **2019,** *12*, 2620-2645.

188. Inocêncio, C. V. M.; Fouda-Onana, F.; Rousseau, J.; Guignard, N.; Napporn, T.; Morais, C.; Kokoh, K. B., A Step Forward: Hydrogen Production on Cobalt Molybdenum Sulfide Electrocatalyst in Anion Exchange Membrane Water Electrolyzer. *ACS Applied Energy Materials* **2022**.

189. Hacker, V.; Mitsushima, S. In *Fuel Cells and Hydrogen: From Fundamentals to Applied Research*, 1st Edition Elsevier, 2018.

190. Huang, G.; Mandal, M.; Hassan, N. U.; Groenhout, K.; Dobbs, A.; Mustain, W. E.; Kohl, P. A., Ionomer Optimization for Water Uptake and Swelling in Anion Exchange Membrane Electrolyzer: Oxygen Evolution Electrode. *Journal of The Electrochemical Society* **2020,** *167* (16), 164514.

191. Henkensmeier, D.; Najibah, M.; Harms, C.; Žitka, J.; Hnát, J.; Bouzek, K., Overview: State-of-the Art Commercial Membranes for Anion Exchange Membrane Water Electrolysis. *Journal of Electrochemical Energy Conversion and Storage* **2021,** *18* (2).

192. Wang, M.; Zhang, L.; He, Y.; Zhu, H., Recent advances in transition-metal-sulfide-based bifunctional electrocatalysts for overall water splitting. *Journal of Materials Chemistry A* **2021,** *9* (9), 5320-5363.

193. Kabir, S.; Lemire, K.; Artyushkova, K.; Roy, A.; Odgaard, M.; Schlueter, D.; Oshchepkov, A.; Bonnefont, A.; Savinova, E.; Sabarirajan, D. C.; Mandal, P.; Crumlin, E. J.; Zenyuk, Iryna V.; Atanassov, P.; Serov, A., Platinum group metal-free NiMo hydrogen oxidation catalysts: high performance and durability in alkaline exchange membrane fuel cells. *Journal of Materials Chemistry A* **2017,** *5* (46), 24433-24443.

194. Faid, A. Y.; Xie, L.; Barnett, A. O.; Seland, F.; Kirk, D.; Sunde, S., Effect of anion exchange ionomer content on electrode performance in AEM water electrolysis. *International Journal of Hydrogen Energy* **2020,** *45* (53), 28272-28284.

195. Garsany, Y.; Baturina, O. A.; Swider-Lyons, K. E.; Kocha, S. S., Experimental Methods for Quantifying the Activity of Platinum Electrocatalysts for the Oxygen Reduction Reaction. *Analytical Chemistry* **2010,** *82*, 6321-6328.

196. Ghoshal, S.; Pivovar, B. S.; Alia, S. M., Evaluating the effect of membrane-ionomer combinations and supporting electrolytes on the performance of cobalt nanoparticle anodes in anion exchange membrane electrolyzers. *Journal of Power Sources* **2021,** *488*, 229433.

197. Ulbrich, K. F.; Souza, B. S.; Campos, C. E. M., Synthesis of n-hydrated nickel sulfates from mechanically alloyed nanocrystalline nickel sulfides. *Green Chemistry* **2021,** *23* (12), 4580-4593.

198. Wu, Z.; Huang, L.; Liu, H.; Li, M.; Wang, H., Surface oxidation of transition metal sulfide and phosphide nanomaterials. *Nano Research* **2020,** *14* (7), 2264-2267.

199. Wan, K.; Luo, J.; Zhou, C.; Zhang, T.; Arbiol, J.; Lu, X.; Mao, B. W.; Zhang, X.; Fransaer, J., Hierarchical Porous Ni 3 S 4 with Enriched High-Valence Ni Sites as a Robust Electrocatalyst for Efficient Oxygen Evolution Reaction. *Advanced Functional Materials* **2019,** *29*, 1-8.

200. Yang, S. L.; Yao, H. B.; Gao, M. R.; Yu, S. H., Monodisperse cubic pyrite NiS2 dodecahedrons and microspheres synthesized by a solvothermal process in a mixed solvent: Thermal stability and magnetic properties. *CrystEngComm* **2009,** *11*, 1383-1390.

201. Suzuki, T.; Uchinokura, K.; Sekine, T.; Matsuura, E., Raman scattering of NiS2. *Solid State Communications* **1977,** *23*, 847-852.

202. Lee, J. U.; Park, J.; Son, Y. W.; Cheong, H., Anomalous excitonic resonance Raman effects in few-layered MoS2. *Nanoscale* **2015,** *7* (7), 3229-36.

203. Politano, G. G.; Castriota, M.; Santo, M. P. D.; Pipita, M. M.; Desiderio, G.; Vena, C.; Versace, C., Physical Investigation of Spin-Coated MoS2 Films. *Materials Proceedings* **2020,** *4* (1), 3.

204. Mignuzzi, S.; Pollard, A. J.; Bonini, N.; Brennan, B.; Gilmore, I. S.; Pimenta, M. A.; Richards, D.; Roy, D., Effect of disorder on Raman scattering of single-layerMoS2. *Physical Review B* **2015,** *91* (19).

205. Xu, X.; Liang, L.; Zhang, X.; Xing, X.; Zhao, Y.; Gao, J.; Wei, A., Design of reduced graphene oxide supported NiMoS4 to enhance energy capacity of hybrid supercapacitors. *Colloids and Surfaces A: Physicochemical and Engineering Aspects* **2020,** *586*, 124289.

206. Sathiyaraj, E.; Gurumoorthy, G.; Thirumaran, S., Nickel(ii) dithiocarbamate complexes containing the pyrrole moiety for sensing anions and synthesis of nickel sulfide and nickel oxide nanoparticles. *New Journal of Chemistry* **2015,** *39* (7), 5336-5349.

207. Bocquet, A. E.; Mamiya, K.; Mizokawa, T.; Fujimori, A.; Miyadai, T.; Takahashi, H.; Môri, M.; Suga, S., Electronic structure of 3d transition metal pyrites MS2
(M = Fe, Co or Ni) by analysis of the M 2p core-level
photoemission spectra. *Journal of Physics: Condensed Matter* **1996,** *8*, 2389-2400.

208. Guichard, B.; Roy-Auberger, M.; Devers, E.; Legens, C.; Raybaud, P., Aging of Co(Ni)MoP/Al2O3 catalysts in working state. *Catalysis Today* **2008,** *130* (1), 97-108.

209. Rickman, J. T.; Linton, R. W., Surface and depth profiling techniques using XPS applied to the study of nickel-containing environmental particles. *Applied Surface Science* **1993,** *68*, 375-393.

210. Zhang, B.; Liu, J.; Wang, J.; Ruan, Y.; Ji, X.; Xu, K.; Chen, C.; Wan, H.; Miao, L.; Jiang, J., Interface engineering: The Ni(OH)2/MoS2 heterostructure for highly efficient alkaline hydrogen evolution. *Nano Energy* **2017,** *37*, 74-80.

211. Oener, S. Z.; Foster, M. J.; Boettcher, S. W., Accelerating water dissociation in bipolar membranes and for electrocatalysis. *Science* **2020,** *369*, 1099-1103.

212. Xu, D.; Stevens, M. B.; Cosby, M. R.; Oener, S. Z.; Smith, A. M.; Enman, L. J.; Ayers, K. E.; Capuano, C. B.; Renner, J. N.; Danilovic, N.; Li, Y.; Wang, H.; Zhang, Q.; Boettcher, S. W., Earth-Abundant Oxygen Electrocatalysts for Alkaline Anion-Exchange-Membrane Water Electrolysis: Effects of Catalyst Conductivity and Comparison with Performance in Three-Electrode Cells. *ACS Catalysis* **2019,** *9* (1), 7-15.

213. Huang, S.; Ma, D.; Hu, Z.; He, Q.; Zai, J.; Chen, D.; Sun, H.; Chen, Z.; Qiao, Q.; Wu, M.; Qian, X., Synergistically Enhanced Electrochemical Performance of Ni3S4-PtX (X = Fe, Ni) Heteronanorods as Heterogeneous Catalysts in Dye-Sensitized Solar Cells. *ACS Appl Mater Interfaces* **2017,** *9* (33), 27607-27617.

214. Rudi, S.; Cui, C.; Gan, L.; Strasser, P., Comparative Study of the Electrocatalytically Active Surface Areas (ECSAs) of Pt Alloy Nanoparticles Evaluated by Hupd and CO-stripping voltammetry. *Electrocatalysis* **2014,** *5*, 408-418.

215. Li, D.; Chung, H. T.; Maurya, S.; Matanovic, I.; Kim, Y. S., Impact of ionomer adsorption on alkaline hydrogen oxidation activity and fuel cell performance. *Current Opinion in Electrochemistry* **2018,** *12*, 189-195.

216. Bates, M. K.; Jia, Q.; Ramaswamy, N.; Allen, R. J.; Mukerjee, S., Composite Ni/NiO-Cr2O3 Catalyst for Alkaline Hydrogen Evolution Reaction. *The journal of physical chemistry. C, Nanomaterials and interfaces* **2015,** *119* (10), 5467-5477.

Sustainable Hydrogen Production on PGM-free Electrocatalytic Materials in Anion Exchange Membrane Water Electrolyzer (AEMWE)

Abstract

Electrochemical production of green hydrogen applying earth-abundant and cheap materials as electrocatalysts of water electrolyzers, will play an important role in energy transition, besides to boost the development of more sustainable processes in the chemical industry sector.
Due to this context, this work proposes the development of alternative cathode, for the replacement of platinum as catalyst of hydrogen evolution reaction (HER). The focus concerned the application of promising discovered materials in an anion exchange membrane water electrolyzer (AEMWE) device. Monometallic and bimetallic transition metal sulfides (TMS), concerning Ni-, Co- and Mo-based materials, were hydrothermally synthesized and physicochemically characterized. Electrochemical studies evidenced a synergistic effect arising from the association of 2H-MoS_2 phase with a second metal compound. Such synergy was attributed to the cobalt and nickel ability to dissociate water, contrary to MoS_2, which is a necessary step in alkaline media. Despite that, nickel molybdenum sulfide ($Ni_{0.5}Mo_{0.5}S_x$) and cobalt molybdenum sulfide ($Co_{0.5}Mo_{0.5}S_x$) showed to have their HER kinetics limited by their conductivity. This issue was overcome by adding Carbon Vulcan XC72R in the ink formulation, which led $Co_{0.5}Mo_{0.5}S_x$ and $Ni_{0.5}Mo_{0.5}S_x$ to deliver a current density of 200 mA cm^{-2} at overpotentials only 66 and 60 mV higher than 40 wt.% Pt/C, respectively.
Besides that, an exploratory study of ink formulations replacing Nafion® ionomer by the Sustainion® XB-7 one was provided, applying $Ni_{0.5}Mo_{0.5}S_x$ as catalyst. It was verified that, to maintain a comparable activity, ionomer content must be reduced, and the solvent ratio also needed to be regulated; higher volume of isopropanol than water was required. It highlights how unique is the catalyst/ionomer interaction and shed light on the importance of studying it.
Finally, an AEMWE single cell was constructed by applying $Co_{0.5}Mo_{0.5}S_x$, Sustainion® X37-50 and Ir black, as cathode, anion exchange membrane and anode, respectively. By operating this cell at 50 ^oC and with 0.1 mol L^{-1} KOH solution recirculation in the anode compartment, a current density of 1.2 A cm^{-2} was obtained at 2 V. This system was then submitted to 40 h stability testing, and showed some current decay during operation, although most of decay can be recovered by stopping voltage application, likely due to the bubbles release. Furthermore, the irreversible current decay was attributed to the Co and Mo segregation, which diminishes their interaction and impact material's activity that comes from a bifunctional behavior.

Keywords: hydrogen evolution; nanomaterials; hydrothermal synthesis; transition metal sulfide; molybdenum; ionomer; water electrolysis; anion exchange membrane.

Réduction de l'eau en dihydrogène sur nanomatériaux d'électrode sans platinoïde

Résumé

La production électrochimique d'hydrogène vert sur des matériaux d'électrode abondants sur terre par électrolyse de l'eau jouera un rôle important dans la transition énergétique, en plus de stimuler le développement de procédés plus durables dans le secteur de l'industrie chimique.
Dans ce contexte, ce travail propose la synthèse et le design d'une cathode alternative au platine comme catalyseur de la réaction de dégagement d'hydrogène (HER) dans un électrolyseur d'eau à membrane échangeuse d'anions (AEMWE). A cette fin, des sulfures de métaux de transition (TMS) monométalliques et bimétalliques, à base de Ni, Co et Mo, ont été préparés par voie hydrothermale et caractérisés physicochimiquement. Des études électrochimiques ont mis en évidence un effet synergique résultant de l'association de la phase 2H-MoS_2 avec un second composé métallique. Cette synergie a été attribuée à la capacité du cobalt ou du nickel à dissocier l'eau, contrairement au MoS_2, qui est une étape prépondérante en milieu alcalin. Ainsi, le sulfure de nickel-molybdène ($Ni_{0,5}Mo_{0,5}S_x$) et le sulfure de cobalt-molybdène ($Co_{0,5}Mo_{0,5}S_x$) ont montré que leur cinétique HER est limitée par leur conductivité, ce qui peut être pallié par l'ajout d'un substrat conducteur électronique (Carbon Vulcan XC72R) dans la formulation de l'encre catalytique. Cela a conduit à une densité de courant de 200 mA cm^{-2} sur $Co_{0,5}Mo_{0,5}S_x$ et $Ni_{0,5}Mo_{0,5}S_x$ avec des surtensions respectives de seulement 66 et 60 mV supérieures à celles obtenues sur Pt/C à un taux de charge de 40 wt.%.
Une étude exploratoire de formulations d'encres catalytiques contenant le catalyseur $Ni_{0.5}Mo_{0.5}S_x$ a aussi été effectuée pour comparer l'efficacité du liant entre les ionomères Nafion® et Sustainion®. Pour maintenir une activité comparable au ionomère Nafion, la teneur en ionomère Sustainion a dû être réduite, et le taux de solvant organique, augmenté dans le ratio isopropanol/eau.
Enfin, un électrolyseur a été construit avec assemblage membrane électrodes (AME) qui est composé de $Co_{0.5}Mo_{0.5}S_x$ (cathode), Ir black (anode), le tout déposé sur la membrane échangeuse anionique Sustainion® X37-50. Il a été mis en fonctionnement à 50 °C et en circulant une solution alcaline (KOH 0,1 mol L^{-1}) dans le compartiment anodique. Une densité de courant de 1,2 A cm^{-2} a été mesurée lorsque la tension de cellule atteint 2 V. L'électrolyseur a ensuite été soumis à des tests de stabilité de plus 40 h et a montré une certaine décroissance du courant due probablement à la formation de bulles. En outre, une décroissance irréversible du courant est attribuée à la ségrégation des particules de Co et Mo. Cela se traduit par une diminution de leur interaction et une baisse d'activité bifonctionnelle du catalyseur bimétallique.

Mot-clés: dégagement d'hydrogène; nanomatériaux; synthèse hydrothermale; sulfure de métal de transition; molybdène; ionomère; électrolyse de l'eau; membrane échangeuse d'anions.